Studies into the Technical Feasibility of the Transverse Horizontal Axis Water Turbine

Ross McAdam

Keble College

Department of Engineering Science
University of Oxford

A thesis submitted for the degree of
Doctor of Philosophy

Trinity 2011

Abstract

Studies into the Technical Feasibility of the Transverse Horizontal Axis Water Turbine
Ross McAdam
Keble College, University of Oxford
A Thesis submitted for the degree of Doctor of Philosophy
Trinity term 2011

The Transverse Horizontal Axis Water Turbine (THAWT) has been proposed as a tidal device which can be easily scaled and requires fewer foundations, bearings seals and generators than a more conventional axial-flow device. The THAWT device is a horizontally deployed variant of the Darrieus cross-flow turbine, in which the blades can be oriented into a truss configuration to produce long, stiff multi-bay rotors.

This thesis establishes and combines a set of numerical models, which predict the hydrodynamic and structural performance of the THAWT device, with sufficient confidence to assess the feasibility of such a device at a full scale installation and to optimise its performance.

Tests of $1/20^{th}$ scale experimental models of the THAWT device have demonstrated that the truss configured device is capable of producing power with an efficiency close to that of the parallel configured turbine. In addition, variations in the configuration of the scale models have indicated how several design parameters affect the hydrodynamic performance of the device.

A two-dimensional Navier-Stokes blade element model has been developed, in which the THAWT device is represented using an actuator cylinder. The addition of a hydrostatic free surface deformation correction has resulted in a model which is capable of matching experimental results with sufficient fidelity and accuracy.

Blade loads from the numerical hydrodynamic model have been applied to a beam finite element analysis, to predict the stresses induced in the hydrofoils of the THAWT device.

The numerical and hydrodynamic models are combined with a Linear Channel Momentum model to predict the performance of the THAWT device at a full scale tidal location. The effect that the device has on the channel flow indicates how much energy is available for extraction and how this energy might be most efficiently obtained. When considering material fatigue the analysis suggests that the structural design considerations dominate over the hydrodynamic considerations.

Acknowledgements

I would first like to thank my two supervisors during my DPhil, Guy Houlsby and Malcolm McCulloch. Throughout the course of this project Guy has given me an incredible amount of motivation and guidance and I owe him a great debt of gratitude for being so generous with his time, especially when his departmental obligations were so consuming. I could not have asked for a better supervisor and I hope our working relationship continues until the world's coasts are covered with THAWTs. Whilst I rarely worked with Malcolm, as the project took a direction less familiar to him, without his enthusiasm and support I would never have started this DPhil. I greatly admire his drive to apply his academic work in the real world and I wish he received more recognition for his contribution in helping us all live sustainably.

I would also like to say thank you to MaryAnn, who has supported me through thick and thin during the last three and a half years. There were times when she was the only thing that kept me pushing and I will always be grateful for having her in my life.

Throughout my nine years in Oxford Martin Oldfield has ever been a presence that has guided me through my academic career and onwards, and I hope we can work together for many years to come. I must also acknowledge the great minds of Scott Draper and Claudio Consul, with whom I will always have fond memories of debating the best ways to design the tidal devices of the future, whether there is a future for them or not. I also cannot conceive how room 11 will push forward the boundaries of CFD research without the input of Esteban Ferrer, whose absolute understanding of fluid numerics has helped shape my work. Despite only working with them for a short period, both Simon McIntosh and Thomas Adcock have had a profound impact on my work and my concept of tidal power in general. The tests at Newcastle could not have gone ahead without the contributions of Yihui Shi, Clarissa Belloni and Justine Schluntz, who all gave up valuable time to help me during the tests.

I would also like to thank my parents for their support and unerring belief in my abilities to go out and do what I want. I owe my dad several journeys up and down the UK motorways.

Over the years I have been lucky to work with many great designers and technicians who have made the design, build and testing of my experimental work possible. More than any, I would like to thank John Hastings, who is better than all the design engineers that I have ever met. At Oxford Clive Baker, Graham Haynes, Bob Scott, John Brumfitt, Paul Bailey, Andy Soffe, Chris Waddup, Maurice Keeble-Smith, Cleve Williams and Bob Sawala have helped to build all of my turbines and taught me to how to be a practical engineer. While at Newcastle Bob Hindhaugh, Peter Bowes, Andrew Smith, Jerry Lambert, Liam Rogerson, Peter and Kieron Fallows saved my bacon on more than one occasion, especially when I arrived with the odd bit of equipment which didn't necessarily do what it was meant to. David Whitney, Anton Chittey, Ben Lavasani, Danny Williams, Charlie Warren, all the guys at FormTech, Acrona Engineering, Racing Fabrications, Si-Teck and Nortek have also been a pleasure to work with in making the experimental tests a success.

Despite pushing me right to the end I must thank my examiners Richard Willden and Trevor Whitaker, who both took the time to read my work, to appreciate it and to give me the final sense of achievement that has allowed me to close this chapter of my life. And finally I would like to thank those at Keble who made my life a pleasure over the last four years; Tom Ouldridge, Bobbles Pittam, Rick Wohlers, Rich Hopkins, Rich Masters, Dan James, Lucy Power, Abi Stone and everyone else in the MCR that I've shared a laugh with.

Contents

Nomenclature ..... **ix**

Chapter 1 Introduction **1**

1.1. Thesis scope 3

Chapter 2 Literature review **6**

2.1. Modern tidal technology 6

2.1.1. Axial-flow turbines 7

2.1.2. Cross-flow marine turbines 8

2.1.3. Oscillating and other devices 11

2.2. Transverse Horizontal Axis Water Turbine (THAWT) 11

2.2.1. Basic mechanics 12

2.3. Steady flow techniques for analysis of tidal devices 13

2.3.1. Actuator disc theory in Darrieus turbine analysis 14

2.3.2. Actuator Cylinder model 16

2.3.3. LMADT in open channel flow 16

2.4. Non-steady flow techniques for analysis of cross-flow devices 20

2.4.1. Vortex model based techniques 20

2.4.2. CFD techniques 22

2.5. Complications of local blade mechanics 24

2.5.1. Flow curvature effects 25

2.5.2. Dynamic stall 26

2.6. Free surface modelling 28

2.7. Tidal stream energy resource 30

2.7.1. Tidal energy around the UK 30

2.7.2. Principles of energy extraction 31

2.7.3. Typical UK tidal stream parameters 33

2.8. Structural analyses of tidal devices 33

2.9. Material fatigue considerations 34

2.10. Previous experimental and analytical work 37

2.10.1. Undergraduate Masters project performed by McAdam (2007) 37

2.10.2. Undergraduate Masters project performed by Swidenbank 39

2.11. Conclusions 41

Chapter 3 Blade Force and Stress Preliminary Analysis 42
3.1. Scenario for dimensional analysis 42
3.2. Variables and dimensionless groups 43
3.3. Dimensional analysis of blade forces 45
3.3.1. Relationship between induction factor and tip speed ratio 45
3.3.2. Derivation of variation of force per unit length 46
3.4. Dimensional analysis of induced stresses 47
3.5. Anticipated effect of negative offset pitch 48
3.6. Conclusions 50
Chapter 4 Newcastle experimental setup 51
4.1. Newcastle University combined wind, wave and current tank 51
4.2. Rotor design 52
4.2.1. Basic dimensions 52
4.2.1. Configuration variants 52
4.2.2. Rotor solidity 53
4.2.3. Hydrofoil design and manufacture 55
4.2.4. Test rotor specification 57
4.3. Test apparatus and instrumentation 57
4.3.1. Flow instrumentation 58
4.4. Experimental schedule 59
4.4.1. Blade pitching 61
4.4.2. Blockage ratio 61
4.4.3. Reversal of flow direction 61
4.4.4. Turbine height in flow 62
4.4.5. Waves 62
4.5. Data calibration 64
4.6. Confidence limits of experimental data 65
Chapter 5 Experimental results 67
5.1. Basic features of the experimental results 68
5.2. Repeatability of results 70
5.3. Comparison of truss blade performance at a blockage ratio of $B = 0.5$ 71
5.4. Comparison of basic configuration variations 73
5.5. Effect of a varied fixed pitch 76

5.6. Variation of the turbine blockage ratio 79
5.7. Effect of waves 80
5.8. Consistency with flow from either direction 81
5.9. Effect of turbine vertical position in the flow 82
5.10. Torque fluctuations 84
5.11. Anticipated trade-offs in structural and hydrodynamic performance 85
5.11.1. Effect of reduced solidity 85
5.11.2. Effect of negative offset pitch 86
5.11.3. Effect of increased blockage 86
5.12. Conclusions 87
Chapter 6 Momentum Blade-Element hydrodynamic model 88
6.1. Blade element model 88
6.2. Linear Momentum Actuator Disc Theory for Open Channel flow model 90
6.3. Combination of two techniques 91
6.4. Comparison of M-BE with experimental results 92
6.4.1. Comparisons of basic parallel-bladed tests 95
6.4.2. Comparison of fixed offset pitch results 98
6.4.3. Comparison of increased blockage prediction 99
6.5. Conclusions 101
Chapter 7 Quasi-steady Navier-Stokes Blade Element model 102
7.1. Methodology 104
7.1.1. COMSOL Multiphysics - Navier-Stokes partial differential equation solver 104
7.1.2. Choice of NS-BE solver technique 104
7.1.3. Solution stabilisation 105
7.1.4. Backward facing step model 107
7.1.5. Stabilisation applied to NS-BE model 111
7.1.6. Turbulence modelling 111
7.1.7. Application of the actuator cylinder forces 112
7.1.8. Lift and drag data 113
7.1.9. Reynolds number variation 114
7.1.10. Conformal mapping 114
7.1.11. Dynamic stall 114
7.1.12. Free surface deformation (NS-BE-FS) 117

7.1.13. Surface-tracking methodology 117
7.1.14. Free surface technique validation 119
7.2. Turbine simulation 120
7.2.1. Problem geometry 120
7.2.2. Boundary conditions 121
7.2.3. Calculation of depth change 122
7.2.4. Meshing 123
7.2.5. Effect of low diffusion 125
7.2.6. Solution convergence criterion 125
7.2.7. Application of the free surface model (NS-BE-FS) 126
7.3. Results for NS-BE model 128
7.3.1. Comparisons of basic three and six-bladed tests at $B = 0.5$ 131
7.3.2. Comparison of fixed offset pitch tests 134
7.3.3. Comparison of increased blockage tests 135
7.3.4. Summary of comparisons with M-BE model 138
7.3.5. NS-BE blade force prediction 138
7.3.6. Force observations of the fixed offset pitch 140
7.3.7. Effect of blockage on blade forces 142
7.3.8. Force comparisons with the analytical preliminary analysis 143
7.3.9. Validity of preliminary analysis assumptions 144
7.4. Results of the FS-NS-BE model 144
7.4.1. Comparison of basic three and six parallel-blade tests at $B = 0.5$ 145
7.4.2. Comparison of fixed offset pitch results 146
7.4.3. Comparison of increased blockage results 148
7.4.4. Summary of NS-BE-FS results and blockage correction 149
7.4.5. Comparison of NS-BE and NS-BE-FS blade forces 151
7.5. Application to truss turbine 153
7.6. Limitations of the NS-BE models 156
7.7. Conclusions 156
Chapter 8 Finite Element Structural Analysis 158
8.1. Numerical structural analysis 158
8.2. Basic configuration 159
8.3. Adopted material properties 160

8.4. Choice of element type 162
8.4.1. Blade elements 162
8.4.2. Support structure 163
8.4.3. Joint degrees of freedom 164
8.5. Order of convergence 164
8.6. Multi-cell analysis technique 166
8.6.1. Basic principles 166
8.6.2. Derivation of shear stress due to shear forces 167
8.6.3. Solution technique 168
8.6.4. Shear centre (X_c, Y_c) 170
8.6.5. Equivalent torsion constant J_{eff} 170
8.6.6. Method of application 170
8.6.7. Multi-cell validation - tube section 172
8.6.8. Multi-cell validation - box section 174
8.6.9. Multi-cell validation - hydrofoil section 175
8.7. Uniform load 176
8.7.1. Single bay parallel model 176
8.8. NS-BE-FS loading 178
8.8.1. Comparisons of loading 179
8.8.2. Multi-bay parallel 179
8.8.3. Single bay truss model 183
8.8.4. Multi-bay truss 185
8.8.5. P-Δ considerations in buckling 188
8.8.6. Pinned truss frame 189
8.8.7. Fatigue considerations 191
8.8.8. Additional centripetal loading 193
8.8.9. Non-rigid supports 195
8.9. Validity of a static analysis 201
8.10. Comparisons with preliminary analysis 202
8.10.1. Length to width ratio scaling 203
8.10.2. Solidity scaling 204
8.11. Concluding remarks 204
Chapter 9 Case study at Papa Westray 206

9.1. Site specification 206
9.2. Effect of thrust on channel flow 207
9.3. Turbine life model 213
9.4. Fatigue life calculation 214
9.5. Basic turbine design 216
9.6. Results 218
9.6.1. Basic configuration 218
9.6.2. Variation of bay length to width ratio β 220
9.6.3. Variation of solidity 221
9.6.4. Alternative variations to the design configuration 222
9.6.5. Power capping or cutting 222
9.7. Device environmental impact 225
9.8. Conclusions 225
Chapter 10 Conclusions and Future Work 227
10.1. Fluid dynamics 227
10.2. Structural analysis 228
10.3. Full scale performance 229
10.4. Completed further work 229
10.5. Future Work 230
10.5.1. Hydrodynamic modelling 230
10.5.2. Structural analysis 230
10.5.3. Basin scale analysis 231
10.5.4. Motor and foundation design 231
Bibliography 232

Nomenclature

a	acceleration due to driving head across tidal channel, m/s^2
A_c	cross-sectional channel area, m^2
A_e	enclosed area of blade cross section, m^2
A_m	area of material in blade cross section, m^2
A_t	projected frontal area of turbine, m^2
A'	area for beam shear calculation, m^2
B	blockage ratio
c	chord length, m
c_v	void fraction
$C_{Frad} \equiv \frac{F_r}{1/2 \rho u_\infty{}^2 A_t}$	radial blade force coefficient
$C_{F\theta} \equiv \frac{F_\theta}{1/2 \rho u_\infty{}^2 A_t}$	tangential blade force coefficient
C_D	coefficient of drag
C_L	coefficient of lift
C_P	coefficient of power
C_T	coefficient of thrust
d	turbine diameter, m
D	drag force, N
E	Young's modulus, Pa
E	extracted energy, J
F	force, N
$\mathrm{Fr} \equiv \frac{u_\infty}{\sqrt{g h_\infty}}$	Froude number
F_c	centripetal force, N
F_e	critical Euler buckling load, N
F_L	radial blade force per unit length, N/m
F_{rad}	radial blade force, N
F_θ	tangential blade force, N
g	gravitational constant, m/s^2
G	shear modulus, Pa
h	flow depth, m
h_c	critical depth, m
H	total head, m
I	second moment of area, m^4
J_{eff}	effective torsion constant, m^4
$k \equiv \frac{\omega c}{2 u_\infty}$	reduced frequency
k	beam natural frequency constant
l	blade length, m

L	lift force, N
L_{bay}	turbine bay length, m
L_c	tidal channel length, m
M	blade moment, Nm
m	mass per unit length, kg/m
$\dot{m}$	mass flowrate, kg/s
n	number of blades
N	number of rotor bays
N	number of fatigue cycles
N_f	number of cycles to failure
p	pressure, N/m^2
P	power, W
q	shear flow, N/m^3
Q	tidal channel volume flow rate, m^3/s
r	blade radius, m
r_p	perpendicular radius to shear vector, m
$R \equiv \frac{\sigma_{min}}{\sigma_{max}}$	stress ratio
Re	Reynolds number
$s \equiv \frac{nc}{\pi d}$	turbine solidity
s	distance around hydrofoil profile, m
s_s	backward facing step height, m
S	shear force, N
t	hydrofoil thickness, m
t_c	actuator cylinder thickness, m
t_w	hydrofoil section wall thickness, m
T	thrust, Nm
u	stream-wise flow velocity, m/s
v	transverse flow velocity, m/s
V_{np}	neap tide velocity 5 m below the surface, m/s
V_{sp}	spring tide velocity 5 m below the surface, m/s
V_R	resultant blade velocity, m/s
w	loading force per unit length, N/m
x	hydrofoil profile coordinate/flow domain stream-wise position, m
y	hydrofoil profile coordinate/flow domain cross-flow position, m
z	flow domain base elevation, m
α	geometric angle of attack, degrees
$\alpha_2 \equiv \frac{u}{u_\infty}$	flow induction factor
$\beta \equiv \frac{L_{bay}}{d}$	bay length to diameter ratio

γ	angle subtended by lift to drag triangle, degrees
δ	deflection, m
δ_b	deflection due to bending, m
δ_s	deflection due to shearing, m
δ_c	deflection at centre of beam, m
ξ	angle subtended by twisted blade, degrees
$\eta \equiv \frac{\mu}{\rho}$	kinematic viscosity, m^2/s
η_{mix}	bypass mixing efficiency of energy extraction
θ	rotation angle, degrees
$\lambda \equiv \frac{r\omega}{u_\infty}$	tip speed ratio
λ_p	tip speed ratio at peak power
μ	dynamic viscosity, Pa s
v	fatigue degradation parameter
φ	average tangential blade sweep angle, degrees
φ_g	phase of water level difference between channel ends
ρ	flow density, kg/ m^3
σ	stress, N/m^2
$\sigma_a \equiv \sigma_{max} - \sigma_{min}$	stress amplitude, N/m^2
$\sigma_m \equiv \frac{\sigma_{max}-\sigma_{min}}{2}$	mean stress, N/m^2
σ_R	residual strength, N/m^2
σ_0	initial strength, either compressive or tensile, N/m^2
τ	shear stress, N/m^2
ω	turbine angular velocity/M2 tidal frequency, rad/s
ω_0	natural frequency, rad/s

Subscripts

c	shear centre coordinate
H	a total head basis
k	a kinetic flux basis
s	coordinate for backward facing step problem
x	in the x-direction
y	in the y-direction
z	in the z-direction
xx	about the x-axis
yy	about the y-axis
xy	product moment of area
*	coordinate system normal to the swept blade axis

Chapter 1

Introduction

This thesis describes a series of scale experiments which confirm that a truss configuration of the Transverse Horizontal Axis Water Turbine (THAWT) is capable of producing significant amounts of power that will exceed the Lanchester-Betz limit, as well as the development of a series of numerical models of the THAWT device, which enable the assessment of the technical feasibility and optimisation of a full scale device for a given tidal location.

Awareness of global warming is becoming increasingly widespread, as climate change is beginning to significantly affect the quality of life of many people around the world. There is increasing scientific evidence that one of the main contributing factors to this effect is the release of greenhouse gases via the production of energy from fossil fuels (Solomon *et al.*, 2007). In an effort to tackle this issue, the UK government has targeted cut-backs in carbon dioxide emissions of 60% by the year 2050 (DTI, 2007). In 2005 the supply from electricity, gas and water utilities contributed an estimated 26% of the total UK emissions in carbon dioxide equivalent, making it the largest contributing sector of greenhouse gases (National Statistics, 2005). The government also predicts that roughly 25 GW of new electricity generation capacity will be required by 2025 to replace closing coal, oil and nuclear power stations (DTI, 2006). Many technologies in the renewable sector, such as wind farms, hydroelectric and solar photovoltaics, have been developed to meet some of this demand, and are now relatively well established. Despite the establishment of these technologies, the intermittency and de-centralisation of renewable resources necessitates a greater range of devices for renewable energy supply to become feasible (Gross *et al.*, 2006).

Tidal power is one such developing technology, which harnesses the kinetic and gravitational potential energy in tidal streams. When compared to other renewable sources, tidal streams are a relatively reliable source of energy, as tidal movements can be accurately predicted in terms of direction, timing and magnitude. The rapid development of devices for tidal energy exploitation is being encouraged by government initiatives and by private

investment (DTI, 2006). The horizontal axis, axial-flow turbine is the most common design of a tidal stream turbine. A number of variants of this type of device, which incorporate features such as flow-guiding shrouds or specific mounting techniques, have been proposed by different developers (O'Rourke *et al.*, 2009), but the underlying hydrodynamics remain similar for these devices. However, a drawback with such designs is that their size cannot be increased significantly, because the limited depth of flow at most sites restricts their diameter. Tidal stream energy is likely to be more expensive than either other renewable resources or combined cycle gas turbines, until at least hundreds of megawatts capacity is installed (Callaghan, 2006). To achieve this scale of power generation using axial-flow devices, many relatively small units (< 5 MW) would have to be deployed. This thesis proposes that it would be more economic to use a device which could be stretched laterally across a tidal flow, and presents the Transverse Horizontal Axis Water Turbine (THAWT) as an alternative design that can be scaled in this way. This device is a variant of the Darrieus concept (Darrieus, 1931), and incorporates a patent pending (Houlsby *et al.*, 2008b) truss design to increase the stiffness and strength of the structure (see Figure 1.1). This increased stiffness and strength allows longer units to be constructed, and reduces the overall costs of foundations, bearings, seals and generators. A full scale device might have a diameter of 10 – 20 m and would operate in a flow depth of 20 – 50 m. Each rotor might be in the range 40 – 80 m long, and would consist of perhaps 3 to 6 ‘bays’ of blades.

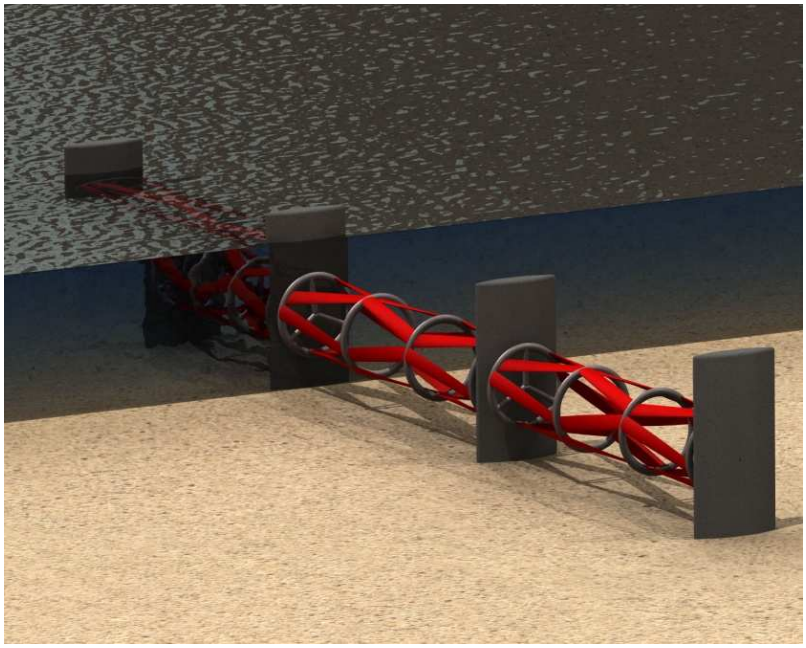

Figure 1.1 – Rendered CAD image of the THAWT device with the sea cut away

1.1. Thesis scope

The aim of this thesis is to investigate the technical feasibility of the truss THAWT concept by understanding how variations in the design of the turbine affect the relationship between the hydrodynamic and structural performance of the device, and their implications for the economic viability of a full scale installation.

To meet this aim the following objectives have been chosen:

- Demonstrate that a truss THAWT device is capable of achieving an efficiency and power output similar to that of the parallel-bladed device, which has been shown to exceed the Lanchester-Betz limit in small scale tests.
- Develop a model of the device hydrodynamics which is capable of predicting the power output and blade forces with a sufficient degree of fidelity and accuracy.
- Develop a structural model of the THAWT rotor, which is capable of predicting the induced blade stresses, based on the blade loads predicted by the hydrodynamic model.
- Combine the results from the hydrodynamic and structural models of the THAWT device to predict how the power produced and expected lifetime of a device are affected by various aspects of design configuration, in a given tidal location.

A major factor that has been identified in the technical feasibility of the THAWT device is the extent to which blade stresses vary with configuration and scale. A review of the literature published on cross-flow turbines, see Chapter 2, indicates that the effect that variations of design configuration and flow condition have on the blade forces and stresses is not explicitly understood. Chapter 3 outlines preliminary analyses, including a dimensional analysis, which predicts how the blade forces and stresses scale with various turbine parameters. As a precursor to more comprehensive numerical analyses, this preliminary analysis informs of which parameters are the most significant in the design of a device and offers a first order validation of numerical simulations, when varying parameters which have not been explored experimentally.

Previous tests of the THAWT device demonstrated the significant potential of the parallel-bladed configuration (McAdam, 2007), but with poor hydrofoil performance due to problems of small scale modelling, the results from the truss configuration were not comparable. To assess whether the structural novelty of the truss configuration has potential for further development, it is necessary to show that the device is capable of producing a significant amount of power, similar to that produced by the parallel-bladed configuration. Whilst the

hydrodynamic performance of the truss THAWT device could be explored by numerical modelling alone, this approach is likely to require considerable development of numerical techniques to achieve a sufficient accuracy. In addition, the confidence in such a method would always be lacking in the absence of validating experimental results. It was decided that the most economical method of demonstrating that the truss THAWT device is capable of producing power, with an efficiency approaching that of the parallel-bladed configuration would be to test a scale model of the device experimentally. A series of 1/20th scale experiments are described in Chapter 4, and the analysis of the results from these tests is conducted in Chapter 5, with both configurations of device exceeding the Lanchester-Betz limit for realistic Froude number flows.

Whilst all numerical models of physical phenomena are based on assumptions, the fidelity and accuracy of these models are likely to depend on whether the most significant physical features are modelled accurately. It is unclear how sophisticated a model of a high solidity cross-flow device in an open channel flow, such as that proposed in this thesis, must be in order to achieve a sufficient level of fidelity and accuracy. However, the simple numerical models of the THAWT device that have previously been developed (McAdam, 2007) are incapable of achieving a satisfactory level of similarity with corresponding experimental results. Simulation of the performance of the device will be improved by identifying the assumptions that are inaccurate and replacing these parts of the simulation with improved models. A first attempt at this process is conducted in Chapter 6, by combining the Linear Momentum Actuator Disc Theory for Open Channel Flow of Houlsby et al. (2008a) with a blade element representation of the turbine members, to produce the Momentum Blade-Element model (M-BE). In comparison with the experimental results of Chapter 5, the accuracy of the underlying assumptions are further refined, leading to the development of the Navier-Stokes approach described in Chapter 7, which displays significantly improved fidelity and accuracy when compared to the M-BE model.

By applying the blade forces, predicted using the hydrodynamic numerical model of Chapter 7, to a structural model of the THAWT rotor it will be possible to perform a more quantitative analysis of the relationship between the hydrodynamic and structural trade-off in the design of a device. This is achieved in Chapter 8 using a beam element finite element model of the THAWT device.

Designing a single generic THAWT device for all tidal sites is unrealistic, and a device should be tailored for each location. When a potential tidal location has been identified, the effect that a device has on the flow regime in that channel must be assessed in order to understand what configuration of turbine will allow the maximum amount of energy to be extracted. However, the technical viability of this device will depend on its ability to produce a useful amount of power for a realistic amount of time. The large oscillatory loads experienced by the blade of a cross-flow device mean that fatigue damage accumulation is likely to dictate the operational lifetime of a device. A synoptic approach to this problem is conducted in Chapter 9, where flow conditions predicted by a simple channel model are applied to the numerical hydrodynamic and structural models of Chapter 7 and Chapter 8, to provide estimates of the power and stress that will be produced. Damage is accumulated in a fatigue analysis, which allows the optimisation of a device based on relevant metrics of performance.

Chapter 2

Literature review

In an effort to minimise the warming effect that humans have on the global environment the rapid development of devices for renewable energy generation is being encouraged by government initiatives and by private investment (DTI, 2007).

Of the various forms of renewable energy which are targeted for exploitation, tidal power has an advantage due to an accurate forecast over long term horizons (Denny, 2009). It is anticipated that tidal power will therefore be less challenging and possibly more economic to integrate into an electrical system than other forms of renewable energy, which are relatively unpredictable.

Further economic incentives for the development of renewable devices are predicted within Europe, with plans to build a renewable power supergrid, which will act as a buffer for excess renewable energy, and offer a market through which the countries surrounding the North Sea may trade clean energy (Jha, 2010). Similar initiatives are likely to reduce the problem of renewable device intermittency, as well as improving the renewable energy market competitiveness.

2.1. Modern tidal technology

The tidal market is adolescent when compared to wind and solar, with no distinct optimum design or location (Khan *et al.*, 2009).

The methods of energy extraction from the tides can be broadly separated into the two categories of tidal range extraction, typically achieved through barrages, and tidal stream extraction. Whilst the energy potential from tidal barrage technology is large, the significant resources required for a single installation and the unclear environmental impacts have prevented its wide scale adoption (DECC, 2010).

The majority of tidal stream devices currently in development can be further split into three categories of design;

- Axial-flow turbines
- Cross-flow turbines

- Oscillating and other devices

2.1.1. Axial-flow turbines

The most common design of tidal device is the conventional axial-flow turbine (Khan *et al.*, 2009), which superficially resembles a wind turbine that has been converted for use underwater. A number of variants of this type of device, which incorporate features such as flow-guiding shrouds or specific mounting techniques, have been proposed by different developers, as shown by examples in Figure 2.1.

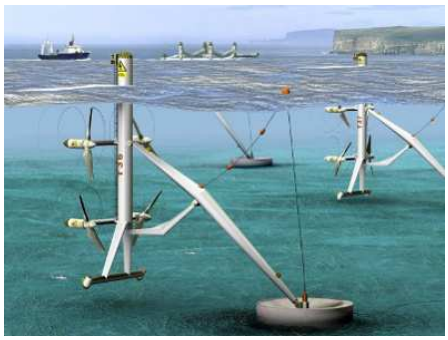

(a) *Triton Tidal stream device (en.wikipedia.org) permission to reproduce this figure granted by Wikipedia*

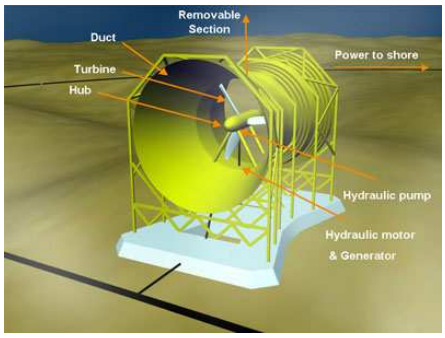

(b) Rotech Lunar Energy device (O'Rourke et al., 2009), permission to reproduce this figure granted by Elsevier Ltd.

Figure 2.1 - Example concept images of axial-flow tidal turbine designs

Investment in axial-flow devices has been driven by a high degree of confidence in the technology, due to a substantial amount of previous research conducted by the wind industry into the fluid dynamic and structural aspects of device design. Predictions of the performance of axial-flow turbines are relatively accurate and simple to perform, using techniques as basic as numerical momentum models (Batten *et al.*, 2006). Control methods such as variable pitch regulation are commonly used to protect devices from high speed flows, and to optimise the efficiency of operation (Khan *et al.*, 2009). The current perceived market leaders in the tidal stream energy sector are Marine Current Turbines, who installed a commercial scale 1.2 MW device, Seagen shown in Figure 2.2, in Strangford Narrows in April 2008. The device has been supplying power to the Irish electricity grid since January 2010 (Fraenkel, 2011).

Figure 2.2 - CAD rendered image of the MCT Seagen device (Fraenkel, 2011) permission to reproduce figure online not granted

A drawback with axial-flow turbines is that their size cannot be increased significantly, because the limited depth of flow at most sites restricts their diameter (Bryden *et al.*, 1998). To achieve a significant scale of power generation using axial-flow devices, many relatively small units must be deployed in an array, each requiring expensive marine foundations. Further costs are likely to be incurred with the maintenance of the many bearings, seals and actuators, especially with the use of variable pitch control, in an environment where maintenance will be inherently difficult and expensive.

2.1.2. Cross-flow marine turbines

The vast majority of cross-flow turbine designs are based on the Darrieus concept, shown in Figure 2.3, originally conceived as a vertical axis wind turbine and patented by the French aeronautical engineer Georges Jean Marie Darrieus (Darrieus, 1931).

Figure 2.3 - Image from the 1931 patent by Georges Darrieus (Darrieus, 1931) permission to reproduce figure online not granted

Whilst the development of the Darrieus turbine receded in the wind industry, due to the wider adoption of the axial-flow wind turbine, the concept has now emerged in several designs of modern tidal devices (Antheaume *et al.*, 2008, O'Rourke *et al.*, 2009). The main

advantage of the cross-flow Darrieus design is the consistency of performance with flow from any direction normal to the axis of the rotor, which reduces the necessity of complex control and yawing mechanisms when compared to the conventional axial-flow device (Fujisawa and Shibuya, 2001).

However, when compared to a conventional axial-flow device the difficulty in predicting the behaviour of a cross-flow device is significantly increased (Ponta and Jacovkis, 2001, Paraschivoiu and Allet, 1988) and suffers from significant inaccuracy for devices in confined flows or with a high blockage (Paraschivoiu, 2002).

A further significant disadvantage of the Darrieus cross-flow device is the large oscillatory loading regime to which the blades are exposed, which leaves them susceptible to fatigue failure (Ashwill and Leonard, 1986, Peace, 2003).

Darrieus cross-flow devices experience accelerations due to variations in torque, as a result of the varied lift and drag produced by the blade during a rotation. The magnitude of the torque ripples is dependent on the number and orientation of blades (Shiono *et al.*, 2000), with an increasing number of blades acting to smooth the torque profile, as well as improving the self-starting ability. The Gorlov turbine (Gorlov, 1997) was designed to address this problem by using a helical system of blades, shown in Figure 2.4.

Figure 2.4 - Image of a Gorlov helical turbine rotor (O'Rourke et al., 2009) permission to reproduce this figure granted by Elsevier Ltd.

The amount of energy that a single turbine may extract from a tidal stream is dependent on the ratio of device swept area to the cross-sectional area of the flow, defined as the blockage ratio *B*, as described in section 2.7.2. Cross-flow devices are capable of achieving greater blockage ratios than conventional axial-flow devices and are therefore capable of extracting a greater amount of energy from the flow with a single unit. Several suggested Darrieus cross-flow devices have been designed to benefit from high blockage effects, including the Blue

Energy Tidal Fence (O'Rourke *et al.*, 2009) and the close-packed vertical axis fence of Salter (Salter, 2009), as shown in Figure 2.5.

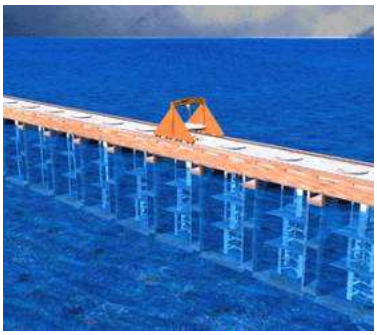

(a) Blue Energy Tidal Bridge System (O'Rourke et al., 2009) permission to reproduce this figure granted by Elsevier Ltd.

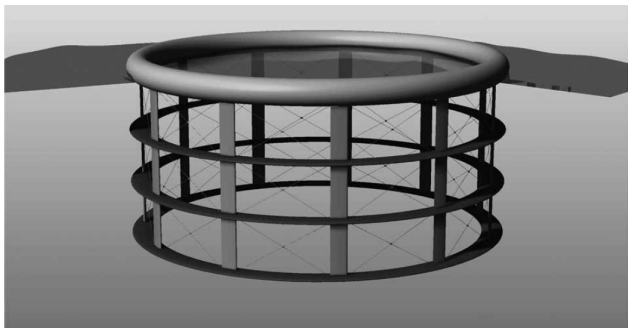

(b) Single vertical axis rotor of the Salter tidal fence (Salter and Taylor, 2007) permission to reproduce this figure granted by SAGE Publications Ltd.

Figure 2.5 - Concept images of proposed cross-flow tidal turbines

It is well accepted that variable pitching of the blades of a Darrieus cross-flow device is likely to increase the efficiency of energy extraction (Camporeale and Magi, 2000, Gretton and Bruce, 2005). However, implementation of variable pitch is substantially more complex in cross-flow devices than axial-flow devices (Fraenkel, 2002), due to the necessity to cyclically pitch the blades, whereas axial-flow devices only require adjustments on a time scale related to the variation in tidal flow. The significant increase in mechanical complexity and potential maintenance costs have prevented the adoption of variable pitching in any commercial propositions of cross-flow devices.

A special mention should be made of the horizontally aligned cross-flow device, TidGen of Ocean Renewable Power, shown in Figure 2.6. Whilst bearing the closest similarity to the THAWT device studied in this thesis, the TidGen device does not make use of the blades as structural members or of the potential application of a high blockage ratio (Fountain, 2010).

Figure 2.6 - Ocean Renewable TidGen device (www.oceanrenewablepower.com) permission to reproduce this figure granted by Ocean Renewable Power Company

2.1.3. Oscillating and other devices

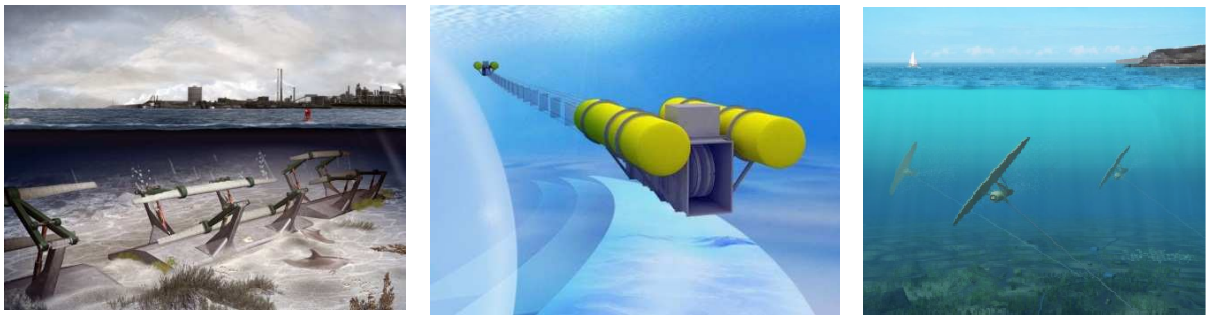

(a) *Pulse Tidal Oscillating Wing (www.pulsetidal.com) permission to use this figure granted by Pulse Group*

(b) Tidal sails (www.tidalsails.com) permission to use this figure granted by Tidal Sails AS

(c) Minesto 'Deep Green' tidal kite (www.minesto.com) permission to use this figure granted by Minesto AB

Figure 2.7 – Rendered images of Oscillating and other tidal stream devices

As shown in Figure 2.7, designs of devices with various mechanisms for extracting energy from tidal streams have been proposed. A comprehensive review of these devices is not carried out in this thesis, due to the wide range of devices which have been proposed. However, it should be noted that while designs of axial or cross-flow devices are likely to be applicable to generic tidal locations, various alternative designs might be more economically or technically feasible in specific tidal flows or locations.

2.2. Transverse Horizontal Axis Water Turbine (THAWT)

Rather than using many relatively small units of conventional axial-flow turbines, it would be more efficient to use a device which could be stretched laterally across a tidal flow. The Transverse Horizontal Axis Water Turbine (THAWT) is a horizontal variant of the Darrieus concept and was conceived at Oxford University in order to meet this requirement, as shown in Figure 2.8.

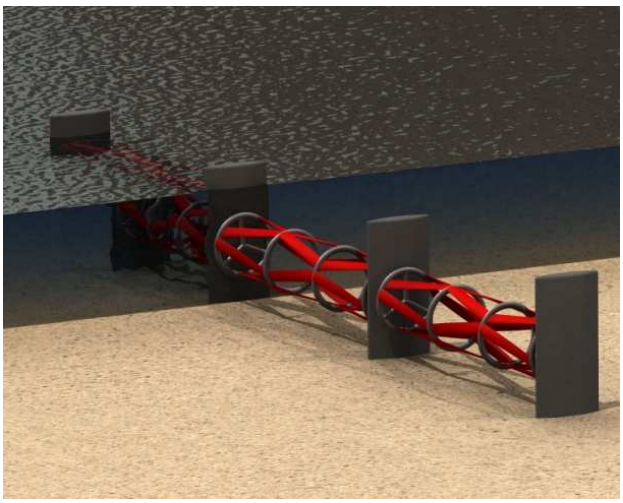

Figure 2.8 – CAD rendered image of a truss THAWT device spanning a stretch of channel

The THAWT device employs a truss design of blades, which is intended to increase the rigidity of the structure, so that it can be stretched across a channel without significant increases in blade stresses.

2.2.1. Basic mechanics

A simplistic analysis of a Darrieus turbine assumes that the flow field is unaffected by the turbine blades, so that the flow is steady and uniform. The basic Darrieus turbine design is made up of a number of hydrofoils, which rotate about an axis in an oncoming flow as shown in Figure 2.9.

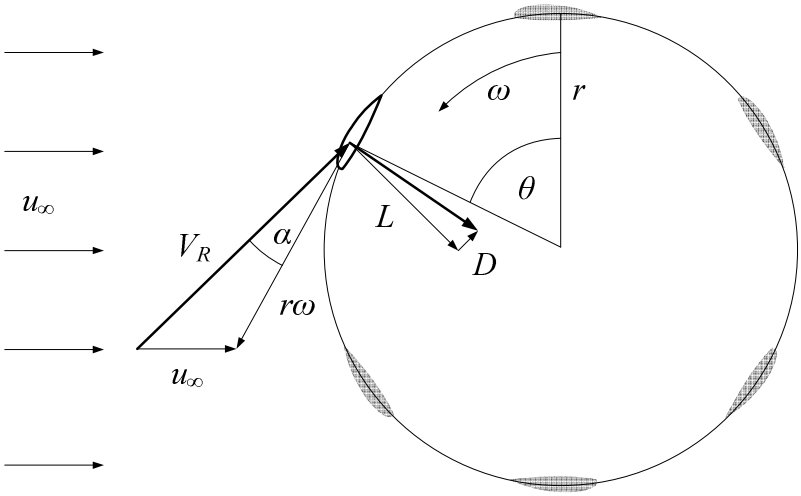

Figure 2.9 - Diagram of velocity components in a basic Darrieus turbine analysis

When the turbine is rotating in a uniform oncoming flow the components of velocity add to give a resultant velocity vector V_R of length:

$$V_R = \sqrt{(r\omega \sin\theta)^2 + (r\omega \cos\theta + u_\infty)^2} \qquad 2.1$$

This resultant velocity acts at an angle of incidence α to the hydrofoil section.

$$\alpha = \tan^{-1}\left(\frac{u_\infty \sin\theta}{r\omega + u_\infty \cos\theta}\right) \qquad 2.2$$

A lift force per unit length is generated perpendicular to the resultant velocity and a drag force per unit length is generated parallel to the resultant velocity.

$$L = {}^1\!/_2\, \rho {V_R}^2 c C_L \qquad 2.3$$

$$D = {}^1\!/_2\, \rho {V_R}^2 c C_D \qquad 2.4$$

These lift and drag forces have components in the tangential direction which result in a torque about the axis of the turbine.

$$\text{Torque} = r(L \sin\alpha - D \cos\alpha) \qquad 2.5$$

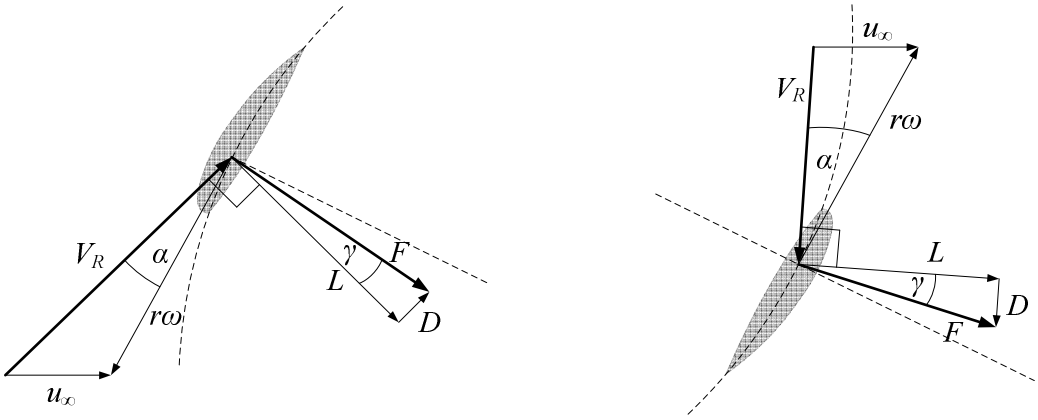

(a) Forces on the upstream half of the device *(b) Forces on the downstream half of the device*

Figure 2.10 - Diagrams of forces generated by resultant velocity components

Figure 2.10 shows that positive torque is produced, at any angle of turbine rotation, as long as the magnitude of the angle of attack α is greater than the angle subtended by the lift to drag ratio γ. This highlights the importance of the choice of blade section and the corresponding lift to drag characteristics on the magnitude of the generated torque and power. Aerofoil sections which appear symmetrical to the flow are commonly used in order to produce positive torque, despite the oscillation of the angle of attack between positive and negative values, during a full turbine rotation (Antheaume *et al.*, 2008, Leclerc, 1997, Shiono *et al.*, 2000). If the profile of the flow incident to the turbine is uniform and the flow is not slowed through the rotor, the device theoretically produces power with equal efficiency in flows from either direction.

2.3. Steady flow techniques for analysis of tidal devices

One of the first techniques used for calculating the amount of energy that may be extracted from a body of fluid by a single stage turbine is the linear momentum actuator disc theory shown in Figure 2.11 (LMADT) (Burton *et al.*, 2001). Momentum theory assumes inviscid, steady, one dimensional flow.

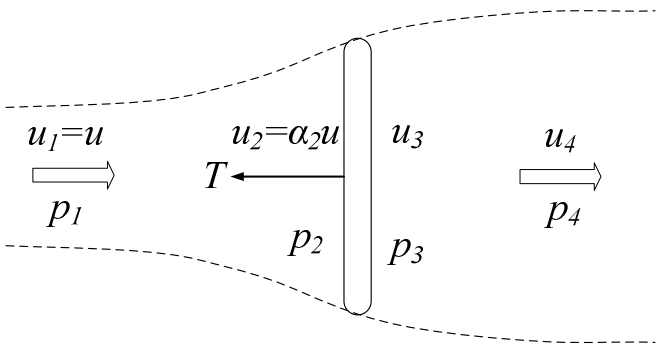

Figure 2.11 - Linear momentum actuator disc theory

In this analysis it is assumed that the overall volume surrounding the disc is unbounded, so that it is only necessary to analyse the flow passing through the turbine. It is also assumed that in the process of extracting energy the turbine imparts a thrust on the fluid, which results in a reduction of linear momentum.

By applying Bernoulli's equation for the regions before and after the turbine and setting up a momentum equation for the entire domain, it is possible to calculate the thrust generated by the turbine, and the power that it absorbs.

$$C_{Pk} = \frac{P}{1/2\,\rho u^3 A_t} = \frac{T u_2}{1/2\,\rho u^3 A_t} \qquad 2.6$$

Differentiation reveals that the maximum occurs when $u_2 = {}^2/_3\,u_1$, giving a maximum power coefficient of $C_{Pk} = {}^{16}/_{27}$. This has become widely known as the Lanchester-Betz limit and is widely accepted in the wind industry as the maximum amount of energy that can be extracted by a single unbounded axial-flow device.

2.3.1. Actuator disc theory in Darrieus turbine analysis

LMADT was first used to model the performance of a Darrieus cross-flow turbine by Templin (1974). Templin's method employed simple blade element theory with lift and drag characteristics taken from experiments at a single Reynolds number and for a given aerofoil section, corresponding to validating experiments. For a given input velocity field the blade element theory predicts the thrust produced by the turbine in the stream-wise direction. This thrust acts as a reduction in momentum across the actuator disc and can be used in LMADT to recalculate the velocity through the turbine. This process is iterated until the co-efficient of thrust generated by both LMADT and blade element theory converge to a single value. As documented by Templin, this method is effective in predicting the amount of power that would be produced by lightly loaded blades at low tip speed ratios and low solidities, as the velocity through the turbine is likely to be relatively uniform. However, the accuracy of the technique is reduced for higher thrust, high solidities or high tip speed ratios.

A more complex multiple-streamtube method was developed by Strickland (1975). In this model the actuator disc is separated into a series of adjacent streamtubes, all aerodynamically independent. This is very similar to the process for a single streamtube except a more accurate flow-field may be calculated, giving more accurate predictions of the power produced. This

improves on the basic streamtube theory, but still suffers from only being able to predict induced velocities in lightly loaded turbines.

A fluid particle passing through a Darrieus cross-flow turbine encounters two sets of blades. One on the front side of the turbine as the fluid enters, and again on the rear side as it leaves. To factor this issue into the momentum calculation, the linear momentum double actuator disc theory (LMDADT) was developed (Newman, 1983). Due to the expansion of the flow, a volume of fluid passing through the first disc does not encounter the second disc, as shown in Figure 2.12. In a similar fashion to single actuator disc theory, Bernoulli's equation is applied to the different regions, but momentum is then applied separately to the central flow and to the flow which bypasses the second disc, so that there are now three equations. This allows independent solutions for the calculation of the thrusts on each disc and the corresponding power co-efficient, as shown in equation 2.7.

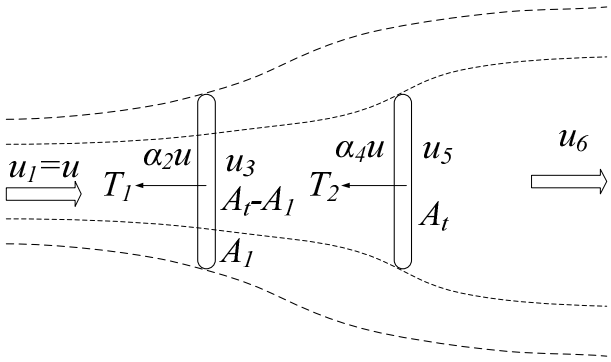

Figure 2.12 - Linear momentum double actuator disc theory

$$C_{Pk} = \frac{T_1 u\alpha_2 + T_2 u\alpha_4}{{}^1/_2\,\rho u^3 A_t} \qquad 2.7$$

Newman showed by differentiation that the maximum power coefficient $C_{Pk} = {}^{16}/_{25}$ occurs when $u_2 = {}^4/_5\, u_1$ and $u_4 = {}^2/_5\, u_1$. This suggests that a double actuator disc turbine is capable of producing approximately 8% more power than a single actuator disc turbine.

Double-multiple streamtube theory was later developed, which is simply an amalgamation of double actuator disc and multiple streamtube theory, and has proven to predict accurately experimental results for lightly loaded wind turbines (Paraschivoiu, 1982).

For multiple streamtube and double actuator disc theory to be valid it has to be assumed that the momentum equations between the adjacent streamtubes, or annuli, are independent, so that the forces between the regions are negligible.

2.3.2. Actuator Cylinder model

It was theorised by Madsen (1982) that a stream tube model would not be able to represent a cross-flow device, because of the differences in the geometry of the flat actuator disc and that of cylindrical turbines.

Madsen's proposed technique distributes the blade forces onto the geometry of a cylinder, based on blade element calculations performed using the local flow field. A new flow field is then calculated by discretising the area around the turbine and performing a two-dimensional momentum balance for each element using the Euler equations and continuity (see Figure 2.13). By alternately performing the two calculations the process converges on consistent thrust values in a similar fashion to the multiple streamtube methods of Paraschivoiu and Strickland. Unlike the methods by Paraschivoiu and Strickland, this technique allows the turbine to apply a non-streamwise momentum change to the flow, which is much more representative of the conditions in a Darrieus cross-flow device.

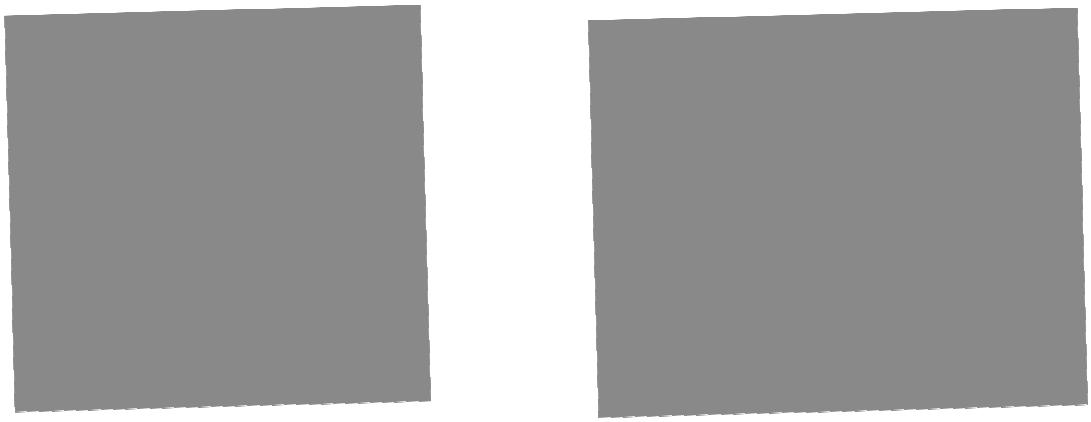

(a) Coarse grid used for calculation *(b) Streamlines based on absolute velocity*

Figure 2.13 - Images of actuator cylinder calculations (Madsen, 1982) permission to reproduce figures online not granted by source

This technique allowed Madsen to predict the performance of the device and the development of the downstream wake. The accuracy of such a technique is unknown due to a lack of validation, and consequently it does not appear to have been adopted since.

2.3.3. LMADT in open channel flow

Despite the success of LMADT for the prediction of wind turbine performance, it is widely accepted that the constraints on air flow are different to the constraints on an open channel flow of water (Bryden *et al.*, 2007). Whereas a volume of decelerating air is relatively free to expand, a volume of open channel water is constrained by its density and the free surface that

forms. For this reason it is now assumed unsuitable to apply basic LMADT to tidal stream flows.

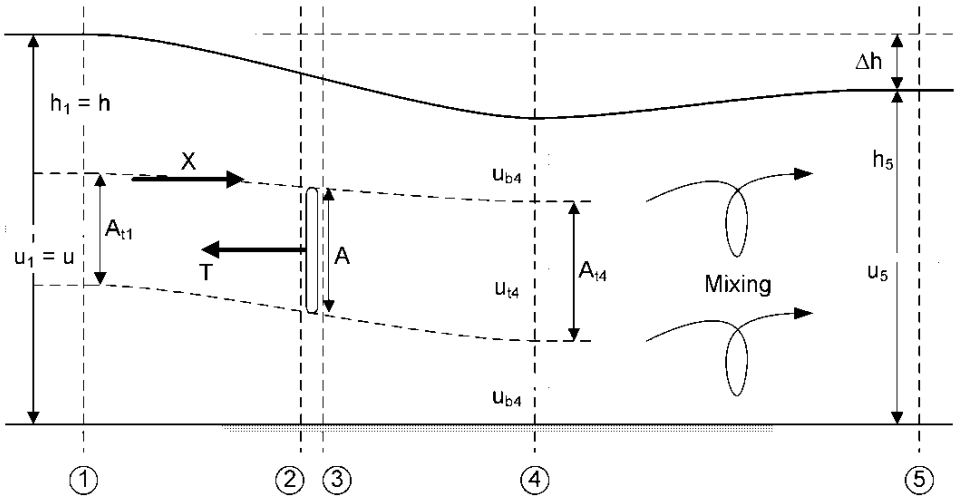

Figure 2.14 - Linear momentum actuator disc theory for open water flow (Houlsby et al., 2008a)

Linear momentum actuator disc theory for open channel flow is a single actuator disc technique to tackle the issue of momentum theory in an open channel flow (Houlsby *et al.*, 2008a). In this technique there is a volume of fluid that decelerates and expands as it passes through the turbine (see Figure 2.14). This volume of fluid is constrained by an accelerated bypass flow and eventually the two flows mix to produce the downstream condition.

The Bernoulli calculation is slightly modified from the techniques described previously and takes into account the total head for regions 1→2 and 3→4. As in previous methods, momentum is calculated across the system and the use of the continuity equations allows a solution to be found.

Non-dimensional variables are used to simplify the analysis of this technique (Table 2.1). One of the key variables is the Froude number Fr (equation 2.8), which describes the state of the upstream flow and is well documented for existing channels.

$$\mathrm{Fr} = \frac{u_\infty}{\sqrt{g h_\infty}} \qquad 2.8$$

The blockage ratio B is defined as the proportion of the channel cross-sectional area occupied by the turbine, and defined in equation 2.9.

$$B = \frac{A_t}{A_c} \qquad 2.9$$

The turbine induction factor α_2, defined in equation 2.10, is simply the ratio of the flow velocity at the turbine to the free stream flow velocity.

$$\alpha_2 = \frac{u}{u_\infty} \qquad 2.10$$

The coefficient of thrust C_T is the amount of thrust generated by the turbine, non-dimensionalised by a product of the dynamic pressure in the upstream flow and the stream-wise area of the turbine, as shown in equation 2.11.

$$C_T = \frac{T}{{}^1/_2 \rho {u_\infty}^2 A_t} \qquad 2.11$$

The power coefficient for the turbine can then be calculated as described in equation 2.12, and is a coefficient which has been non-dimensionalised by the incident upstream kinetic flux.

$$C_{Pk} = \alpha_2 C_T \qquad 2.12$$

Given three of the variables in Table 2.1 the remaining two variables can be calculated using LMADT-OCF, which allows the prediction of the effect that a specific device will have on a flow, or conversely, to predict what design of device would impart a specific effect on a tidal flow.

Variable	Symbol
Froude number	Fr
Blockage ratio	B
Flow induction factor	α_2
Thrust coefficient	C_T
Depth change	${}^{dh}/_{h_\infty}$

Table 2.1 - Non-dimensional variables used in LMADT for open channel flow

The power coefficients calculated by LMADT for open channel flow describe a perfectly efficient inviscid turbine, where the only losses in the system are those in mixing downstream. This means that the amount of power available to the turbine is the amount of head power extracted, less the power lost to mixing, so by minimising the mixing losses one would expect the turbine performance to improve. We can define the efficiency of this system as the amount of power available to the turbine in relation to the amount of power extracted from the flow, as shown in equation 2.13.

$$\eta_{mix} = \frac{C_{Pk}}{C_{PH}} = \frac{C_{Pk}}{C_{Pk} + C_{Pk-mixing}} \qquad 2.13$$

Mixing losses occur due to the difference in the velocities of the flow through the turbine and the bypass flow. For a given value of depth change across the device, losses due to mixing can be reduced by a combination of increasing the blockage ratio and by reducing the

difference in velocity between the flow through the turbine and the bypass flow, so that the flow behind the turbine is more uniform.

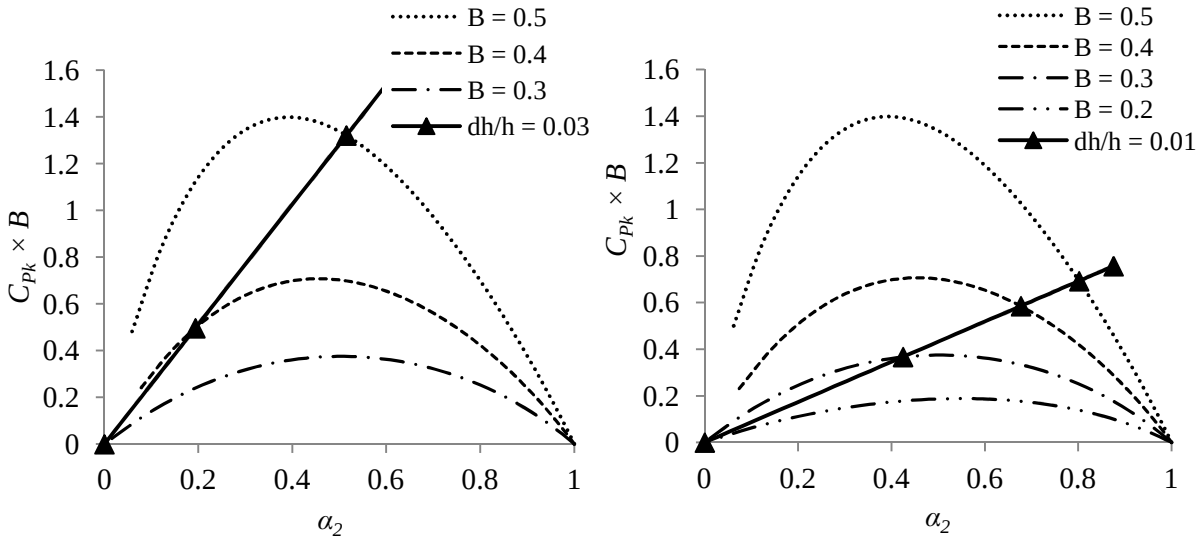

(a) dh/h = 0.03 *(b) dh/h = 0.01*

Figure 2.15 - Inviscid kinetic power coefficient multiplied by blockage ratio at Fr = 0.15 for several fixed blockage ratios and depth change, calculated using LMADT-OCF (Houlsby et al., 2008a)

Figure 2.15 illustrates the amount of power that can be extracted from a flow at a Froude number of 0.15, for several fixed blockage ratios and fixed depth change. It is evident that in the situation where the depth change across the device is not limited, increasing the blockage ratio of a device results in a significant increase in the amount of power that is available to the device. However, it is also evident that if the amount of power that could be extracted and the corresponding depth change across the device were limited for any reason, be it environmental, social or other, a greater proportion of the power removed from the flow would be available to a higher blockage ratio device, which would achieve the depth change at a significantly greater induction factor. Indeed, a device with a low blockage ratio would not be capable of achieving some values of depth change, at which point multiple rows of device would be required to extract the available head from the flow.

Figure 2.15(a) shows that when a high depth change (3% of upstream depth) is available from the flow, utilising an increased blockage ratio significantly increases the amount of power that is available to the device, therefore reducing downstream mixing losses. However, if the depth change is limited to a relatively low value (1% of upstream depth), such as that shown in Figure 2.15(b), the benefits of increasing the blockage ratio are less significant.

The amount of power that can be converted to useful energy is always less than the inviscid prediction of LMADT-OCF, due to viscous losses in the turbine rotor itself. The maximum

useful power output from a device is therefore likely to occur when the maximum proportion of energy is made available to the turbine and the viscous losses at that point are minimised.

2.4. Non-steady flow techniques for analysis of cross-flow devices

Whilst the sophisticated momentum actuator disc models are capable of predicting the performance of the Darrieus rotor under lightly loaded conditions and at attached flow angles of attack, they are relatively inadequate for several reasons (Strickland *et al.*, 1979). Predictions of turbine performance and blade loads become inaccurate for even moderately high thrust devices, due to an oversimplifying set of assumptions about the flow field. The wake structure and propagation cannot be accurately simulated, which has been identified as important when considering the placement of rotors in close proximity to each other. Additional models must be implemented, of at least semi-empirical nature, in order to model the hydrofoil performance due to non-steady and separated flow phenomena. Several non-steady numerical approaches have been developed in an effort to overcome these issues.

2.4.1. Vortex model based techniques

Altering the simple momentum models to alleviate these issues was thought to be impractical and the increases in the use of computational power led to the development of several free vortex models of Darrieus type turbines during the 1970s (Fanucci and Walters, 1976, Wilson, 1978). The vortex method is based on potential flow, but often features extra conditions to correct for phenomena due to viscosity. One of the most developed three dimensional free vortex model of the Darrieus rotor to date was developed by Strickland (1979). Whilst the single line vortex used in Strickland's model to represent the aerofoil is a simplification on some previous techniques, it was felt that this would model the flow adequately at distances greater than roughly one chord length from the aerofoil. Strickland also overcame the inadequacies of the less sophisticated momentum techniques to model aerofoil stall by combining the Kutta-Joukowski law with aerofoil section test data. Whilst the accuracy of predictions of the device performance and blade forces were improved (see Figure 2.16), the computational cost was significantly increased.

Figure 2.16 - Power coefficient against tip speed ratio for the Strickland free vortex model (1979) permission to reproduce figure online not granted by publisher

The applicability of the basic vortex method is limited due to the use of published aerofoil data to dictate the blade forces. Questions have been raised over the validity of modelling circulation about a pitching aerofoil over a curvilinear path, using published data from experiments on non-pitching, non-rotating sections (Ponta and Jacovkis, 2001). Whilst some vortex models include adjustment terms to compensate for some flow effects, these adjustments tend to be specific to the aerofoils or configuration of turbine, and render the models relatively inflexible.

In an attempt to improve the accuracy of the blade force prediction whilst maintaining a relatively low computational cost, some attempts have replaced the region close to the blade with a more sophisticated 'micro-model', as shown in Figure 2.17, such as the Constant-curl Laplacian approach of Ponta and Jacovkis (2003) or the panel method of Wang *et al.* (2007). These models are intended to offer a more accurate simulation of the foil hydrodynamics, using an alternative method to the basic vortex model.

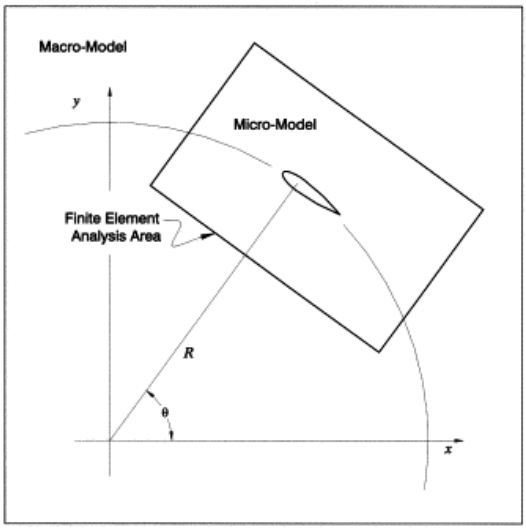

Figure 2.17 - Method used in combined free vortex-finite element model (Ponta and Jacovkis, 2001) permission to reproduce figure granted by Elsevier Ltd.

However, despite the successful simulation of phenomena, such as dynamic stall using vortex methods for other applications (Ekaterinaris and Platzer, 1998), the 'micro-models' which have been used to date have not addressed fully the complex flow phenomena to which foils in a cross-flow device are prone.

2.4.2. CFD techniques

Most modern methods for approaching fluid dynamic problems solve the Navier-Stokes (N-S) momentum and continuity equations given in equations 2.14 and 2.15. There are various techniques that can be utilised to solve the N-S equations with a high degree of accuracy. However, the substantial requirement of computational resources mean that they have not been widely adopted until recently (Ekaterinaris and Platzer, 1998).

$$\rho \frac{\delta \mathbf{u}}{\delta t} - \mu \nabla^2 \mathbf{u} + \rho(\mathbf{u} \cdot \nabla)\mathbf{u} + \nabla p = \mathbf{F} \qquad 2.14$$

$$\nabla \cdot \mathbf{u} = 0 \qquad 2.15$$

A mesh is used to discretise the flow field so that the N-S equations can be solved numerically as a set of algebraic equations. There are two main methods of discretising and solving the N-S equations; Finite-Element (FE) and Finite-Volume (FV).

The FV technique subdivides the solution space into a finite number of control volumes, which can be of a structured or unstructured shape, and form a grid (Ferziger and Peri'c, 2002). The N-S conservation equations are integrated over the surface, volume and time and applied to each control volume to form an algebraic equation per control volume, which involves unknowns from the control volume centre, as well as the neighbouring volumes. The equations must be linearised, which requires an iterative solution method. One of the benefits of the FV technique is that the integration approach for each individual control volume produces a solution that inherently conserves all of the appropriate physical quantities.

The FE technique employs a similar methodology to that used for structural analysis. The solution space is separated into a series of elements using a mesh. Functions of a given order are used to approximate the variation of fluid parameters in each element. This results in a matrix of equations for the solution domain, which are solved by minimising the weighted residual error. Unlike FV, conservation conditions are only achieved over the entire domain,

but this is not seen as a disadvantage if the approximation of the flow parameters is superior to that of the FV approach (Zienkiewicz *et al.*, 2005).

The main problem in solving the N-S equations is the scale at which turbulence and transition should be modelled. The full N-S equations can be solved by direct numerical simulation (DNS), in which case the solution will include turbulence and transition of the scale of the mesh elements. However, for most problems the scale of turbulence which significantly affects the solution is small and requires a mesh with a very high number of degrees of freedom. This comes at a substantial computational cost and limits the method to solutions that are not relevant to engineering problems, with flows of very low Reynolds number where the range of turbulent length scales is reduced.

The Reynolds-averaged Navier-Stokes (RANS) and Large eddy simulation (LES) techniques use time averaging and spatial averaging, or filtering, respectively of the N-S equations in order to avoid the necessity of resolving small scale turbulence (Johansen *et al.*, 2002). Instead of resolving the small scale turbulence, these techniques use separate models to approximate the effect of the ignored turbulence, which tends to contribute to the N-S equations as an added turbulent viscosity term. However, there is no turbulence model which is applicable to all situations and these models often struggle to accurately simulate transition.

The large computational cost of simulating both the flow field and local blade mechanics of a cross-flow device have often led to the use of N-S modelling in only one or the other. Brahim et al. (1995) applied the RANS equations to a three dimensional vertical axis wind turbine model. Due to the computationally expensive requirements of modelling the blade physics in 3D, the problem was simplified by applying a force from the blades through the terms in the momentum equations at the appropriate locations. The forces were calculated based on the aerofoil lift and drag characteristics, which were evaluated using a 2D model (Tchon and Paraschivoiu, 1994). This model provided a small increase in the accuracy of turbine performance prediction, when compared to the free vortex model of Strickland (1979). The marginal improvements were considered to be relatively expensive in terms of computational effort when compared to the simpler vortex method.

Work by Antheaume et al. (2008) predicted the performance of a vertical axis Darrieus tidal turbine using a three-dimensional N-S model, in which the forces applied by the blades were applied to the N-S momentum equation in an actuator cylinder approach. The blade forces

were simply evaluated from static aerofoil test data, which means that no dynamic stall effects were taken into consideration. Whilst the numerical model compared favourably at high tip speed ratios with wind turbine experiments performed at Sandia Laboratories, the poor correlation of low tip speed power coefficients may be due to the inaccuracies of using static blade characteristics in such a dynamic system, as shown in Figure 2.18.

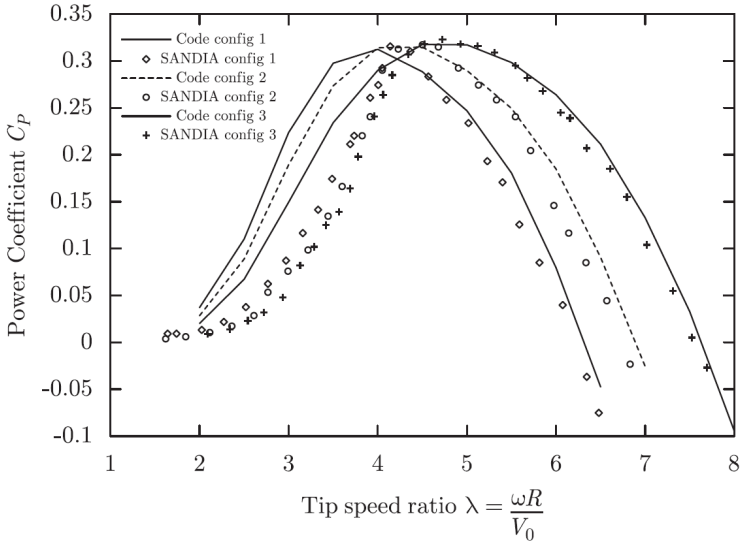

Figure 2.18 - Results from Sandia National Laboratories experiments and the three-dimensional N-S model by Antheaume (2008) permission to reproduce figure granted by Elsevier Ltd.

Further increases in available computational power have led to the development of models of entire rotors and their surrounding flow field (Consul *et al.*, 2009, Howell *et al.*, 2010). However, the accuracy of performance prediction of these models is rarely a significant improvement over that of other less computationally expensive techniques.

2.5. Complications of local blade mechanics

When predicting the forces generated by an aerofoil it is most common to use simple aerofoil theory and published aerofoil data, which assumes that the lift and drag produced by an aerofoil section is a function of three basic variables; the incident velocity, the Reynolds number of the flow and the angle of attack relative to the blade chord. It has now become accepted that, due to the unsteady flow experienced by a turbine blade in Darrieus motion, to accurately predict the lift to drag characteristics of an aerofoil it is necessary to understand the flow field around the blade in greater detail (Strickland *et al.*, 1979, Tchon and Paraschivoiu, 1994, Wang *et al.*, 2007).

2.5.1. Flow curvature effects

A turbine blade in Darrieus motion experiences a curvilinear flow, as opposed to the rectilinear flow in which the majority of published aerofoil data has been produced (Migliore *et al.*, 1980). This results in a variation of the angle of attack experienced by the section along the length of the chord, as shown in Figure 2.19.

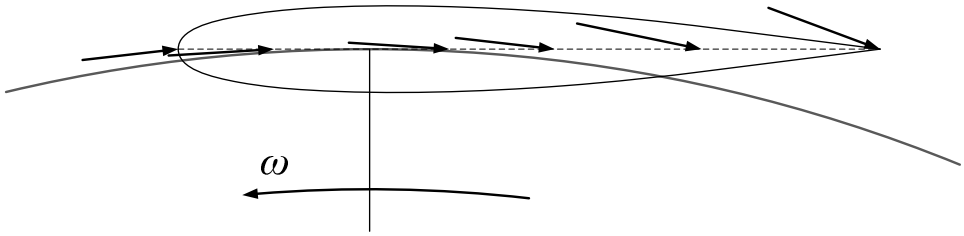

Figure 2.19 - Image showing relative velocity vectors on a blade in a curvilinear flow field, modified from Migliore et al. (1980)

Migliore (1979) used conformal transformation to show that by using a symmetrical aerofoil in a curvilinear flow there is a change in effective camber and an introduction of an effective angle of incidence, in addition to the usual blade angle of attack. A Darrieus cross-flow device using straight chorded blades experiences an increased effective angle of attack on the upstream half of the device and a reduced effective angle of attack on the downstream half. This causes the upstream half of the device to stall at a higher tip speed ratio and the downstream half to stall at a lower tip speed ratio. It is unclear from the research by Migliore whether this phenomenon is beneficial to the performance of the device. As one would expect, the magnitude of this virtual camber and virtual incidence are strongly dependent on the solidity of the device.

During scale tests of the THAWT device by McAdam (2007), in an attempt to negate the effects of flow curvature the profile of a symmetrical hydrofoil section was ‘wrapped’ around the circumference of the turbine using equations 2.16 and 2.17.

$$x' = (r + y)\sin\left(\frac{x}{r}\right) \qquad 2.16$$

$$y' = (r + y)\cos\left(\frac{x}{r}\right) \qquad 2.17$$

The resulting section, shown in Figure 2.20(b), is anticipated to produce no virtual incidence or camber and to achieve zero lift when rotating in a stationary flow. This is intended to allow the performance of the hydrofoil in the curvilinear flow to be modelled by published aerofoil data, measured using symmetrical aerofoil in rectilinear flows.

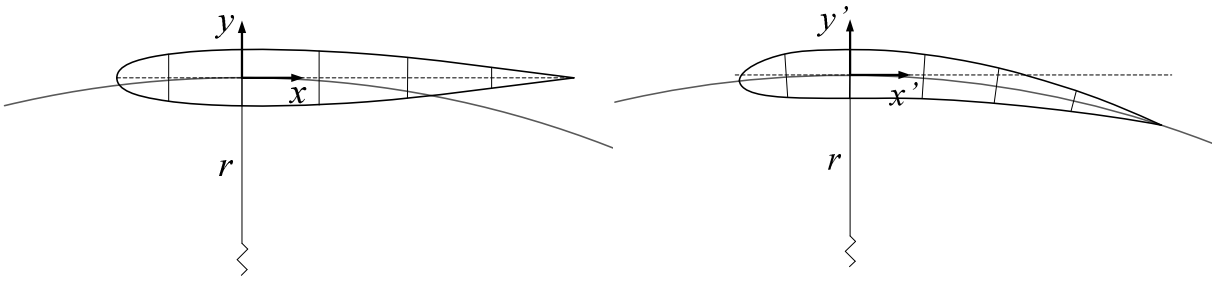

(a) Rectilinearly symmetrical section *(b) Circumferentially 'wrapped' section*

Figure 2.20 - Images of blade sections used in experiments by Consul

To explore the effect on the performance achieved by a Darrieus device using hydrofoils wrapped onto the turbine circumference, Consul (2008) performed a series of experiments on symmetrical and cambered blades using the Darrieus rotor apparatus developed during the undergraduate Masters project of McAdam (2007). The results from these experiments are shown in Figure 2.21, and demonstrate that the rotor using the wrapped blade sections produces significantly more power than the rotor in which the rectilinearly symmetrical blades are adopted.

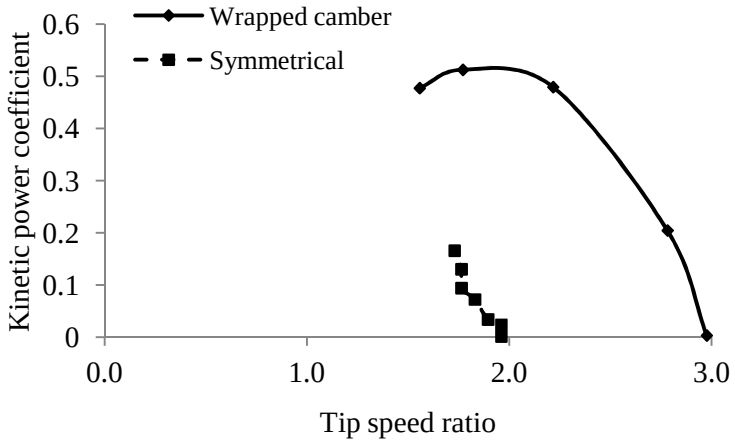

Figure 2.21 - Power curves for rectilinearly symmetrical and wrapped blade rotors in a 0.3 m/s flow

As well as experiencing a curvilinear flow, a blade section in Darrieus motion also imparts a centripetal acceleration on the generated surface boundary layer (Migliore *et al.*, 1980). These centripetal forces will modify the boundary layer development on the blade surface and possibly force separation or delay separation depending on the orientation of the high and low pressure surfaces of the aerofoil. This phenomenon may act to delay stall on the upstream half of the turbine and accelerate stall on the downstream half of the device.

2.5.2. Dynamic stall

It is relatively widely accepted that dynamic stall has a significant effect on Darrieus cross-flow devices (Brochier *et al.*, 1986, Paraschivoiu and Allet, 1988). Dynamic stall is the

process by which rapidly increasing the angle of attack delays the onset of stall to greater angles of attack and corresponding greater lift coefficients. However, when stall does eventually occur it tends to be more severe than in the static case.

Experiments have shown that dynamic stall occurs because of the shedding and passage of a vortex-like disturbance which induces a highly non-linear pressure field (McCroskey, 1981). If the frequency and amplitude of the oscillation are large enough, the vortex shedding is well organised and clearly defined.

(a) Lift *(b) Drag*

Figure 2.22 - Foil performance characteristics during dynamic stall on a Vertol VR-7 aerofoil at M = 0.06 and k = 0.10 (McCroskey, 1981) permission to reproduce figures online not granted

Instead of the usual mechanism of stall, in which separation of the boundary layer due to adverse pressure gradients causes a decrease in lift and an increase in drag, a vortex is shed from the leading edge, which remains attached to the foil and moves towards the trailing edge (1→2 of Figure 2.22). When stall does occur it is more severe than for the static case and re-attachment of the flow is often delayed, resulting in a hysteresis of lift and drag.

The characteristics of a foil during dynamic stall are affected by many factors such as the pitching rate of the foil, the Mach number of the flow, the foil section profile and the range of angle of attack (Francis and Keesee, 1985, McCroskey *et al.*, 1982). However, experiments have shown that the effects of dynamic stall are most significant at low Mach numbers (M < 0.3), and for values of reduced frequency, a dimensionless measure of the pitch rate of an aerofoil (Tang and Dowell, 1995) defined in equation 2.18, greater than 0.05.

$$k = \frac{\omega c}{2u_\infty} \qquad 2.18$$

The blades of a tidal turbine exclusively operate in Mach number flows significantly lower than 0.3. Assuming that the velocity term in equation 2.18 can be approximated by the mean

blade velocity in a cross-flow device, the reduced velocity can be expressed purely as a function of the turbine solidity and number of blades, as shown in equation 2.19.

$$k = \frac{\omega c}{2u_\infty} = \frac{\omega c}{2V_R} = \frac{\omega c}{2\omega r} = \frac{c}{2r} = \frac{\pi \times solidity}{n} \qquad 2.19$$

It would therefore be expected that a device with six or fewer blades is likely to be significantly affected by dynamic stall when configured with a solidity greater than 0.1, which includes all of the THAWT devices tested and analysed in this work.

Despite the significant reduction in the performance of the foil post dynamic stall, greater performance than that theoretically calculated is often attributed to the positive effect of dynamic stall (Brochier *et al.*, 1986).

Whilst limited simulation of the dynamic stall phenomena has become possible due to the increase in computational power applied to numerical models (Consul *et al.*, 2009, Ekaterinaris and Platzer, 1998, Johansen *et al.*, 2002), the current time required to simulate this complex flow phenomenon and the low level of accuracy renders this method unsuitable for integration into most global turbine models.

Several models, not based on numerical analysis, exist for the prediction of the dynamic stall characteristics of foils, which tend to track the progress and history of the foil pitching, in order to predict the performance characteristics at any given time. Some 'synthesis' models require the use of load measurements from oscillating foils in wind tunnel experiments (Reddy and Kaza, 1987), while others use semi-empirical equations, which extend the static foil performance into the dynamic stall phenomena (Leishman, 2002). Whilst the availability of experimental data on a chosen foil can often prevent the use of synthesis methods, many semi-empirical models lack rigour and generality when applied to different foil sections.

2.6. Free surface modelling

Whilst the performance of a wind device can be relatively accurately modelled using numerical models or momentum approaches (Burton *et al.*, 2001, Paraschivoiu, 2002), the prediction of the performance of a tidal device is further complicated by the boundary constraint of the free surface. As described in section 2.7.2, the mechanism by which energy is extracted from a tidal flow is the reduction of total head. For the sub-critical open channel flows, which account for the vast majority of the tidal stream sites around the UK, a reduction in total head results in a decrease in depth and an increase in the average velocity of the flow.

The influence of the free surface on the flow field means that common momentum techniques used to calculate the performance of cross-flow devices are inappropriate. As described in section 2.3.3, LMADT-OCF demonstrates that the amount of energy available to a device in an open channel flow is greater than the amount of energy available to a device in an unbounded flow. As shown in Figure 2.23, for relatively low blockage devices the amount of extra power available is relatively small, when compared to the unbounded case.

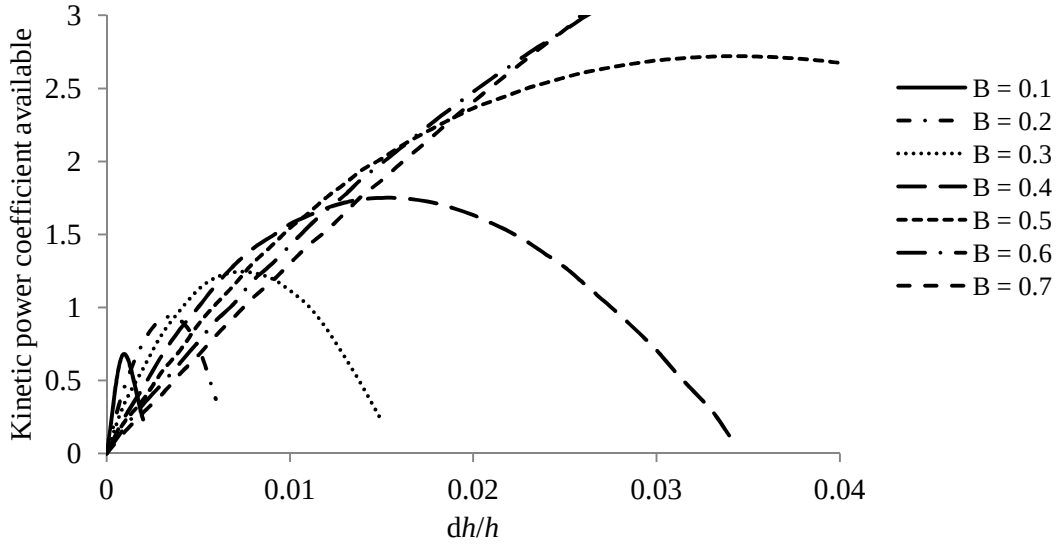

Figure 2.23 - Kinetic power coefficient available to a device for a range of blockage ratios B, calculated using LMADT-OCF (Houlsby et al., 2008a)

Due to the complexity and computational cost of numerically modelling the deformation of the free surface, most two dimensional studies of cross-flow tidal devices have ignored free surface deformations (Antheaume *et al.*, 2008, Gretton and Bruce, 2005). Some argue that modelling the free surface is not necessary, as the reduction in accuracy is small when modelling relatively low blockage scenarios. However, when modelling devices of greater blockage ratio, $B = 0.5$ for example, the amount of power available is significantly increased by a factor of up to 4.6.

There are two main approaches to computing free surface flows; interface-tracking and interface-capturing. Interface-tracking is commonly used in both Finite-Element and Finite-Volume techniques (Mahrenholtz and Markiewicz, 1999, Zienkiewicz *et al.*, 2005). This method is concerned with simulating a single phase of fluid and changing the geometry of the free surface boundary in order to model the deformation of the interface. Most commonly, functions are set up calculate the deformation of the free surface, based on the constraint of flow parallel to the free surface (Carrica *et al.*, 2005, Zienkiewicz *et al.*, 2005). The geometry

of the free surface can then be updated and the model can be remeshed at each time step, so that the solution can be obtained iteratively. The process of repeated mesh updating can be computationally costly, and so a simpler approach is to use hydrostatic adjustment (Zienkiewicz *et al.*, 2005). In the hydrostatic adjustment technique a numerical model with a fixed domain is allowed to progress to an advanced solution, before the free surface is adjusted, by assuming a hydrostatic distribution of pressure. Hydrostatic adjustment also requires several iterations to achieve an accurate solution.

Interface-capturing is most commonly used in Finite-Volume techniques (Mahrenholtz and Markiewicz, 1999). The usual implementation of this technique, called Volume of Fluids (VOF), is to assign each control volume with a void fraction of a given phase, c_v. The solution domain extends over the fluid and air phases with the void fraction set $c_v = 1$ for liquid and $c_v = 0$ for air. Control volumes with a void fraction between $0 < c_v < 1$ contain the interface and the change in void fraction is governed by a transport equation.

Upwinding techniques are commonly used to add artificial viscosity in the stream-wise direction to stabilise the oscillations which occur in solving the Navier-Stokes equations, when the convective terms dominate over the diffusive terms (Zienkiewicz *et al.*, 2005). The volume of fluid method often requires relatively complex schemes to prevent the smearing of the interface by upwinding techniques and to establish the exact location of the interface. The computation costs are also increased by the necessity of modelling the dynamics of the fluid, gas and interface phases. However, this technique is particularly suited to modelling flows in which air becomes trapped in the liquid phase or when the forces applied to the fluid by the air phase are significant.

2.7. Tidal stream energy resource

2.7.1. Tidal energy around the UK

The renewable resource of the rise and fall of the tide is predominately caused by the gravitational pull of the moon on the oceans and the earth. This periodic swell of water can be thought of as a wave whose amplitude varies between coastal regions around the world, depending on the bathymetry of the continental shelves and the local channels and basins (Arbic and Garrett, 2010, Garrett, 1972). The total amount of energy dissipated in the global tidal system has been relatively well established at 3.7 TW, of which roughly two thirds can be accounted for by the principal M2 semi-diurnal tide (Cartwright, 1993). The dissipated

energy is assumed to be predominantly due to the formation of boundary layers at the bottom of shallow seas (Jeffreys, 1921), although more recent research has indicated that 25-30% may be dissipated in deep oceans (Egbert and Ray, 2001). The interaction of tidal movements between oceans, continental shelves and local coastlines is complex, but using mechanical analogues of the global tidal system, Arbic and Garrett (2010) predicted that only a fraction of the present dissipation rate is available for human use. This implies that tidal power can never meet the needs of more than a small fraction of human energy demands, although it could provide useful amounts of energy in certain locations. The European Shelf has been identified as an area of high tidal energy dissipation, as shown in Figure 2.24, with 170-260 GW of energy dissipation (Egbert and Ray, 2001).

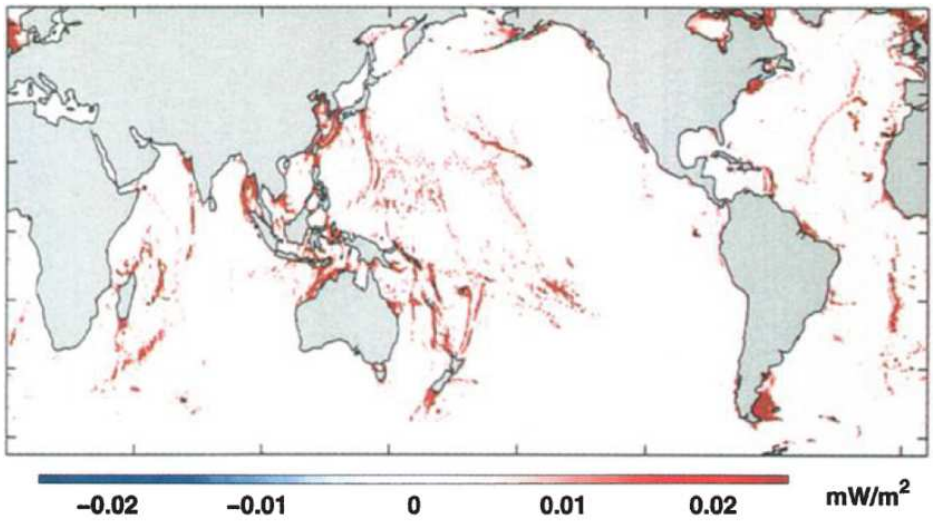

Figure 2.24 - Chart of global tidal dissipation (Egbert et al., 2004) permission to use figure granted by the American Geophysical Union

Charts produced by the UK Department of Trade and Industry suggest that of the tidal power available to the UK, the majority is localised at specific sites (DTI, 2004). Estimates at these sites indicate that power in the order of gigawatts is available for extraction (Burrows *et al.*, 2009, Rainey, 2009). This would allow the feasible extraction of tidal energy using large scale devices that benefit from economies of scale, and supply up to 6% of the UK electricity demand (Black&Veatch, 2005).

2.7.2. Principles of energy extraction

Until recently it has been assumed that the energy drawn from a tidal flow is extracted as kinetic energy. On that basis, most tidal turbines are rated by their kinetic power coefficient, shown in equation 2.20, and many have assumed that the theoretical Lanchester-Betz limit of 59% (Manwell, 2002) in air also applies to underwater turbines (Khan *et al.*, 2006).

$$C_{Pk} = \frac{Energy_{out}}{Energy_{in}} = \frac{Energy_{out}}{{}^{1}/_{2}\,\rho u_{\infty}{}^{3} A_t} \qquad 2.20$$

Another general assumption is that as kinetic energy is extracted, the flow velocity will decrease and the depth will increase due to a conservation of mass. Experimental tests have proven this assumption to be incorrect, as energy extraction from flows of a Froude number similar to that of real tidal channels causes the depth of the flow to decrease (McAdam *et al.*, 2010, Myers and Bahaj, 2007).

The explanation for this decrease in flow depth stems from the fact that an extraction of energy from an open channel flow results in a reduction of the total head, defined in equation 2.21 (Massey and Ward-Smith, 1998).

$$H = h + \frac{u^2}{2g} \qquad 2.21$$

As almost all tidal flows are subcritical, a reduction in total head results in an increase in flow velocity and a decrease in depth, as shown in Figure 2.25.

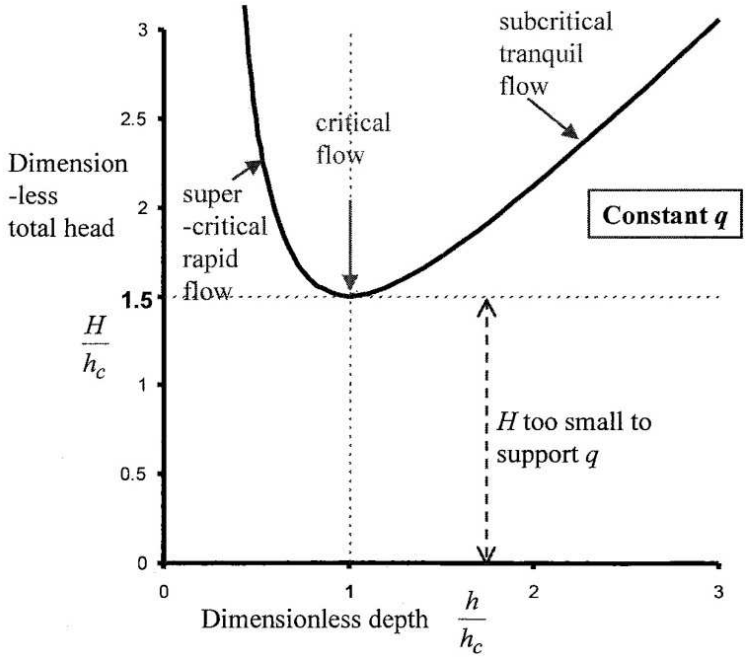

Figure 2.25 - Variation of total head with flow depth for a constant volume flow rate (Oldfield, 2004)

Turbine efficiency, or head power coefficient, can now be defined as the amount of mechanical power produced non-dimensionalised by the amount of total head extracted from the flow, as shown in equation 2.22.

$$C_{PH} = \frac{P_{turbine}}{\dot{m} g (H_1 - H_2)} \qquad 2.22$$

Current research and commercial developers tend to quote the kinetic efficiency of a device, because an understanding of head extraction from open channel flows has only recently become a familiar concept. As the blockage ratio tends towards zero the maximum attainable head efficiency limits towards the Lanchester-Betz limit. Because the majority of tidal devices in development only achieve small blockage ratios it could be argued that it is not necessary to measure the performance of a tidal stream turbine using the head efficiency metric. In practice the head power coefficient is the correct measure of how efficient a turbine is at extracting energy from a flow and will allow for fair comparisons of all tidal stream devices in the market.

2.7.3. Typical UK tidal stream parameters

Figure 2.26 shows the Froude number of several potential tidal stream sites around the UK that were studied by Black & Veatch (2005), during a tidal assessment of the UK.

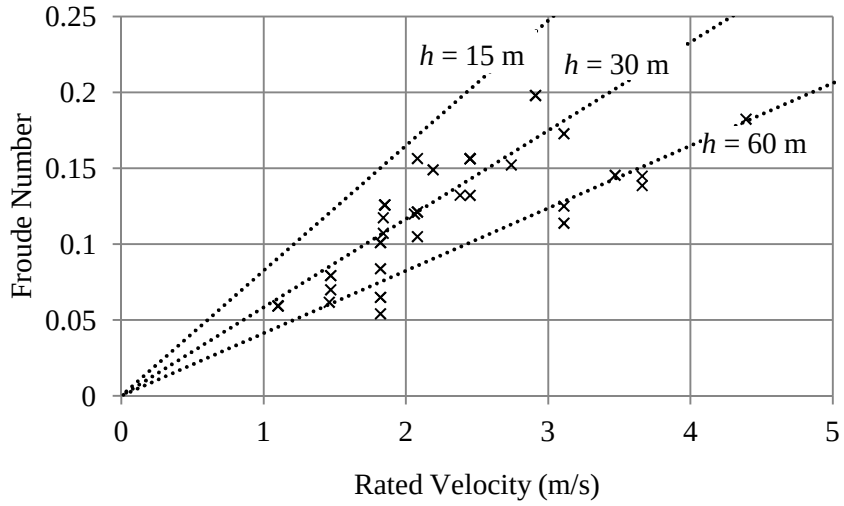

Figure 2.26 - Froude number of potential tidal stream sites around the UK, based on data in (Black&Veatch, 2005)

The reported data shows that of the tidal streams with a rated flow velocity greater than 2 m/s, which might be considered those with the greatest energy potential, most are within the Froude number range of $0.1 < Fr < 0.2$. This indicates that potential tidal sites in the UK are exclusively subcritical and have a significantly greater proportion of potential head available for extraction than kinetic head.

2.8. Structural analyses of tidal devices

Very little data has been published regarding structural analyses of tidal devices, perhaps due to the commercial adoption of most designs and the reluctance of private companies to

make such information publicly available. However, the tools and methodologies required for a structural analysis of a tidal turbine are likely to be similar to those previously undertaken by the wind industry.

'Bladed for Windows', developed by Garrad Hassan, is a commercial program originally designed to predict the aerodynamic and structural performance of wind turbines, and is used commonly throughout the wind industry. The program uses a combination of blade element theory and momentum actuator disc theory, with various corrections and extensions for different flow phenomena, to predict the performance and loading of a turbine rotor (Bossanyi, 2003). As well as performing an analysis of the blade and tower natural frequencies using a modal analysis, the aerodynamic and inertial loads are applied using beam theory to predict the stresses induced in the structure. Based on the expected cycle of loads a fatigue analysis is conducted using the assumption of linear cumulative damage.

Whilst the 'Bladed' method from Garrad Hassan is good at providing parameter optimisation and feasibility estimates for an initial turbine design, more specific designs of rotor blades are commonly performed using (shell) finite element models, in order to optimise the use of material (Bechly, 1997, Kong *et al.*, 2005). These designs often focus on the effect of material fatigue due to industry standard loading patterns (Delft *et al.*, 1997, Kong *et al.*, 2005).

Design for fatigue in wind turbines has become essential as, despite the relatively low amplitude fluctuations in blade stress experienced by wind turbine blades, a significant proportion of blades fail due to material fatigue (Hartman and Corning, 2006). Due to the large oscillatory loads experienced by the blades of a Darrieus cross-flow device (Ashwill and Leonard, 1986, Peace, 2003), fatigue is also likely to be a significant factor on the stress limits of any structural design.

2.9. Material fatigue considerations

A major factor that is anticipated to severely affect the design of a cross-flow tidal device is the reduction in stress at failure over the lifetime of the turbine due to cyclic fatigue. During a single rotation of a cross-flow device the angle of attack and lift force produced by the blades reverse direction, resulting in an oscillating load on the blade members. Over the design lifetime of the device, which can be as long as 30 years, the rotor blades are likely to be subjected to 10^8 or more fatigue cycles (Hartman and Corning, 2006), which is likely to result

in material failure at a level of stress significantly lower than the static material strength. It is therefore important to understand how to design a rotor structure and to choose a blade material so that cyclic fatigue damage is minimised.

The mechanism of fatigue is not completely understood and is commonly believed to commence via small cracks in the atomic structure of a material, and to develop from the first few cycles of stress, over several thousands of millions of subsequent cycles, until eventual failure (Benham and Warnock, 1976). It is generally assumed that in the cyclic process of fatigue, material damage is accumulated, which can be through plastic (low cycle < 10^5) or elastic (high cycle > 10^5) fatigue. The onset of fatigue can also be affected by several factors such as locations of stress concentrations, variations in temperature and chemical corrosion.

Despite a significant amount of research into the prediction of the service life of a material subjected to significant cyclical stress, the complexity of the mechanisms mean that there is no complete solution. The cyclical stresses applied to a material are typically characterised by three main factors; the mean stress, stress amplitude and the stress ratio, shown in equations 2.23, 2.24 and 2.25 respectively.

$$\sigma_m = \frac{\sigma_{max} + \sigma_{min}}{2} \qquad 2.23$$

$$\sigma_a = \sigma_{max} - \sigma_{min} \qquad 2.24$$

$$R = \frac{\sigma_{min}}{\sigma_{max}} \qquad 2.25$$

S-N plots are commonly used as an empirical method of predicting how many cycles of a given stress amplitude and mean stress that a material can endure before failure is expected to occur, as shown in Figure 2.27(a). The modified Goodman relationship can be used to predict how the fatigue life is further affected by the mean stress and stress ratio, as shown in Figure 2.27(b). Note that the alternating stress in Figure 2.27(b) is defined as half of the stress amplitude. Miner's rule (Miner, 1945) is then commonly applied to calculate how various states of cyclic stress accumulate damage in a material and lead to eventual failure.

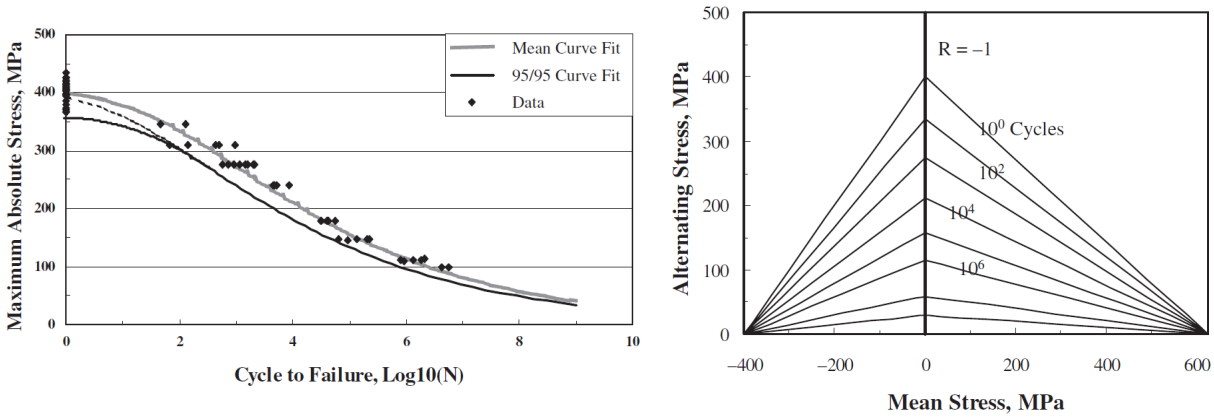

(a) S-N curve at R=-1 *(b) Goodman diagram*

Figure 2.27 - Typical S-N and Goodman diagram for a GFRP material (Sutherland and Mandell, 2005) permission to use figure granted by John Wiley and Sons

The blades of large scale axial-flow wind devices are commonly constructed using glass fibre reinforced plastic (GFRP) composite due to its relatively low cost and good strength and stiffness to weight ratio (Delft *et al.*, 1997, Kong *et al.*, 2005, Sutherland and Mandell, 2005). The favourable properties of this material, and the existing experience in manufacturing large scale aerofoil structures for the wind industry, has incentivised the use of composite materials in the construction of new tidal devices (Young *et al.*, 2010).

Despite the favourable properties of composite materials for blades of a tidal device, the prediction of fatigue failure is further complicated due to the non-homogenous structure and anisotropic properties of the fibre-resin matrix. A stress cycle in which the material experiences a tensile stress and a compressive stress (T-C) has been shown to degrade more rapidly than one that simply experiences a varying tensile load (T-T), due to accelerated debonding of the fibres and resin around transverse fibres (Gamstedt and Sjogren, 1999). This means that the fatigue life of a multi-laminate composite material is likely to have an increased dependence on the stress ratio, when compared to a more homogenous material (Mandell *et al.*, 2003, Philippidis and Vassilopoulos, 2002, Sutherland, 2004), and a more comprehensive Goodman diagram is required, such as that shown in Figure 2.28.

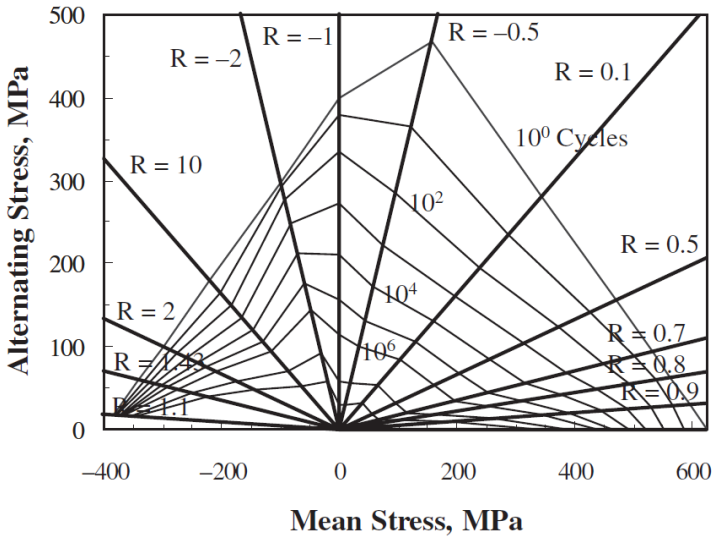

Figure 2.28 - Goodman diagram illustrating the variation in fatigue life with stress ratio for an industry standard layup of GFRP (Sutherland and Mandell, 2005) permission to use figure granted by John Wiley and Sons

It has also been suggested that variable amplitude loading, as might be expected on a tidal device in a sinusoidally varying tidal range, may cause accelerated degradation of the material (Delft *et al.*, 1997). Techniques such as residual stiffness and residual strength methods have been used to improve the prediction of the fatigue life of a specimen under variable amplitude loading, and have been successfully validated by experiments on material samples (Schaff and Davidson, 1997, Sutherland and Mandell, 2005). However, the significant differences in material properties between various designs of composite layup mean that it is often necessary to use experiments in order to calibrate one or more degradation parameters (Wahl, 2001).

2.10. Previous experimental and analytical work

There appears to be no prior published research in horizontally mounted cross-flow tidal devices. Prior to this DPhil project three undergraduate Masters projects were carried out (Banfield, 2006, Burgess, 2006, McAdam, 2007), the most comprehensive being the work by McAdam.

2.10.1. Undergraduate Masters project performed by McAdam (2007)

In undergraduate masters work by McAdam (2007) the hydrodynamic performances of three main rotor variants, shown in Figure 2.29, were tested experimentally, each rotor being of a diameter of 0.16m and solidity of 0.3. During these experiments the parallel three-bladed device produced power with a kinetic efficiency significantly greater than the Lanchester-Betz limit, highlighting the significant potential of the THAWT device. However, tests of a truss

configured device were ineffective, due to the significant variations in hydrofoil performance with moderate changes in Reynolds number, when reducing the blade chord.

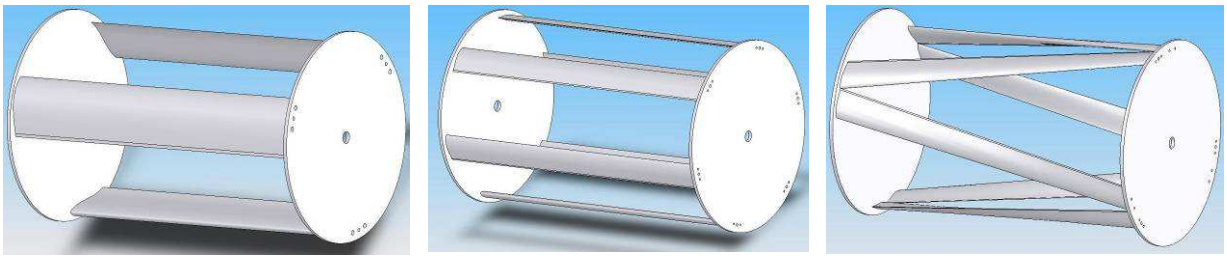

(a) Three parallel blades *(b) Six parallel blades* *(c) Six trussed blades*

Figure 2.29 - CAD images of rotors tested by McAdam (2007)

The experimental data were used in an attempt to calibrate a simple numerical spreadsheet, which solved the basic blade element equations 2.1 - 2.5. It was hoped that this model could be used to predict the mechanical power produced by any scale or configuration of the device. This process proved to be unsuccessful due to the gross simplification of the hydrodynamics behind the numerical model. A poor understanding of the variability in aerofoil performance with varying Reynolds number, as well as the assumption of steady and uniform flow at the velocity of the upstream flow meant that the torque and power produced by the turbine could not be predicted with any accuracy.

The simple hydrodynamic model was used in an attempt to predict the forces acting on the turbine blades, which were applied to a simplified finite element model of the turbine, as shown in Figure 2.30.

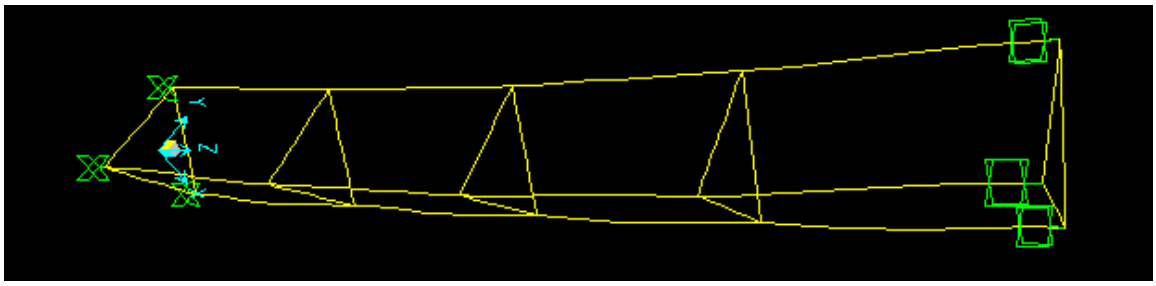

Figure 2.30 - Post-processing images of exaggerated deformation of the parallel three-bladed device from the structural analysis program (SAP)

Despite the inaccuracy of the forces produced by the numerical model, the structural analysis suggested a significant decrease in stress and deflection in the truss configuration of the device, when compared to the parallel-bladed turbine.

The findings of this study demonstrated that, if the hydrodynamic performance of the parallel-bladed device could be replicated in the truss configuration, it would be possible to

create a structurally rigid device with the potential to produce power at efficiencies greater than the Lanchester-Betz limit.

2.10.2. Undergraduate Masters project performed by Swidenbank

In order to improve the hydrodynamic modelling of the THAWT device, Swidenbank (2009) implemented a numerical model of a parallel-bladed THAWT device during her undergraduate Masters project, using a combination of CFD and blade element theory. The model specifications were matched to the 1/20th scale THAWT experiments performed in 2008 at Newcastle University, described in more detail in Chapter 4, the results from which were used to validate the numerical model. In order to improve the prediction of the flow field around the device, when compared to previous techniques, Swidenbank used the COMSOL multi-physics package, a partial differential equation solver, to solve the N-S equations. The rotor was modelled using an actuator cylinder in which the forces were predicted using blade element theory, as shown in Figure 2.31.

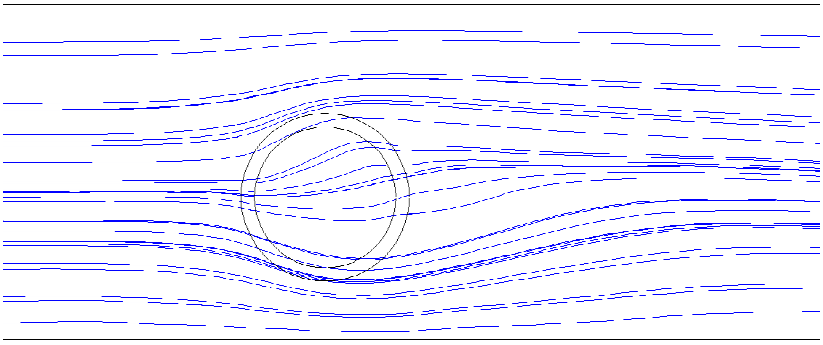

Figure 2.31 - Visualisation of streamlines through an actuator cylinder (Swidenbank, 2009)

The velocities predicted by the N-S equations were used to perform the blade element calculations, which required the resultant velocity and angle of attack to be calculated in terms of the stream-wise and vertical velocity components as shown in equations 2.26 and 2.27.

2.26

2.27

After recognising the significance that dynamic stall has on the performance of the turbine, Swidenbank chose to use lift curves modified in accordance with empirical dynamic stall data, as shown in Figure 2.32. Despite the effect of dynamic stall on the drag characteristics of the aerofoil, the drag curves were unchanged from the static case.

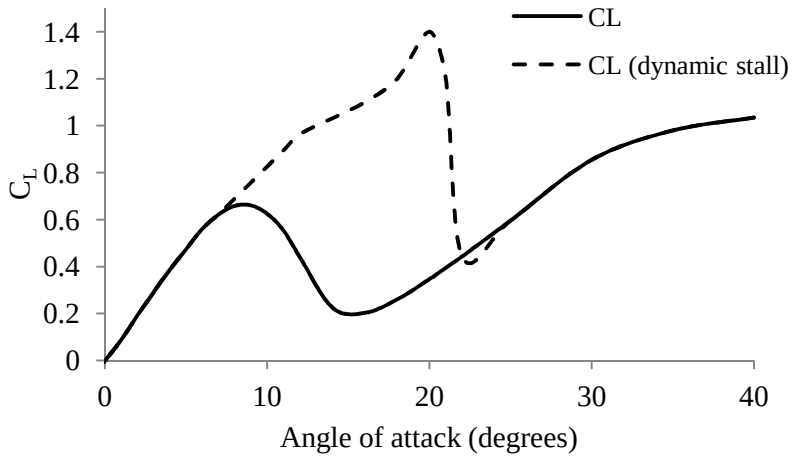

Figure 2.32 - NACA 0018 lift curves modified for COMSOL analysis based on data in (Swidenbank, 2009)

In order to achieve results in a short period of time, Swidenbank chose to use a solution algorithm which converges on a steady state solution. To converge on a steady state solution turbulent eddies and vortices must be stabilised, so that no significant time varying perturbations exist in the solution. To stabilise the solution and remove time varying perturbations it was decided to apply artificial isotropic diffusion, which adds viscosity to the flow, greater than that which would be expected in practice.

As well as the need for an unrealistically large amount of viscosity, the requirements of the steady state solver resulted in the failure of convergence below a tip speed ratio of roughly 2.4, at which point the maximum angle of attack is approximately 22°. As the angle of attack reaches 22° the hydrofoil characteristics begin the onset of dynamic stall, causing a severe drop in lift and a large shear that is likely to induce high vorticity, which prevents convergence of the steady state solution.

When performing this analysis, one might choose the thickness of the actuator cylinder to be equal to the thickness of the hydrofoils, so that the turbine influence is limited to the swept area of the device. Unfortunately, the inability of the steady state solver to deal with high shear meant that to allow convergence the actuator disc must be substantially thicker than the blade thickness, so that the applied force from the disc is applied across a greater area.

Despite the limitations of the steady state solver, and recognising that calculations using blade element theory lack the ability to model accurately the more complex flow phenomena anticipated in a Darrieus cross-flow device (see section 2.5), the accuracy in prediction of power curve was significantly improved when compared to previous models, as shown in Figure 2.33.

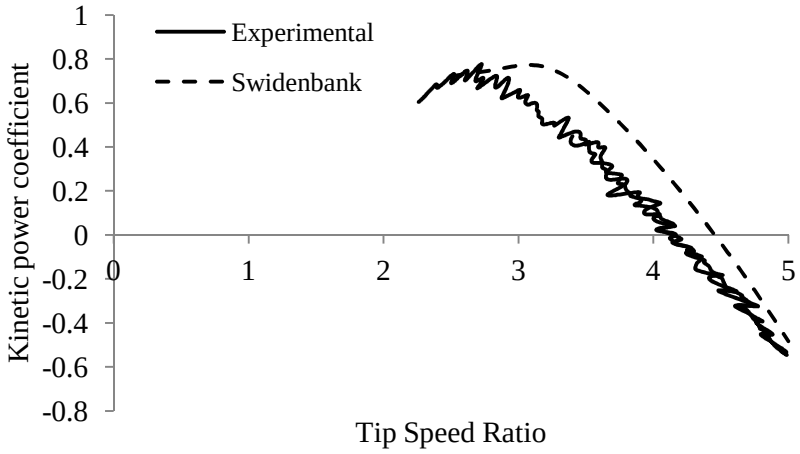

Figure 2.33 - Comparison of predicted kinetic efficiency for the 1/20th scale turbine at a Froude number of 0.17 and a blockage ratio of 0.5 based on data in (Swidenbank, 2009)

The main drawbacks of the model developed by Swidenbank are the poor consistency of convergence of a solution and the large amount of fine tuning that is required, which are both due to the use of the steady state solver. These issues make the model difficult to validate and apply to devices of a varying geometry or with different flow parameters.

2.11. Conclusions

From the available literature it is unclear which aspects of the design of the THAWT device will dominate the technical feasibility of a full scale turbine. It has therefore been decided to obtain experimental data and develop numerical models in order to perform a quantitative comparison of the factors which most significantly affect the structural and hydrodynamic performance of the device. With an understanding of the relationship between the structural and hydrodynamic performance, it will be possible to assess which factors affect the technically feasibility, when the conditions of a real tidal location are considered.

Chapter 3

Blade Force and Stress Preliminary Analysis

In order to assess the feasibility of the THAWT device it is necessary to explore how the blade forces and induced stresses vary with the design configuration and flow parameters. It is possible to create sophisticated numerical models of the turbine hydrodynamics and structural performance. However, a simple understanding of the effect that varying the design configuration has on blade force and stress quickly indicates which aspects of design are most significant in the optimisation of a device, and allows the first order validation of numerical analyses, when experimental results are not available.

This chapter outlines an application of simple dimensional analysis to the THAWT device, followed by preliminary analyses which can be quickly used to assess how variations in the design configuration and upstream flow parameters will affect the structural feasibility of the device. The accuracy of the preliminary analysis is explored by comparing with the numerical models of Chapter 7 and Chapter 8.

3.1. Scenario for dimensional analysis

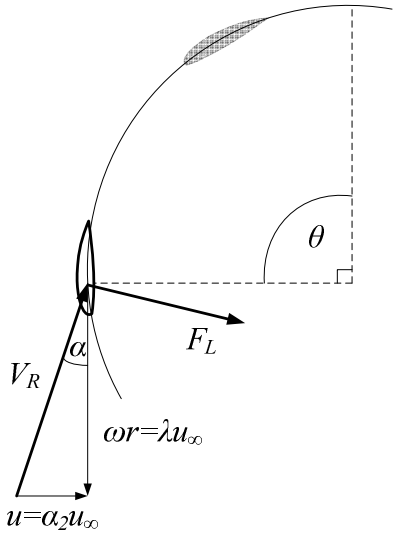

Figure 3.1 - Diagram of velocity components in a basic Darrieus turbine

This analysis focuses on the derivation of the maximum radial force produced by a blade of a cross-flow Darrieus turbine, and the maximum induced blade stress, at the operating tip

speed ratio. It is assumed that the maximum blade force and corresponding stress are induced at the furthest upstream point of the rotor, where the maximum angle of attack is anticipated to occur. The combination of velocity components experienced by the blade result in a lift force, which is perpendicular to the resultant component of blade velocity, as shown in Figure 3.1.

3.2. Variables and dimensionless groups

Table 3.1 lists the variables that are considered in this analysis and their dimensions of length, mass and time.

Variable	Symbol	Dimension
Blade lift force per unit length	F_L	ML/T^2
Density	ρ	M/L^3
Resultant blade velocity	V_R	L/T
Angle of attack	α	-
Chord length	c	L
Upstream flow velocity	u_∞	L/T
Component of blade velocity	ωr	L/T
Velocity incident at turbine	u	L/T
Turbine diameter	d	L
Flow depth	h	L
Number of blades	n	-
Maximum blade moment	M_{max}	ML^2/T^2
Blade second moment of area	I	L^4
Blade thickness	t	L
Maximum stress	σ_{max}	M/LT^2
Bay length	L_{bay}	L
Gravitational acceleration	g	L/T^2

Table 3.1 – Variables used during the dimensional analysis of the THAWT turbine

With 15 variables and three dimensions there are 12 dimensionless groups that can be used to relate the variables, which may be conveniently selected as shown in Table 3.2.

Group	Symbol	Relation to variables
Coefficient of lift	C_L	$\frac{F_L}{{}^1/_2 \rho {V_R}^2 c}$
Tip speed ratio of peak power	λ_p	${}^{r\omega}/_{u_\infty}$
Flow induction factor	α_2	${}^{u}/_{u_\infty}$
Solidity	s	$\frac{nc}{\pi d}$
Blockage ratio	B	${}^{d}/_{h}$
Dimensionless bending factor	-	$\frac{\sigma_{max} I}{M_{max} t}$
Dimensionless moment factor	-	$\frac{M_{max}}{F_L {L_{bay}}^2}$
Dimensionless blade velocity factor	-	${}^{\omega r}/_{V_R}$
Dimensionless second moment of area	-	$\frac{I}{t^3 c}$
Bay length to width ratio	β	${}^{L_{bay}}/_{d}$
Froude number	Fr	$\frac{u_\infty}{\sqrt{gh}}$
Thickness to chord ratio	-	${}^{t}/_{c}$

Table 3.2 – Dimensionless groups used during the dimensional analysis of the THAWT turbine

Several of the dimensionless groups in Table 3.2 have been derived from meaningful physical relationships of the problem. As shown in Figure 3.2, a blade member can be approximately modelled as a pin-jointed beam under the uniform loading of the blade force.

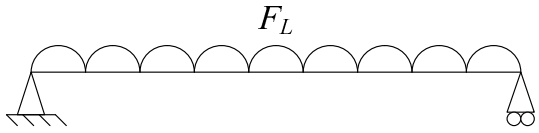

Figure 3.2 - Representation of a turbine blade as a simply supported beam

The maximum moment induced in the blade is given by equation 3.1 and is used to derive the dimensionless moment factor.

$$M_{max} = \frac{F_L {L_{bay}}^2}{8}$$
$$\therefore \frac{M_{max}}{F_L {L_{bay}}^2} \approx {}^1/_8 \qquad 3.1$$

The stress induced due to this bending moment is calculated using equation 3.2, which is used to derive the dimensionless bending factor.

$$\sigma_{max} = \frac{M_{max} y_{max}}{I}$$
$$\therefore \frac{\sigma_{max} I}{M_{max} t} \approx {}^1/_2 \qquad 3.2$$

It is assumed that the operating angle of attack is small, so that the blade lift force is generated approximately perpendicular to the blade chord about the weaker blade axis. The second moment of area about the blade axis is calculated using equation 3.3 and is used to derive the dimensionless second moment of area factor, as shown in equation 3.4, which applies to geometrically similar blades.

$$I = \int y^2 \, dA \qquad 3.3$$

$$\frac{I}{t^3 c} \approx const \qquad 3.4$$

This analysis assumes that the turbine spans the entire channel width, so that the blockage ratio *B*, defined as the proportion of the cross-sectional channel area that is occupied by the device, can be defined as the ratio of the rotor diameter *d* and the flow depth *h*.

3.3. Dimensional analysis of blade forces

3.3.1. Relationship between induction factor and tip speed ratio

It is assumed that for any configuration of the cross-flow Darrieus turbine, at the operating tip speed ratio the angle of attack at the most upstream point of rotation is fixed. This value would be just less than the angle that would induce stall, so that higher angles of attack would cause blade stall and poorer turbine performance. We might expect this to be the angle of attack which induces the optimum lift to drag ratio for the hydrofoil. It is also assumed that the performance characteristics of the hydrofoil do not vary with changes in configuration or flow parameters, such as due to changes in Reynolds number.

For small angles, the angle of attack can be expressed as:

$$\alpha \approx \frac{u}{\omega r} \qquad 3.5$$

Substituting relations for the flow induction factor and the tip speed ratio into equation 3.5 demonstrates that the induction factor therefore varies proportionately with the tip speed ratio, as shown in equation 3.6.

$$constant = \frac{u}{\omega r} = \frac{\alpha_2 u_\infty}{\omega r} = \frac{\alpha_2}{\lambda_p} \qquad 3.6$$
$$\therefore \alpha_2 \propto \lambda_p$$

This relationship is significant in understanding how variations in the turbine configuration are likely to affect the hydrodynamic and structural performance of the device. If a change in the configuration of the device results in a variation of the produced thrust and the

accompanying flow velocity through the rotor, as shown in Figure 3.3, it would be expected that the operating point of the device would occur at a different tip speed ratio.

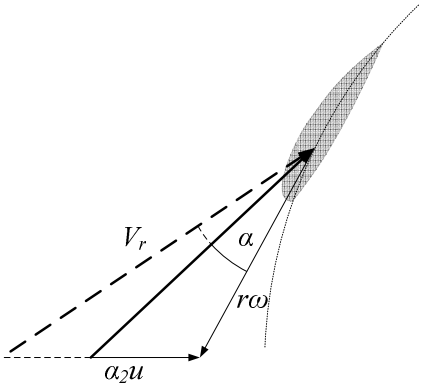

Figure 3.3 - Illustration of the effect on angle of attack by increasing the induction factor

3.3.2. Derivation of variation of force per unit length

It has been assumed that the coefficient of lift is fixed at the point of maximum radial force, at the operating tip speed ratio. It is further assumed that the operating tip speed ratio is high enough for the component of blade velocity to be significantly larger than the incident flow velocity. Therefore, the resultant velocity can be approximated as equal to the blade component of velocity as shown in equation 3.7.

$$\begin{gathered} \lambda_p u_\infty \gg u \\ \therefore V_R \approx \lambda_p u_\infty \end{gathered} \qquad 3.7$$

Substituting equation 3.7, the solidity and the blockage ratio into the relation for lift per unit length produces equation 3.8.

$$C_L = constant = \frac{F_L}{{}^1\!/_2\, \rho {\lambda_p}^2 {u_\infty}^2 c} = \frac{F_L n}{{}^1\!/_2\, \pi \rho {\lambda_p}^2 {u_\infty}^2 sBh} \qquad 3.8$$

By substituting the expression for Froude number into equation 3.8, it is possible to conclude that the lift force per unit length varies as shown in equation 3.9.

$$\begin{gathered} C_L = \frac{F_L n}{{}^1\!/_2\, \pi \rho {\lambda_p}^2 {u_\infty}^2 sBh} = \frac{F_L n}{{}^1\!/_2\, \pi \rho g {\lambda_p}^2 \mathrm{Fr}^2 sBh^2} \\ \therefore \frac{F_L}{pgh^2} \propto \frac{{\lambda_p}^2 \mathrm{Fr}^2 sB}{n} \end{gathered} \qquad 3.9$$

It is assumed that the fluid density and gravitational constant do not vary with changes to the device scale or configuration.

This analysis therefore demonstrates that the most significant change of radial blade force is a quadratic increase due to the Froude number of the flow, the operating tip speed ratio and the length scale of the entire problem.

3.4. Dimensional analysis of induced stresses

The dimensionless moment factor is constant for a given set of blade end restraints. By combining this expression with the dimensionless bending factor, an expression can be derived which relates the blade stress to the force per unit length, as shown in equation 3.10.

$$\frac{\sigma_{max} I}{F_L {L_{bay}}^2 t} \propto {}^1/_{16} \qquad 3.10$$

Substituting the dimensionless second moment of area factor, the bay length to width ratio, the solidity and blockage ratio into equation 3.10 produces an equation as shown in equation 3.11.

$$const \propto \frac{\sigma_{max} I}{F_L {L_{bay}}^2 t} \propto \frac{\pi \sigma_{max} s^3}{F_L n^3 \beta^2 B} \left(\frac{t}{c}\right)^2$$
$$\therefore \frac{h\sigma_{max}}{F_L} \propto \frac{n^3 \beta^2}{s^3 \left({}^t/_c\right)^2 B} \qquad 3.11$$

Combining equations 3.9 and 3.11 produces an equation describing the scaling of stress, in relation to all of the variables in question, and indicates the most significant variables in the scaling of induced blade stress, as shown in equation 3.12.

$$\frac{\sigma_{max}}{pgh} \propto \frac{{\lambda_p}^2 \mathrm{Fr}^2 n^2 \beta^2}{s^2 \left({}^t/_c\right)^2} \qquad 3.12$$

Equation 3.12 therefore indicates that for a given Froude number of flow the stresses induced in the turbine blades scale linearly with the geometric size of the entire domain, at the most upstream point of rotation and at the operating tip speed ratio. The stresses experienced in a scale model of a device should be multiplied by the geometric length scale in order to predict the stresses experienced by a full scale device, if the Froude number is conserved.

For the case that the Froude number is not conserved, equation 3.13 suggests that the blade stress scales with the square of the flow velocity, which is obtained by substituting the expression for the Froude number into equation 3.12. This expression illustrates that for a given flow velocity the blade stress does not vary with the length scale of the domain.

$$\frac{\sigma_{max}}{\rho {u_\infty}^2} \propto \frac{{\lambda_p}^2 n^2 \beta^2}{s^2 \left({}^t/_c\right)^2} \qquad 3.13$$

It should be noted that this analysis is derived on the assumption that the hydrofoil lift and drag characteristics do not change significantly with scale. In practice, an increase in Reynolds number will result in an increased lift to drag ratios at higher angles of attack. The effect that an increased Reynolds number has on stress scaling is unclear due to the competing factors of a higher lift coefficient and a reduced tip speed ratio.

3.5. Anticipated effect of negative offset pitch

Equation 3.12 suggests that reducing the operating tip speed ratio of the device is likely to significantly reduce the stresses induced in the rotor blades. It is proposed that applying an offset to the blade pitch is one method which might be used to reduce the operating tip speed ratio of the device.

The blades of a Darrieus turbine are most commonly angled so that the blade chord is neutrally pitched, which is defined as when the chord is tangential to the rotor pitch circle. A simple analysis, in which the flow is unaffected by the presence of the turbine, would suggest that this results in similar performance from the upstream and downstream halves of the device. However, basic momentum theory and experimental observations (Shiono *et al.*, 2000) indicates that a high solidity device, such as that suggested in this thesis, may be capable of producing a great enough thrust to vary the flow pattern experienced by the upstream and downstream halves of the device. The occurrence of a reduced velocity on the downstream half of the device is confirmed numerically in Chapter 7. The lower flow velocity experienced by the downstream half of the device is anticipated to result in a reduced angle of attack and corresponding lift coefficient. This analysis therefore assumes that the majority of the power is produced by the upstream half of the rotor.

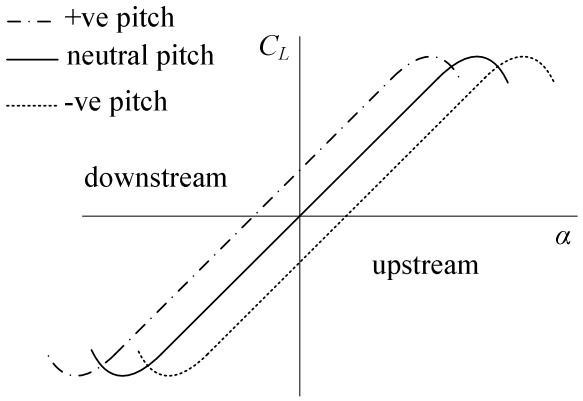

Figure 3.4 – The effect on lift coefficient of varying the blade offset pitch

Varying the blade pitch offset changes the position of the lift and drag polars with angle of attack, as shown in Figure 3.4. Positive pitch is defined as one which increases the apparent angle of attack on the upstream half of the device. The peak in lift coefficient on the upstream half of the device is achieved at a reduced angle of attack for a positive offset pitch, which would require an increase in tip speed ratio.

By applying a negative fixed offset pitch, it is anticipated that the operating tip speed ratio is reduced and that the magnitude of the geometric angle of attack incident to the blades is increased. As shown in Figure 3.5, the combination of an increased magnitude of angle of attack and a negative fixed offset pitch is expected to significantly improve the lift performance of the downstream blades.

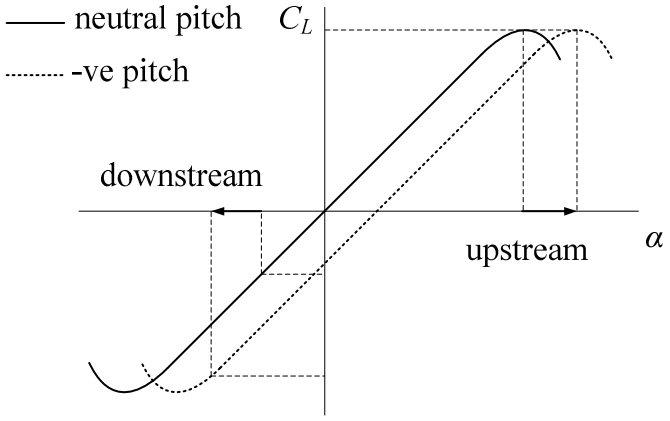

Figure 3.5 – The effect on lift coefficient of a negative offset pitch

In addition to the improved lift performance of the downstream blades, by operating at an increased angle of attack the resultant force is anticipated to orient the resultant force vector in a more tangential direction, as shown in Figure 3.6.

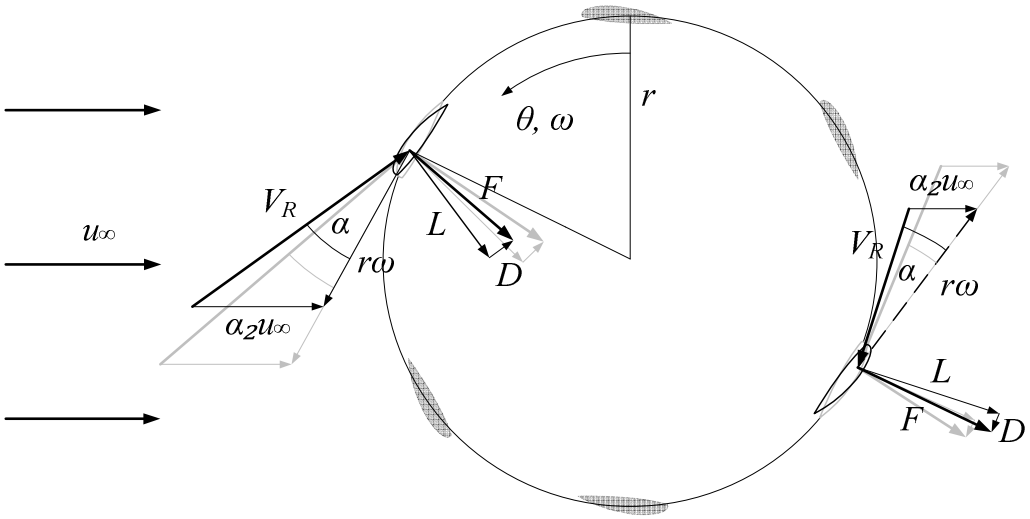

Figure 3.6 - Vectors of relative velocities and forces for a device with a negative fixed offset pitch. Grey lines represent the vectors of a neutrally pitched device at a higher tip speed ratio

By operating at a reduced tip speed ratio the magnitude of the upstream lift and drag vectors is likely to decrease. However, the change to the power and thrust produced by the device is not obvious, due to the additional contribution from the downstream half of the turbine.

It is anticipated that by applying a negative fixed offset pitch, the hydrofoil lift to drag performance is improved and that the ratio of produced power to thrust is likely to increase.

While a small improvement in the performance of a cross-flow device due to a negative pitch has previously been noted (Freris, 1990), the effect to a high solidity device of a high blockage has not been studied in detail.

3.6. Conclusions

The analytical dimensional analysis of a Darrieus type device with varied flow and design parameters illustrates the significant role that various parameters play in the scaling of blade forces and the corresponding stresses.

Minimising the aspect ratio of the rotor and the number of blades, and maximising the solidity and blade thickness, appear to be the most effective ways to reduce the stresses induced in the turbine blades.

The use of negative fixed offset pitch is suggested as a method of reducing the operating tip speed ratio and may potentially result in improved hydrodynamic performance of the device.

Chapter 4

Newcastle experimental setup

Previous experiments on the THAWT device had proven the potential of the parallel-bladed configuration (McAdam, 2007). However, it was identified that varying the turbine configuration from three to six blades resulted in a reduction in Reynolds number, which severely affected the performance of the device, and a reduced accuracy of the hydrofoil profile. The results from the truss configuration were therefore not useful for comparison with other configurations or representative of a larger scale device. The ability to validate analytical or numerical models of the device was severely limited, due to the complexity of the low Reynolds number (hydrofoil $Re \approx 4 \times 10^4$) flow phenomena.

It was decided that a set of experiments on a larger scale model of the device would offer the ability to compare the performance of various design configurations, as well as to allow the validation of numerical models, which could then be used to predict the performance of the device at full scale.

4.1. Newcastle University combined wind, wave and current tank

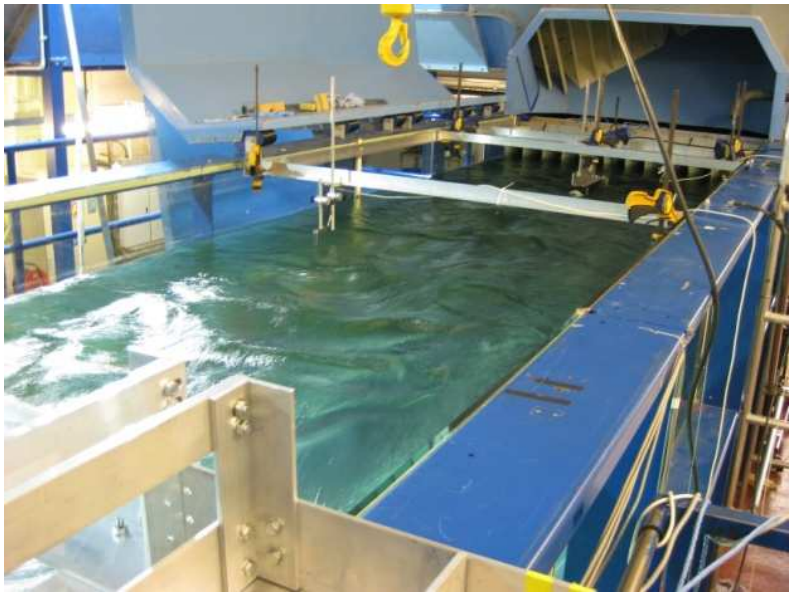

Figure 4.1 – Photograph looking downstream the unobstructed CWWC tank, with a flow depth of 1m

The combined wind, wave and current (CWWC) tank at Newcastle University was chosen for the simple factors of availability and price. With a width of 1.8 m, a maximum depth of 1

m and a working section length of 11.25 m, this indoor flume tank offers the ability to simulate flows of up to 1 m/s (see Figure 4.1).

4.2. Rotor design

4.2.1. Basic dimensions

It was decided that geometric similarity would be maintained with the device tested by McAdam (2007), with the initial intention of allowing a simple comparison of rotor performance with an increased Reynolds number. Based on this criterion a rotor diameter of 0.5 m and blade length of 0.875 m was chosen.

A full scale THAWT device would feature several turbine units attached end-to-end, creating a long, multi-bay rotor. To simulate this in a scale model a single bay is isolated, minimising the flow that may pass around the sides of the device, and only allowing flow to pass above and below the rotor. This was achieved by narrowing the span of the flume to a width of 0.96 m, as shown in Figure 4.2.

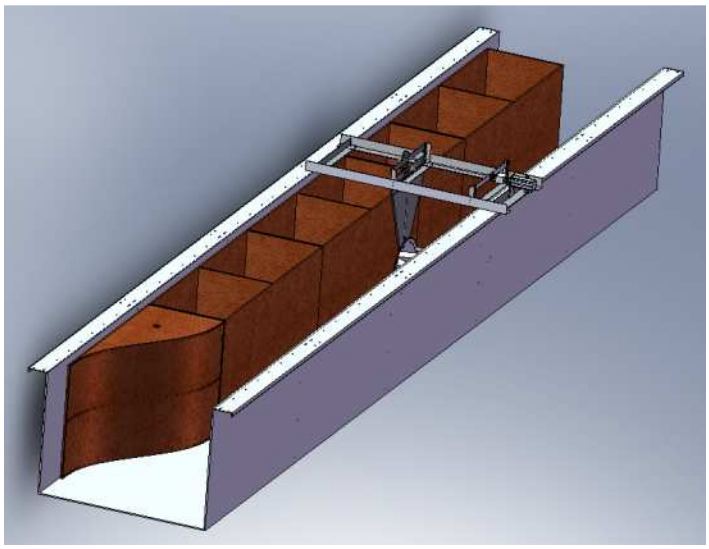

Figure 4.2 – CAD rendered image of the CWWC tank with the flow partition installed

The flow is narrowed using a 5th order polynomial inlet contraction (Bell and Mehta, 1988), which significantly reduced the flow turbulence, as well as narrowing the channel.

4.2.1. Configuration variants

The ‘truss’ THAWT device, shown in Figure 4.3(b), is the main focus of the experimental programme, but two other configurations of turbine were chosen as variants for comparison. A parallel six-bladed device, shown in Figure 4.3(a), is simply a horizontal implementation of the Darrieus concept, and is the main variant for comparison. By removing half of the blades, a three parallel-bladed variant of half the turbine solidity was also available to test.

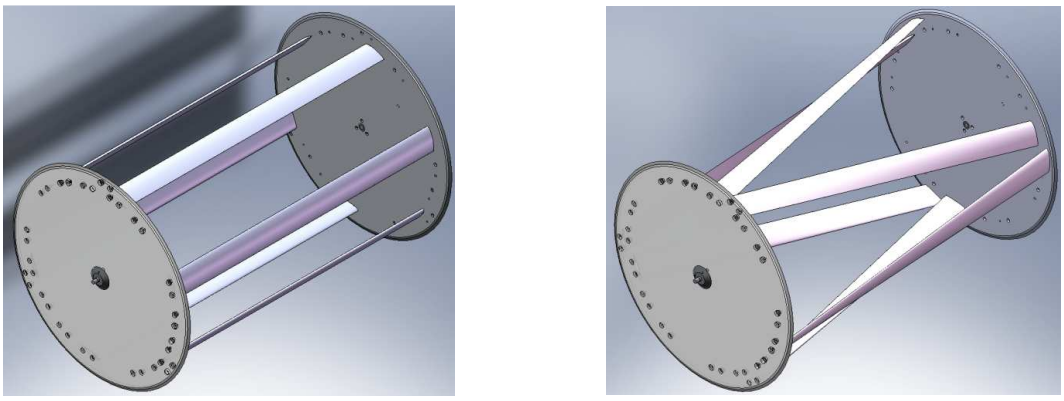

(a) Parallel configuration *(b) Truss configuration*

Figure 4.3 – Main variants of THAWT device used for tests at Newcastle

The truss turbine consists of blades which have a straight axis, but twist from one end of the rotor to the other, as shown in Figure 4.4(b).

The configuration of the truss blades is improved over the previous design of McAdam (2007). As shown in Figure 4.4(a) the blades of the truss rotor at each end are radially offset, so as to reduce the effect on the trailing blade of the wake generated by the leading blade, on the upstream half of the device. This means that the twist of the blades is non-uniform, due to the requirement of the hydrofoil chord being tangential to the pitch circle at each point.

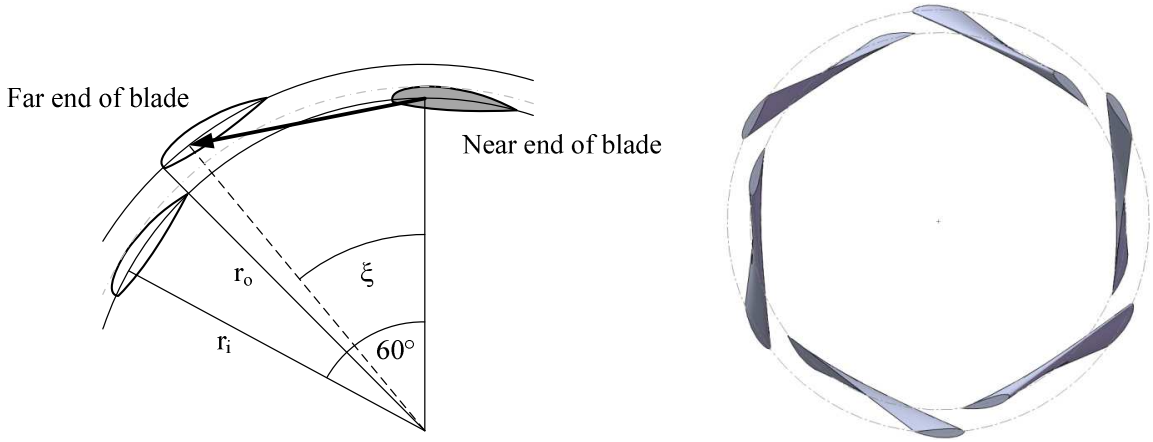

(a) Truss blade end geometry *(b) CAD rendered truss blade assembly*

Figure 4.4 – Demonstrations of truss blade geometry and assembly

The distance for the radial offset was arbitrarily chosen as approximately half the length of the blade chord, 30 mm. The radial positions of the blade ends were subsequently chosen so that the mean radius over the entire blade length is equal to the radius of the parallel-bladed configurations at 0.25 m.

4.2.2. Rotor solidity

Shiono et al. (2000) concluded that the solidity, defined in equation 4.1, which would yield the greatest efficiency in a vertical axis Darrieus type water turbine is approximately 0.18.

$$s = \frac{nc}{\pi D} \qquad 4.1$$

However, this result was obtained using a vertical axis turbine of an undefined blockage ratio in an undefined range of Reynolds number flows. The turbine tested by McAdam (2007) was designed with a solidity of 0.3, below which the chosen method of blade manufacture was unfeasible. It was decided that a more scientific approach to choosing the rotor solidity for the Newcastle tests should be employed.

During the design of the Newcastle turbine the Momentum-Blade Element (M-BE) model, the most advanced open channel flow model of the THAWT device available at the time and described in Chapter 6, was used to predict the most appropriate value of solidity. The M-BE model combines the Linear Momentum Actuator Disc Theory for Open Channel Flow (LMADT-OCF) with basic hydrofoil theory to predict the forces acting on the turbine blades, and is capable of accounting for the effects of blockage ratio and Froude number.

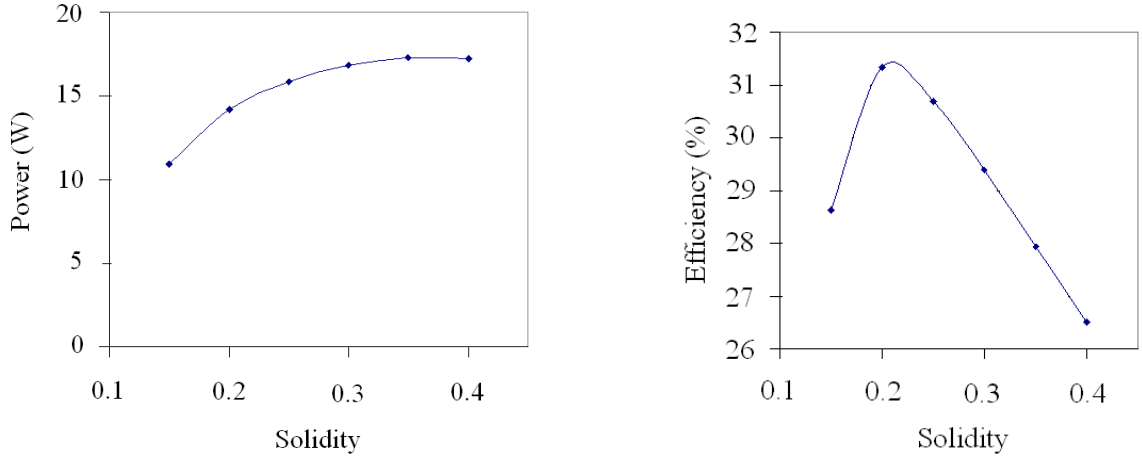

(a) Power output *(b) True efficiency*

Figure 4.5 – Predictions of the performance of the Newcastle prototype rotor using the M-BE model, at a flow velocity of 0.4m/s and with a varied blockage ratio

Figure 4.5(a) shows that a peak in power output is predicted for a solidity of approximately 0.35. However, Figure 4.5(b) suggests that the true efficiency, defined as the amount of power extracted non-dimensionalised by the total amount of power extracted from the flow, falls sharply for values of solidity greater than 0.2. Based on this information it was decided to use a turbine solidity of 0.25, which combines a high power output and a high efficiency. With half of the number of blades, the solidity of the three bladed device is s = 0.125 The chord length of the truss blades, perpendicular to the blade axis, is reduced by the cosine of the azimuthal sweep, so that the total fraction of the turbine circumference occupied by blades is the same as that in the parallel configurations.

4.2.3. Hydrofoil design and manufacture

The preliminary analysis in Chapter 3 demonstrates that the stresses induced in the blades of the THAWT device are highly dependent on the hydrofoil thickness to chord ratio. A basic analysis, during the previous experiments on the THAWT device by McAdam, led to the choice of the NACA 64_3-021 symmetrical hydrofoil section, because of its ease in manufacture and its favourable lift characteristics.

A simple study performed by Consul (2008) using the hydrofoil analysis tool Xfoil (Drela, 2004) indicated that a hydrofoil significantly thicker than 18% is likely to suffer early boundary layer separation at the low Reynolds number flows expected in the Newcastle tests. The 18.4% thick ClarkY-sym hydrofoil (generated by mirroring the upper surface of the standard ClarkY foil), was therefore suggested as the most suitable for the Newcastle turbine, due to its ability, at the expected Reynolds number, to maintain a greater lift to drag ratio to higher angles of attack than other similar hydrofoil sections.

The M-BE model of Chapter 6 indicates that the peak in performance for a fixed pitch cross-flow device occurs when the hydrofoils are symmetrical and neutrally pitched, where no lift is produced with a zero angle of attack. Migliore (Migliore and Wolfe, 1979, Migliore *et al.*, 1980) used conformal mapping to predict that an aerofoil with a straight chord in the curvilinear flows experienced by a cross-flow turbine would induce an increased effective incidence. In an effort to achieve a neutral pitch, previous experiments performed on the THAWT design by McAdam (2007) used a symmetrical hydrofoil whose chord was 'wrapped' onto the pitch circle of the turbine, as shown in Figure 4.6.

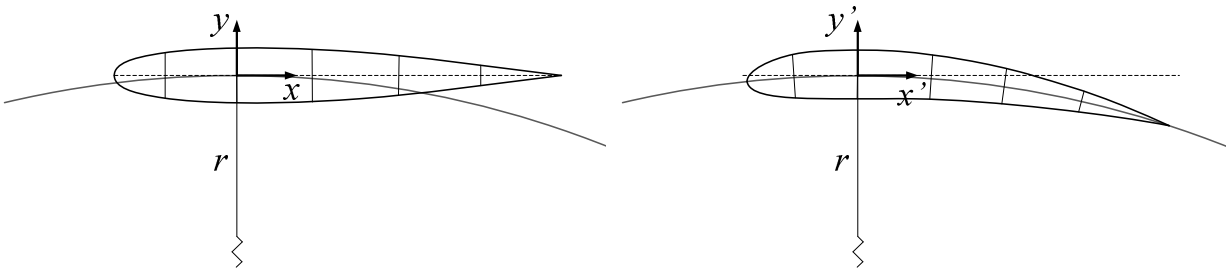

(c) Rectilinearly symmetrical section *(d) Circumferentially 'wrapped' section*

Figure 4.6 - Images of straight and wrapped hydrofoil sections

In the case of the truss device, the hydrofoil section is defined in a plane normal to the blade axis. The choice of a curved hydrofoil is supported by experiments performed by Consul, which demonstrate that the turbine performance is significantly higher when curved blades are used, as opposed to straight chorded blades, as shown in Figure 4.7.

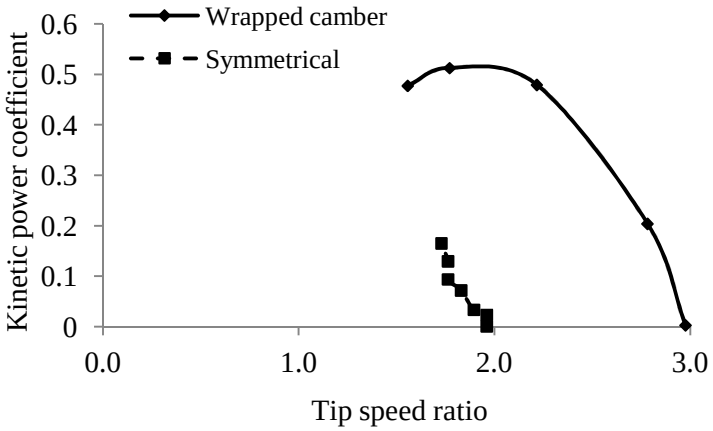

Figure 4.7 – Comparison of straight chord and curved chord blades, based on data in Consul (2008)

After exploring the available manufacturing options it was decided to produce the turbine blades from carbon composite material. Three pairs of moulds were CNC milled and polished from 2014 Dural Aluminium, one pair for the parallel blades and one pair of moulds for each of the two twist geometries.

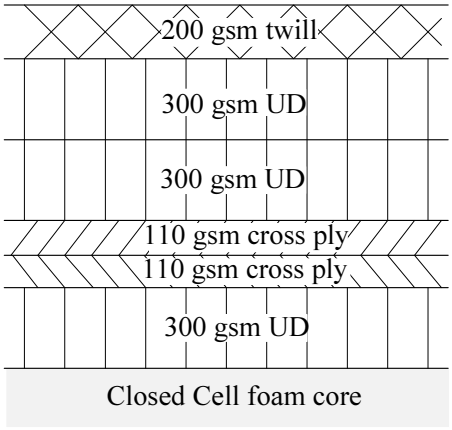

Figure 4.8 – Carbon fibre composite layup

A close cell foam core was wrapped in the 1.3 mm thick carbon fibre composite layup, shown in Figure 4.8, before curing in a heated press, as shown in Figure 4.9(a).

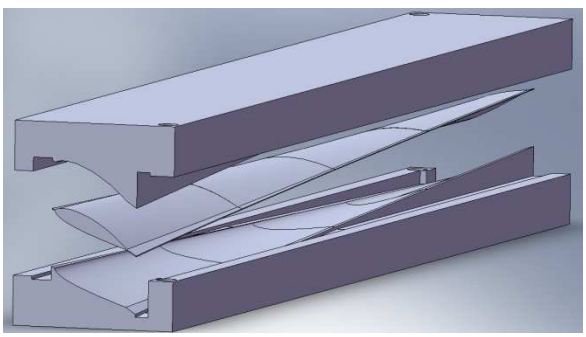

(a) *CAD rendered image of moulding process*

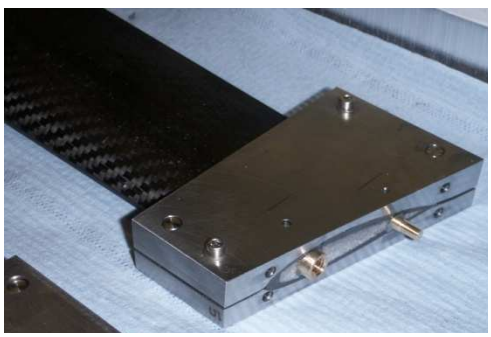

(b) Finished truss blade with jig and inserts in place

Figure 4.9 - Manufacturing process of the Newcastle blades

After excess flash was removed from the leading and trailing edges, the blades were cut off to the appropriate length, and compound angle in the case of the truss blades, before inserts were glued and pinned into the blade ends for attachment to the endplates, as shown in Figure 4.9(b).

4.2.4. Test rotor specification

The specification of the turbines used in the Newcastle tests is given in Table 4.1.

Default axis height above flume base (m)	0.425
Average diameter D (m)	0.5
Rotor length L_{bay} (m)	0.875
Truss blade r_o (m)	0.277
Truss blade r_i (m)	0.247
Truss blade length (m)	0.899
Endplate thickness (m)	0.010
Truss blade average tangential sweep φ (°)	12.0
Rotor solidity s	0.25
Parallel chord (mm)	65.45
Truss chord in plane normal to blade axis (mm)	64.02
Hydrofoil thickness to chord ratio	0.184

Table 4.1 – Newcastle test rotor specifications

4.3. Test apparatus and instrumentation

The mechanical and structural components of the test apparatus were designed, manufactured and assembled as part of this project. The turbine was mounted in the flume using a frame constructed from aluminium angle section, as shown in Figure 4.10.

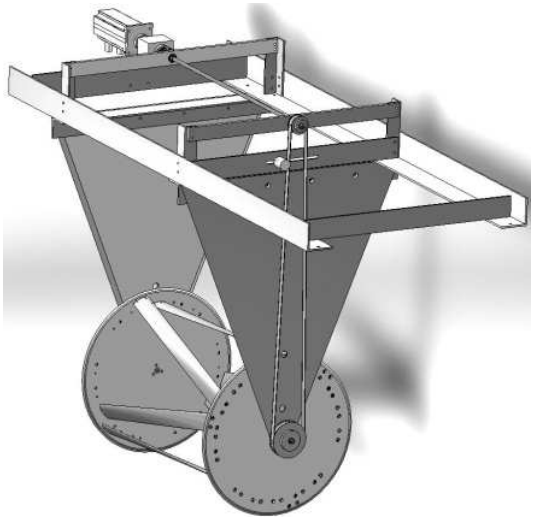

Figure 4.10 – CAD rendered image of frame and turbine assembly

A gap in the wooden partition allowed the turbine shaft to pass through to the pulley system, which operated in the still water of the partitioned section, so that the free stream flow

was undisturbed. The power was transferred from the turbine using a toothed pulley system to a driven shaft, and then through a flexible coupling to a 6 Nm TORQSENSE RWT320 rotary torque and speed sensor, which was commercially calibrated by Sensor Technology to measure speed to within one revolution per minute and torque with an accuracy of 0.015 Nm (0.25% of the full torque capacity). The torque sensor was then flexibly coupled to a Telemecanique Lexium 05 BSH 1003P servo motor, which was operated in PI speed control by a D28M2 controller with the factory default speed loop proportional gain of 0.0153 A/rpm and an integral time of 13.2 ms, in order to apply or absorb the power necessary to achieve a steady rotational speed.

A 2:1 gearing ratio in the toothed pulley system was used to double the angular velocity at the torque sensor, so that the torque was reduced to within the accurate range of the sensor. This is anticipated to increase the error on the measurements of torque and decrease the error on the measurements of rotational speed by a factor of 2.

4.3.1. Flow instrumentation

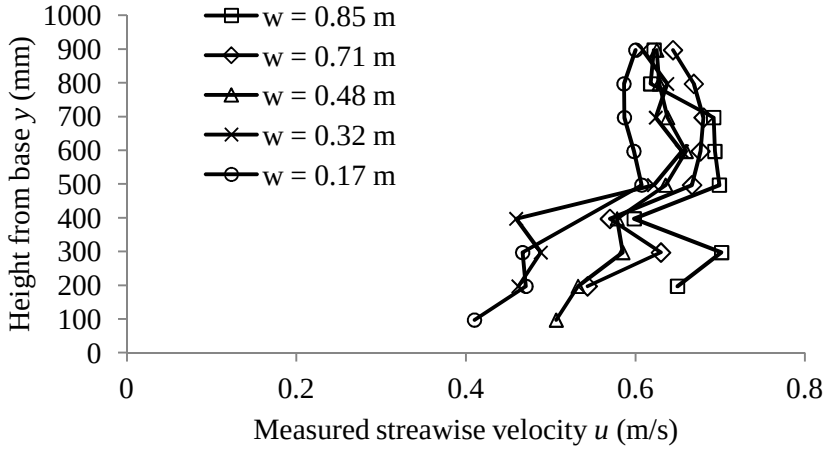

Figure 4.11 – Point measurements of velocity by the ADV at various flume spanwise positions

As shown in Figure 4.11, point velocity measurements were taken across the width and depth of the flume tank at several volume flow rates, using a Nortek Vectrino acoustic Doppler velocimeter (ADV), with an accuracy of ± 0.5% of measured value ±1 mm/s. The velocity profile was fitted to the expression given in equation 4.2, where y and x are the distances from the flume base and wall respectively and w is the channel width. The remaining variables in equation 4.2 were found by minimising the sum of the square of the error for forty four positions in the channel cross-section.

$$u = (A + By)y^m x^{n_1}(w - x)^{n_2} \qquad 4.2$$

The volume averaged flow velocity was approximated by integrating the velocities over the channel area. The ratio of the flow velocity measurement at a point 0.1 m below the flow surface and approximately mid-span of the channel, shown in Figure 4.12, to the volume averaged velocity was calculated and used to approximate the volume averaged flow velocity for the subsequent tests.

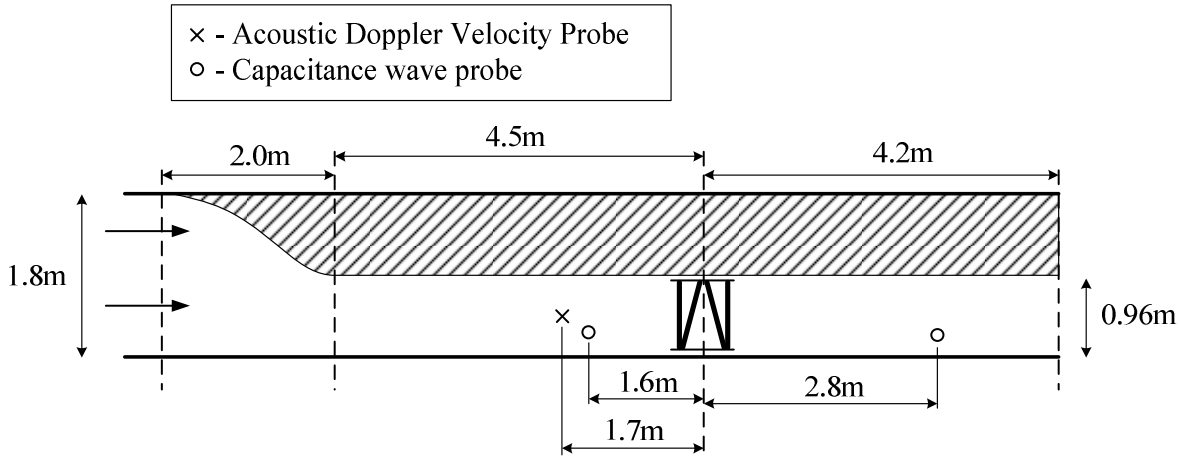

Figure 4.12 – Plan view of flume setup including instrumentation locations

The stream-wise position of the ADV was chosen to maintain satisfactory distances from the inlet contraction and the turbine axis of rotation, so that a relatively free stream velocity measurement could be obtained during the experiments. A capacitance wave probe was placed upstream of the turbine, close to the velocity probe in order to measure consistent upstream flow conditions. A second wave probe was placed as far downstream as possible in an attempt to measure the depth of the downstream flow after free surface perturbations due to the turbine had subsided. However, in many cases surface perturbations continued to the end of the flume, and datasets in which inaccurate measurements of depth change across the device occurred are highlighted in Chapter 5 and excluded from the subsequent analysis. The capacitance wave probes were assumed to offer a linear variation in depth with capacitance and were calibrated on site each day to minimise the measurement error due to instrument drift and tank leakage. Data acquired from the flow sensors, as well as the rotary torque and speed sensor, were recorded digitally using the commercial package LabView.

4.4. Experimental schedule

There are two main dimensionless variables which can be used to scale the geometry and flow conditions for a set of scaled tidal stream model experiments; the Reynolds number and Froude number, defined respectively in equations 4.3 and 4.4.

$$\mathrm{Re} = \frac{u_\infty c \rho}{\mu} \qquad 4.3$$

$$\mathrm{Fr} = \frac{u_\infty}{\sqrt{g h_\infty}} \qquad 4.4$$

The Froude number and Reynolds number cannot both be scaled simultaneously, so when scaling it must be decided whether to maintain a realistic scaled Froude number or Reynolds number (Massey and Ward-Smith, 1998). This is a trade-off between free surface effects and local blade effects, which has been encountered by ship designers for decades.

As the Reynolds number of the flow increases, the drag coefficient of a hydrofoil reduces and the maximum lift coefficient, limited by stalling, increases. If a turbine of very small blockage ratio were used in a relatively low velocity tidal channel, variations in the Froude number would have a significantly smaller effect on the performance of the turbine than variations in the flow velocity and Reynolds number. However, the performance of a turbine of a relatively large blockage ratio in a relatively high velocity channel would be dominated by variations in the Froude number rather than the Reynolds number. This is because the effects of variations in the Reynolds number on hydrofoil lift and drag coefficients decrease as the Reynolds number increases (Sheldahl and Klimas, 1981). The Froude number is a non-dimensional ratio of the kinetic and gravitational potential energy in a fluid flow. Neglecting any effect from varying Reynolds number, using Linear Momentum Actuator Disc Theory for Open Channel Flow (Houlsby *et al.*, 2008a) it is possible to show that the power available to a turbine is a function of Froude number only.

Limitations on flow velocity meant that in the Newcastle flume it would not be possible to replicate flow conditions with a Reynolds number as high as that experienced by a full scale device. For this reason it was decided to scale within a realistic range of Froude number, $0.1 < \mathrm{Fr} < 0.22$, which could be experienced in a full scale tidal stream. If the linear dimensions are scaled by a factor N, in order to maintain Froude similarity the velocity of the flow should be scaled by the factor $\sqrt{N}$.

By scaling with constant Froude number, the power produced by the turbine would be conservative, as the relatively low Reynolds number would reduce the performance of the turbine when compared to a full scale device.

4.4.1. Blade pitching

Several studies have indicated that the performance of a Darrieus type device may be improved by using a dynamic pitching scheme (Gretton and Bruce, 2005, Salter and Taylor, 2007). Despite this fact it was decided to use fixed blades, as this would allow for a single piece rotor, which is structurally stiff and requires relatively little maintenance.

As described in section 3.5, the anticipated deceleration of the flow through the device is likely to result in differing power take-off from the upstream and downstream halves of the device. The use of a fixed offset pitch has been suggested as a method for varying the turbine operating tip speed ratio and is anticipated to result in changes to the device performance.

To explore this experimentally the apparatus allows for the parallel turbine blades to be pitched by 2° both positively and negatively (a positive pitch acting to increase the apparent angle of attack on the upstream half of the turbine).

4.4.2. Blockage ratio

The depth of flow for the majority of the tests in this series of experiments is 1 m, which results in the turbine occupying 50% of the depth of the flow. LMADT-OCF demonstrates that, for a given Froude number flow, the blockage ratio of a rotor has a significant effect on the potential performance of the device (Houlsby *et al.*, 2008a). In order to explore the effect of the blockage ratio on the turbine performance, a set of tests were performed with reduced depth of 0.8 m, producing a blockage ratio of 0.625. For a given Froude number, the flow velocity and anticipated Reynolds number of the flow is reduced for the higher blockage test, but it is assumed that small variations in Reynolds number at this scale do not have a significant effect on the hydrofoil performance, as shown in Figure 6.1.

4.4.3. Reversal of flow direction

By swapping the attachments at each end of the turbine, and turning it around so that the device rotates in the opposite direction, it is possible to test the turbine in reverse without changing the direction of the flow in the flume. (Where “forward” flow is defined as the bottom of the turbine rotating in the same direction as the flow.) Tests were performed with a “reversed” device to explore whether the performance of the turbine changes significantly when the direction of the tidal flow is reversed.

4.4.4. Turbine height in flow

A simple analysis of the THAWT device using LMADT-OCF does not indicate that the amount of power available to the device varies with the vertical position in the flow. In order to explore this, a set of experiments were performed with the rotor axis moved to 0.2 m above the default position, raising it to 0.625 m above the flume base.

4.4.5. Waves

An auxiliary test was conducted using the wave making capability of the CWWC tank. The CWWC tank wave paddles submerge into the flow from above, to a height of 0.3 m above the flume base, and move in a stream-wise motion to project waves, as shown in Figure 4.13. The generated waves are not fully representative of true offshore waves, which tend to occupy only the top region of a channel. The period and amplitude of the waves were arbitrarily set at 1 s and 25 mm respectively, corresponding to full scale waves of approximately 4.5 s period and 0.5 m amplitude, using Froude scaling (Newman, 1977).

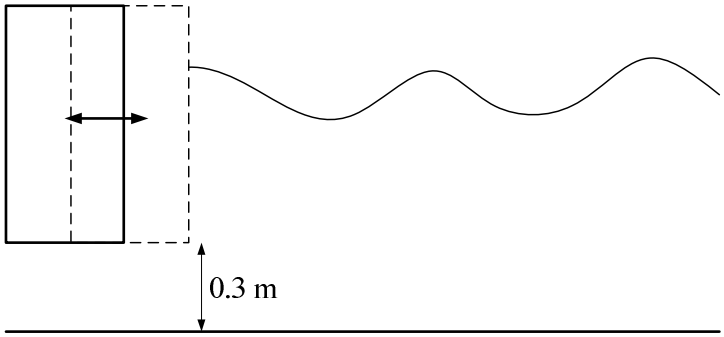

Figure 4.13 – Side view of oscillating wave paddles in the Newcastle CWWC tank

The final schematic of tests undertaken is given in Table 4.2.

h_∞ (m)	1.0				0.8		
B	0.5				0.625		
u_∞ (m/s)	0.3	0.4	0.5	0.7	0.3	0.4	0.5
Fr	0.096	0.13	0.16	0.22	0.11	0.14	0.18
Truss	*	*	*	*	*	*	*
Reverse Truss	*		*				
Truss with waves			*				
Truss position varied vertically	*		*	*			
Parallel six blade	*	*	*	*	*	*	*
Reverse six blade	*		*				
Pitched six blade	*		*				
Parallel three blade	*	*	*	*	*	*	*

Table 4.2 – Schematic of experimental tests

Ideally, for each set of flow conditions and configuration, a power curve would be produced in which each point represents the performance of the turbine while operating at a steady state. To test in steady state conditions at regular increments of tip speed would be very time consuming, and due to limited time in the Newcastle facility a more convenient scheme was required. The chosen solution was to use the motor controller to accelerate the turbine gradually using a low gradient ramp, as shown in Figure 4.14, so that the system had time to react continuously and simulate steady state conditions.

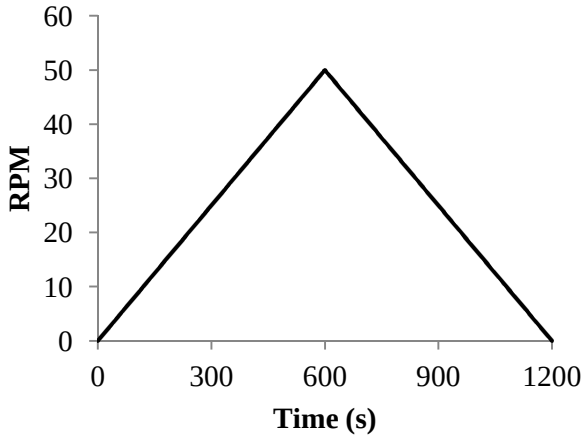

Figure 4.14 – Example of speed ramping during an experiment, at 5 rpm/min

The validity of estimating the steady state performance of the device with a ramping speed of 5 rpm/min was explored both by studying the hysteresis of the rising and falling ramps, as well as through tests of the device with a ramp of half the gradient, as shown in Figure 4.15.

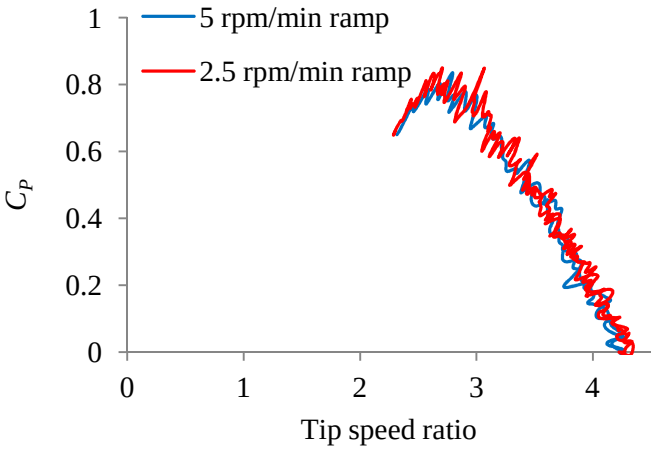

Figure 4.15 – Tests of the six parallel bladed device at 0.5 m/s, with 5 and 2.5 rpm/min ramps

With no visible difference between the results, it was assumed that the quasi-steady assumption was valid.

4.5. Data calibration

Figure 4.16(a) shows an example of the torque data directly measured from the torque-speed sensor, in which the large fluctuations at the end of the test are due to the high angles of attack and unsteady stall experienced by the turbine blades, as the tip speed ratio is reduced. Negative values of torque indicate regions in which power must be applied by the motor-generator in order to achieve the desired tip speed ratios. Figure 4.16(b) shows a magnified section of this torque trace in which the fluctuations are due to a combination of the frequency response of the motor speed control loop and the varying blade forces during a turbine rotation.

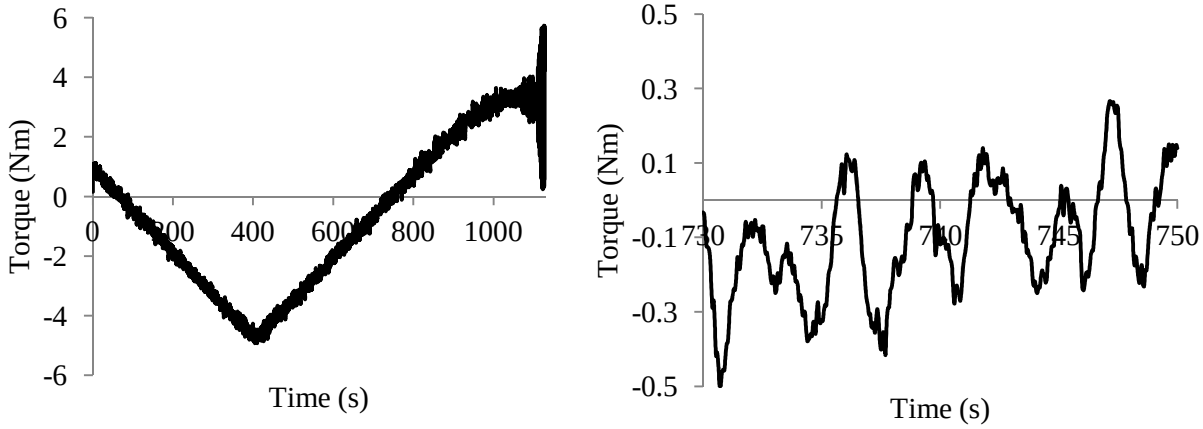

(a) Raw torque measurement *(b) Magnified section of torque measurement*

Figure 4.16 - Raw measurements of torque for the truss turbine at Fr *= 0.17 and B = 0.5*

The raw data were re-sampled down to 20 Hz using linear interpolation, and a 500 sample width Hamming window was applied to smooth the data, as shown in Figure 4.17(a). After smoothing, the data were corrected using the following calibration values, an example of which is shown in Figure 4.17(b).

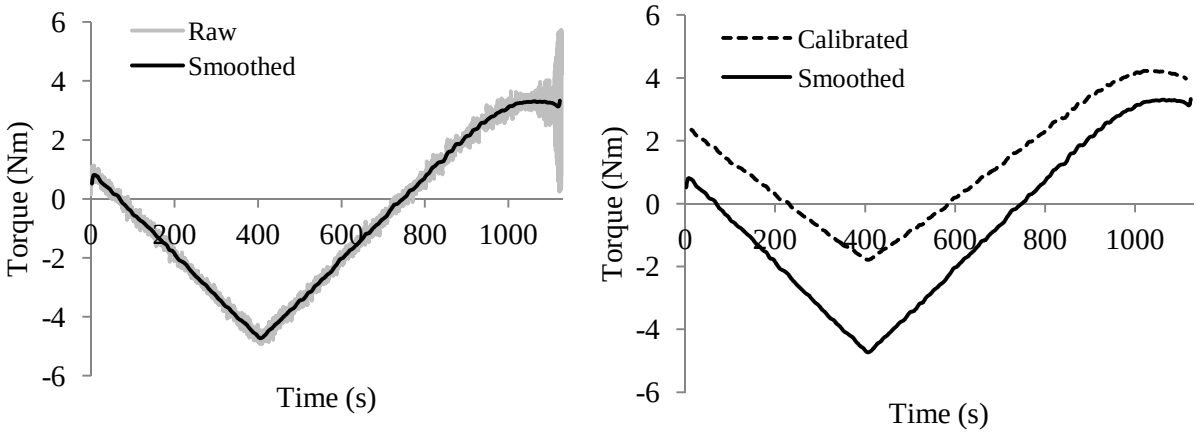

(a) Smoothing process of torque *(b) Calibration process of torque*

Figure 4.17 - Post processing of data for the truss turbine at Fr *= 0.17 and B = 0.5*

The measurements of flow velocity at the ADV velocity probe were calibrated using the method described in section 4.3.1, to provide a measurement of the volume averaged flow velocity over the course of each test.

By running the apparatus with the endplates mounted on a shaft in place of the turbine, the torque due to the drag on the endplates and friction in the power train was measured. This process was carried out at several values of flow velocity and over a range of angular velocities. The measurements of torque were calibrated using these values, to isolate the torque produced by the turbine alone.

At the beginning of each day the value of each depth probe was recorded with no flow, so that the drift on the instrument amplifier could be measured. Measurements of depth were also taken at various flow velocities and with no turbine in place, so that the head loss generated due to the velocity profile shear could be quantified. Applying these calibration values to the experimental results allowed the depth change due to the turbine to be isolated.

4.6. Confidence limits of experimental data

It is necessary to perform an error analysis to establish the confidence limits on the data obtained from the experimental tests. Based on the quoted accuracy of each piece of instrumentation the possible measurement errors for each quantity are given in Table 4.3.

	Maximum value at peak power		Minimum value at peak power	
	Value	Instrument error (%)	Value	Instrument error (%)
Measured torque	5.07 Nm	0.59%	0.46 Nm	6.47%
Torque calibration	2.43 Nm	1.23%	0.48 Nm	6.20%
Angular velocity	88.0 rpm	0.28%	29.5 rpm	0.85%
Flow velocity	0.68 m/s	0.65%	0.29 m/s	0.84%

Table 4.3 – Possible measurement errors due to instrument accuracy

The percentage instrumentation errors for each quantity are smaller when the measured values are greater and use a larger proportion of the useful instrumentation range.

When used to calculate metrics such as the kinetic power coefficient at peak power, the greatest anticipated error is a linear combination of the individual errors, with the minimum measured values for each respective quantity. Assuming that the error contributed by the torque calibrations is proportional to the fraction of the total torque, the worst case error in the calculation of C_{PK} is ±16.3%. However, it should be noted that when the measured quantities occupy their greatest values during the experiments, the linear combination of errors predict an error bound of C_{PK} of ±3.4%.

Applying the same process to the calculation of confidence limits for the tip speed ratio of peak power, λ_p, results in error bounds of ±1.7% and ±0.9%, respectively for the maximum and minimum measured quantities.

The probability that the maximum error for each piece of instrumentation will occur simultaneously is remote. The quoted values of error are therefore likely to be conservative estimates. These bounds in error should be taken into account when observing the accuracy of comparisons with the numerical models of Chapter 6 and Chapter 7, and when assessing the performance of a full scale device in Chapter 9.

It should be noted that further error is likely to be incurred in the calculation of the volume averaged flow velocity due to the approximation of the flow field using equation 4.2.

The capacitance wave probes were the only pieces of equipment which were not calibrated to within a given measure of accuracy. Measurements of the flow depth were of a lower priority than the other measurements and so the time was not allocated to measure the accuracy of the wave probe instrumentation. As such, the calculated depth changes across the device are not the main focus of the experimental or numerical analyses. There is likely to be an increased error in the measurement of depth changes across the device due to the fact that the downstream flow measurements were too close to the device to measure fully recovered flow. This issue is highlighted in the analysis of the experimental results and in comparisons with the later numerical models.

Chapter 5

Experimental results

In this chapter the performance of the different device configurations are compared in terms of the kinetic power coefficient, defined in equation 5.1, and the head power coefficient, defined in equation 5.2.

$$C_{Pk} = \frac{P}{1/2\,\rho A_t u_\infty^3} \qquad 5.1$$

$$C_{PH} = \frac{P}{\dot{m} g \Delta \left(h + \frac{u^2}{2g}\right)} \qquad 5.2$$

The kinetic power coefficient, also widely known as the power coefficient or kinetic efficiency, is commonly used in both the wind and tidal stream industry, in order to compare device performance. This metric assumes that the mechanism for the extraction of energy from a flow is the conversion of a proportion of the incident kinetic flux to useful power, and a reduction in the total kinetic energy of the flow. Whilst this is accurate for relatively unconstrained flows, the mechanism of energy extraction from an open channel flow is the conversion of total head to useful power. The head power coefficient is presented here as a more comprehensive metric for the comparison of tidal stream devices. In order to calculate the head coefficient of power it is necessary to know the change in total head due to the device, which can be calculated from the depth change between fully mixed locations upstream and downstream of the turbine. As described in Chapter 4 this was not fully achieved during the experimental tests, but it is believed that in the tests on low Froude number flows the depth was sufficiently recovered to offer estimates of the head efficiency of the device. Using this metric the true efficiency of the various design configurations can be compared.

5.1. Basic features of the experimental results

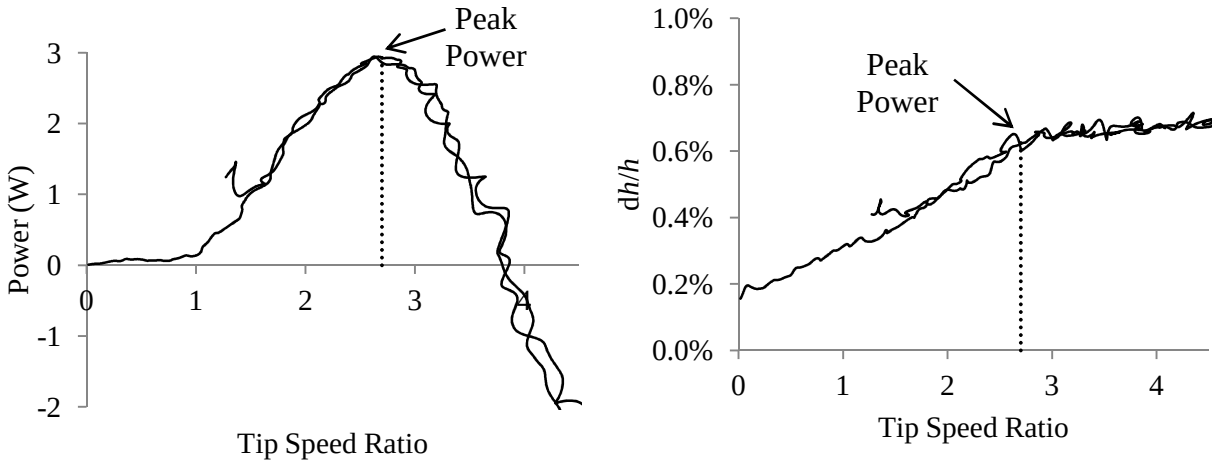

(a) Measured power *(b) Measured depth change*

Figure 5.1 - Results for the six truss-bladed device at an average Froude number of 0.09 and a blockage ratio of B = 0.5

Figure 5.1(a) shows a typical power curve recorded during an experiment, after the smoothing and calibration process has been applied, as described in Chapter 4. The motor speed has been ramped to obtain the performance of the device over the entire power curve in a quasi-steady fashion. The power curve exhibits a bell shape in which power is reduced at high tip speeds due to low angles of attack and high drag, and at low tip speeds due to stall at high angles of attack. While a steady rotational speed is achieved over the majority of the power curve by braking the turbine, using the motor as a generator, negative power is measured at higher tip speed ratios by applying positive torque.

Figure 5.1 (b) shows the measurement of depth change across the device as the tip speed ratio is varied and demonstrates that the depth change increases with an increase in tip speed ratio. The increase in depth change is due to the increase in thrust produced by the device as the tip speed ratio is increased.

The salient values of turbine performance over the entire range of tests are listed in Table 5.1, in which the performance of the device and the corresponding flow parameters correspond to those measured at the tip speed ratio of peak power output λ_p. The values of flow velocity and Froude number are calculated from the average flow velocity during an individual test. These salient values are those used during the subsequent analyses. The tests described as 'Top bearing' refer to the apparatus configuration in which the turbine axis position is raised vertically by 0.2 m, as described in section 4.4.4.

Test	Configuration	Notes	U_∞ (m/s)	Fr	Power (W)	λ_p	dh/h	C_{pk}	C_{ph}
1	Truss		0.29	0.09	2.93	2.71	0.6%	56%	17%
2	Truss		0.41	0.13	8.77	2.74	1.2%	62%	20%
3	Truss		0.55	0.17	24.37	2.80	2.5%	71%	20%
34	Truss		0.67	0.21	54.90	2.93	**6.5%**	85%	**14%**
36	Truss	Repeat	0.53	0.17	23.46	2.72	2.0%	71%	23%
4	Truss	Repeat	0.67	0.21	54.03	2.78	**6.3%**	80%	**14%**
5	Truss	Reverse	0.29	0.09	2.19	2.72	0.6%	41%	13%
6	Truss	Reverse	0.54	0.17	23.84	2.80	2.4%	70%	20%
15	Truss	Top bearing	0.29	0.09	3.00	2.94	0.7%	57%	16%
16	Truss	Top bearing	0.54	0.17	33.98	3.06	3.0%	100%	22%
35	Truss	Top bearing	0.66	0.21	70.10	3.10	4.5%	110%	25%
37	Truss	Waves	0.54	0.17	23.43	2.70	1.9%	69%	25%
9	Six parallel		0.29	0.09	3.18	2.71	0.6%	57%	19%
10	Six parallel		0.41	0.13	9.57	2.59	1.2%	65%	21%
11	Six parallel		0.54	0.17	27.52	2.65	2.6%	78%	20%
12	Six parallel		0.66	0.21	59.29	2.78	6.4%	92%	15%
38	Six parallel	Repeat	0.29	0.09	3.53	2.71	0.6%	67%	22%
39	Six parallel	Repeat	0.55	0.17	28.42	2.68	2.9%	79%	19%
7	Six parallel	Reverse	0.29	0.09	2.85	2.72	0.7%	53%	16%
8	Six parallel	Reverse	0.54	0.17	26.77	2.68	2.6%	77%	21%
19	Six parallel	2° -ve pitch	0.29	0.09	3.84	2.32	0.4%	66%	35%
20	Six parallel	2° -ve pitch	0.55	0.17	29.87	2.41	1.5%	84%	38%
17	Six parallel	2° +ve pitch	0.29	0.09	2.70	3.19	0.5%	51%	21%
18	Six parallel	2° +ve pitch	0.54	0.17	23.44	3.27	3.0%	71%	16%
21	Three parallel		0.29	0.09	5.10	3.36	0.4%	95%	45%
22	Three parallel		0.41	0.13	13.44	3.40	1.0%	88%	34%
23	Three parallel		0.55	0.18	34.12	3.31	1.7%	93%	38%
24	Three parallel		0.67	0.22	69.45	3.47	**4.6%**	100%	**24%**
31	Truss	h = 0.8m	0.26	0.09	3.92	3.57	1.3%	102%	19%
32	Truss	h = 0.8m	0.35	0.12	12.34	3.53	2.2%	129%	27%
33	Truss	h = 0.8m	0.51	0.19	57.30	3.69	6.4%	179%	28%
28	Six parallel	h = 0.8m	0.26	0.09	4.41	3.33	1.3%	122%	22%
29	Six parallel	h = 0.8m	0.37	0.13	15.88	3.31	3.1%	151%	23%
30	Six parallel	h = 0.8m	0.53	0.19	67.05	3.28	**6.6%**	192%	**30%**
25	Three parallel	h = 0.8m	0.26	0.09	5.21	3.90	1.0%	129%	33%
26	Three parallel	h = 0.8m	0.39	0.14	19.22	4.15	1.6%	152%	50%
27	Three parallel	h = 0.8m	0.53	0.19	60.26	4.25	3.8%	174%	48%

Table 5.1 – Full table of experimental results after smoothing and calibration, with bold type representing depth change measurements that are unlikely to be fully recovered

5.2. Repeatability of results

Figure 5.2 shows that the recorded peak power, depth change and λ_p for the selected tests are repeated with a mean error of less than 5%, 9% and 2.3% respectively. It is assumed that the error in the repeatability of the depth change is due to the close proximity of the turbine to the downstream depth probe.

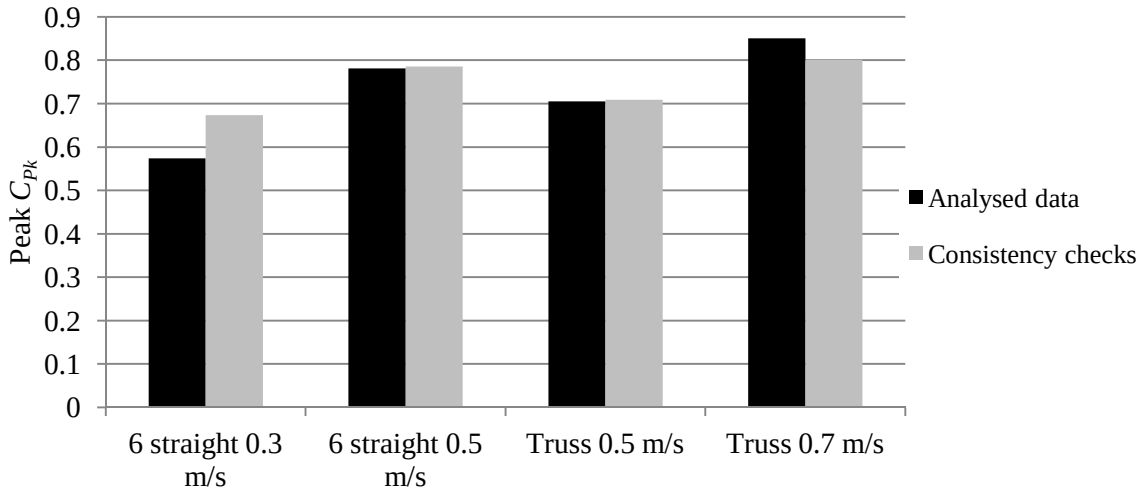

(a)

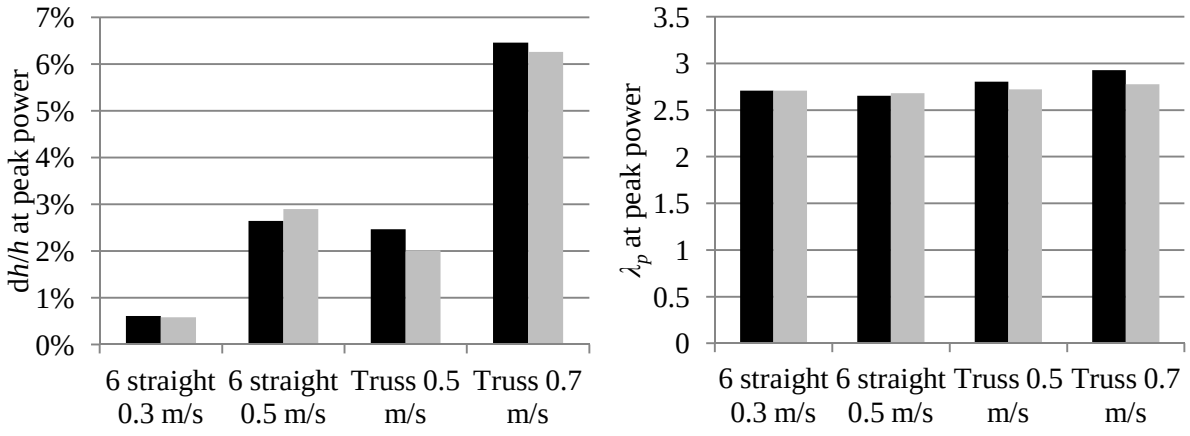

(b) *(c)*

Figure 5.2 - Comparison of analysed data with repeatability tests performed at matching velocities and setups

5.3. Comparison of truss blade performance at a blockage ratio of *B* = 0.5

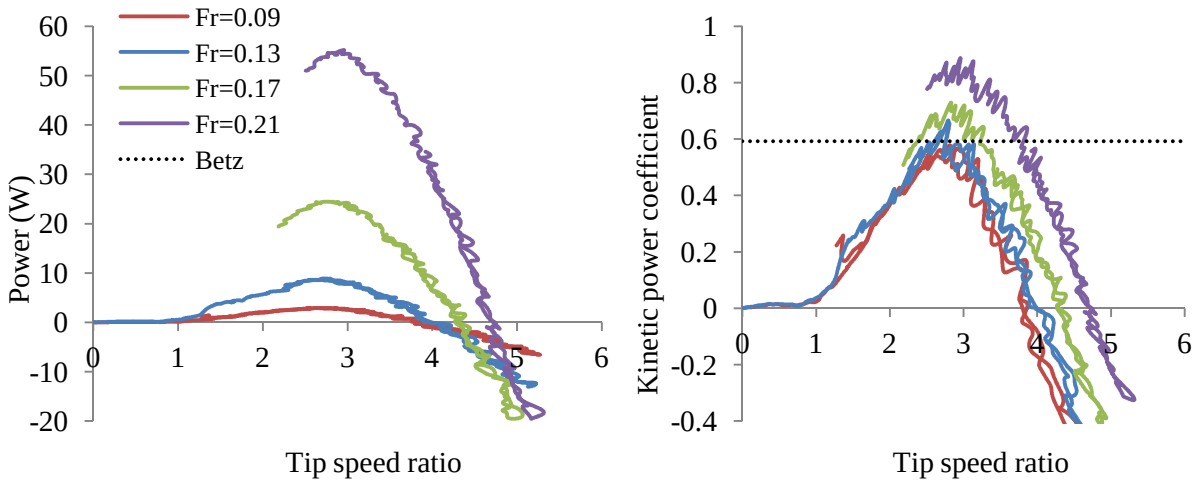

(a) Power vs. tip speed ratio

(b) C_{Pk} vs. tip speed ratio

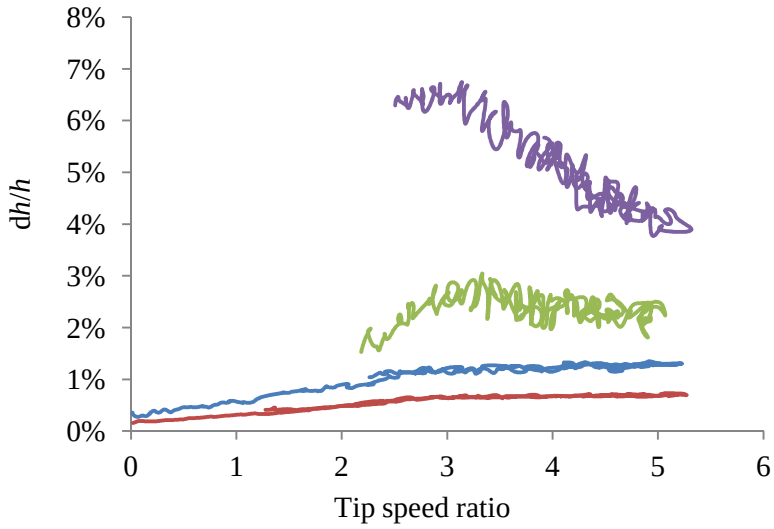

(c) dh/h vs. tip speed ratio

Figure 5.3 - Comparison of performance curves for the truss-bladed device over a range of Froude numbers at a blockage ratio B = 0.5

Figure 5.3(a) shows power against tip speed ratio curves for four Froude number flows, and demonstrates that the truss THAWT device produces a peak in power at a tip speed ratio of between $2.7 < \lambda_p < 2.9$. This suggests that the optimum variation in angle of attack experienced by the blades, throughout a rotation, occurs at a consistent tip speed ratio over a range of Froude number flows. The preliminary analysis of Chapter 3 suggests that a consistent tip speed ratio over a range of Froude number indicates that the induction factor experienced by the device remains relatively constant at the point of maximum power extraction. This is significant in the design of a full scale THAWT device, as it demonstrates that for a given flow geometry, the tip speed ratio of maximum power would remain relatively constant over the whole tidal cycle.

It is also clear that as the velocity and Froude number is increased, the turbine produces positive power up to a greater tip speed ratio. This is likely to be due to a combination of two factors; a reduction in hydrofoil drag coefficient as the Reynolds number increases with Froude number, allowing positive components of torque to be achieved up to greater tip speed ratios, and an increased deflection of the flow-field as the Froude number is increased, resulting in an increased angle of attack. At such a small scale, where relatively small changes in Reynolds number have perceptible effects on the lift and drag characteristics of the hydrofoils, the assumption used in the preliminary analysis of Chapter 3, that changes to the scale of the device and blades will have a negligible effect on the hydrofoil characteristics, may only be valid for very small changes in Reynolds number.

Unfortunately, the low tip speed ratio data for the higher Froude number flows is unavailable due to a poor frequency response of the motor controller at the low tip speeds, where the turbine behaviour is highly unsteady.

Figure 5.3(b) illustrates that the THAWT device exceeds the Lanchester-Betz limit of kinetic power coefficient, used in wind turbine theory, for flows of a Froude number greater than roughly Fr = 0.15. This compares favourably to experimental results performed on more conventional horizontal axis devices (Bahaj *et al.*, 2007).

A kinetic power coefficient greater than the Lanchester-Betz limit is possible due to channel blockage effects and the sub-critical nature of the flow, as described in Chapter 2. Tidal flow conditions differ from those assumed in the classical Lanchester-Betz solution, in that (a) the flow is of finite depth and (b) gravitational effects on the fluid are significant (Houlsby *et al.*, 2008a, Whelan *et al.*, 2007). When these effects are taken into account, a greater amount of power can be extracted than indicated by the simple Lanchester-Betz analysis. For instance, at a Froude number of 0.14 and a blockage ratio of 0.5, Linear Momentum Actuator Disc Theory for Open Channel Flow (Houlsby *et al.*, 2008a) suggests that the amount of energy made available for extraction by a device is increased by a factor of 4.6, when compared to a kinetic flux analysis. The phenomenon of increased power in tidal flows has previously been observed in tests of more conventional, axial-flow tidal devices (Myers and Bahaj, 2007).

Figure 5.3(c) demonstrates that for Froude number flows up to Fr = 0.13 the depth change across the device increases with the tip speed ratio, suggesting an increase in the thrust

produced by the turbine, up to the tip speed ratio of peak power λ_p. This is likely to be due to a greater proportion of the rotor achieving attached flow and producing an increased amount of lift, as the average angle of attack decreases with an increasing tip speed ratio. The gradient of the depth change decreases significantly for values of tip speed greater than λ_p, which suggests that the thrust produced by the device remains relatively constant in this region. Assuming that the flow obeys the assumptions of LMADT-OCF, these results suggest that the average induction factor experienced by the device also remains constant in this region (Houlsby *et al.*, 2008a).

However, whilst the results at lower Froude numbers ($Fr \leq 0.13$) suggest that the thrust remains relatively constant at tip speed ratios greater than λ_p, the results differ for the highest Froude number experiment $Fr = 0.22$, which exhibits a gradual decrease in depth change across the device with an increase in tip speed ratio. This is likely to occur due to the measurement of unmixed, and unrecovered flow, at the downstream depth probe, but as the tip speed ratio increases the added turbulence from the device causes accelerated mixing, and the flow at the probe is increasingly recovered. Standing waves may also contribute to the variability of the depth change measurements at higher flow velocities. The erroneous depth change results are highlighted in bold text in Table 5.1 and are disregarded throughout the course of this analysis.

Over a Froude number range of $0.09 < Fr < 0.17$ the truss device achieves a peak head power coefficient of between 17.3% and 20.0%, while LMADT-OCF suggests that between 63.5% and 65.5% of the total energy removed from the channel is available for useful extraction. Whilst these values would be expected to increase marginally if the depth were measured at a point further downstream, where further height recovery might be expected, they give an approximation of the efficiency with which the device converts the available energy into useful power. This would indicate that the truss THAWT device is less efficient than more conventional horizontal axis devices (Bahaj *et al.*, 2007).

5.4. Comparison of basic configuration variations

Three basic variations of device were tested. The parallel six-bladed device with a solidity of 0.25, the six-bladed truss with a solidity of 0.25 and the parallel three-bladed device with a solidity of 0.125, which will be referred to as the ‘low solidity’ case.

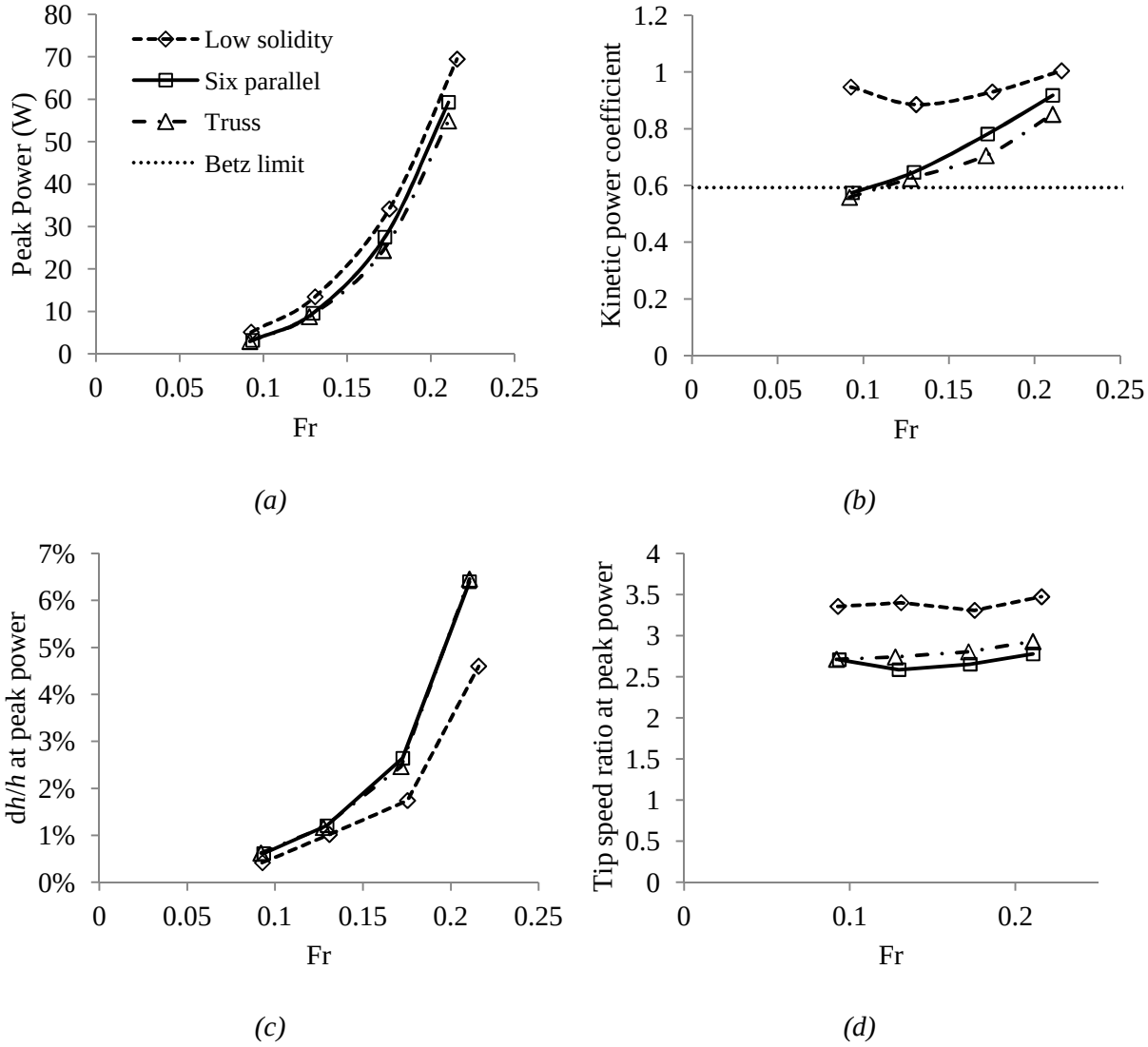

Figure 5.4 - Comparison of performance achieved at peak power by the three basic THAWT configurations over a range of Froude number at a blockage ratio B = 0.5

Figure 5.4(a) shows that the low solidity device outperformed both the six parallel-bladed device and the six truss-bladed device in terms of power output at a given flow velocity by a factor of between 1.09 – 1.65. The difference in performance is highlighted when the power produced by the devices is non-dimensionalised by the incident kinetic flux in Figure 5.4(b). This suggests that reducing the solidity from s = 0.25 is likely to result in more favourable hydrofoil lift to drag performance over a greater proportion of the turbine rotation. However, the preliminary analysis of Chapter 3 indicates that reductions in solidity are likely to result in significant increases in blade stress.

Figure 5.4(b) shows that the six parallel-bladed device achieves kinetic power coefficients greater than the truss-bladed device by factors of between 1.03 - 1.08, resulting in head power coefficients greater by factors of 1.04 - 1.09 respectively.

Figure 5.4(c) demonstrates that the depth changes across the six parallel and truss-bladed devices are substantially greater than that across the low solidity device. Based on the Froude number, depth change and blockage ratio for each configuration, LMADT-OCF is used to predict the thrust experienced by the device. The kinetic power coefficients achieved at the respective values of thrust are shown in Figure 5.5. In this figure, the total amount of power that is extracted across the affected region of flow is plotted as 'Total Power'. Some of this power is lost in downstream mixing and all of the remaining power is theoretically available for extraction by a device with no viscous losses, which is interpreted as the inviscid maximum power available to the device.

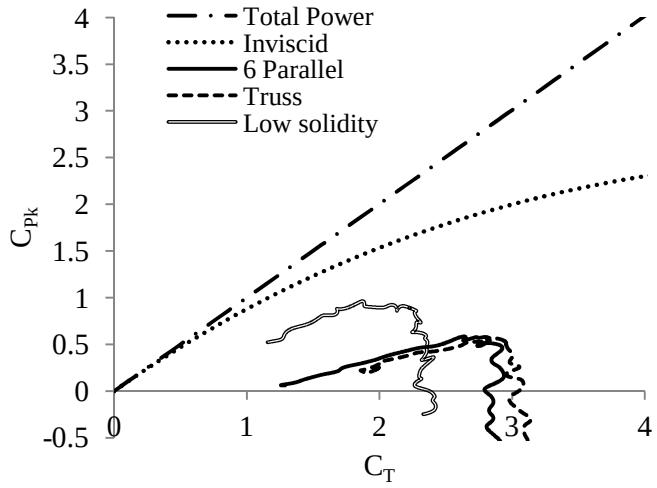

Figure 5.5 - Kinetic power coefficients of total power extraction for the theoretical inviscid case (Houlsby et al., 2008a) and experimental results for the three and six parallel-bladed and truss-bladed configurations at a Froude number of Fr*=0.09 and a blockage of B=0.5*

Figure 5.5 shows that the thrust produced by the low solidity device is reduced when compared to the higher solidity devices, which suggests a higher average induction factor through the low solidity device. At the higher induction factor the losses in the channel due to downstream mixing, represented by the distance between the total power curve and the inviscid power curve, are smaller than for the high solidity devices. As well as reducing the mixing losses in the downstream region, the low solidity device produces less viscous losses in the rotor, represented by the distance between the experimental power curve and the inviscid power curve, indicating that the efficiency, or head power coefficient (the ratio of the height of the power curve to the height of the total power line), is significantly higher for the low solidity case. The mean peak C_{PH} achieved by the lower solidity device over the range of experimental Froude numbers is 39%, which is substantially higher than the C_{PH} values of 19% and 20% achieved by the truss and six parallel-bladed device respectively. The improved

performance of the three-bladed device agrees with the prediction of LMADT-OCF, that a design which induces in a high induction factor is hydrodynamically superior to one which significantly slows the flow.

With a greater flow velocity through the low solidity device, the preliminary analysis of Chapter 3 suggests that the rotor must operate at an increased tip speed ratio in order to maintain the optimum angle of attack and to avoid blade stall. This is confirmed in Figure 5.4 (d), which shows that the peak powers in the three-bladed tests occur at an average tip speed ratio 0.6 greater than the six parallel and truss-bladed configurations.

None of the three devices experience significant variations in λ_p as the Froude number is increased, with an average increase of 4.7% over the experimental range. It is believed that the small increase in λ_p with Froude number is due to a small increase in the induction factor and a corresponding increase in angle of attack, as the depth change is increased and the flow is constricted to higher velocities through the device. This effect appears to be more significant than the increase in the stall angle with an increasing Reynolds number, which would be expected to reduce both the induction factor and operating tip speed ratio.

5.5. Effect of a varied fixed pitch

As described in section 3.5, an anticipated deceleration of the flow through the turbine is likely to result in differing power take-off from the upstream and downstream halves of the device. A negative fixed offset pitch was suggested as a method for reducing the operating tip speed ratio of the turbine and is expected to improve the device performance.

To explore this experimentally, slots in the endplates of the turbine allow for the blades to be pitched by 2°, both positively and negatively (a positive pitch acting to increase the apparent angle of attack on the upstream half of the turbine), as shown in Figure 5.6.

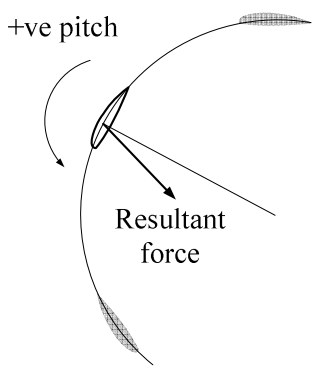

Figure 5.6 - Illustration of the direction of positive pitch

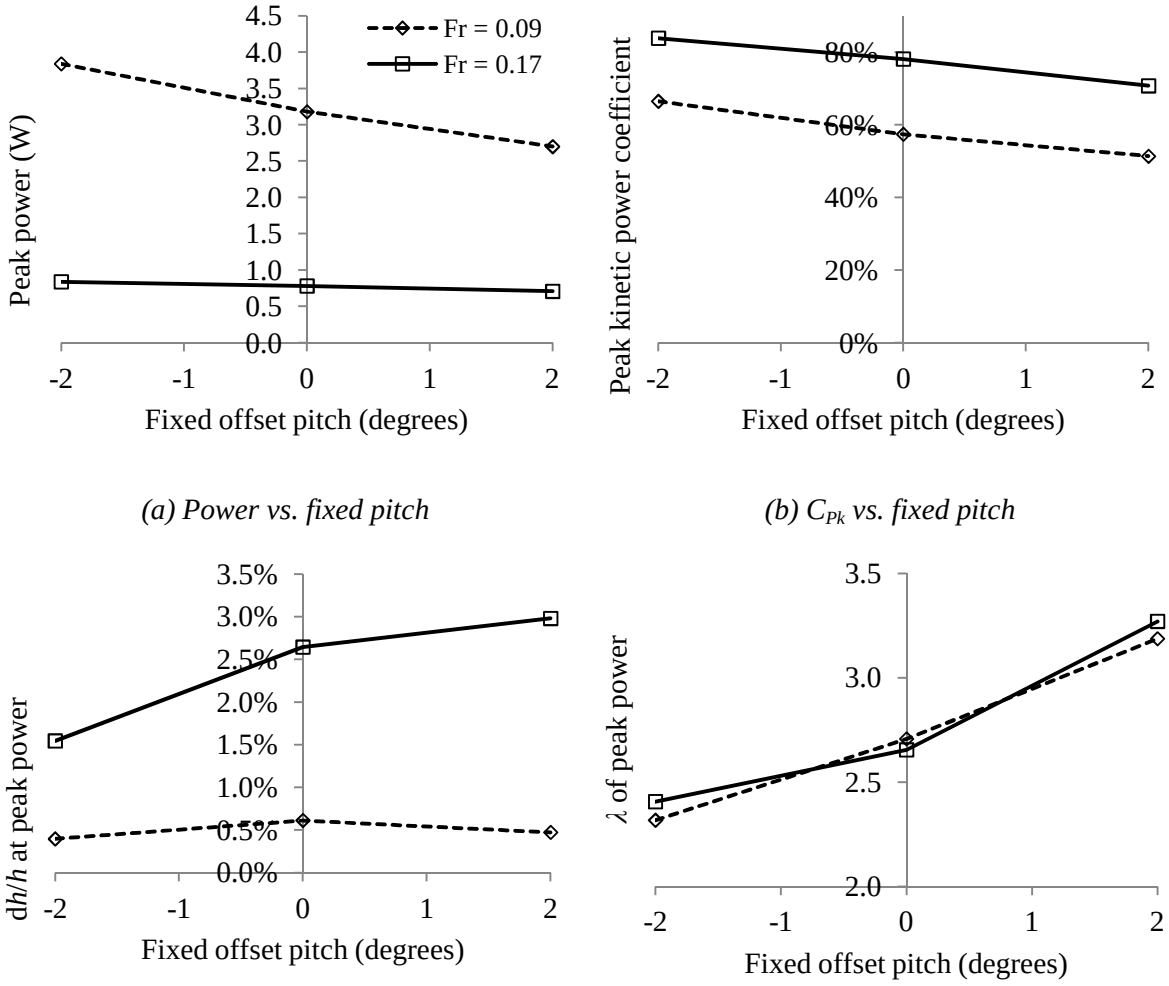

(a) Power vs. fixed pitch

(b) C_{Pk} vs. fixed pitch

(c) dh/h vs. fixed pitch

(d) λ_p vs. fixed pitch

Figure 5.7 - Comparison of performance achieved by the six parallel-blade device with a fixed offset pitch and a blockage ratio B = 0.5

As shown in Figure 5.7(a) and (b), by applying a 2° negative fixed offset pitch to the six parallel-bladed device the performance of the turbine is significantly improved. When compared to the neutrally pitched case, the peak kinetic power coefficients are increased by factors of 1.16 and 1.07 for the Fr = 0.09 and Fr = 0.17 cases respectively.

As demonstrated in Figure 5.7(c) the negatively pitched device further benefits from a reduced depth change across the flow domain, causing an increase in the average head power coefficient, from 19.6% for the neutrally pitched configuration, to 36.0% for the negatively pitched configuration. This significant increase in efficiency indicates that a high solidity six-blade device is capable of achieving levels of performance approaching that of a lower solidity device, by use of a negative fixed offset pitch.

LMADT-OCF suggests that with a reduced depth change, the induction factor through the device is increased. One might expect that that the device must therefore operate at a greater tip speed ratio in order to maintain the optimum distribution of angle of attack. However, due to the effective 2° reduction in the angle of attack experienced by the hydrofoils, as a result of the fixed offset pitch, on average λ_p occurs at a value 0.3 lower than the neutrally pitched device, as shown in see Figure 5.7(d).

Using an analysis similar to that described in section 5.4, the kinetic power coefficients achieved by the negatively pitched device at a Froude number of 0.09 are plotted for the respective values of thrust coefficient in Figure 5.8.

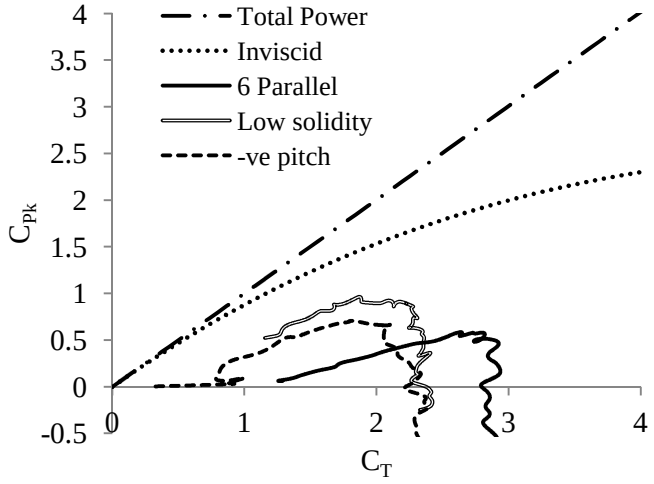

Figure 5.8 - Kinetic power coefficient for the, total power extraction, the theoretical inviscid case (Houlsby et al., 2008a) and experimental results for the three and six parallel bladed and truss bladed configurations at a Froude number of Fr=0.09 and a blockage of B=0.5

Figure 5.8 shows that by applying a 2° negative pitch the thrust produced by the device has been significantly reduced, to a value even lower than the low solidity device. This reduction in thrust results in an increase in head power coefficient to an average of 36.5%, and marks a significant improvement in efficiency over the neutrally-bladed configuration.

These results suggest that the reduced tip speed ratio, improved downstream blade performance and improved orientation of the resultant force vectors, as described in section 3.5, have a net effect of increasing power output while reducing the overall thrust. This effect is observed and explored more quantitatively in the torque traces predicted by the Navier-Stokes Blade-Element model of Chapter 7.

5.6. Variation of the turbine blockage ratio

In order to minimise the amount of apparatus required for the series of experiments the effect of variations in blockage ratio were explored by reducing the depth of the flow in the flume tank. By reducing the depth of flow from approximately 1.0 m to 0.8 m, the blockage ratio was increased from 0.5 to 0.625.

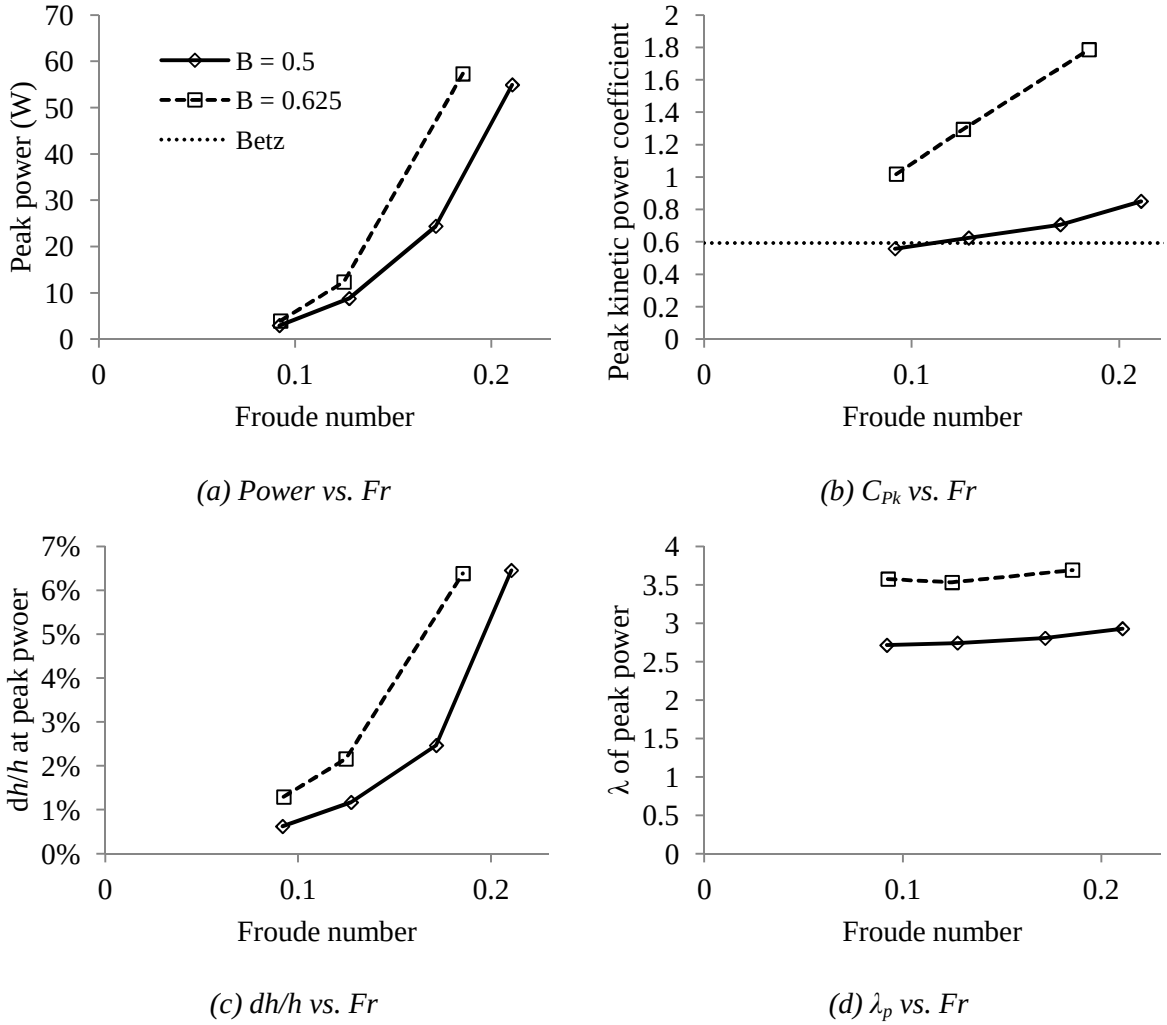

(a) Power vs. Fr *(b) C_{Pk} vs. Fr*

(c) dh/h vs. Fr *(d) λ_p vs. Fr*

Figure 5.9 - Comparison of performance achieved by the six truss-bladed device with a blockage ratio of B = 0.5 and B = 0.625

Figure 5.9(a) shows that by increasing the blockage ratio from B = 0.5 to B = 0.625 the amount of power that is produced by the turbine is significantly increased. The kinetic power coefficient that is achieved suggests that the device is extracting more power than is available from the upstream incident kinetic flux. This is due to the increased extraction of total head, indicated by Figure 5.9(c), which shows that with the increase in blockage there is an accompanying increase in the depth change across the device. An increase in depth change suggests that the thrust produced by the higher blockage device has been significantly increased, which will increase the horizontal load requirements of the turbine foundations.

Despite the increase in depth change across the device the head power coefficient is increased from C_{PH} = 18% for the B = 0.5 case to C_{PH} = 24% for the B = 0.625 case. By blocking a greater proportion of the channel area, an increased thrust can be maintained, whilst achieving a high induction factor and low mixing losses. These observations are supported by numerical simulations of the device, conducted in Chapter 7.

The accelerated flow through the device also results in an increase in the angle of attack experienced by the hydrofoils and therefore the device is likely to stall at a higher tip speed ratio, as indicated by Figure 5.9(d). This is detrimental to the structural performance of the device, both due to the increased thrust and an increase in the forces that are acting on the turbine blades.

However, the benefits of increasing the blockage ratio and maximising the head extraction may significantly outweigh the additional requirements on the structure and foundations. It is likely that the blockage of a device will be limited by a combination of constraints, most of which will be site dependent. The amount of clearance above and below is likely to be dictated by the size of rolling and floating objects in the flow, as well as shipping restrictions. It is also possible that a given turbine fence will be limited to a certain depth change, corresponding to either a reduced thrust device or a reduced blockage ratio.

5.7. Effect of waves

A solitary test was performed with waves of 1 s period and 25 mm amplitude, corresponding to approximately 4.5 s period and 0.5 m amplitude at full scale, to briefly explore whether waves would affect the performance of the device.

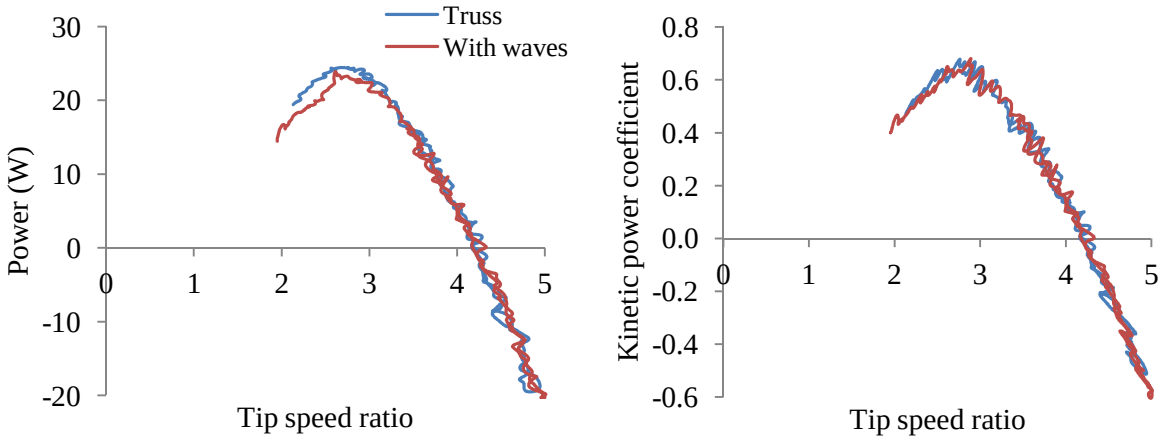

(a) Power vs. tip speed ratio *(b) C_{Pk} vs. tip speed ratio*

Figure 5.10 - Comparison of performance achieved by the six truss-bladed device at a Froude number of 0.17 with and without waves of 1 hz and approximately 25 mm amplitude

Figure 5.10(a) shows that the power curve produced by the device with waves was less smooth than that of the steady current conditions. This is not surprising as the velocity field experienced by the device is much more variable. However, the maximum kinetic power coefficient of the device in waves was the same as that of the steady flow device. While these results suggest that the performance of the turbine will not be severely impaired by waves on a full scale installation, the effect on a device of different configuration and waves of differing frequency and amplitude are likely to be more significant.

5.8. Consistency with flow from either direction

One of the commonly stated advantages of the Darrieus turbine is its ability to operate efficiently with flows from any direction, normal to the rotor axis. In order to validate this assumption for the THAWT device the ends of the rotor were swapped, so that the turbine would rotate in the opposite direction, as shown in Figure 5.11, allowing the effect of flow from the opposite direction to be explored, without reversing the direction of the flow in the flume.

(a) forward configuration *(b) reverse configuration*

Figure 5.11 - Setup of forward and reversed configured devices

Figure 5.12 shows that a device in a reversed configuration achieves a kinetic power coefficient that is close to, but slightly lower than that achieved by the forward configured device. The low power outputs for low Froude number flows means that a small error in power measurement can cause large differences between results of a given flow velocity. It is therefore assumed that there is an uncharacteristically large error in the measurement of the reversed configuration of the truss device at a flow velocity of 0.3 m/s. The average reduction in kinetic power coefficient when using a reversed configured device for the remaining three tests was 3.2%, and λ_p was repeated with an error of 0.6%.

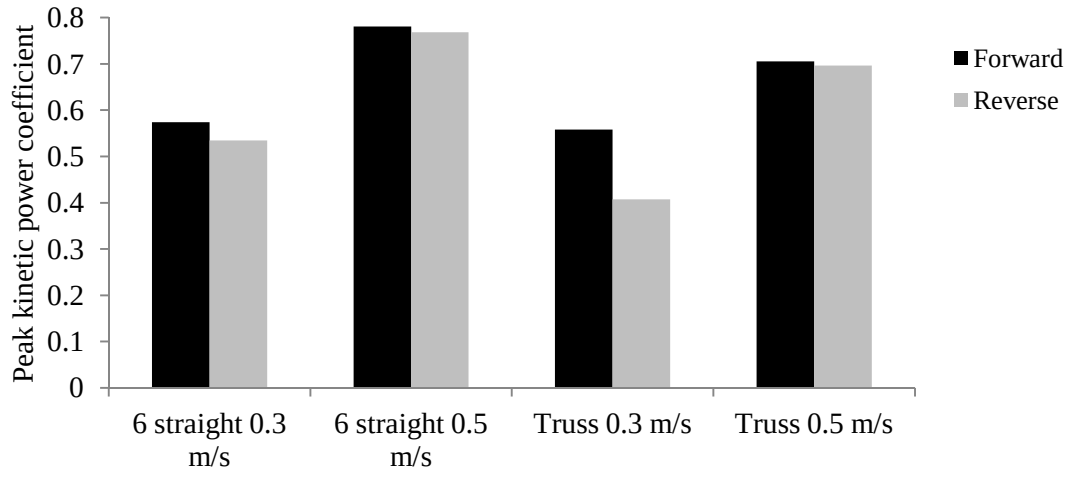

Figure 5.12 - Comparison of the performance of forward and reverse configured devices

The reduction in power achieved by the reversed device is an expected result as the effect of the free surface deformation is to accelerate the flow over the top half of the device, and any velocity profile due to shear at the base of the flume will cause a reduction in velocity at the bottom half of the device. While both of these changes in velocity are beneficial to the forward configured device, where accelerations at the top and decelerations at the bottom will increase the velocities experienced by the turbine blades, both effects will reduce the velocities experienced by the reverse configured device and are therefore expected to reduce the produced power.

Whilst the consistency of the performance of the device with flow from either direction indicates that the differences in velocity at the top and bottom of the test flume are relatively small, the flow field experienced by a full scale device may be significantly different due to turbulence, stratification of the flow and an exaggerated velocity profile due to bed roughness. These factors should be explored in more depth, possibly on a site by site basis.

5.9. Effect of turbine vertical position in the flow

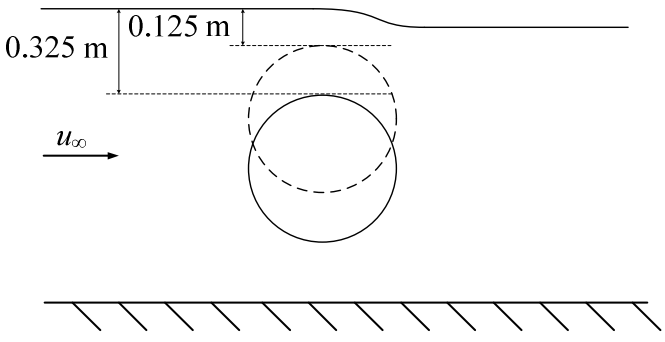

Figure 5.13 - Distance to the free surface in experiments exploring the effect of vertical position

In order to assess how the vertical position of the device in the water column affects the performance of the turbine, tests were performed with the axis of the truss-bladed rotor raised so that the distance to the free surface was reduced from 0.325 m to 0.125 m, as shown in Figure 5.13.

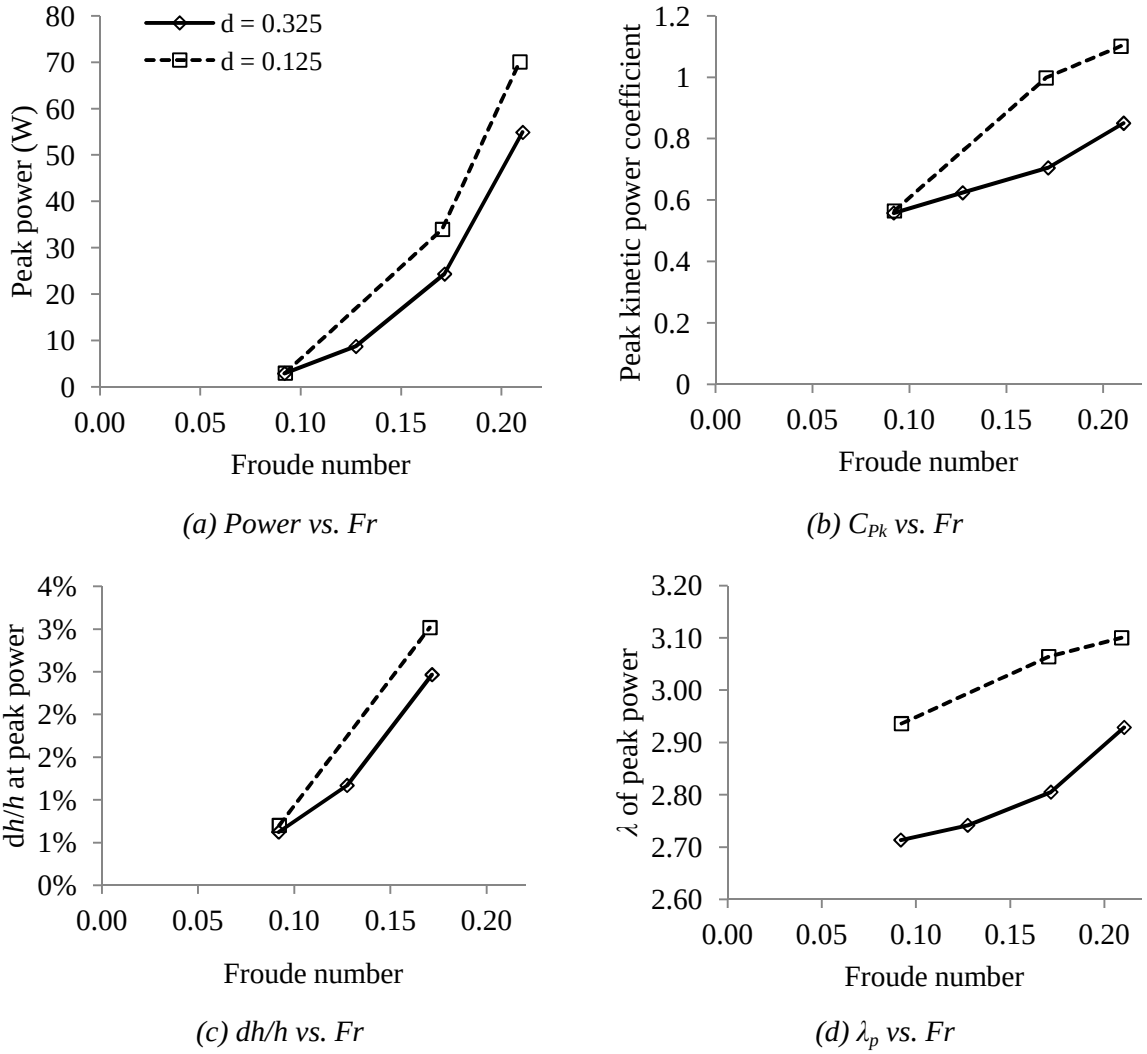

(a) Power vs. Fr

(b) C_{Pk} vs. Fr

(c) dh/h vs. Fr

(d) λ_p vs. Fr

Figure 5.14 - Comparison of performance achieved by the six truss-bladed device with a blockage ratio of B = 0.5 and mounted at two vertical positions so that the top blade is 0.125 m and 0.325 m from the free surface

Figure 5.14(a) shows that by reducing the distance of the turbine from the free surface, the power produced by the THAWT device is increased at higher Froude number flows. The increase in power, with an increase in vertical height, results in an increase in the kinetic power coefficients by factors of between 1.01 – 1.42, as shown in Figure 5.14(b).

The increase in power at higher Froude number flows may be due to the acceleration of the flow near to the free surface as the depth is reduced across the device. The proximity of the high solidity turbine to the deforming free surface is expected to force a high velocity stream

through the bypass, which will cause an increase in the velocity experienced by the turbine blades. The increase in λ_p, shown in Figure 5.14(d), supports this theory as an increase in the angle of attack experienced by the blades at a given tip speed ratio suggests an increase in the velocity through the device.

Despite an increase in the depth change across the higher positioned device, shown in Figure 5.14(c), the average head efficiency is increased from 19.0% to 21.0%, suggesting an improvement in the true efficiency of the device. Whilst the performance of the device is improved by moving the rotor closer to the free surface, it is anticipated that this will reduce the performance of a device in a reversed configuration, where the blades at the top of the rotor will be moving in the same direction as the accelerated flow. Accelerating the flow in a narrow region close to the free surface is likely to cause supercritical flow at a lower Froude number and so a design should maintain a given distance to the free surface during an entire tidal cycle, which prevents any possibility of supercritical bypass flow from occurring. There may also be limitations on how close to the free surface the turbine can be placed due to site specific constraints.

5.10. Torque fluctuations

Any basic analysis of a Darrieus turbine predicts that the magnitude of torque fluctuations is reduced as the number of blades increases (Paraschivoiu, 2002, Shiono *et al.*, 2000). Designs of turbines with swept or helical blades have been developed in order to reduce the torque fluctuations, without requiring an increase in the number of turbine blades (Gorlov, 1997, Zanette *et al.*, 2010).

Figure 5.15 shows a plot of torque fluctuations recorded for the three and six parallel-bladed devices, which has been calculated by subtracting the average torque for the period from each data point to illustrate the magnitude of fluctuations. As expected, the magnitude of torque fluctuations are significantly reduced by using a six-bladed design rather than a three-bladed design, with rms values of 0.17 and 0.06 for the three and six-bladed devices respectively.

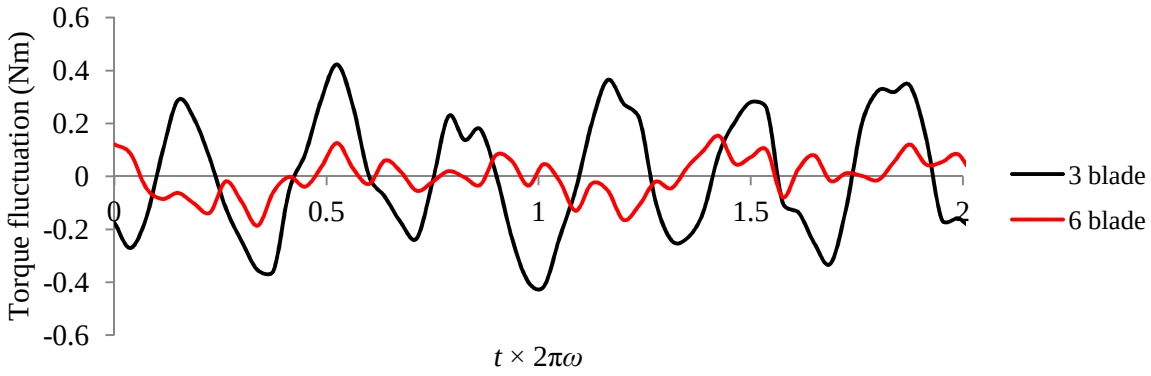

Figure 5.15 - Comparison of raw torque traces over two turbine rotations by the three and six parallel-bladed devices at a Froude number of 0.09 and a speed of 45rpm

Despite the use of swept blades in the truss design, there is no improvement in torque fluctuation when using the six-bladed truss, as opposed to the six parallel-bladed device, with rms values of 0.07 and 0.06 respectively. This may be due to similar torque fluctuations between the two designs or due to the magnitude of the actual torque fluctuations being smaller than those due to the feedback control loop of the motor controller.

5.11. Anticipated trade-offs in structural and hydrodynamic performance

By applying the preliminary analysis of Chapter 3 to the gathered experimental data, the effect that configuration variations have on the blade stress can be predicted.

$$\frac{\sigma_{max}}{\rho g h} \propto \frac{{\lambda_p}^2 \mathrm{Fr}^2 n^2 \beta^2}{s^2 \left({}^{t}/_{c}\right)^2} \qquad 5.3$$

The effect that variations in the design configuration have on the induced blade stress is explored using equation 5.3 of the analytical preliminary analysis. As the configuration of the truss device was not varied during the experiments, the results from the parallel-bladed device at a Froude number of 0.17 are analysed using the dimensional analysis. The assumption that variations in design configuration have similar effects on the truss and parallel-bladed device is explored in Chapter 7 and Chapter 8.

5.11.1. Effect of reduced solidity

Tests were performed with a six parallel-bladed device of solidity s = 0.25 and with a three-bladed device of reduced solidity s = 0.125. By reducing the solidity of the device from 0.25→0.125 the kinetic power coefficient and head power coefficient are increased by factors of 1.19 and 1.88 respectively. This improvement in performance is anticipated to occur due to a reduced thrust and an increased velocity of flow through the rotor, so that the turbine

blades operate with improved lift to drag characteristics for a greater proportion of the turbine rotation. The improvement in performance for the reduced solidity turbine was also accompanied by an increase in the operating tip speed ratio by a factor of 1.25.

When combining the changes to the turbine solidity, the number of blades and the operating tip speed ratio, the net effect of reducing the turbine solidity from 0.25 → 0.125, predicted using equation 5.3, is an increase in blade stress by a factor of 1.56. It should be noted that the anticipated increase in blade stress when reducing the turbine solidity is significantly more severe when the number of blades remains constant, which is likely to be the case for variations in the design of the truss configured device.

5.11.2. Effect of negative offset pitch

Tests were performed with the turbine blades configured at a neutral pitch of 0° and a negative fixed offset pitch of -2°. By reducing the fixed offset pitch from 0° to -2° the kinetic power coefficient and head power coefficient are increased by factors of 1.07 and 1.86 respectively. This increase in performance is anticipated to occur due to an increase in the amount of power produced by the downstream half of the device and a decrease in the produced thrust. Due to the use of a negative offset pitch, the improvements in device performance were accompanied by a decrease in the operating tip ratio by a factor of 0.91.

With no other salient variation in the turbine configuration, equation 5.3 predicts that the reduction in operating tip speed ratio will result in a reduction of blade stress by a factor of 0.82. This analysis therefore suggests that applying a negative offset pitch is a more favourable method of increasing performance, when compared to reducing the device solidity.

5.11.3. Effect of increased blockage

The results for increased blockage are compared at a Froude number of 0.13, due to an inaccurate measurement of depth change at greater flow velocities for the high blockage tests. Tests were performed on devices with blockage ratios of B = 0.5 and an increased blockage ratio of B = 0.625. By increasing the blockage ratio from 0.5 to 0.625 the kinetic power coefficient and head power coefficient are increased by factors of 2.32 and 1.12, respectively. This improvement in device performance is anticipated to occur due to an acceleration of the flow through the device, which results in an increase in the tip speed ratio of peak power by a factor 1.28.

With no anticipated variation in blade stress due to a varied blockage ratio and ignoring the change in the length scale of the experimental domain, equation 5.3 predicts that the increase in operating tip speed ratio when increasing the blockage ratio will result in an increase in blade stress by a factor of 1.64. This analysis suggests that while the amount of power extracted and the available energy to the device can be significantly increased by increasing the blockage ratio, a significantly detrimental increase in blade stress is likely to be incurred.

5.12. Conclusions

This chapter uses a series of scale model experiments to show that the truss variant of the THAWT produces power with a kinetic power coefficient close to that of the conventional parallel-bladed device. The results show that both the parallel and truss-bladed devices are capable of producing power at kinetic power coefficients greater than the Lanchester-Betz limit. Furthermore, the power available to the THAWT device is not simply a function of the incident kinetic flux, but is increased because of blockage effects.

A fixed negative pitch (relative to the tangent of the pitch circle) has been shown to increase the power produced by the turbine, as well as reducing the depth change across the device and reducing the tip speed ratio at which the peak power is extracted. This is achieved by redistributing the magnitude of the angle of attack between the upstream and downstream halves of the high solidity device, and is predicted to reduce blade stress.

Increasing the blockage ratio and reducing the rotor solidity have been shown to improve the performance of the device. However, applying the preliminary analysis of Chapter 3 indicates that these hydrodynamic improvements are likely to be accompanied by significant increases in the induced blade stress. Furthermore, the effects of reversing the flow direction have been shown to have a negligible effect on the power produced by the turbine in the Newcastle flume. However, it should be noted that the flow conditions that might be expected at a full scale installation, such as increased turbulence, stratified flow and a varied velocity profile, will affect the performance of the THAWT device, but the significance of these effects is likely to be site-specific and require further testing and analysis once a site has been chosen.

It is anticipated that blades on a full scale device will experience flows of a greater Reynolds number, resulting in improvements in the lift and drag characteristics of the hydrofoil, and an increase in the efficiency of the device.

Chapter 6

Momentum Blade-Element hydrodynamic model

A numerical model of the THAWT hydrodynamics is necessary in order to predict the power produced, the blade forces and the effect of design configuration variations, for any scale of device. Whilst experiments provide performance measurements with a high degree of confidence, the costs of performing extensive parameter searches is often too high. Therefore, the results from key experiments are commonly used to validate numerical models, which can perform these parameter searches more economically.

Comparisons of previous numerical models of the THAWT device with corresponding experimental results (McAdam, 2007) indicated that some underlying assumptions were inaccurate. The main identified inaccuracies were the assumptions of no disturbance to the flow-field due to the device and hydrofoil performance characteristics that did not vary with Reynolds number.

In order to address these problems it was decided to model the flow field using Linear Momentum Actuator Disc Theory for Open Channel Flow (LMADT-OCF) (Houlsby *et al.*, 2008a) and to model the performance of the hydrofoils using published lift and drag data, and interpolating with Reynolds number. The use of a combined LMADT and blade element theory has previously been attempted by Templin (1974), but by utilising the LMADT-OCF this technique is applied to a tidal turbine in a flow constrained by a free surface. This technique is only applicable to a two-dimensional analysis of the device, which allows comparisons and validations to be drawn with the experimental results from the parallel-bladed device of Chapter 5.

6.1. Blade element model

The forces acting on the turbine blades are calculated using the blade element equations 6.1 to 6.5, and differ from the more basic equations in section 2.2.1 with a reduction in velocity through the turbine, dictated by an induction factor α_2.

$$V_R = \sqrt{(r\omega \sin\theta)^2 + (r\omega \cos\theta + \alpha_2 u_\infty)^2} \qquad 6.1$$

$$\alpha = \tan^{-1}\left(\frac{\alpha_2 u_\infty \sin\theta}{r\omega + \alpha_2 u_\infty \cos\theta}\right) \quad 6.2$$

$$L = {}^1\!/_2\,\rho {V_R}^2 c C_L \quad 6.3$$

$$D = {}^1\!/_2\,\rho {V_R}^2 c C_D \quad 6.4$$

$$\text{Torque} = r(L\sin\alpha - D\cos\alpha) \quad 6.5$$

The radial and tangential forces are calculated using equations 6.6 and 6.7.

$$F_{radial} = L\cos\alpha + D\sin\alpha \quad 6.6$$

$$F_{tangential} = L\sin\alpha - D\cos\alpha \quad 6.7$$

The stream-wise thrust produced by a blade is calculated using equation 6.8.

$$T = L\sin(\theta - \alpha) + D\sin(\theta - \alpha) \quad 6.8$$

These calculations are performed over 5° increments of turbine rotation in an attempt to yield time average values of torque and thrust.

As described in Chapter 4, the 18.4% thick ClarkY-Sym hydrofoil was selected for use in the experimental tests at Newcastle University. Whilst the ClarkY-Sym section proved to be effective during these experiments, there is no published hydrofoil performance data available over the range of experimental Reynolds number. Due to limited experimental facilities and the time required to accurately model the hydrofoil characteristics numerically, it was decided to use lift and drag coefficients interpolated from published data of a NACA 0018 aerofoil by Sheldahl and Klimas (1981) (see Figure 6.1), based on the angle of attack and Reynolds number.

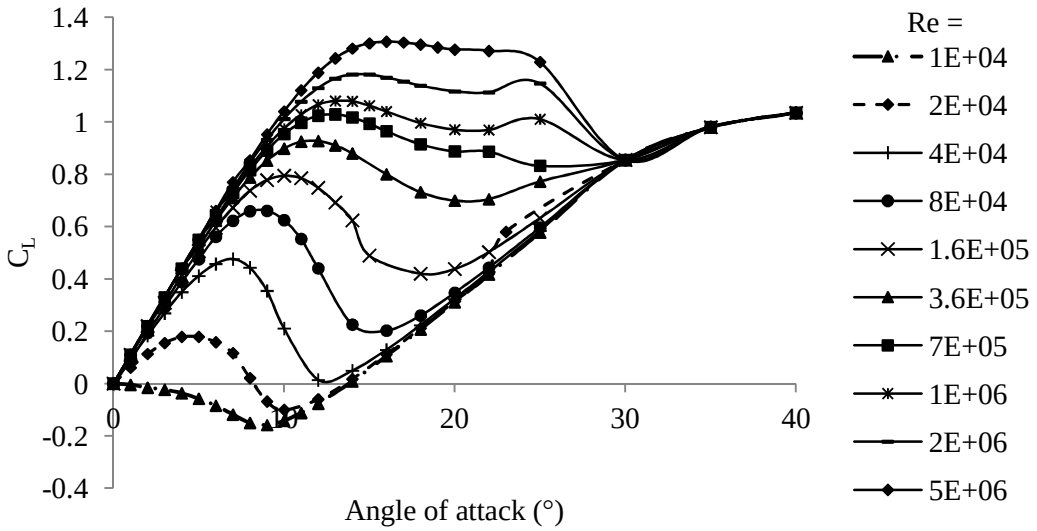

Figure 6.1 – NACA 0018 lift coefficients at various Reynolds numbers, based on data in (Sheldahl and Klimas, 1981)

Due to similar predicted performance of the NACA 0018 section and the ClarkY-Sym, as shown in Figure 6.2, there is believed to be little additional error introduced in the M-BE model through the use of NACA0018 aerofoils in place of the ClarkY-Sym aerofoils used in the experimental campaign.

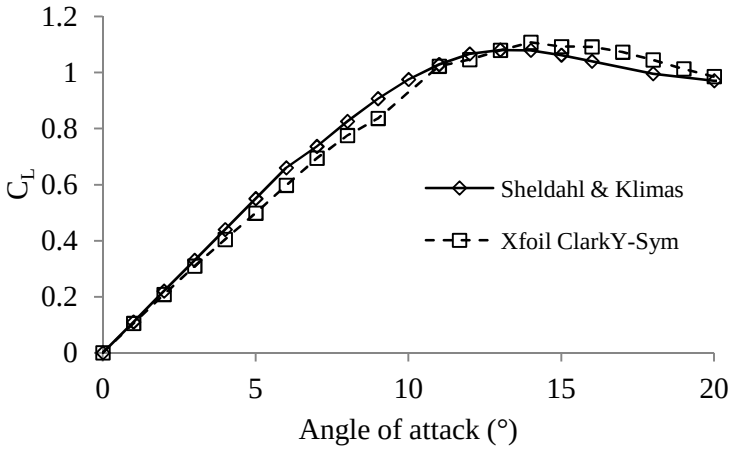

Figure 6.2 - Comparison of lift curves predicted for the NACA 0018 section (Sheldahl and Klimas, 1981) and the ClarkY-Sym section predicted by X-foil (Drela, 2004) at Re = 1×10^6

6.2. Linear Momentum Actuator Disc Theory for Open Channel flow model

For a realistic Froude number flow it can be shown using LMADT-OCF (Houlsby *et al.*, 2008a) that as the induced depth change across a tidal device is increased, the total amount of power available for extraction increases significantly above the total kinetic power in the upstream flow (see Figure 6.3).

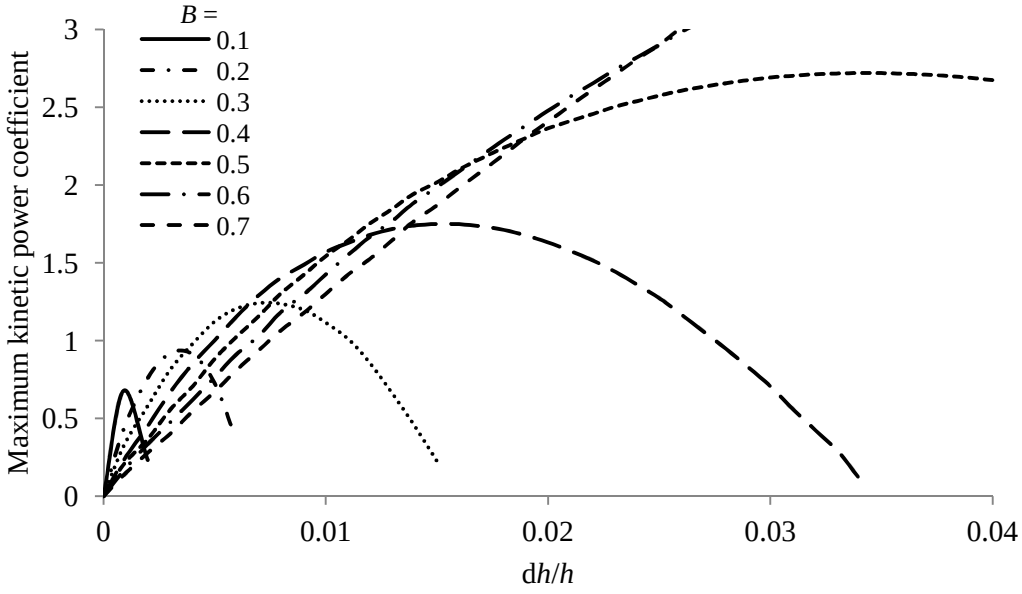

Figure 6.3 - Maximum Kinetic Power coefficient against depth change at a Froude number of 0.13 and for a range of blockage ratios, calculated using LMADT-OCF (Houlsby et al., 2008a)

With a blockage ratio of 0.5 and measured experimental depth changes in the range $0.004 < dh/h < 0.065$, LMADT-OCF predicts that the amount of energy available to the experimental turbine of Chapter 5 is a factor of up to 2.7 times greater than the amount of kinetic energy in the upstream incident flow.

Whilst the Double Actuator Disc Theory (LMDADT) of Newman (1983), multiple streamtube method of Stickland (1975) and double-multiple streamtube method of Parschvoiu (2002) offer the ability to vary the flow velocity in accordance with the thrust from the turbine, none of these techniques are capable of modelling the constraint due to a free surface and the accompanying increase in available energy. These models may provide adequate results for low Froude number flows or low blockage scenarios, but it is felt that they are not able to predict the results achieved during the Newcastle experiments and are not suitable to extrapolate to larger scales.

In order to maintain a consistent specific energy available to the device, to allow validation against experimental measurements, it was decided to use LMADT-OCF to predict the velocity at the turbine for the blade element calculations. Based on the coefficient of thrust C_T, calculated using blade element theory, and the non-dimensional flow parameters for Froude number Fr and blockage ratio *B*, an estimate of the induction factor is calculated using LMADT-OCF.

6.3. Combination of two techniques

In order to predict the performance of the THAWT device the Momentum-Blade Element (M-BE) model requires the upstream flow parameters of velocity and depth, as well as the turbine geometry parameters of solidity *s*, number of blades *n*, radius *r* and length *l*. An estimate of the initial induction factor provides the required information for the forces acting on the blades to be predicted using blade element theory. The coefficient of thrust is calculated from the mean of the blade thrust force, which has been calculated using equation 6.8. Based on the coefficient of thrust and the non-dimensional flow parameters of Froude number and blockage ratio, an improved estimate of the induction factor is calculated using LMADT-OCF. A solution is found by repeating this process until the change in thrust coefficient between iterations falls below a suitable threshold. By repeating this process over a range of tip speed ratios a power curve can be derived and compared to other numerical hydrodynamic models or experimental results (see Figure 6.4).

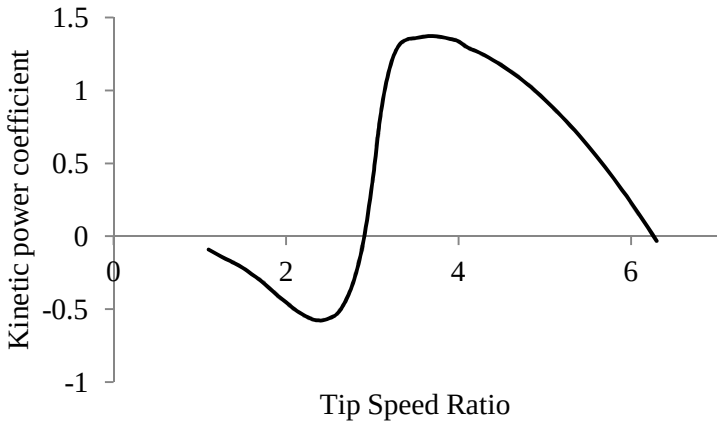

Figure 6.4 - Typical power curve produced by the M-BE model

6.4. Comparison of M-BE with experimental results

The results from the experiments performed on the 1/20th scale THAWT prototype at Newcastle University, described in Chapter 5, have been used to assess the accuracy with which the M-BE model predicts the performance of the THAWT device. The two main sets of experiments used for comparison in this chapter are those performed on the three-bladed and six-bladed parallel devices. The performance of the truss device is initially neglected due to the additional complexity involved in the three-dimensional effects of the configuration. The results used for comparison are shown in Table 6.1.

h_∞ (m)	1.0				0.8		
B	0.5				0.625		
u_∞ (m/s)	0.3	0.4	0.5	0.7	0.3	0.4	0.5
Fr	0.096	0.13	0.16	0.22	0.11	0.14	0.18
Parallel six blade	*	*	*	*	*	*	*
Pitched six blade	*		*				
Parallel three blade	*	*	*	*	*	*	*

Table 6.1 – Experiments used as comparison for M-BE model

Comparisons of the reversed configuration and varied vertical position experiments are not explored, as there is no change to either the Linear Momentum model or the blade element modelling, and so variations of these factors will have no effect on the M-BE predictions.

Ratios of the performance predicted by the numerical M-BE model to the experimental results for the kinetic power coefficient C_{Pkn}/C_{Pke}, tip speed ratio $\lambda_{pn}/\lambda_{pe}$ and depth change $(dh/h_n)/(dh/h_e)$, each at the point of peak power, are used to assess the accuracy and fidelity of the M-BE model.

As described in Chapter 5 the depth change measurements from the experiments at higher Froude number flows were inaccurate due to a lack of full depth recovery. The depth

measurements that are suspected to be erroneous, which are indicated in Chapter 5, are therefore omitted from the subsequent analysis of the M-BE model.

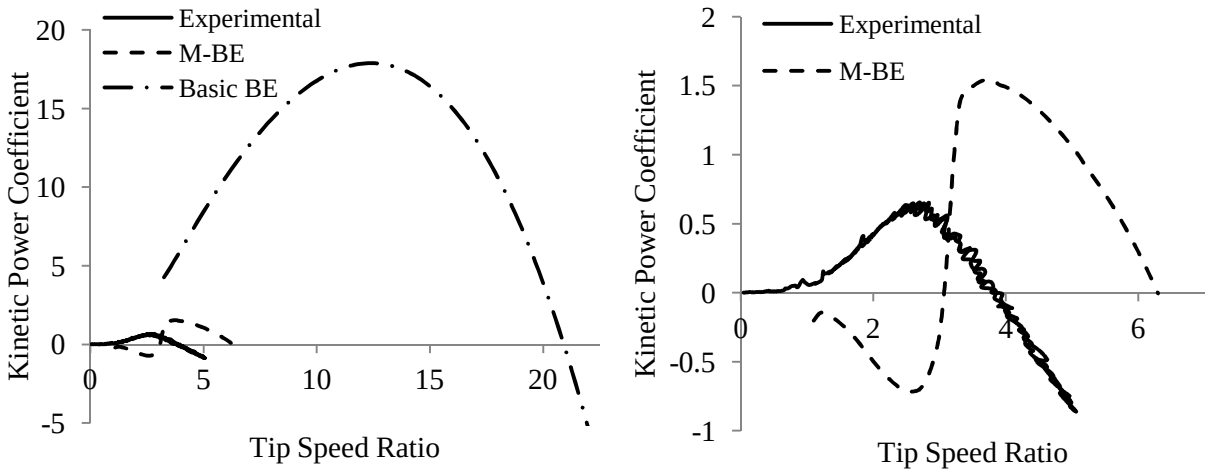

(a) Comparison of experimental, Momentum-Blade Element model and basic Blade Element model of McAdam (2007)

(b) Comparison of experimental, Momentum-Blade Element model

Figure 6.5 - Comparison of experimental results and numerical predictions of the six bladed THAWT device at a Froude number of 0.13 and a blockage ratio of 0.5 in the Newcastle flume tank

Figure 6.5 illustrates that the M-BE model offers a significant improvement in the prediction of the THAWT device performance, when compared to the previous basic Blade Element model, developed by McAdam (2007). The peak power output and the tip speed ratio predicted by the M-BE model is significantly lower than those predicted by the simple Blade Element model, and has notably improved the fidelity with the experimental data. The similarity of the predicted power curve using the M-BE model, for tip speed ratios greater than the peak power, appears to match the shape of the experimental results. However, the lack of a model for the complex flow phenomena during stall for a pitching hydrofoil is likely to contribute to the sharp drop in power predicted by the M-BE model at low tip speed ratios and high angles of attack.

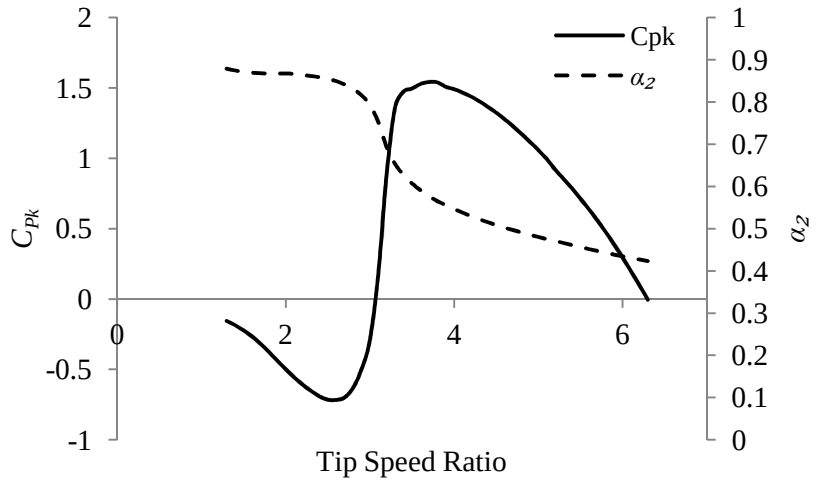

Figure 6.6 - Predicted kinetic efficiency and accompanying induction factor for the six-bladed THAWT device, using the M-BE model at a Froude number of 0.13 and a blockage ratio of 0.5

The improvement in accuracy prediction of the M-BE model over the basic Blade element model is due to a reduced velocity predicted at the turbine by the LMADT-OCF, and used in the blade element calculations. Figure 6.6 shows that as the tip speed ratio increases, the impedance of the turbine also increases, causing a reduction in the flow velocity. For example, the M-BE model predicts that a six parallel-bladed device operating in a Froude number flow of 0.13 and with a blockage ratio of 0.5 experiences a peak in power when the velocity at the turbine is 58% of the free stream velocity. The operating angle of attack is reduced due to the reduction in velocity at the turbine, resulting in a reduction of the tip speed ratio of free running and of peak power.

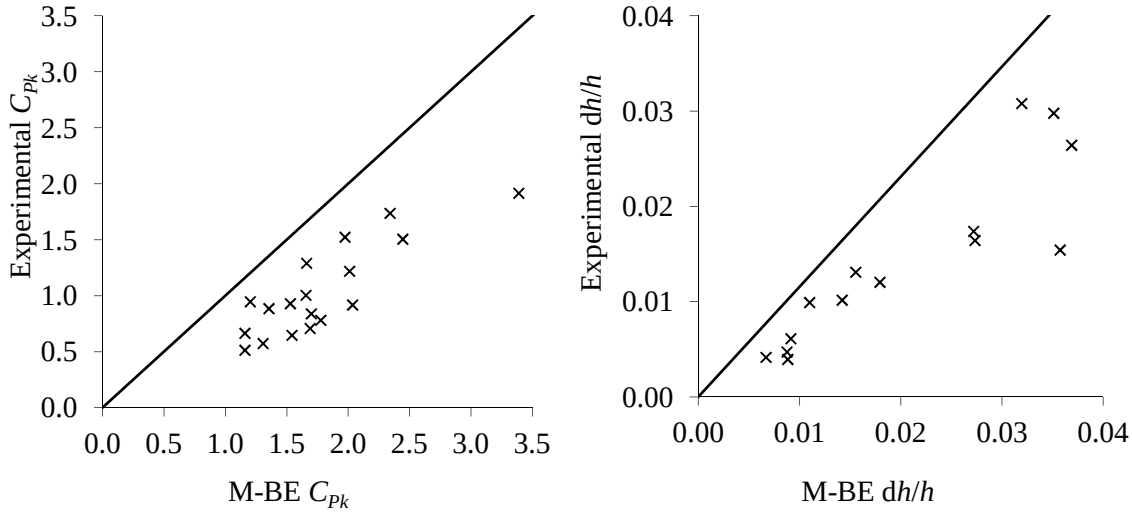

(a) *Kinetic power coefficient* *(b) Depth change*

Figure 6.7 - Graph comparing predictions using the M-BE model and recorded by experiment over the range of simulated experiments

However, as shown in Figure 6.7 the M-BE model systematically over-predicts the kinetic power coefficient and depth change of the various configurations of device by mean ratios of C_{Pkn}/C_{Pke} = 1.82 and $(dh/h_n)/(dh/h_e)$ = 1.54.

6.4.1. Comparisons of basic parallel-bladed tests

Figure 6.8 demonstrates that the mean ratios of C_{Pkn}/C_{Pke} for the three-bladed and six-bladed devices predicted using the M-BE model are 1.52 and 2.29 respectively, which indicates a significant over-prediction of the predicted peak power. Whilst the accuracy of the prediction of the performance of the device is relatively poor, the M-BE model successfully simulates the increase in available energy as the Froude number is increased and allows for the simulation of a device which is capable of exceeding the Lanchester-Betz limit.

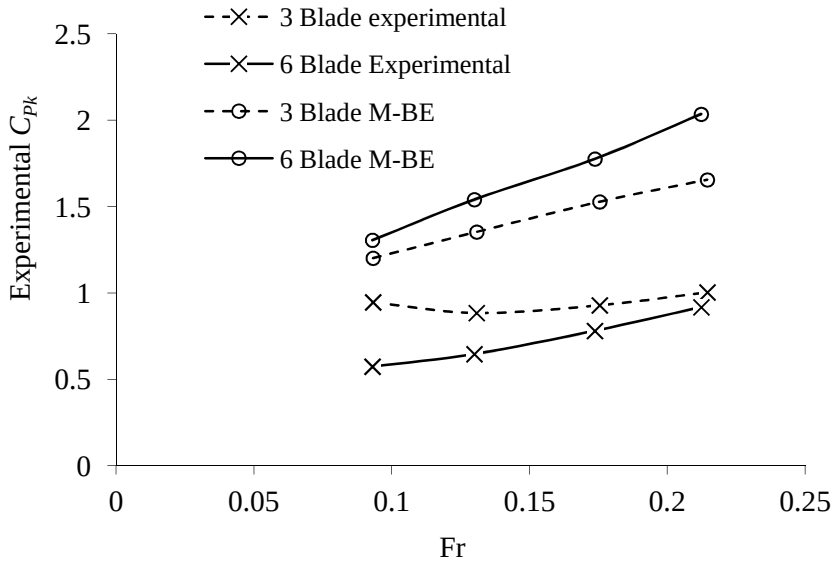

Figure 6.8 - Graph comparing kinetic efficiencies predicted using the M-BE model and recorded by experiment at a blockage ratio of 0.5

The main cause for the over-estimate of power prediction is due to the simplicity of the flow field provided by the LMADT-OCF, for use in the blade element calculations. LMADT-OCF predicts a reduction in stream-wise flow at the device and a corresponding increase in the velocity of the flow in the bypass. In order for this to occur a proportion of the upstream flow must be displaced vertically, the vector and rate of which cannot be predicted by LMADT-OCF alone. A set of experiments were carried out on the 1/20th scale device at Newcastle University, in which the path of bubbles passing through the turbine were imaged using Particle Image Velocimetry (PIV) (Shi, 2008), the results of which are not discussed in this thesis. During these tests it was observed that the thrust from the upstream half of the

device caused a reduction in flow velocity within the turbine to a near standstill, which affected the blades on the downstream half of the rotor. A large proportion of the error in the prediction of peak power by the M-BE model can therefore be attributed to an unrealistically high estimate of the velocity on the downstream half of the device. For a turbine of relatively low impedance this effect will be negligible, but will become more significant as the stream-wise thrust produced by the device becomes more significant, or as the blockage ratio is decreased.

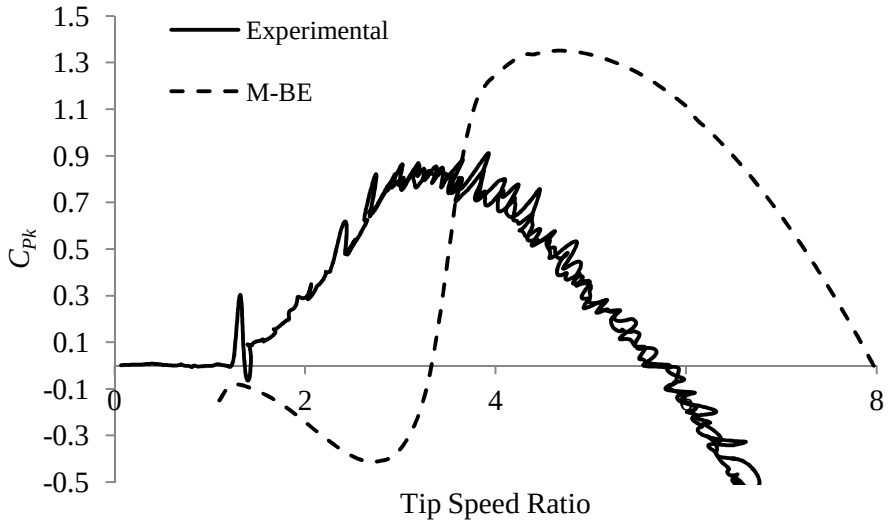

Figure 6.9 - Comparison of the kinetic power coefficient predicted by M-BE and experimental tests for the three bladed THAWT at a Froude number of 0.13 and a blockage ratio of 0.5

A lack of accuracy when modelling the reduction in velocity through the device also produces the disparity in the accuracy of prediction between the three and six-bladed devices. Figure 6.8 and Figure 6.9 show that the error in the prediction of peak power by the M-BE model is lower for the three-bladed device than the six-bladed turbine. The three-bladed device offers a lower impedance to the flow, so that the reduction in velocity through the turbine is relatively low, and the modelled flow conditions by the M-BE model are more representative. This evidence suggests that in order to model high solidity devices using the M-BE model, the reduction in velocity between the upstream and downstream halves of the device must be accounted for.

The inaccuracies in the M-BE model due to the deflection of the flow field also affect the predictions of depth change. Whilst the predicted power output of the blade element calculations are dependent on the induction factor, the depth change across the device is predominantly affected by the variation in the coefficient of thrust produced by the device.

With an unrealistically high velocity experienced by the blades on the downstream half of the device, the depth change predicted by the M-BE model is greater in magnitude than the experimental measurements, as shown in Figure 6.10.

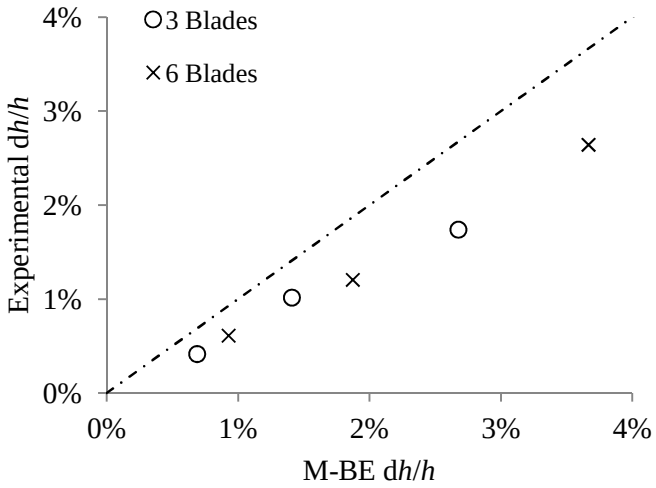

Figure 6.10 - Graph comparing depth changes predicted at peak power using the M-BE model and recorded by experiment

Over the basic range of parallel-bladed experiments the M-BE model over-predicts the tip speed ratio at which peak power occurs by an average ratio of $\lambda_{pn}/\lambda_{pe} = 1.42$. In Figure 6.11 we can see that for the six parallel-bladed device the error in λ_p is relatively constant, and can be seen in the power curves as a shift of the curve to higher tip speed ratios, as shown in Figure 6.5(b) and Figure 6.9.

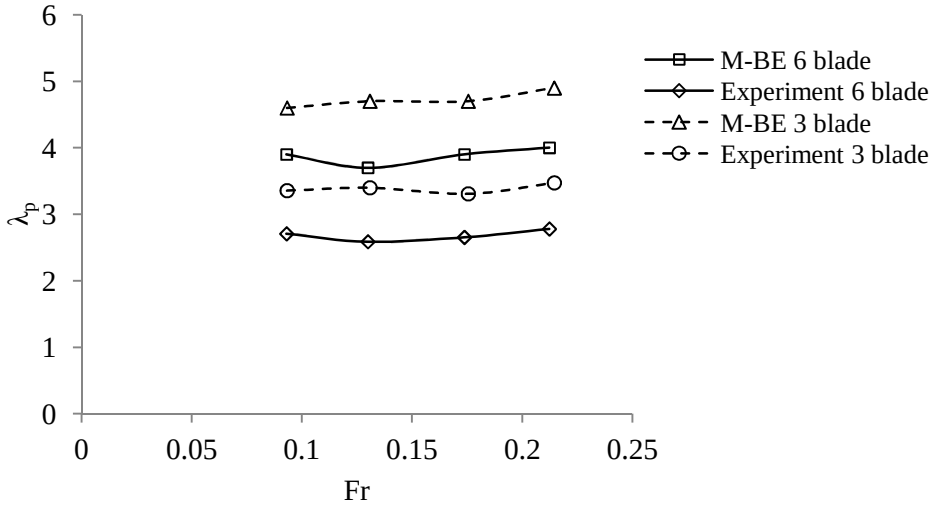

Figure 6.11 - Comparison between experimental results and M-BE predictions of λ_p for the six parallel-bladed device at a blockage ratio of 0.5, over a range of Froude numbers

6.4.2. Comparison of fixed offset pitch results

In a similar fashion to the basic parallel-bladed tests, the M-BE model over-predicts the amount of power produced by the six parallel-bladed turbine with a fixed offset pitch, as shown in Figure 6.12 (a). The assumption that the optimum turbine performance occurs for a device in a uniform steady flow when the pitching angle is neutral is supported by the M-BE model, which predicts a small reduction in power for both the negatively and positively pitched tests when compared to the neutrally pitched prediction.

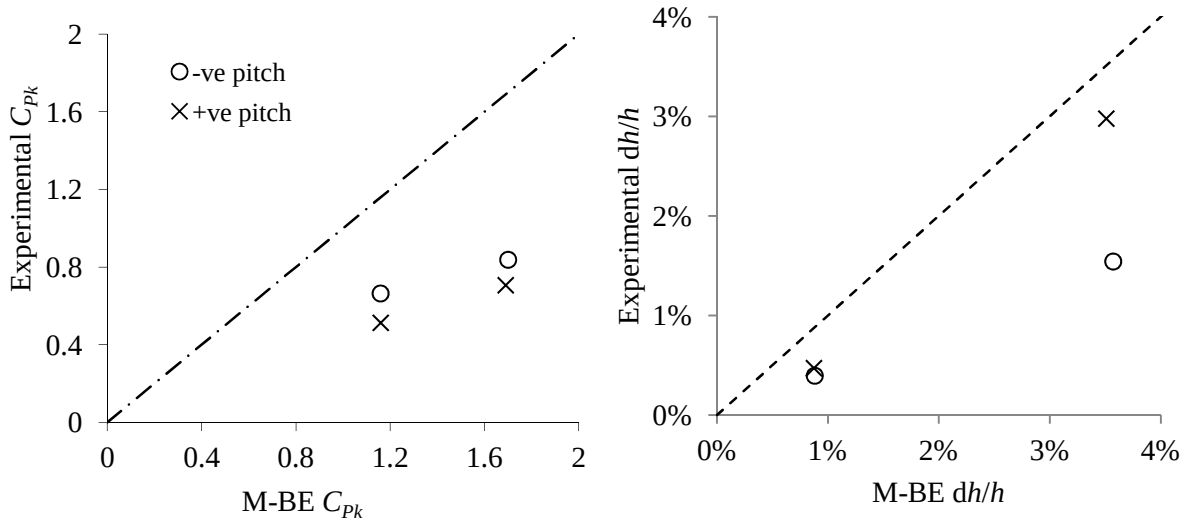

(a) Comparison of C_{pk} *(b) Comparison of dh/h*

Figure 6.12 - Graph comparing M-BE predictions and experimental results for the six parallel-bladed device with a fixed offset pitch at a blockage ratio of 0.5

The M-BE model also overestimates the depth change, with the greatest error occurring in the simulation of the negatively pitched experiments, as shown in Figure 6.12(b).

The fixed offset pitch experiments performed at Newcastle indicate that a negative offset pitch (a positive pitch acts to increase the apparent angle of attack on the upstream half of the turbine) improves the performance of the device by increasing the power output, reducing the operating tip speed ratio and decreasing the depth change across the turbine. Due to the assumption of the uniform, steady velocity through M-BE model turbine, a fixed offset to the blade pitch does not cause any significant change to the predicted performance. This is because an increase in pitch will cause an increase in the angle of attack on the leading side of the device and a reduction in the angle of attack on the downstream half of the device. When compared to the neutrally pitched predictions by the M-BE, the same flow conditions incident on both halves of the device result in a slight reduction in power output for the fixed offset pitch design, and the tip speed ratio of peak power remains relatively unchanged. As shown

by Figure 6.13, the M-BE model does not predict the changes in λ_p that were observed during the experiments.

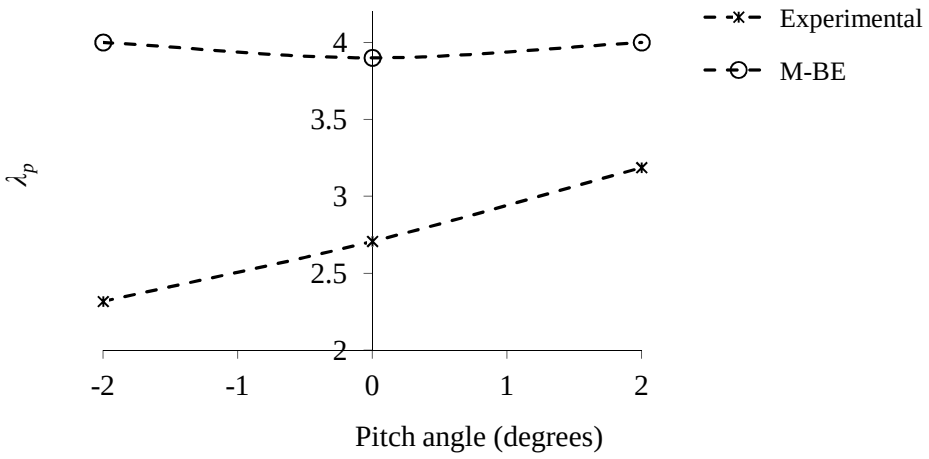

Figure 6.13 - Comparison between experimental results and M-BE predictions of λ_p for the six parallel-bladed device at a blockage ratio of 0.5, at Fr = 0.09

This indicates that it is necessary to model the change in velocity between the upstream and downstream halves of the device in order to accurately predict the performance of a device with a varying fixed offset pitch.

6.4.3. Comparison of increased blockage prediction

An additional set of experiments were performed at Newcastle University with an increased blockage ratio, which was achieved by reducing the depth of the flow from 1 m to 0.8 m, so that B = 0.625. Experimental results demonstrate that increasing the blockage ratio causes a significant increase in the power output, the tip speed ratio of peak power and the depth change across the device.

The LMADT-OCF procedure is limited to predicting the velocity through the device and the corresponding depth change when the bypass flow remains sub-critical. If the bypass flow becomes supercritical then a non-isentropic hydraulic jump occurs, which means that Bernoulli's equation can no longer be applied to the bypass flow downstream of the turbine. A device would not be designed to produce a hydraulic jump, which induces significant mixing losses. A configuration of device that induces a supercritical flow does not produce a real solution in the LMADT-OCF model, and indicates that the thrust produced by this device is too great and is an unfeasible design.

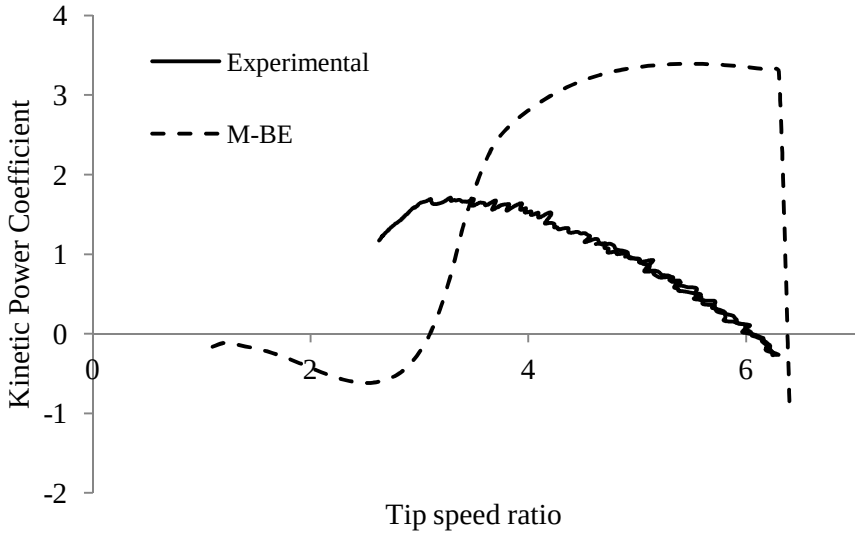

Figure 6.14 - Power curve for the six parallel-blade device at a Froude number of 0.19 and a blockage ratio of 0.625

In the calculation of the power curve for the six-bladed device at a flow velocity of 0.5 m/s and a blockage ratio of B = 0.625, the thrust predicted by the M-BE model increases to the point that the bypass flow becomes supercritical; meaning no real solution is available. Figure 6.14 shows the predicted power curve up to the point of supercritical bypass flow and the breakdown of the solution. This suggests that a combination of such a high blockage, solidity and flow velocity does not allow for a feasible design of device.

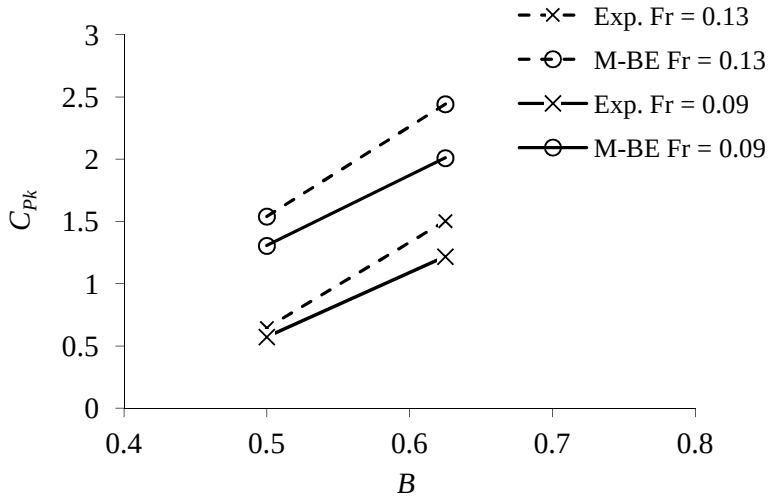

Figure 6.15 – Comparison of kinetic power coefficient measured experimentally and predicted by the M-BE model, for the six parallel-bladed device at varied blockage ratio and Froude number

In a similar fashion to the lower blockage predictions, the M-BE model over-predicts the power produced by the six and three parallel-bladed devices with a blockage of B = 0.625 by factors C_{Pkn}/C_{Pke} of 1.68 and 1.31 respectively. The reduced error in performance prediction at the higher blockage ratio of B = 0.625 is anticipated to occur due to a higher velocity flow

through the device, which is closer to the LMADT-OCF approximation. However, the M-BE model achieves the correct qualitative changes when predicting the increase in performance of the device as the blockage ratio is increased, as shown in Figure 6.15. This suggests that whilst the M-BE model is unsuitable for accurately predicting the performance of a higher blockage device, it is still a useful tool for predicting how changes in blockage ratio might affect the turbine performance characteristics.

6.5. Conclusions

The Momentum Blade Element model (M-BE) demonstrates a significant improvement over the basic Blade Element model of McAdam (2007), when compared to the experimental results of Chapter 5. The improvement in the prediction of the device performance is due to the more accurate modelling of the hydrofoil characteristics in the lower Reynolds number flows and the calculation of the velocity incident with the rotor blades, using the Linear Momentum Actuator Disc Theory for Open Channel Flow (LMADT-OCF).

Despite its improvement over the basic Blade Element model, the M-BE model achieves a relatively poor level of accuracy when predicting the performance of the THAWT device and is incapable of simulating the change in performance with a fixed offset pitch. However, the model achieves good fidelity when simulating the change in performance with variations in blockage ratio and Froude number.

The main deficiencies in the M-BE model, which can be identified from comparisons with experimental results are:

- An inability to model the two-dimensional nature of the flow field, especially with respect to the downstream half of the device.
- Poor prediction of the hydrofoil characteristics, especially the dynamic stall simulation of the turbine blades, which affects the prediction of the device performance at low tip speed ratios.

Whilst the prediction of the hydrofoil characteristics can be improved, the limitation of the one-dimensional momentum model does not allow for the simulation of even simple two-dimensional flow fields. With this severe hindrance it is felt that a reasonable amount of time spent improving the model will not achieve a significant improvement in the prediction of the performance of a relatively high solidity device. An improved method of modelling the flow field is therefore required, with a greater sophistication than a simple momentum technique.

Chapter 7

Quasi-steady Navier-Stokes Blade Element model

One of the main objectives of this thesis is to develop a numerical model of the THAWT device, which is capable of predicting the power output and blade forces with a sufficient degree of fidelity and accuracy.

As demonstrated in Chapter 6, combining Linear Momentum Actuator Disc Theory for Open Channel Flow (LMADT-OCF) with basic blade element theory results in an over-prediction of the device performance by a mean factor of 1.82, when compared to experimental data. The main deficiencies in the Momentum Blade Element model (M-BE), which have been identified from comparisons with experimental results are:

- An inability to model the two dimensional nature of the flow field, especially with respect to the downstream half of the device.
- Poor prediction of the hydrofoil characteristics and especially the simulation of dynamic stall of the turbine blades, which affects the prediction of the device performance at low tip speed ratios.

In order to improve the model fidelity and accuracy of prediction, a numerical model has been adopted, based on the undergraduate masters project work of Swidenbank (2009) (see Chapter 2). Swidenbank demonstrated that the accuracy of performance prediction for the THAWT device is significantly improved, as shown in Figure 2.33, by solving the two-dimensional incompressible Navier-Stokes equations to model the flow field around the device.

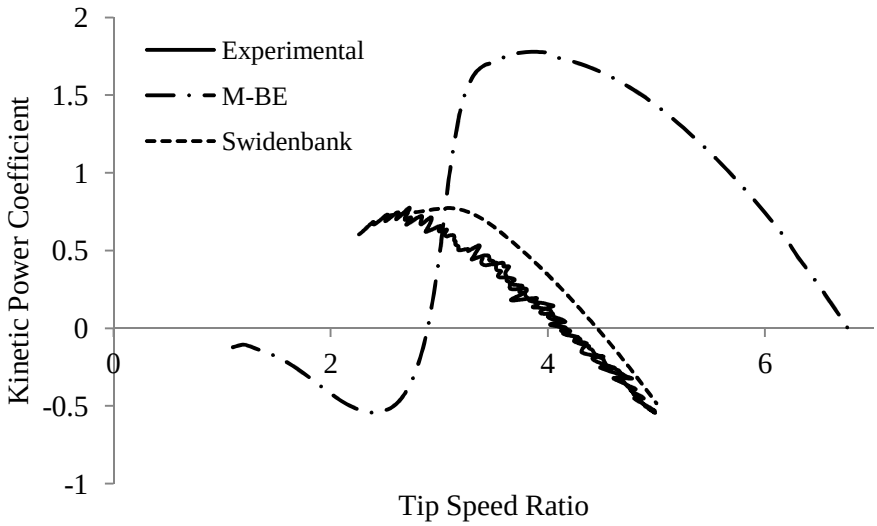

Figure 7.1 - Comparison of predicted kinetic efficiency for the 1/20th scale turbine at a Froude number of 0.17 and a blockage ratio of 0.5, based on data in (Swidenbank, 2009)

This technique models the THAWT device as an actuator cylinder, as shown in Figure 7.2, where the forces produced by the blades are calculated using blade element theory, in a similar fashion to the model developed by Antheaume (2008).

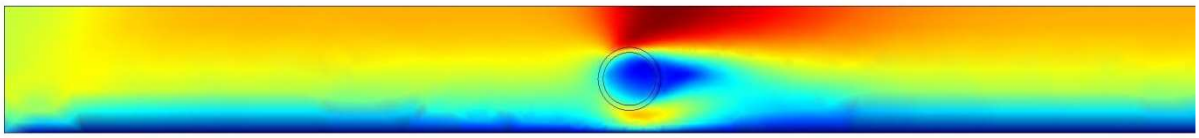

Figure 7.2 – Surface plot of the velocity field in a NS-BE model (Swidenbank, 2009)

The improved fidelity and accuracy of prediction in power, when compared to the experimental results of Chapter 5, suggests that the simulation of the flow hydrodynamics and blade forces are also likely to be significantly improved. However, the poor robustness of the steady state solver in the Swidenbank model means that it cannot be easily applied to devices of varying configuration and scale, making it unsuitable for exploring various turbine configurations and flow parameters. In order to solve this problem it was decided to develop an improved Navier-Stokes blade element model (NS-BE), based on the work by Swidenbank, with a focus on achieving an accurate solution for a range of flow conditions and turbine configurations.

A hydrostatic assumption of pressure variation in the flow is used to simulate the deformation of the free surface and to create the NS-BE-FS model. This model allows the effect of the free surface deformation on the performance of the device to be explored and indicates to what extent the increased solution time of such a method is necessary.

Finally, a set of equations are defined in order to approximate the change in performance and blade force when a truss configured device is simulated.

The models described in this section are intended to model the performance of the THAWT device in idealised conditions that were experienced by the experimental device of Chapter 5. As such they do not include complicating factors such as blade end effects or any other three dimensional effects. It should also be noted that these models therefore do not account for flow phenomena which are likely to be experienced by a full scale device, such as breaking waves, gusting flow or device end effects.

7.1. Methodology

7.1.1. COMSOL Multiphysics - Navier-Stokes partial differential equation solver

In a continuation of the work performed by Swidenbank, the application chosen to create the NS-BE model is the fluid dynamics module of the COMSOL Multiphysics package. While being relatively simple, this commercial software package offers an improved method of flow field simulation over the M-BE technique, without the extensive time investment required by more comprehensive CFD applications. The fluid dynamics module of COMSOL Multiphysics solves the incompressible form of the Navier-Stokes equations (see equations 7.1 and 7.2) using the Galerkin finite element method (Zienkiewicz *et al.*, 2005). The Galerkin method solves the Navier-Stokes equations using trial functions for the variables in question and minimises the weighted residual error.

$$\rho \frac{\partial \mathbf{u}}{\partial t} - \nabla \cdot \left[\mu\left(\nabla \mathbf{u} + (\nabla \mathbf{u})^{\mathrm{T}}\right)\right] + \rho(\mathbf{u} \cdot \nabla)\mathbf{u} + \nabla p = \mathbf{F} \qquad 7.1$$

$$\nabla \cdot \mathbf{u} = 0 \qquad 7.2$$

where **u** is the flow velocity vector, p is the pressure in the element, ρ is the fluid density and **F** is the vector of body force acting on the element. 'Linear' or 'Quadratic' elements can be selected, which use trial functions of either linear or quadratic order respectively, in the variable approximations of the N-S equations.

7.1.2. Choice of NS-BE solver technique

Swidenbank selected a "stationary" solver in order to simplify the post processing of results, which converges to a solution in which there are no time dependent perturbations. It was assumed that by using a time averaged static representation of the turbine and by

damping out any unsteady eddies and vortices using a large amount of isotropic diffusion (explained further in section 7.1.3), that a steady state solution would achieve an accurate prediction of the device performance.

Despite the heavy use of isotropic diffusion, the requirement for the problem to reach a steady solution caused the model to lack robustness, which rendered the model inflexible, due to the required fine tuning of the flow and turbine parameters to achieve convergence. Simulation of hydrofoil stall was not possible due to the relatively fast change in lift force around the cylinder circumference, close to stall, causing high shear and shed vortices, so that a steady state solution could not be reached. It was necessary to spread the force applied by the actuator cylinder over a large area so that the thickness of the cylinder was significantly larger than that of the blades, resulting in a greater field of influence than that which would be experienced in practice.

It was decided for the NS-BE model, that a time dependent solver would be implemented to overcome the restrictive nature of the steady state solver and to allow a more stable convergence on a steady or non-steady solution. The IDA solver, a time dependant differential-algebraic equation (DAE) solver with both direct and preconditioned Krylov subspace methods for the linear systems (DASPK) (Hindmarsh *et al.*, 2005), has been chosen to solve the finite element discretisation of the N-S equation. The IDA solver uses an implicit time-stepping scheme and includes a Newton solver to solve the resulting nonlinear system of equations. This solver was chosen over the alternative methods due to a good robustness and applicability to a wide range of problems, as suggested by software documentation (COMSOL, 2008).

The UMFPACK (Unsymmetric MultiFrontal method) (Davis, 2004) direct solver was chosen over the alternative direct and iterative methods to solve the linear system, also due to robustness.

7.1.3. Solution stabilisation

When using the Galerkin finite element method, numerical oscillations occur due to the convective terms dominating over the diffusive terms and make the solution inherently unstable (Zienkiewicz *et al.*, 2005). COMSOL uses stabilisation techniques to reduce the numerical oscillations and allow convergence to a unique solution. This is achieved by

adding artificial viscosity μ_{art} to the diffusion term of the N-S equation, as shown in equation 7.3.

$$\rho\frac{\delta\mathbf{u}}{\delta t} - \nabla\cdot\left[(\mu+\mu_{art})\left(\nabla\mathbf{u}+(\nabla\mathbf{u})^{\mathrm{T}}\right)\right] + \rho(\mathbf{u}.\nabla\mathbf{u}) + \nabla p = \mathbf{F} \qquad 7.3$$

In COMSOL Multiphysics there are three in-built techniques for modifying the added artificial diffusion term; an isotropic diffusion method, a Galerkin least-squares (GLS) method and a streamwise-upwind Petrov-Galerkin (SUPG) method, supplemented by crosswind diffusion. Whilst more sophisticated than an SUPG technique, trial simulations of the NS-BE model using GLS rarely result in the convergence to a stable solution, and has therefore been discarded.

Added isotropic diffusion is controlled using the tuning parameter δ_{id}, which is incorporated into the added viscosity term, given in equation 7.4, in which h represents the mesh element size.

$$\mu_{art} = \delta_{id} h\|\mathbf{u}\| \qquad 7.4$$

By increasing the diffusion term of the N-S equation the introduction of isotropic diffusion will reduce the dominance of the convection term and reduce spurious oscillations.

The SUPG method varies the weighting functions applied to the N-S equations to change the influence of diffusion in the direction of the velocity vector, and resulting discontinuities normal to the stream-wise direction are smoothed using the crosswind method (John and Knobloch, 2007). This technique is more sophisticated than the isotropic diffusion method and allows the convergence of a solution using a significantly reduced amount of added diffusion. The amount of crosswind diffusion that is introduced is controlled using a tuning parameter C_k, the range for which should be $0 < C_k < 0.5$ for low Mach number incompressible flows (COMSOL, 2008). However, the exact equations used to implement this technique in COMSOL are not documented and the influence of C_k must therefore be explored for each problem.

Swidenbank chose to use only isotropic diffusion as the stabilisation technique to remove oscillations in the solution, as well as to damp any time varying eddies and vortices. Due to the poor stability of the steady state solver, the amount of viscosity required to achieve convergence was unrealistic of the actual flow conditions in the flume. Swidenbank recognised that increasing the amount of stabilising artificial viscosity resulted in an increase in the power produced by the turbine. This was attributed to additional inertia transferred

from the bypass to the flow immediately downstream of the device, where in practice the turbine wake has a low velocity. The value chosen by Swidenbank for the tuning parameter was 0.2, but the coarse meshes used (see Figure 7.20) also contributed to an increase in effective viscosity due to the element size variable in the added viscosity factor of equation 7.4.

7.1.4. Backward facing step model

In order to understand the dependency of the NS-BE model on artificial diffusion, a backward facing step problem has been used to demonstrate how the various techniques and stabilisation parameters affect the solution. In a backward facing step problem, a discontinuity in the channel width causes a separation of the flow and an area of recirculation, as shown in Figure 7.3. The length from the discontinuity to the reattachment point is dependent on the Reynolds number, step height and momentum thickness (Etheridge and Kemp, 1978). As the Reynolds number of the flow is increased additional separations and recirculations have been shown to occur downstream of the primary separation point (Armaly *et al.*, 1983).

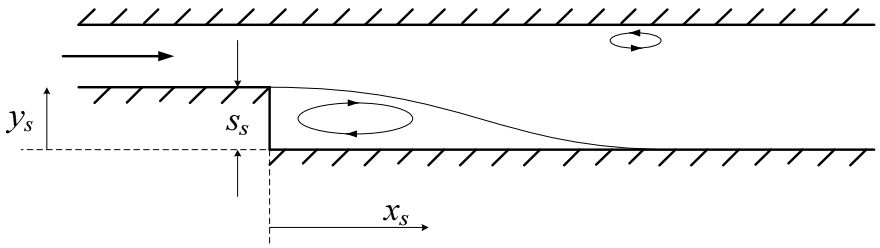

Figure 7.3 - Illustration of typical backward facing step problem, including areas of recirculation

With no turbulence model (see section 7.1.6) it is assumed that the model is unable to resolve turbulence of a scale smaller than the elements used, validation using the backward facing step exercise must be performed using low Reynolds number laminar flows. Armaly et al. (1983) used laser Doppler imaging to measure the development of the flow downstream of a backward facing step in an air tunnel with an expansion ratio of 1.94, over a range of $100 < Re < 7000$, where the characteristic length for the Reynolds number is the inlet width. Comparisons between experimental results and numerical predictions by Armaly demonstrated that for flows of a Reynolds number greater than roughly 400 the nature of the flow becomes three dimensional, when multiple circulation zones occur, so that a two dimensional numerical model is unable to predict the separation and reattachment lengths. Using the fluid mechanics module of COMSOL Multiphysics, a Navier-Stokes model of the

apparatus has been created with matching dimensions and boundary conditions to those of the experiments performed by Armaly (see Figure 7.4).

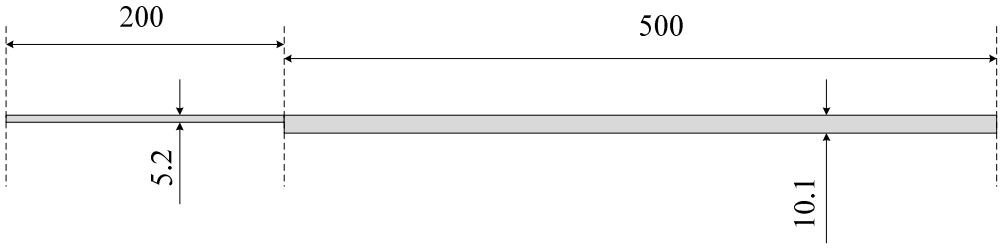

Figure 7.4 - Dimensions of backward facing step setup in (Armaly et al., 1983) dimensions in mm

A mesh has been used in which the element density is increased at the non-slip boundaries and at the step discontinuity, so that the resolution of the steep velocity gradients is maximised, as shown in Figure 7.5.

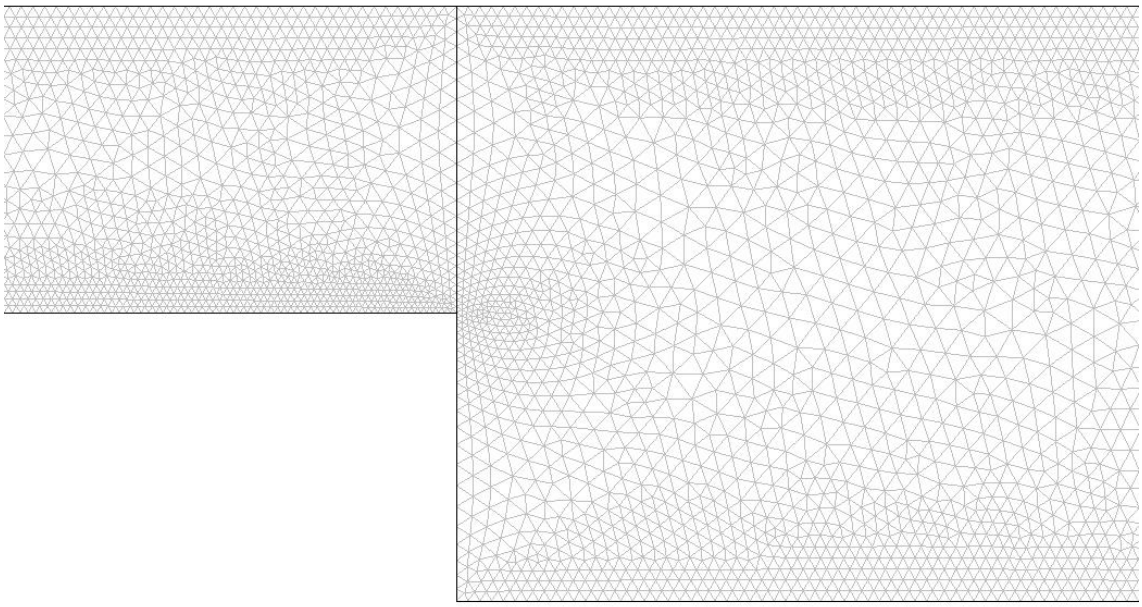

Figure 7.5 – Mesh density used for the back step problem

A grid convergence test explores the solution accuracy with varied grid refinement, element order and stabilisation techniques. Figure 7.6 demonstrates that using quadratic order elements and SUPG stabilisation, convergence is rapid and allows for a greater variation in element scale factor without significantly reducing the accuracy of the simulation, when compared to linear elements or isotropic diffusion.

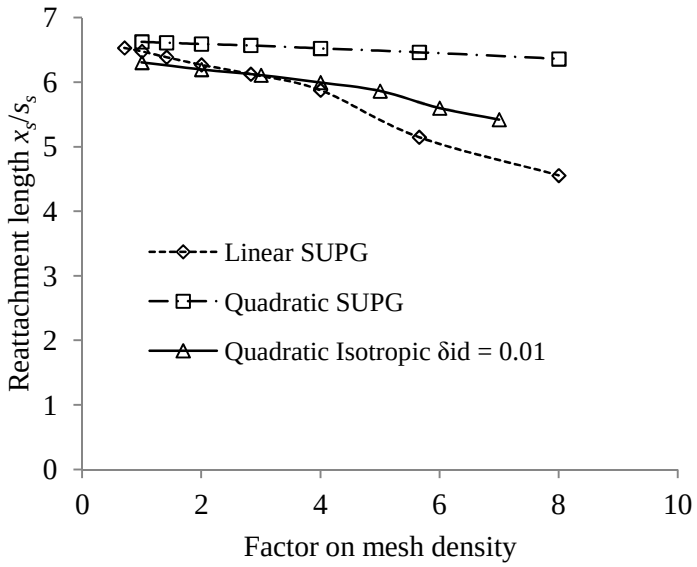

Figure 7.6 - Predictions of reattachment length at Re = 100 for linear and quadratic elements using either crosswind or isotropic artificial diffusion over a range of grid mesh spacing

Figure 7.7 demonstrates that using quadratic order elements and SUPG stabilisation the numerical backward facing step model achieves good agreement with the numerical predictions and experimental results of Armaly et al.

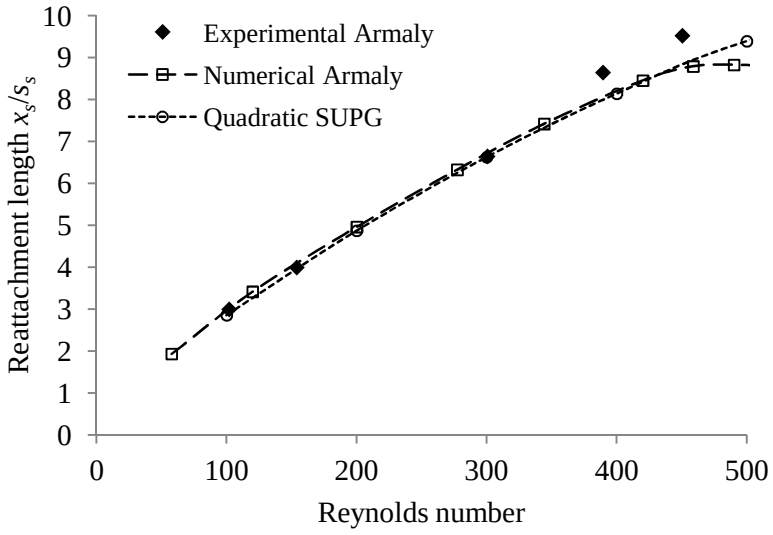

Figure 7.7 - Reattachment lengths over a range of Reynolds number for numerical and experimental data from Armaly et al. (1983) and numerical calculations in COMSOL using SUPG diffusion

As shown in Figure 7.8, variations in the value of the isotropic diffusion parameter δ_{id} have a significant effect on the accuracy of the solution. This is likely to occur because increasing the isotropic diffusion parameter simply increases the flow viscosity and effectively decreases the Reynolds number. In contrast, variation of the crosswind diffusion constant C_k has little to no effect on the solution, possibly due to only minor application of streamwise upwinding at such a low Reynolds number.

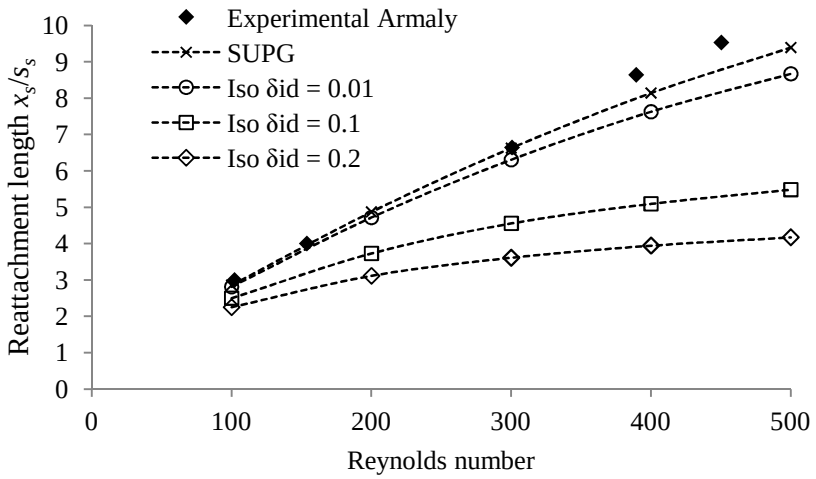

Figure 7.8 - Comparison of reattachment lengths between experimental data from Armaly et al. (1983) and numerical calculations in COMSOL using a range of isotropic diffusion tuning parameters

Figure 7.9 demonstrates that using quadratic order elements with SUPG stabilisation, the velocity profiles predicted using the numerical model closely match those recorded by Armaly *et al*. This suggests that the use of this technique offers greater accuracy than isotropic diffusion in simulations of the THAWT device.

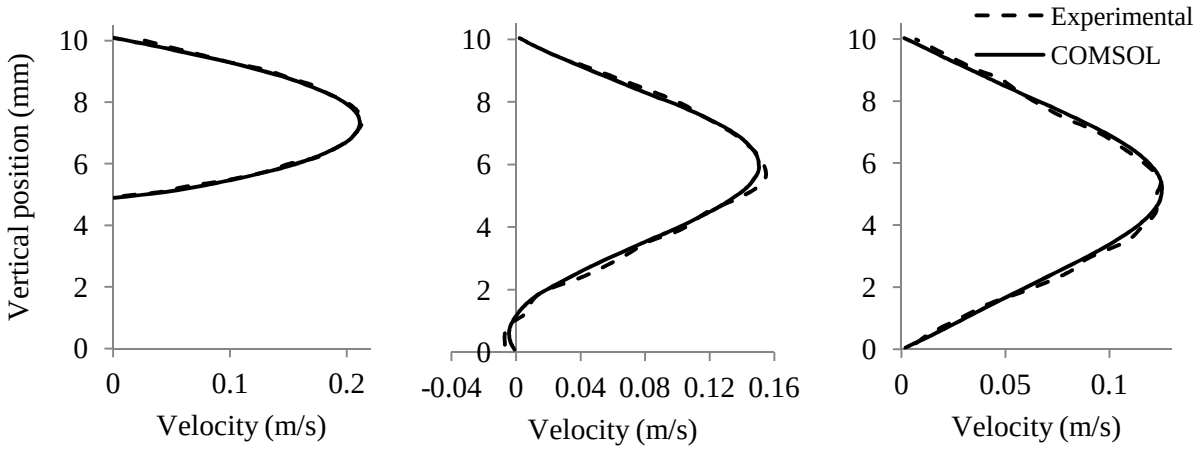

(a) $x_s/s_s = 0$ *(b) $x_s/s_s = 2.55$* *(c) $x_s/s_s = 4.18$*

Figure 7.9 - Comparison of reattachment lengths at Re = 100 and various distances from the step between experimental results recorded by Armaly et al. (1983) and predicted using COMSOL using SUPG diffusion

Figure 7.10 shows that increasing the isotropic diffusion parameter δ_{id} results in an increase in the error of prediction of the maximum velocity in the velocity profile at the step discontinuity. Both Figure 7.10 and Figure 7.8 suggest that the level of added isotropic diffusion in the simulations by Swidenbank is likely to have had a significant effect on the effective Reynolds number in the flow.

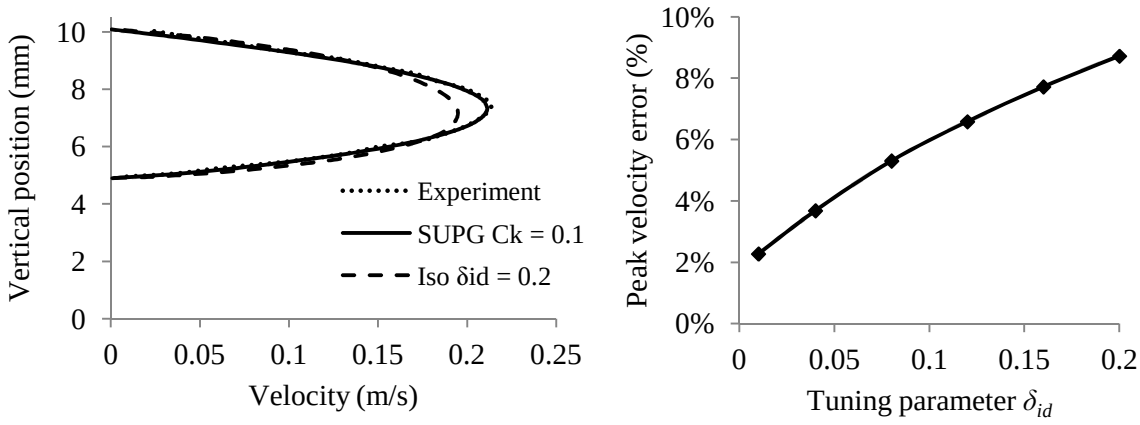

(a) Comparison of velocity profiles *(b) Error in peak velocity prediction*

Figure 7.10 - Demonstration of the increase in error of velocity profile prediction by increasing δ_{id} when compared to experimental results by Armaly et al. (1983) at x_s/s_s = 0 and Re = 100

7.1.5. Stabilisation applied to NS-BE model

Despite accurate results and no variation with a varied C_k for the backward facing step exercise, initial tests of the NS-BE model demonstrated that variations in C_k affect the prediction of the performance of the THAWT device. In a higher Reynolds number flow, where the convective terms dominate over the diffusive terms and there are greater discontinuities in the crosswind direction generated by upwinding, the amount of diffusion added in the direction normal to the flow streamlines should be calibrated and minimised for a given geometry and mesh.

In the case of the NS-BE simulation of the THAWT experiments, SUPG stabilisation with crosswind diffusion alone does not add sufficient viscosity to stabilise the solver. A combination of SUPG and isotropic diffusion is necessary in order to consistently reach a solution, for the varied turbine and flow configurations. Of the two techniques, isotropic diffusion appears to introduce more error to the solution than increased crosswind diffusion, and so the focus of the balance between these two techniques is to minimise the isotropic component, while maintaining a stable solution and a low overall additional viscosity.

The chosen artificial diffusion parameters of C_k = 0.05 and δ_{id} = 0.003, result in an approximated over-prediction of 1% on power, but allow the convergence of a stable solution for NS-BE simulations of the experimental tests described in Chapter 5.

7.1.6. Turbulence modelling

As noted in section 2.4.2 modelling turbulence is an open field in the numerical simulation community, with no single technique established as the most suitable. There is no turbulence

model applied to the simulation of the NS-BE model, due to the simplicity of the COMSOL MultiPhysics software. Recent research suggests that the use of numerical stabilisation alone can substitute for the addition of explicit viscosity due to modelled turbulence of a scale smaller than the elements used (Guasch and Codina, 2007). However, for the NS-BE model it has been assumed that the scale of turbulence which can be resolved is of the scale of the elements. In the absence of additional explicit viscosity from a turbulence model, the accuracy of the model will depend to what degree the scales of significant turbulence have been simulated. By using the actuator cylinder approach, the necessity of modelling the significant small scale turbulence in the blade boundary layer has been removed. However, the simulation of the flume velocity profile and the wake development is likely to be inaccurate. It has been assumed that these inaccuracies do not result in significant errors and do not dominate the solution.

7.1.7. Application of the actuator cylinder forces

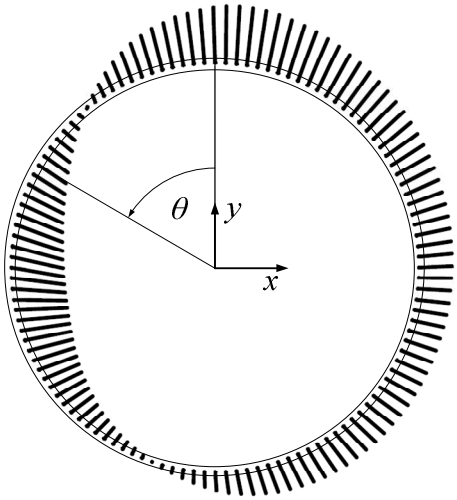

Figure 7.11 – An example of blade force vectors distributed through the actuator cylinder

The actuator cylinder provides a time averaged representation of the THAWT device. The force applied by a blade at a specific point on the actuator cylinder is calculated using basic aerofoil theory, and is divided by the area of the cylinder and multiplied by the number of blades, as shown in equations 7.5 and 7.6 and illustrated in Figure 7.11. This is intended to achieve the application of the time averaged force of each location on the actuator cylinder.

$$F_L = \frac{{}^1\!/_2\,\rho c {V_R}^2 C_L n}{2\pi r t_c} \qquad 7.5$$

$$F_D = \frac{{}^1\!/_2\,\rho c {V_R}^2 C_D n}{2\pi r t_c} \qquad 7.6$$

With both cross-flow and stream-wise components of velocity, the calculation of the resultant velocity and angle of attack differ from the previous M-BE model, as shown in equations 7.7 and 7.8.

$$V_R = \sqrt{(u + \omega y)^2 + (v - \omega x)^2} \tag{7.7}$$

$$\alpha = \tan^{-1}\left(\frac{xu + yv}{xv - yu - \omega r^2}\right) \tag{7.8}$$

where ω is the angular velocity of the blade.

The values of resultant velocity and angle of attack are used to approximate the lift and drag coefficients, as described in section 7.1.8. The forces in the stream-wise and cross-flow directions are calculated using equations 7.9 and 7.10.

$$F_x = \frac{F_L(v - \omega x) + F_D(u + \omega y)}{V_R} \tag{7.9}$$

$$F_y = \frac{F_D(v - \omega x) - F_L(u + \omega y)}{V_R} \tag{7.10}$$

A gravitational force of ρg is applied to all elements, which becomes physically significant when later modelling free surface flows.

The power output is calculated in a similar fashion to the Swidenbank model, in which the torque applied within the actuator cylinder is multiplied by the angular velocity, as shown in equation 7.11.

$$P = \int_A \omega\left(xF_y - yF_x\right) dA \tag{7.11}$$

While this method largely ignores the effect of downstream blades interacting with the vortices generated by upstream blades (Fujisawa and Shibuya, 2001). The severe reduction in velocity through the upstream half of the device is anticipated to reduce the Reynolds number of the flow significantly, so that viscous forces dominate over inertial forces and eddies and vortices are dissipated. This assumption is reinforced by observations of bubbles passing through the rotor during PIV imaging of the Newcastle experiments (Shi, 2008).

7.1.8. Lift and drag data

It was noted that the performance of the THAWT device could be predicted with greater accuracy by improving the approximation of the hydrofoil lift and drag characteristics. In order to improve the accuracy with which the lift and drag characteristics of the hydrofoils are predicted, it is clear that the complex flow phenomena must be better approximated.

7.1.9. Reynolds number variation

Over the full range of the Newcastle experiments, the Reynolds number experienced by a non-stalled blade is likely to vary between roughly $5.3 \times 10^4 < \mathrm{Re} < 2.7 \times 10^5$. As illustrated in Figure 7.12, this variation in Reynolds number is likely to induce significantly different hydrofoil characteristics and that it is necessary to account for the variations in lift and drag with Reynolds number, when predicting the device performance. It was therefore decided to interpolate the appropriate lift and drag curves based on published aerofoil data by Sheldahl and Klimas (1981) in a similar fashion to the M-BE model (see section 6.1).

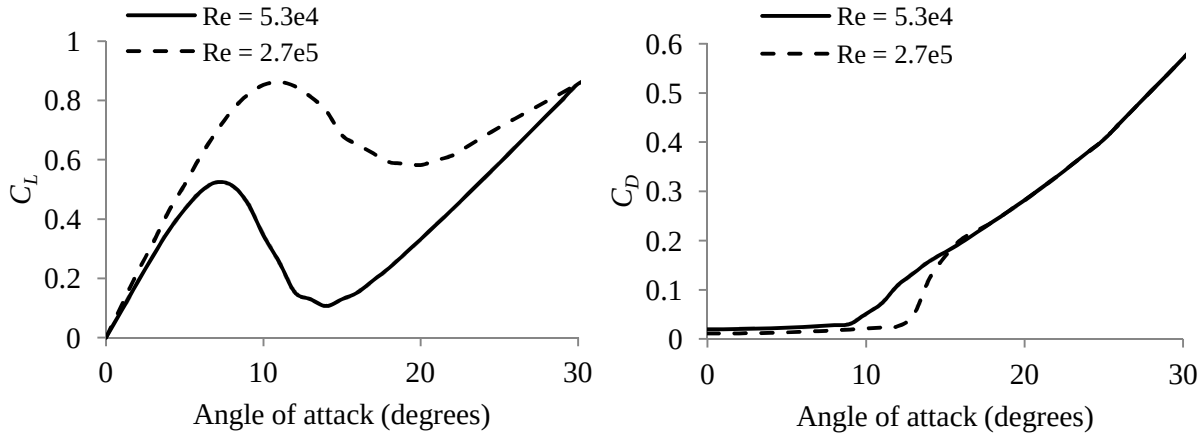

(a) Comparison of lift coefficient *(b) Comparison of drag coefficient*

Figure 7.12 - Comparison of aerofoil characteristics interpolated from NACA 0018 tables produced by Sheldahl and Klimas (1981)

7.1.10. Conformal mapping

Research by Migliore et al. (1980) suggests that a straight chorded blade in a curvilinear flow will experience a virtual incidence, which will increase the effective angle of attack of the blade. Resultant velocity components, predicted using conformal mapping, suggest that a straight chorded blade in a linear flow and a blade 'wrapped' around the circumference of the turbine pitch circle in a curvilinear flow have similar profiles. It is therefore assumed that published aerofoil lift and drag characteristics will offer a good approximation of the performance of the blades of the THAWT device.

7.1.11. Dynamic stall

The hydrofoils of the THAWT device experience an oscillating angle of attack, which is likely to induce the effects of dynamic stall, as described in section 2.5.2 and illustrated in Figure 7.13.

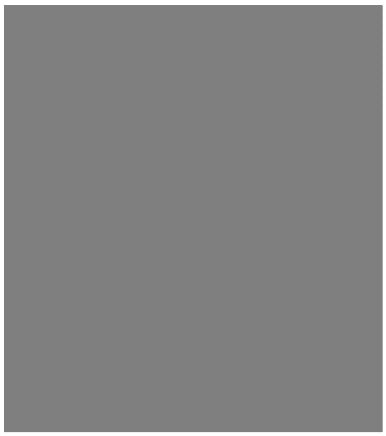

Figure 7.13 - Example lift curve of a NACA0012 aerofoil during dynamic stall at a reduced frequency of k = 0.26 (McCroskey, 1981) permission to reproduce figure online not granted

While numerical models have been developed which are able to predict the effect of dynamic stall of aerofoils with a relatively high degree of accuracy (Ekaterinaris and Platzer, 1998, Tchon and Paraschivoiu, 1994), the time required to simulate the complex flow phenomena make these methods unsuitable for integration with the NS-BE model.

There are two main categories of technique for predicting the performance of aerofoils during dynamic stall that are not based on numerical analysis; 'synthesis' and semi-empirical methods (Reddy and Kaza, 1987). However, both of these methods calculate the performance of the hydrofoil based on the current local flow and the stall history of the blade, which makes them unsuitable for application to the actuator cylinder approach of the NS-BE model. The calculation of the blade forces at a point in the actuator cylinder cannot simply refer to the conditions at a previous time-step, as would normally be done with a dynamic stall approximation, as the blades have effectively been 'smeared' throughout the area of the cylinder.

While the approximated lift and drag characteristics of a hydrofoil could be calculated prior to the NS-BE simulation and simply used as a lookup table, the range of angle of attack varies with changes in the turbine solidity, blockage, Froude number and tip speed. It has therefore been decided to approximate the effects of dynamic stall by simply extending the lift curve predicted by Sheldahl and Klimas (1981), so that no stall of the hydrofoil occurs, as shown in Figure 7.14. There have been no modifications applied to the drag curves of the hydrofoils.

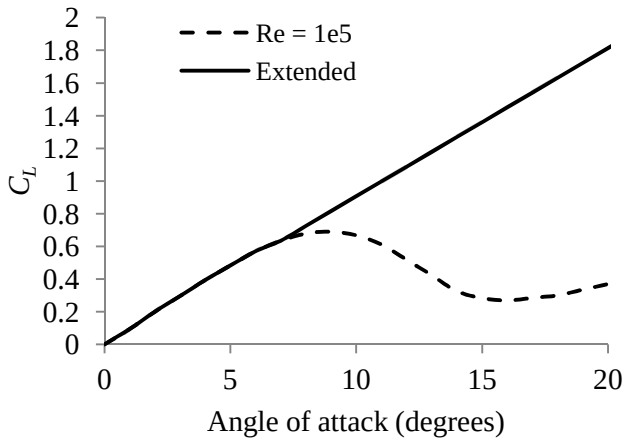

Figure 7.14 - Comparison of static lift curve with linear lift curved used in NS-BE COMSOL analysis

By ignoring the effect of stall, the power curve at tip-speed ratios lower than that at which dynamic stall is expected to occur is unlikely to be accurate, but it is hypothesised that the performance of the device at greater tip speed ratios should be representative.

It should also be noted that in the absence of stall, as the tip speed ratio is reduced, a plateau of the power curve occurs due to the increase in predicted drag. Despite the fact that this mechanism is unlikely to be accurate, it is clear that predictions of the performance of the THAWT device in the Newcastle flume are highly dependent on the inclusion of a dynamic stall approximation. Figure 7.15 shows that without the effect of extended lift the NS-BE model predicts stall of the device at a significantly greater tip speed ratio than that achieved during the Newcastle experiments.

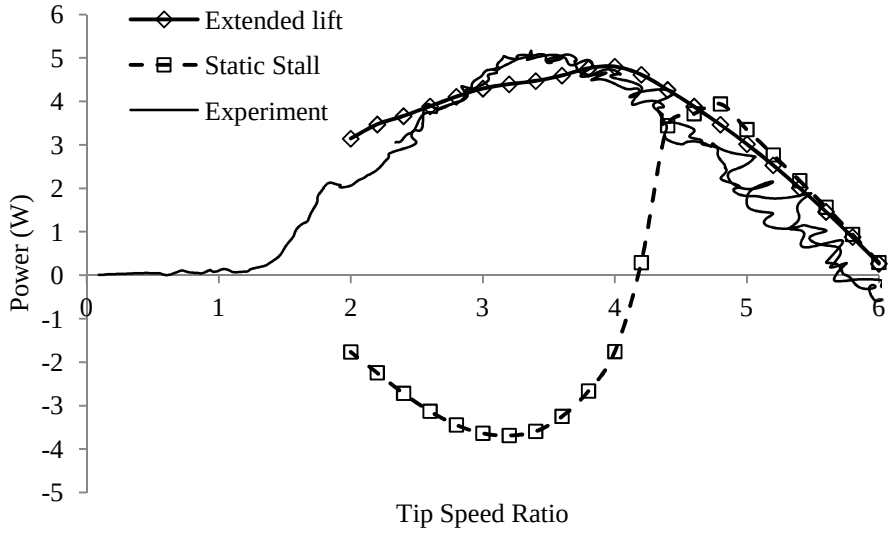

Figure 7.15 - Comparison of power curves predicted by the NS-BE model using static C_L curves and dynamic C_L curves for a three parallel-bladed device at a Froude number of 0.09 and blockage of 0.5

7.1.12. Free surface deformation (NS-BE-FS)

The mechanism by which energy is extracted from an open channel flow is a reduction in the total head. Due to a constant pressure at the free surface, the change in the amount of total head across a fixed width domain can be expressed using equation 7.12, if the flow is steady at the measurement points.

$$\Delta H = \Delta\left(h + \frac{u^2}{2g}\right) \qquad 7.12$$

The experiments at Newcastle University were performed in a sub-critical open channel flow, where a reduction in total head results in a decrease in depth and an increase in flow velocity. The fixed domain of the NS-BE model does not allow for variations in depth, and therefore effectively simulates a flow in a fixed diameter tube, where the extraction of energy results in a reduction in pressure (Massey and Ward-Smith, 1998). It is possible to calculate the corresponding open channel depth change from the pressure drop across the rigid domain by equating the thrust produced by the device in the two regimes. However, the velocity field experienced by the device is not identical in these two scenarios, as variations in the depth of an open channel flow cause an acceleration of the fluid, which tends to improve the performance of the turbine.

In order to understand how significant this effect is it is necessary to simulate a domain of varying depth with a free surface of a constant pressure. Several established techniques are capable of accurately modelling free surface changes (Carrica *et al.*, 2005, Mahrenholtz and Markiewicz, 1999, Zienkiewicz *et al.*, 2005), however the majority of these techniques significantly increase the computational costs in achieving a solution. Due to the relatively simple shape of the free surface during the experiments, with no breaking waves or other complex anomalies, a surface-tracking method presents itself as a superior approach to the surface-capture method. A surface-tracking method has therefore been chosen for the NS-BE-FS model.

7.1.13. Surface-tracking methodology

Computations using the surface-tracking approach are suitable, as there is no expected air trapped in the fluid phase, and the pressure applied by the air to the liquid phase is negligible and does not vary along the channel length. However, the common application of free surface deformation involves calculating the location of the free surface, before redefining the

boundary and re-meshing for each time step. It is felt that this significant increase in computational requirements is beyond the scope of the simple numerical model.

The hydrostatic adjustment method (Zienkiewicz *et al.*, 2005) has been chosen to model the free surface deformation in the NS-BE-FS model, which is a less computationally costly approach of surface-tracking. In this method a rigid boundary model is run to an established solution, before pressure variations at the free surface are used to predict the deflection of the domain boundary, by assuming a hydrostatic pressure distribution in the fluid. This is performed on the NS-BE-FS model once the convergence criterion (see section 7.2.6) for the given boundary geometry has been met, at which point the pressure distribution at the free surface is averaged over the previous simulation period, as shown in Figure 7.16.

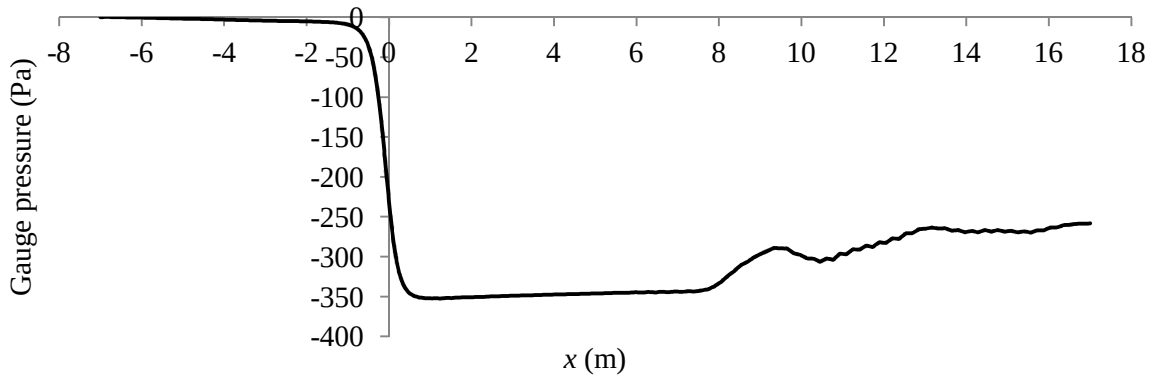

Figure 7.16 - Time averaged variation of pressure at the top of the rigid domain in the NS-BE model

By assuming that the pressure distribution in the flow above the free surface is approximately hydrostatic, as shown in Figure 7.17, the domain lid deflection at each point required to achieve zero gauge pressure is approximated using equation 7.13.

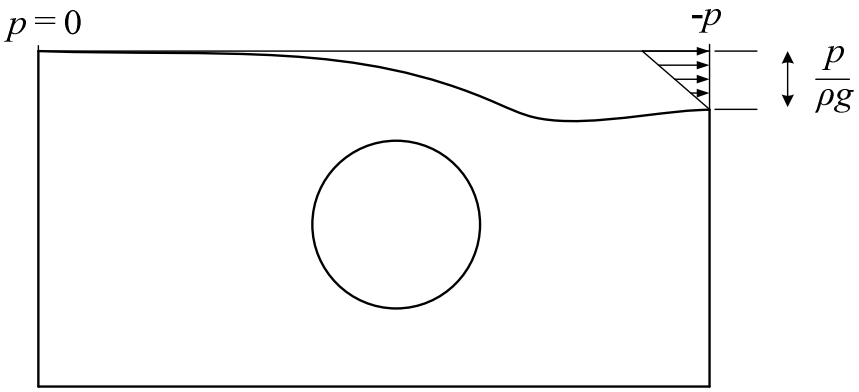

Figure 7.17 – Illustration of the method for locating the free surface based on the rigid lid pressure distribution and assuming a vertical hydrostatic pressure distribution above the free surface

$$h_{n+1} = h_n + \frac{p}{\rho g} \qquad 7.13$$

With a new free surface profile along the channel, the geometry for the domain is updated by fitting cubic Bezier curves to the shape of the free surface. The definition of a true free surface is one along which the pressure is constant and the flow at the surface is parallel to the boundary. The first iteration of free surface displacement does not meet these conditions, due to inaccuracies in the assumption of a hydrostatic pressure distribution, and a modified velocity flow field due to the change in the boundary position. However, iterating this process allows the convergence of a more accurate solution. Over a series of iterations the domain geometry is updated until the difference in free surface profile falls below a given threshold, and the solution is deemed to have converged.

7.1.14. Free surface technique validation

In order to assess the accuracy with which the NS-BE-FS is able to track the deformation of the free surface it was decided to perform a simple validation test by artificially reducing the total head of the flow using a small increase in base height, as shown in Figure 7.18.

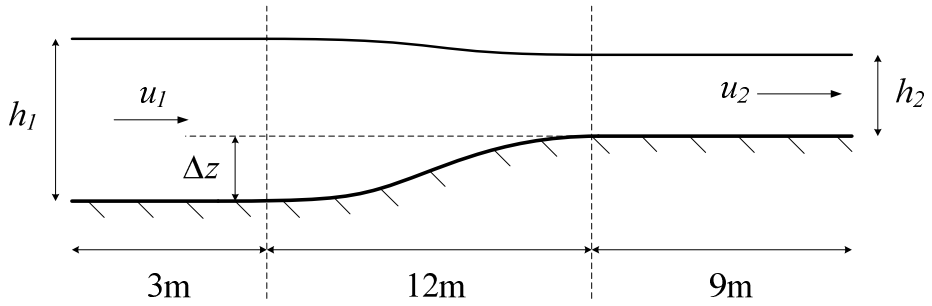

Figure 7.18 - Layout of free surface validation model created using COMSOL Multi-physics

By elevating a subcritical flow to a greater height a proportion of the total head is converted to potential energy. The reduction in total head results in an increase in velocity and decrease of the depth of the flow. The difference in the total head between the upstream and downstream boundaries should be equal to the increase in potential energy, caused by elevating the flow, as shown in equation 7.14.

$$\Delta E = \dot{m}g\Delta z = \dot{m}g\Delta H = \dot{m}g\Delta\left(h + {u^2}/{2g}\right) \qquad 7.14$$

For a given set of inlet flow conditions and for a given elevation in height, the depth of the outlet flow can be calculated using equation 7.15, by noting the conservation of mass between the upstream and downstream boundaries.

$${h_2}^3 + \left(\Delta z - h_1 - {{u_1}^2}/{2g}\right){h_2}^2 + \frac{{u_1}^2{h_1}^2}{2g} = 0 \qquad 7.15$$

The validation model has been created using the same parameters and meshing as the main domain of the NS-BE and NS-BE-FS models, differing only in the use of symmetry boundaries for both the base and free surface. By using symmetry boundaries the only significant extraction of energy from the flow is due to the increase in potential energy across the elevation. The base of the flow is elevated using a cubic Bezier curve in order to maintain a smooth domain. The model converges much more quickly than the NS-BE and NS-BE-FS models due to the lack of a turbine, and so only a few iterations of each domain geometry and sequential geometry updates are required to reach a steady state solution.

	Theory	**NS validation model**
h_1 *(m)*	1	1
u_1 *(m/s)*	0.544	0.544
z (m)	0.2	0.2
h_2 *(m)*	0.7910	0.7915
u_2 *(m/s)*	0.6878	0.6873

Table 7.1 – A sample result from the NS free surface validation model

As shown in Table 7.1 the error in the prediction of the depth change across the elevation by the NS validation model was 0.07% for both the depth of flow and velocity of flow. It is felt that this is a sufficient degree of accuracy and so it is expected that the NS-BE-FS model should accurately match the free surface elevation to the amount of total head in the simulated flow.

7.2. Turbine simulation

7.2.1. Problem geometry

The NS-BE model adopts a similar domain geometry to the Swidenbank model, but with upstream and downstream lengths extended to more realistic dimensions. The flume domain is a rectangular section, whilst the turbine is modelled using an actuator cylinder that is bounded by two circles. The average radius and thickness of the actuator cylinder are, r = 0.25 m and t_c = 0.012 m, the same as the hydrofoils used in the Newcastle experiments. The distance of the centre of the actuator cylinder from the base of the flow region is 0.425 m, to match the geometry of the devices tested in Newcastle. The height of the main rectangular region can be altered to allow the model to simulate the experimental flows of a varied blockage ratio, and the length of the domain can be varied in an effort to maximise the downstream height recovery of the flow (see Figure 7.19).

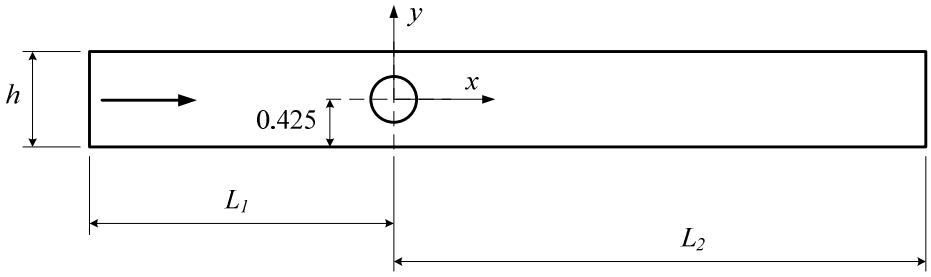

Figure 7.19 - Geometry of the NS-BE model

7.2.2. Boundary conditions

The channel floor and channel lid boundary conditions used for the NS-BE model are the same as those in the Swidenbank model, with non-slip and symmetry boundaries respectively.

Ideally the outlet conditions for the NS-BE model would be representative of the Newcastle apparatus so that the measured experimental depth change could also be used to validate the numerical model. However, this cannot be achieved due to several complications. As described in Chapter 4 the close proximity of the wave probe downstream of the device resulted in measurements of depth prior to the full mixing and recovery of the flow. When combined with the unknown turbulence intensity of the flow in the Newcastle flume it would be very difficult to accurately simulate the wake development that occurred during the experiments.

By using a time dependent solver and a low amount of added viscosity (see section 7.1.5) the NS-BE model requires a very long downstream section for the flow to mix fully and to reach a hydrostatic pressure condition. The length of domain downstream of the device that is required, whilst maintaining a fine enough grid, is greater than that which can be achieved using the available computing resources. The turbulence that occurred in the experimental flume may contribute by reducing the mixing length of the wake to more realistic values (MacLeod *et al.*, 2002), but this cannot be simulated in the current simple numerical model.

The positioning of the outlet boundary is further complicated by the three dimensional nature of the flume exit at the Newcastle flume. At a distance of 4.2 m downstream from the device the flow separator ends and the channel opens up from 0.96 m to a 1.8 m wide section, which is “beached” to prevent the reflection of waves. The flow exits through a grill at the base of the outlet region and is re-circulated to the upstream section. It is not possible to model the three-dimensional flow effects in this outlet region using the two-dimensional NS-BE model.

Due to these complications it has been accepted that the flow will not achieve full mixing before the outlet. It has been assumed that despite a non-uniform velocity at the outlet of the fluid domain, variations in pressure due to the fluctuations in velocity are small compared to the hydrostatic body force and so the pressure can be approximated using a hydrostatic distribution. This is imposed using a normal stress distribution at the outlet using equation 7.16, which is a standard option of the COMSOL package.

$$\left[-p\mathbf{I} + \mu\left(\nabla\mathbf{u} + (\nabla\mathbf{u})^{\mathrm{T}}\right)\right]\mathbf{n} = -F_0\mathbf{n} \qquad 7.16$$

where **n** is the vector normal to the boundary.

Equation 7.16 implies that the total stress in the tangential direction is dictated by F_0. This boundary condition implicitly sets a constraint on the pressure, which for two-dimensional flows can be described using equation 7.17.

$$p = 2\mu\frac{\delta u_n}{\delta n} + F_0 \qquad 7.17$$

If $\delta u_n/\delta n$ is small then equation 7.17 can be interpreted as $p \approx F_0$. In order to achieve a hydrostatic body force at the outlet F_0 is given a value, as described in equation 7.18.

$$F_0 = \rho g h - \rho g y \qquad 7.18$$

where h is the flow depth and y is the distance from the base of the flume.

The distance of the outlet boundary from the device, L_2 = 17 m, was large enough to maintain a consistent convergence of the model, and to prevent destabilisation due to large vortices reaching the hydrostatic outlet boundary.

In a similar fashion to the outlet, the inlet boundary condition is also complicated due to three-dimensional constraints in the Newcastle flume. On entering the flume the flow passes underneath a set of wave paddles before being narrowed by the flow contraction. It is not possible to model these three-dimensional effects using the two-dimensional NS-BE model, and it was therefore decided to simply use a uniform inlet flow with a velocity equal to the volume averaged flow velocity, and to allow the velocity profile to develop with L_1 = 7 m, in a similar fashion to the experimental setup.

7.2.3. Calculation of depth change

Linear Momentum Actuator Disc Theory for Open Channel Flow (LMADT-OCF) (Houlsby *et al.*, 2008a) suggests that, for a given Froude number flow and blockage ratio, the thrust produced by the device will dictate the depth change across the domain. The validation

of depth change prediction by the NS-BE model is therefore an important process, and would suggest that the thrust produced by the device and the energy extracted from the flow are being modelled correctly.

With an inability to simulate the length of domain necessary to achieve full mixing of the turbine wake, LMADT-OCF has been chosen to predict the fully mixed depth change for each given set of flow parameters and predicted thrust. This technique will allow comparisons with the experimental results of lower Froude number flows, where measurements of depth change were taken after substantial flow mixing had occurred, as described in Chapter 5.

7.2.4. Meshing

Grid convergence analyses indicate that significant improvements in accuracy can be achieved using a finer mesh than the relatively coarse mesh used by Swidenbank, shown in Figure 7.20.

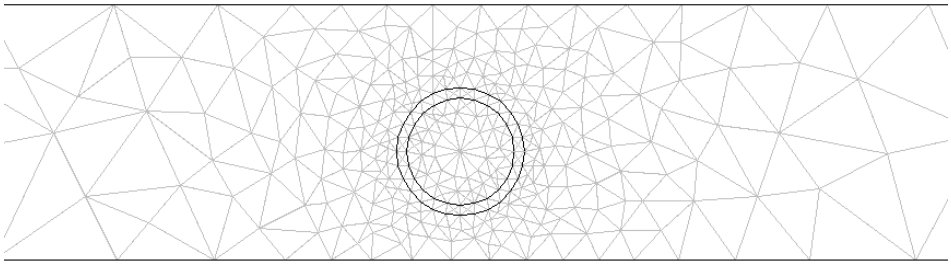

Figure 7.20 - An unstructured mesh used by Swidenbank (2009)

An increased element density has been used in the domain of the turbine, so that the deflection of the flow due to the applied turbine forces is modelled accurately, and along the non-slip wall at the base of the channel, so that the energy dissipation in the high shear boundary layer is more accurately simulated. In order to establish whether such a mesh is suitable a simple grid convergence analysis has been performed, in which the basic mesh is defined in Table 7.2, and shown in Figure 7.21.

	Maximum element size (m)	Maximum element growth rate
Sub-domain 1	0.2	1.1
Sub-domain 2	0.012	N/a
Sub-domain 3	0.1	1.1
Non-slip boundary	0.1	N/a

Table 7.2 – Definition of basic mesh used for grid convergence analysis

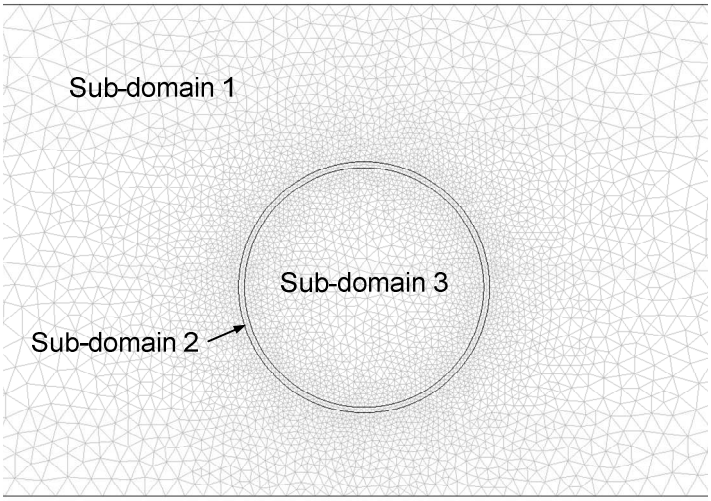

Figure 7.21 - The element mesh used in the NS-BE model

Figure 7.22 shows the change in predicted power as the size of elements used is varied from that listed in Table 7.2, by an element scale factor.

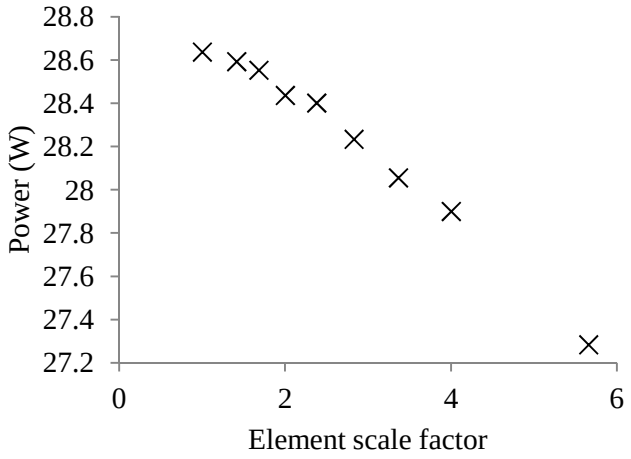

Figure 7.22 – Plot of Power vs. Element scale factor by the NS-BE model for the six parallel-bladed device at a flow speed of 0.54m/s and a blockage of 0.5

Based on an estimate of the expected value at zero grid spacing, the order of convergence can be calculated from the slope of a plot of $\log_{10}(E)$ against $\log_{10}(h)$, where E is the prediction error and h is the element scale factor (Roache, 1998), as shown in Figure 7.23. The expected value with zero grid spacing can be calculated using the Richardson extrapolation technique (Roache, 1998), from which new estimates of the prediction error can be calculated. Iterating this process results in an expected power at zero grid spacing of 28.71W and indicates that the mesh spacing with an element scale factor of 1 achieves a solution with an error of 0.24% on the prediction of power. The order of convergence of this scheme is 1.74.

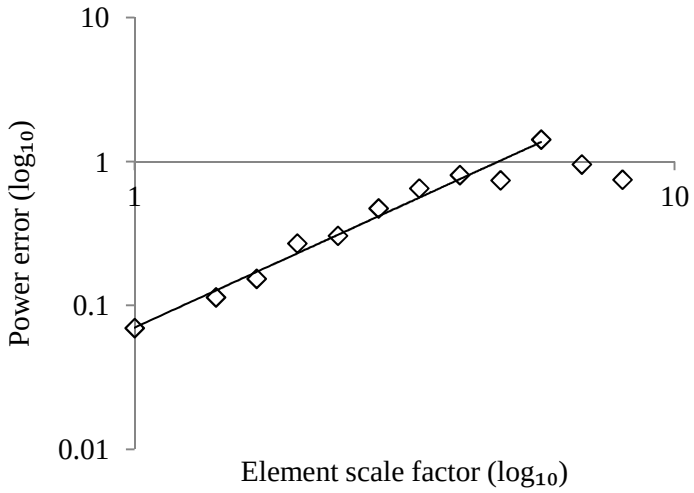

Figure 7.23 – Log-Log plot of error in power prediction vs. element scale factor by the NS-BE model for the six parallel-bladed device at a flow speed of 0.54m/s and a blockage of 0.5

7.2.5. Effect of low diffusion

With little added viscosity, when compared to the Swidenbank model, vortices and eddies are shed in the wake of the device and make the solution time varying. Figure 7.24 shows the mechanism by which vortices are created in the wake, which was also observed experimentally by Ball et al. (1997) on tests of flow past porous bodies.

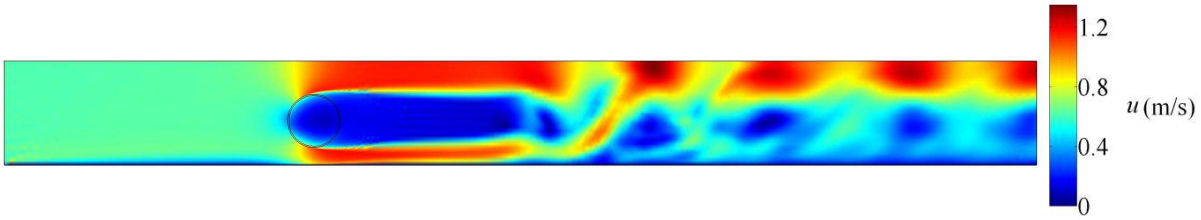

Figure 7.24 - Velocity contour plot of a six-bladed THAWT device with the same dimensions as that tested at Newcastle produced by the NS-BE model with $\bar{u}$ = 0.54m/s, B = 0.5, δ_{id} = 0.01

While the accuracy of the solution is significantly improved, the presence of time varying shed vortices significantly increases the time to reach a periodically or statistically steady solution, when compared to the heavily damped model developed by Swidenbank.

7.2.6. Solution convergence criterion

The NS-BE model simulates a 15 s period, after which the simulation can be re-run using the previous velocity field as the initial conditions, if the convergence criterion is not met. Convergence of the model is defined as occurring once the main variables used for subsequent analysis have reached steady or periodic values. The variables chosen for the convergence criterion are the power output and thrust.

Estimates of the expected values of power output and thrust are calculated from a third order polynomial fit of experimental data from the Newcastle tests described in Chapter 5, for

the six parallel-bladed device over a range of velocities. Convergence is defined as having occurred once the variation in power and thrust have fallen below 0.1%, of the expected values, over a 15 s period of simulation.

As demonstrated in Figure 7.25, for a standard simulation of the THAWT device, the values of power and thrust are within 0.1% of their final value after 16 seconds of simulation.

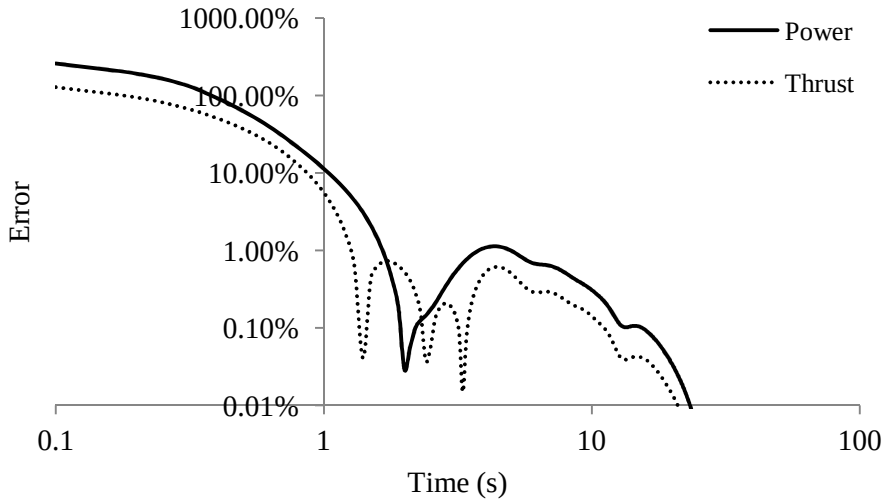

Figure 7.25 - Development of expected error in power and thrust over time for the NS-BE model for the six parallel-bladed device at a blockage ratio of 0.5 and a Froude number of 0.17

In order to ensure that the free surface pressure distribution is representative, the simulation is run until the wake generated by the turbine reaches the domain outlet. The amount of time required for this to occur is rarely shorter than the time required to achieve the basic convergence criterion. This process is also carried out for each free surface geometry update of the NS-BE-FS model, as described in the following section.

7.2.7. Application of the free surface model (NS-BE-FS)

The solution to the NS-BE model can be separated into two distinct zones. As shown in Figure 7.26, the variation in pressure along the channel is relatively smooth until a few metres downstream of the device, at which point the predicted depth becomes more variable. If the actual blades of the turbine were to be modelled in a time varying manner, fluctuations in the force produced by the turbine would result in a non-steady free surface over the turbine. However, the free surface over the device is steady, due to the implementation of the time averaged actuator cylinder representation of the turbine.

Despite the use of a time averaged rotor the induced wake is non-steady, due to vorticies generated in the wake and results in significant perturbations of the free surface profile.

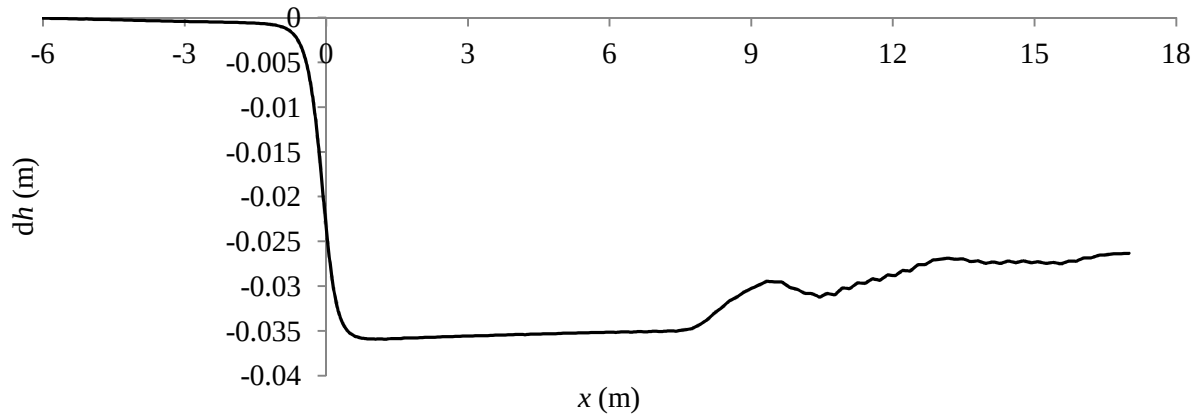

Figure 7.26 – Free surface profile predicted by the NS-BE-FS model for the six parallel-bladed device at Fr = 0.17 and B = 0.5, where the turbine is located at x = 0

The variation of the surface pressure over subsequent iterations of the free surface deformation indicates that the flow upstream of the shed vortices settles to a steady state solution relatively quickly, while the flow downstream of this point is continuously variable and does not show any signs of reaching a periodic state (see Figure 7.26). In order to define when the free surface deformation process has converged, a point is established in the steady state region, immediately downstream of the turbine and prior to the wake perturbations, as a reference point for the rate of change of the free surface. As shown by Figure 7.27, for the simulation of a standard experimental test, after the third geometry update the depth change and power do not vary between 15 s iterations by more than 0.40% and 0.56% respectively.

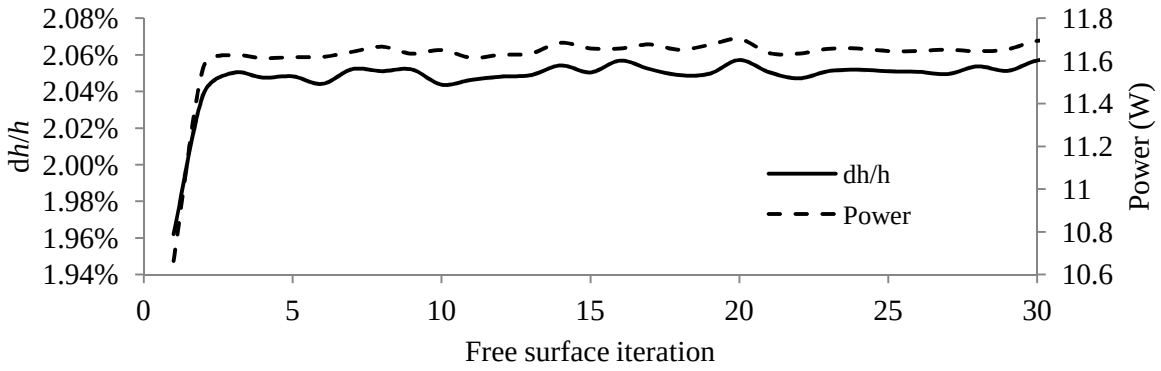

Figure 7.27 - Convergence of depth change and power with iterations of the free surface geometry for the six parallel-bladed device at Fr = 0.13, a tip speed ratio of 3 and B = 0.5

The criterion for convergence that has been chosen is that the free surface profile in the steady state region should change by no more than 0.4% between consecutive iterations of the free surface geometry update, and that the predicted power should change by no more than 0.5% of the expected value over consecutive 15 s periods.

7.3. Results for NS-BE model

In a similar way to most turbine designs, experimental power curves for the THAWT device exhibit a bell shape, with low power output at high tip speed ratios, due to low angles of attack, and at low tip speed ratios, due to hydrofoil stall. Figure 7.28 shows a typical power curve predicted by the NS-BE model and demonstrates that, unlike the experimental results, the predicted power output falls gradually for values of tip speed ratio lower than peak power. This is due to the use of the linear, extended lift curve to approximate the response of the hydrofoil to dynamic stall. The point at which dynamic stall would actually occur is very difficult to assess, however the increasing drag at greater angles of attack causes a 'knuckle' on the power curve, which has been taken as the approximate point of maximum power. It is assumed that for tip speed ratios lower than this point, the lift and drag characteristics are inaccurate and these regions are therefore ignored.

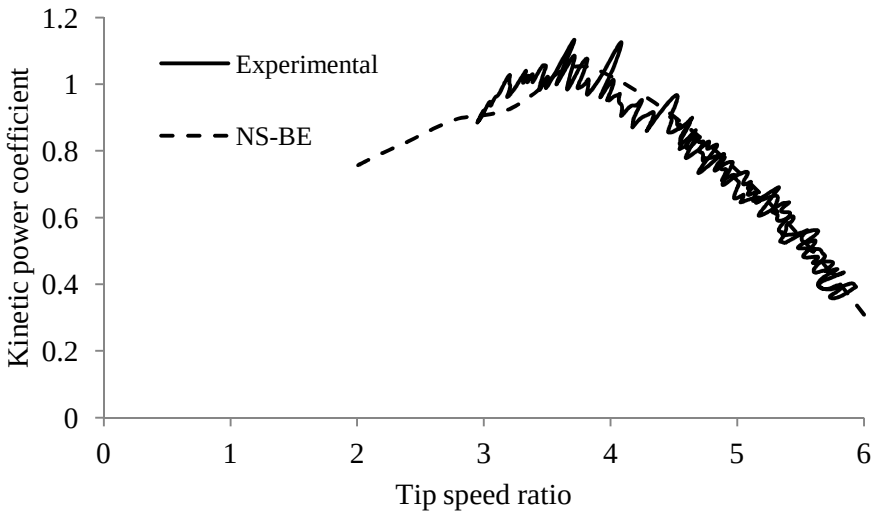

Figure 7.28 - Graph comparing the kinetic power coefficient predicted by NS-BE and experimental tests for the three-bladed THAWT at a Froude number of 0.13 and a blockage ratio of 0.5

While the full mechanics behind the dynamic stall phenomenon are largely ignored, this approach offers a simple numerical insight into the performance of the device when the hydrofoil stall is delayed. Due to the complexity of the dynamic stall phenomenon it is felt that this approach is appropriate in order to approximate the forces that act on the turbine blades.

Despite the simplification of the effects of dynamic stall, Figure 7.29 shows that the fidelity with which the NS-BE model is able to predict the performance of the THAWT device is a significant improvement over the M-BE model. The accuracy of performance prediction is

similar, and in some cases significantly better, than predictions using much more sophisticated numerical models of lower solidity devices (Howell *et al.*, 2010).

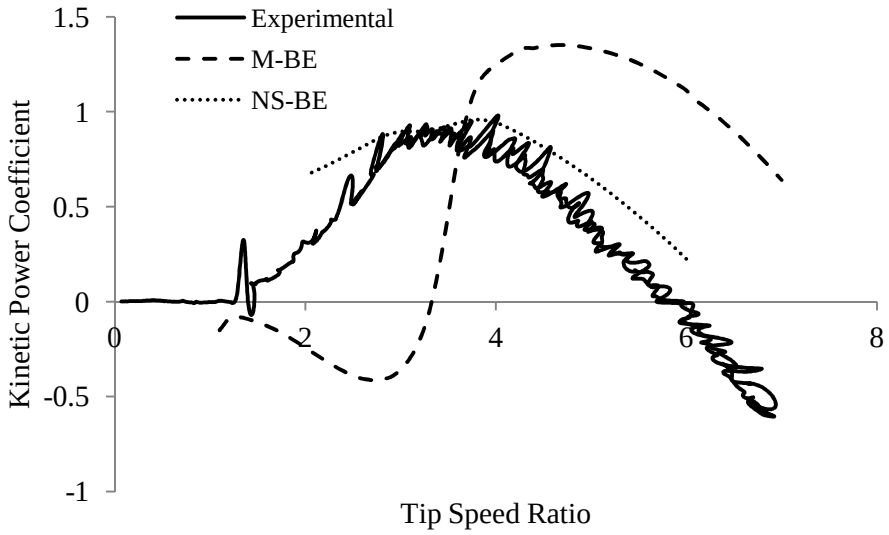

Figure 7.29 - Comparison of kinetic power coefficients predicted by M-BE, NS-BE and experiments for the three parallel-bladed device at a Froude number of 0.13 and a blockage ratio of 0.5

The peak kinetic power coefficients and the corresponding tip speed ratios and depth changes have been tabulated in Table 7.3 for the experimental results, the M-BE model, the NS-BE model and the NS-BE-FS model. The experimental depth changes which are anticipated to be erroneous, due to a lack of flow recovery, are highlighted in bold.

				Experiment			**M-BE**			**NS-BE**			**NS-BE-FS**		
Fr	***B***	***N***	**Pitch**	C_{Pk}	λ_p	**d*h*/*h***	C_{Pk}	λ_p	**d*h*/*h***	C_{Pk}	λ_p	**d*h*/*h***	C_{Pk}	λ_p	**d*h*/*h***
0.09	0.5	3	0	0.95	3.36	0.42%	1.20	4.6	0.67%	0.88	4	0.50%	0.91	4	0.51%
0.13	0.5	3	0	0.88	3.40	1.02%	1.35	4.7	1.42%	0.96	3.8	0.99%	1.01	3.8	1.02%
0.18	0.5	3	0	0.93	3.31	1.74%	1.53	4.7	2.72%	1.01	3.8	1.78%	1.11	4	1.94%
0.21	0.5	3	0	1.00	3.47	**4.60%**	1.66	4.9	4.46%	1.05	3.8	2.74%	1.21	3.8	3.01%
0.09	0.5	6	0	0.57	2.71	0.61%	1.31	3.9	0.91%	0.64	3.1	0.58%	0.65	3.3	0.60%
0.13	0.5	6	0	0.65	2.59	1.20%	1.54	3.7	1.79%	0.76	3.1	1.12%	0.83	3.1	1.18%
0.17	0.5	6	0	0.78	2.65	2.64%	1.78	3.9	3.69%	0.81	3.1	2.01%	0.94	3.2	2.24%
0.21	0.5	6	0	0.92	2.78	**6.40%**	2.04	4	6.12%	0.85	3.1	3.03%	1.11	3.3	3.67%
0.09	0.5	6	-2	0.66	2.32	0.40%	1.16	4	0.88%	0.71	2.9	0.57%	0.74	2.9	0.58%
0.17	0.5	6	-2	0.84	2.41	1.54%	1.70	3.9	3.57%	0.88	2.7	1.90%	1.02	2.9	2.17%
0.09	0.5	6	2	0.51	3.19	0.47%	1.16	4	0.87%	0.43	3.7	0.60%	0.45	3.7	0.62%
0.17	0.5	6	2	0.71	3.27	2.98%	1.69	3.9	3.51%	0.67	3.5	2.05%	0.78	3.7	2.31%
0.08	0.625	3	0	1.29	3.90	0.99%	1.66	5.3	1.10%	1.29	4.4	0.82%	1.35	4.4	0.85%
0.12	0.625	3	0	1.52	4.15	1.64%	1.97	5.7	2.73%	1.39	4.2	1.72%	1.53	4.4	1.88%
0.17	0.625	3	0	1.74	4.25	**3.85%**	2.34	6.1	6.06%	1.46	4.2	3.37%	1.78	4.6	4.06%
0.08	0.625	6	0	1.22	3.33	1.31%	2.01	4.6	1.55%	1.10	3.7	0.97%	1.21	3.8	1.03%
0.12	0.625	6	0	1.51	3.31	3.08%	2.44	4.4	3.19%	1.31	3.6	1.97%	1.57	3.6	2.22%
0.17	0.625	6	0	1.92	3.28	**6.61%**	3.39	5.5	9.85%	1.40	3.6	4.35%	2.49	4	6.58%

Table 7.3 – List of salient values for experiments and simulations by the M-BE, NS-BE and NS-BE-FS models

Over the range of experiments that were simulated using the NS-BE model, the ratios of the numerically predicted kinetic power coefficient C_{Pkn}/C_{Pke} and tip speed ratio $\lambda_{pn}/\lambda_{pe}$ to that measured during experiments are 0.98 and 1.22, with standard deviations of 0.12 and 0.06 respectively. This is a significant improvement on the basic M-BE model, which achieved average ratios of C_{Pkn}/C_{Pke} and $\lambda_{pn}/\lambda_{pe}$ 1.82 and 1.39, with standard deviations of 0.40 and 0.13 respectively.

The significant improvement in the accuracy of the prediction of the performance of the THAWT device is due to the improved simulation of the flow field. Figure 7.30 shows that the velocity field predicted by the NS-BE model would not be accurately represented using the simple steady, uniform stream-wise flow that is assumed by the M-BE model. The velocity vectors demonstrate that there are significant lateral velocity components in the flow field around the actuator cylinder of the NS-BE model, reducing the angle of attack on the upstream half of the device when compared to a uniform flow of the same magnitude.

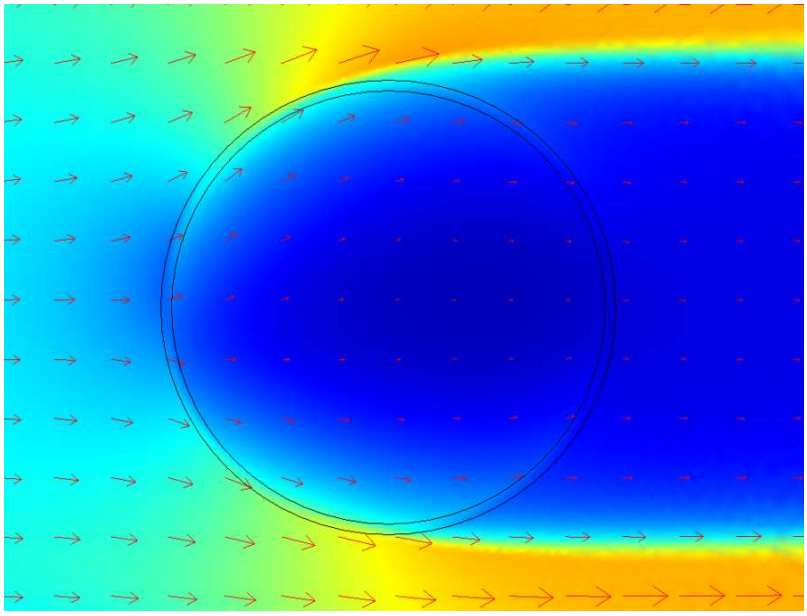

Figure 7.30 - Flow vectors overlaid on velocity field surface plot around the actuator cylinder in the NS-BE model for the six-bladed THAWT at Fr *= 0.13, B = 0.5 and a tip speed ratio of 3*

As illustrated in Figure 7.31, the deflection of the flow at the turbine significantly alters the resultant velocity and angle of attack experienced by the turbine, where $u' = u + v$. Due to the resulting vertical components of velocity the blades at the top and bottom of the device, which in uniform flow would have no angle of attack, now experience an accelerated flow velocity at an angle of attack and produce lift. The reduced velocity on the rear-side of the device results in a lower angle of attack and a reduced lift to drag ratio when compared to a device experiencing a uniform flow.

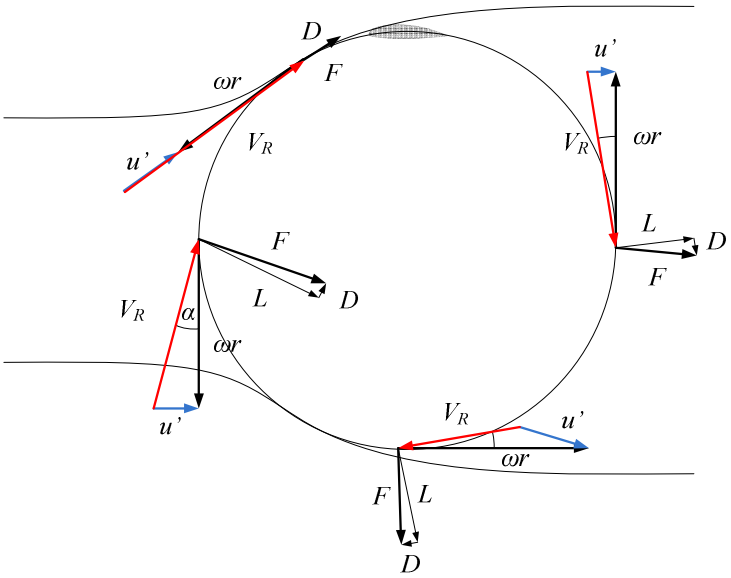

Figure 7.31 – Velocity vectors and resultant forces acting on a high thrust cross-flow device

Figure 7.32 shows that the two-dimensional flow-field results in a lower predicted average angle of attack, despite the peak positive angle of attack remaining roughly the same, so that positive torque is produced at a lower tip speed ratio, as observed in the Newcastle experiments. It is also worth noting that with a two-dimensional flow field, the point on the turbine circumference at which the angle of attack is zero has shifted towards the front of the turbine, so that the proportion of the upstream half of the device experiencing a positive angle of attack is reduced.

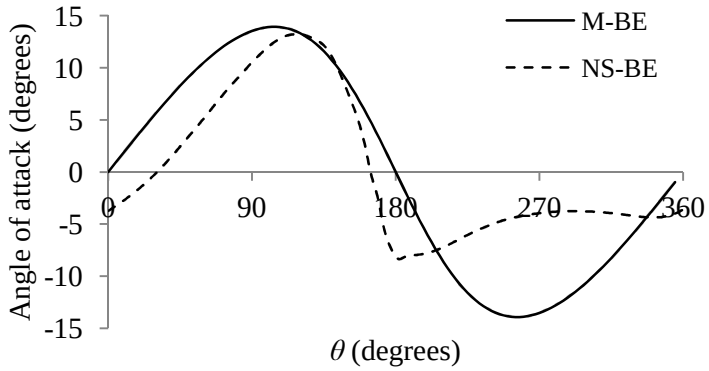

Figure 7.32 - Comparison of angle of attack around the circumference of the device for the six-bladed THAWT at a Froude number of 0.13 and a blockage ratio of 0.5, predicted using the M-BE and NS-BE models

7.3.1. Comparisons of basic three and six-bladed tests at $B = 0.5$

Figure 7.33 shows that the average ratios of C_{Pkn}/C_{Pke} for the three and six parallel-bladed devices are 1.04 and 1.07, with standard deviations of 0.074 and 0.11 respectively. The

consistency of prediction with both the three and six-bladed devices indicates that the NS-BE model is capable of accurately simulating the variation of velocity through the device.

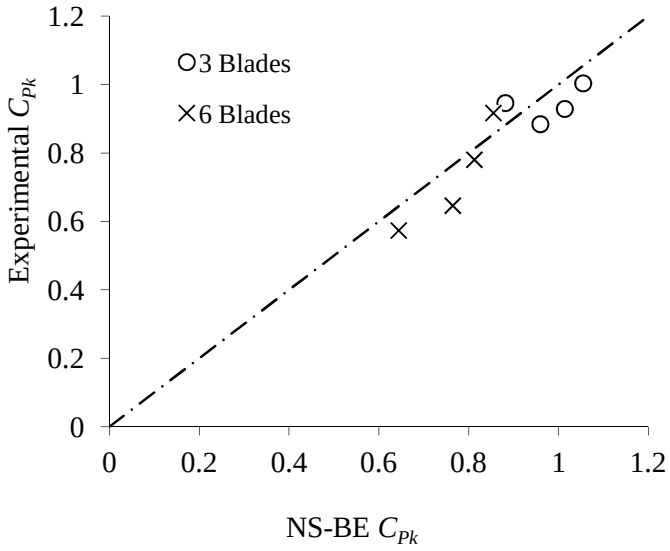

Figure 7.33 - Comparison of kinetic power coefficients predicted using the NS-BE model and recorded by experiment for the parallel-bladed devices at a blockage ratio of 0.5

The accuracy of the prediction of the kinetic power coefficient is not uniform with Froude number and the NS-BE model appears to under-predict the power produced by the six parallel-bladed device at a Froude number of 0.21. It is believed that this is due to the rigid domain of the NS-BE model, which does not simulate the acceleration of the flow through the device, as the physical flow is constricted through a narrowed region by the free surface deformation.

The accuracy of the prediction of the tip speed ratio at which the peak power occurs, λ_p, is also significantly improved when compared to the M-BE model. Figure 7.34, shows that the average ratio of $\lambda_{pn}/\lambda_{pe}$ for the basic three and six-bladed tests achieved by the NS-BE model is 1.15, with a standard deviation of 0.037, which is a significant improvement over the M-BE model with a mean of 1.42 and standard deviation of 0.032. This improvement can also be attributed to the accuracy with which the flow field is modelled when compared to the M-BE model. By simulating the vertical velocity components, the angle of attack on the upstream half of the device is reduced, so that the turbine is able to operate at a lower tip speed ratio before the onset of stall.

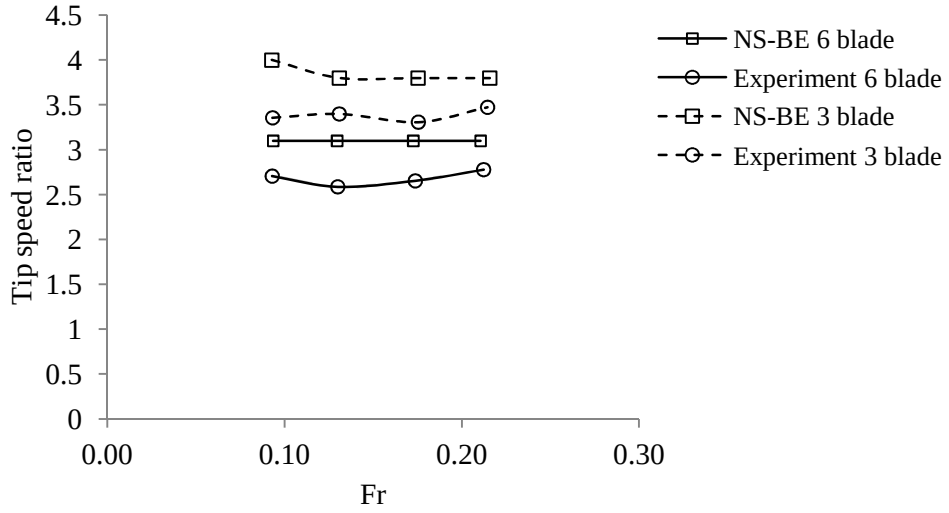

Figure 7.34 - Comparison of tip speed ratio of peak power predicted using the NS-BE model and recorded by experiment for the parallel bladed devices at a blockage ratio of 0.5

The reason for the mean over-estimation of tip speed ratio is thought to be due to details of the assumptions about the hydrofoil performance. For instance the hydrofoil section which has been wrapped onto the pitch circle, operating in a curvilinear flow, has been assumed to behave like a straight chorded blade in a rectilinear flow. However, the shift of the power curves to higher tip speed ratios predicted by the NS-BE model may suggest that the cambered blades of the experimental turbine experience a negative incidence, which has not been accounted for in the numerical model.

A further contribution to the positive shift of the tip speed ratio of peak power may be due to the effect of dynamic stall on the drag performance of the hydrofoil. When a hydrofoil undergoes delayed stall the drag remains relatively low until close to stall, when there is a dramatic increase in drag, as shown in Figure 7.35. With a delayed increase in drag, the power produced by the device would continue to increase into lower tip speed ratios.

Figure 7.35 – An example drag curve of a NACA0012 aerofoil during dynamic stall at a reduced frequency of $k = 0.26$ (McCroskey, 1981) permission to reproduce figure online not granted

Unfortunately, the complicating aspects of predicting the hydrofoil performance is likely to require extensive studies before any significant improvements in the model can be implemented.

Figure 7.36 shows that the depth change predicted using the NS-BE model is accurate for values up to 2%. It is believe that values of depth change greater than 2% are underestimated primarily due to the measurement of un-recovered depth during the higher velocity experimental tests. The underestimated depth change is likely to be further influenced by the use of a rigid lid in the NS-BE simulations.

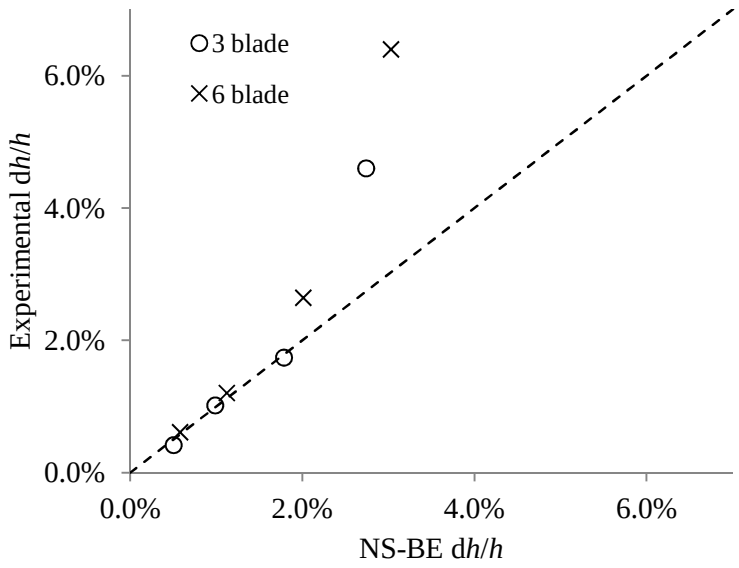

Figure 7.36 - Comparison of depth change calculated from NS-BE thrust and recorded by experiment for the parallel bladed devices at a blockage ratio of 0.5

7.3.2. Comparison of fixed offset pitch tests

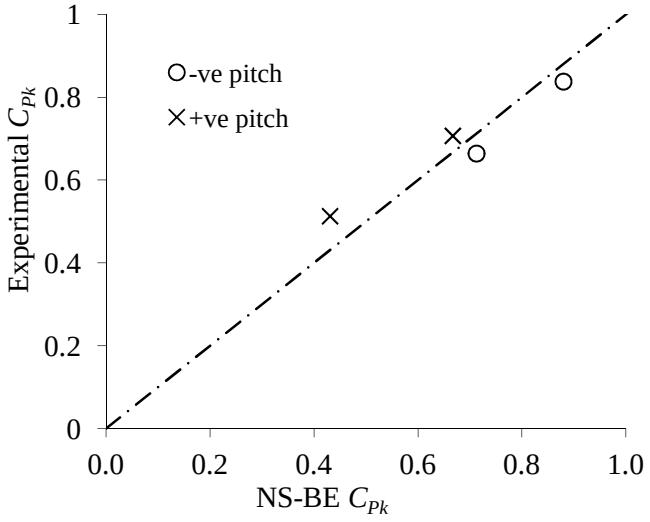

Figure 7.37 - Comparison of kinetic power coefficients predicted using the NS-BE model and recorded by experiment for the parallel bladed devices with a fixed offset pitch at a blockage ratio of 0.5

As demonstrated in Figure 7.37, the mean ratio of C_{Pkn}/C_{Pke} predicted by the NS-BE model for rotors with blade pitch offsets is 0.98, with a standard deviation of 0.090, which is another significant improvement over the mean of 2.10 and standard deviation of 0.28 achieved by the M-BE model. Unlike the M-BE model, the NS-BE model also correctly predicts that the device produces more power with a fixed negative pitch when compared to the neutral pitch, and a reduced power for the positive offset pitch.

The NS-BE model shows good fidelity in simulating the change in tip speed ratio with an applied fixed offset pitch, as shown in Figure 7.38, despite an overestimate of λ_p similar to that of the neutrally pitched tests.

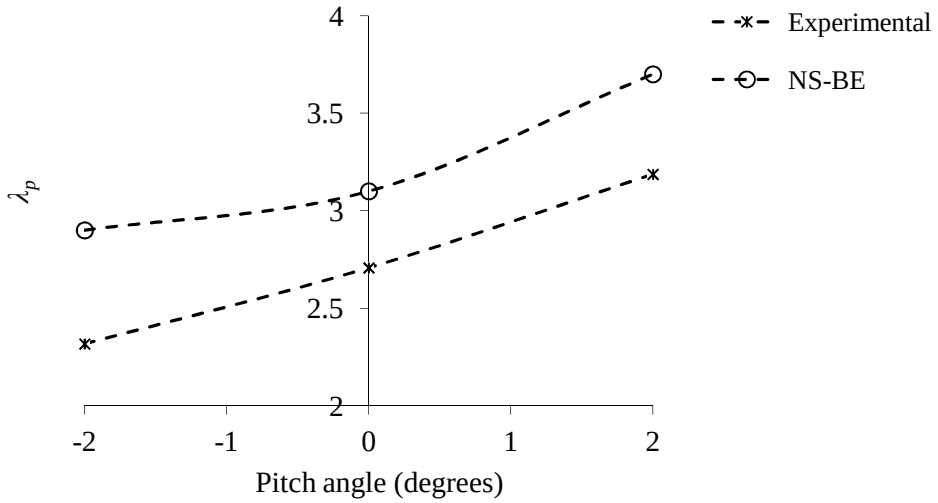

Figure 7.38 - Comparison of tip speed ratio of peak power predicted using the NS-BE model and recorded by experiment for the parallel bladed devices with a fixed offset pitch at B = 0.5

The ratio of depth change predicted by the NS-BE model to the experimental measurements $(\mathrm{d}h/h_n)/(\mathrm{d}h/h_e)$ for the negatively pitched rotor is 1.33 on average, and is significantly higher than the mean ratio for the neutrally pitched tests with $B = 0.5$ of 0.97. This suggests that the thrust predicted by NS-BE model for the negatively pitched device is also over-estimated.

7.3.3. Comparison of increased blockage tests

In a similar fashion to the basic parallel-bladed tests, the fidelity and accuracy with which the NS-BE model predicts the power produced by the increased blockage turbine has been significantly improved, as shown in Figure 7.39. The model is most accurate when simulating the performance at low Froude numbers where the rigid lid approximation of the NS-BE model is more accurate. The fidelity of the higher Froude number simulations is expected to improve with the simulation of the free surface deformation.

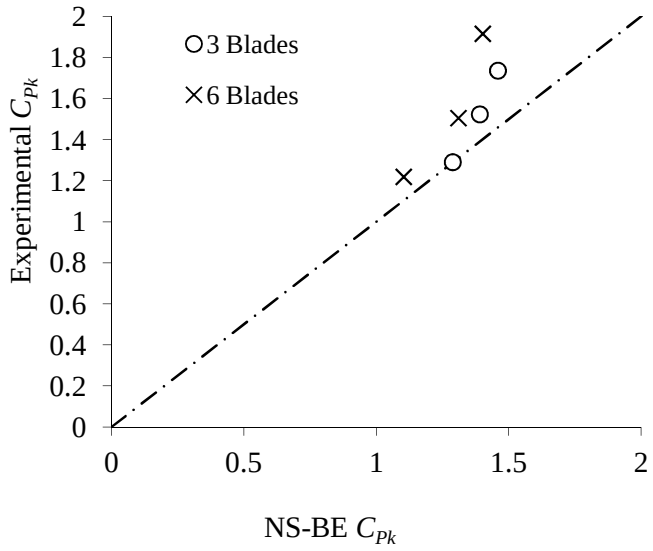

Figure 7.39 - Comparison of kinetic power coefficients predicted using the NS-BE model and recorded by experiment for the parallel bladed devices at a blockage ratio of 0.625

As shown in Figure 7.40, the error in the prediction of λ_p is reduced when simulating an increased blockage of B = 0.625. The mean ratio of $\lambda_{pn}/\lambda_{pe}$ for the higher blockage simulations is 1.07 with a standard deviation of 0.057, which is lower than the mean and standard deviation for the NS-BE predictions of the overall range of experiments of 1.12 and 0.063 respectively.

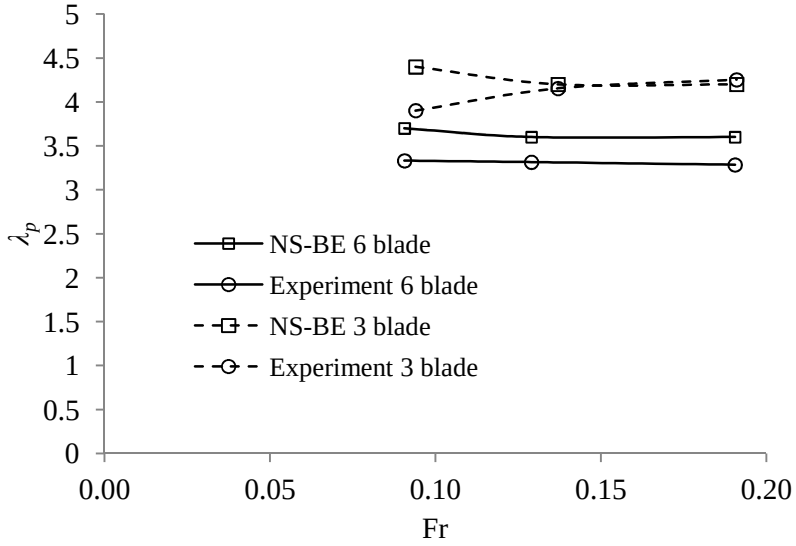

Figure 7.40 - Comparison of tip speed ratio of peak power predicted using the NS-BE model and recorded by experiment for the parallel bladed devices at a blockage ratio of 0.625

During the series of experiments, increasing the blockage ratio from B = 0.5 to B = 0.625 resulted in an increase of the tip speed ratio of peak power for the three and six parallel-bladed devices by a mean factor of 1.22. By analysing the results of the NS-BE model, the

reason for this increase in λ_p becomes clear. The effect of the increased blockage is to force a greater proportion of the flow through the turbine region. Figure 7.41 shows that by increasing the blockage ratio the induction factor α_2 at the upstream point of the device is increased, which causes an increase in the angle of attack experienced by the turbine blades and an increased stalling tip speed ratio.

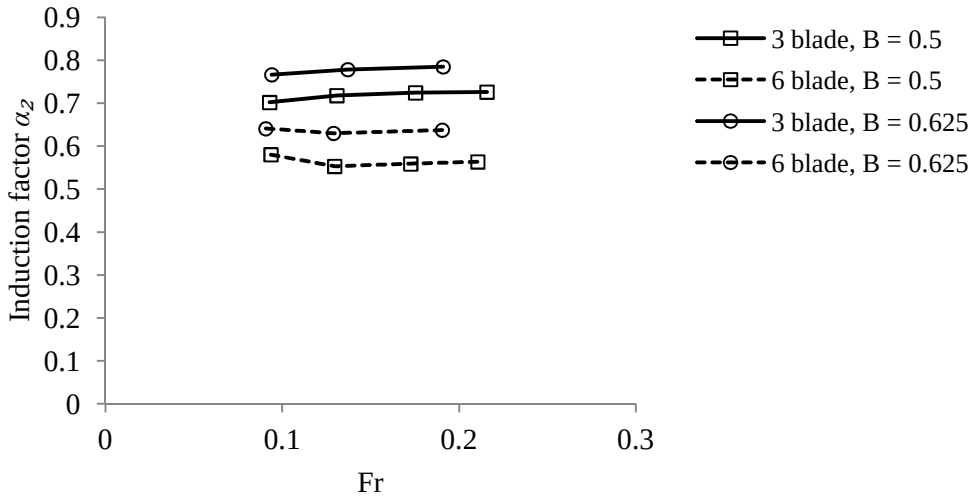

Figure 7.41 – Comparison of induction factors at the upstream point of the device, predicted using the NS-BE model

In a similar fashion to the lower blockage simulations, the NS-BE model predicts accurately the depth change across the device for values up to 2%, as shown in Figure 7.42. As the Froude number is increased, the measurement of unrecovered downstream depths is anticipated to result in an underestimate of the depth change by the NS-BE model and further error is likely to be incurred due to the influence of the rigid lid.

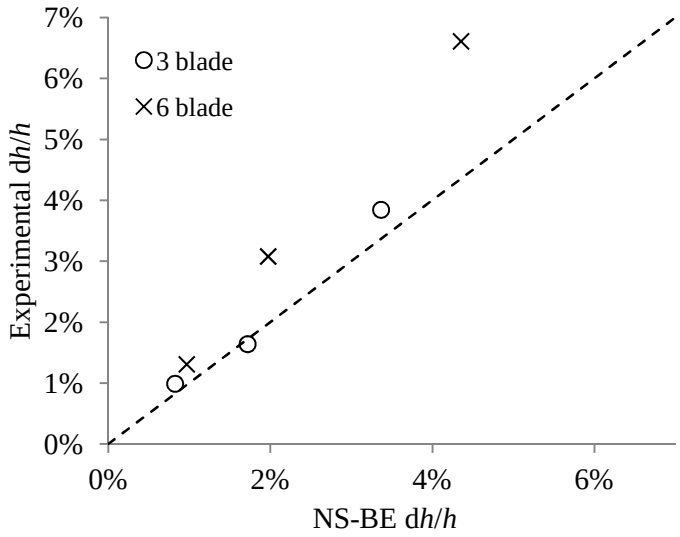

Figure 7.42 - Comparison of depth change calculated from NS-BE thrust and recorded by experiment for the parallel bladed devices at a blockage ratio of 0.625

7.3.4. Summary of comparisons with M-BE model

Table 7.4 shows that using the NS-BE model the fidelity of the prediction of the performance of the THAWT device is significantly improved when compared to the M-BE model, over the entire range of simulated experiments.

	M-BE		NS-BE	
C_{Pkn}/C_{Pke}	**Mean**	**St. dev**	**Mean**	**St. dev**
3 blade	1.52	0.18	1.04	0.074
6 blade	2.29	0.069	1.07	0.11
Pitched	2.10	0.28	0.98	0.090
***B* = 0.625**	1.50	0.21	0.88	0.089
Over-all	1.82	0.40	0.98	0.12

Table 7.4 – Ratios of kinetic power coefficient predicted by the M-BE and NS-BE models to experimental results for parallel-bladed experiments

As well as improving the prediction of the power produced by the device, Table 7.5 indicates that the NS-BE model is also able to predict the tip speed ratio at which the peak power occurs with a significantly greater accuracy than the M-BE model.

	M-BE		NS-BE	
$\lambda_{pn}/\lambda_{pe}$	**Mean**	**St. dev**	**Mean**	**St. dev**
3 blade	1.40	0.023	1.14	0.042
6 blade	1.44	0.017	1.16	0.035
Pitched	1.45	0.26	1.15	0.062
***B* = 0.625**	1.42	0.13	1.07	0.057
Over-all	1.39	0.13	1.12	0.063

Table 7.5 – Ratios of tip speed ratio of peak power predicted by the M-BE and NS-BE models to experimental results for parallel-bladed experiments

7.3.5. NS-BE blade force prediction

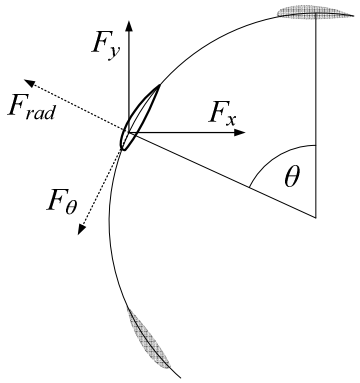

Figure 7.43 – Definition of blade forces

One of the primary roles of the NS-BE model in this project is to predict the forces acting on the blades of the THAWT device, in order to maximise the accuracy of any subsequent structural analysis.

The tangential and radial force at each point around the circumference of the actuator cylinder is calculated using the predicted vertical and horizontal forces, as shown in equations 7.19 and 7.20.

$$F_\theta = -F_x \cos\theta - F_y \sin\theta \qquad 7.19$$

$$F_{rad} = -F_x \sin\theta + F_y \cos\theta \qquad 7.20$$

For the following analysis of the forces predicted by the NS-BE model, the radial and tangential forces are non-dimensionalised as shown in equations 7.21 and 7.22. This will allow the comparison of varied blockage ratios, where the Froude number remains constant, but the upstream velocity has changed.

$$C_{F_{rad}} = \frac{F_{rad}}{\frac{1}{2}\rho {u_\infty}^2 A_t} \qquad 7.21$$

$$C_{F_\theta} = \frac{F_\theta}{\frac{1}{2}\rho {u_\infty}^2 A_t} \qquad 7.22$$

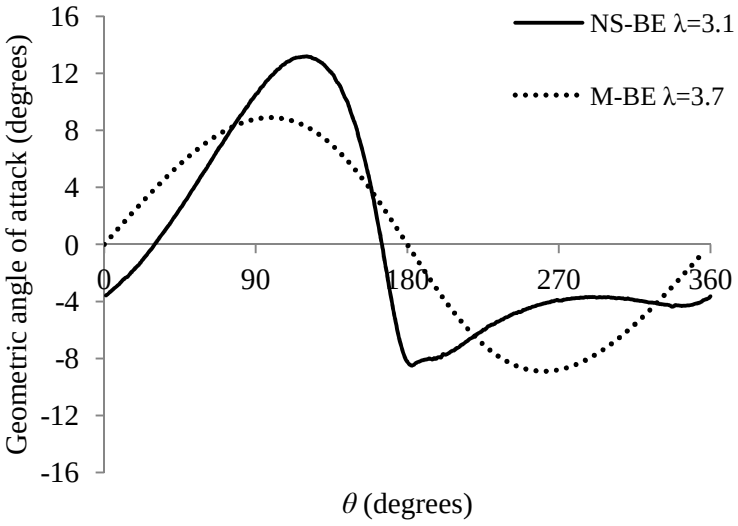

Figure 7.44 - Comparison of angles of attack predicted by the M-BE and NS-BE models for the six parallel-bladed device at Fr = 0.13 at the tip speed ratios of peak power, blockage B=0.5

Figure 7.44 shows that the use of a non-uniform velocity field in the NS-BE model predicts a significantly different distribution of the angle of attack from the M-BE model around both the upstream and downstream halves of the device. The assumption of constant velocity in the M-BE model results in a symmetrical distribution of angle of attack. The NS-BE model predicts a narrower region of turbine circumference in which positive angles of attack are achieved and the angle of attack on the downstream half of the device is significantly altered, when compared to the M-BE model.

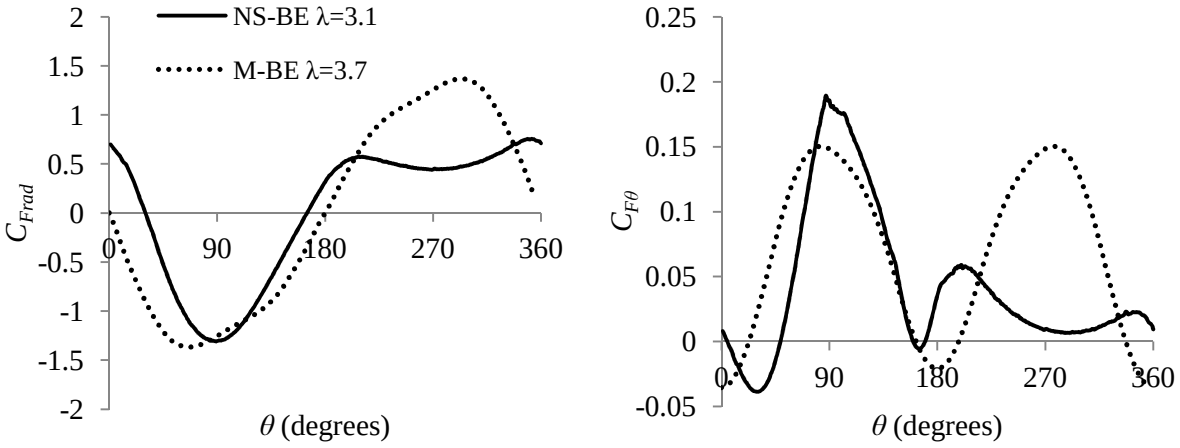

(a) Radial force coefficient *(b) Tangential force coefficient*

Figure 7.45 - Comparison of radial and tangential force coefficients predicted by the M-BE and NS-BE models for the six parallel blade device at Fr = 0.13, B=0.5 and tip speed ratio of peak power

As shown in Figure 7.45 the changes to the angle of attack predicted by the NS-BE model, when compared to the M-BE model, cause significant differences in the predicted radial and tangential forces. The region of turbine circumference in which negative radial force occurs is narrowed and the maximum force on the downstream half is reduced. Figure 7.45(b) shows that the torque predicted by the NS-BE model on the neutrally pitched turbine is produced mostly on the upstream half of the turbine.

7.3.6. Force observations of the fixed offset pitch

By applying a fixed offset pitch to the blades of the six-bladed parallel configured device, the power produced is increased, while decreasing the operating tip speed ratio and depth change across the flow domain. As previously demonstrated in this section, the significant reduction in velocity through the upstream half of the device means that the majority of the power is extracted from the upstream half of the turbine. By applying a negative offset pitch the optimum distribution of angle of attack occurs at a lower tip speed ratio, which reduces the thrust produced by the device and increases the induction factor at the upstream point of the turbine by roughly 3%.

The variation of geometric and effective angle of attack for a device with a negative fixed offset pitch are plotted in Figure 7.46, where geometric angle of attack is defined as the angle between the blade component of velocity and the resultant flow velocity and the effective angle of attack is defined as the angle between the blade chord at the quarter chord point and the resultant flow velocity.

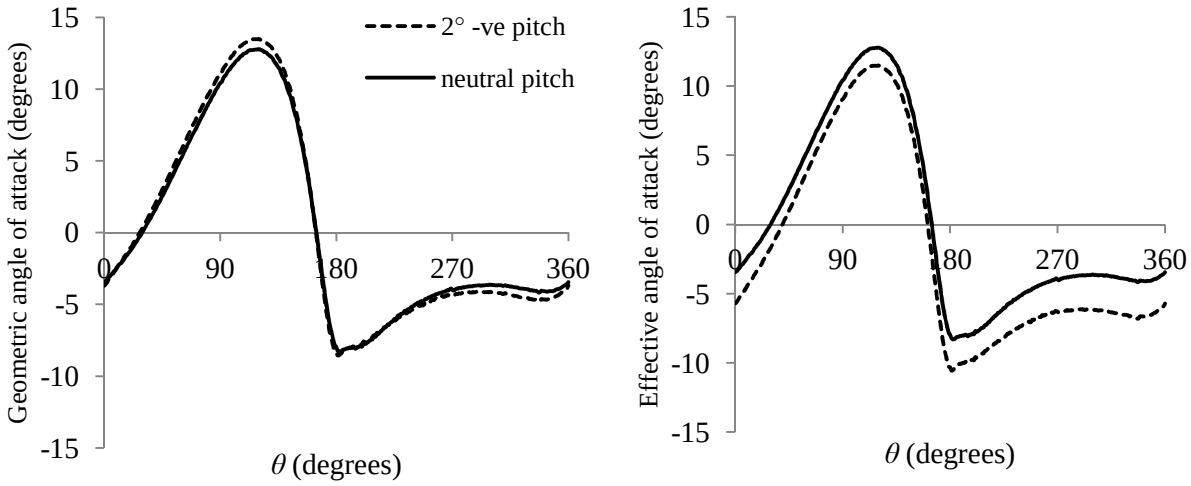

(a) Geometric angle of attack *(b) Effective angle of attack*

Figure 7.46 - Comparison of angles of attack predicted by the NS-BE models for the six parallel-blade device with negative and neutral fixed offset pitch at Fr = 0.09, B = 0.5 and the corresponding λ_p

Figure 7.46(a) shows that by operating at a lower tip speed ratio the angle of attack of the blades of the negatively pitched device are increased by a small amount. During a full rotation of the device the geometric angle of attack ranges from $-8.6° < \alpha < 13.5°$. Figure 7.46(b) demonstrates that by applying the 2° negative fixed offset pitch the effective angle of attack, from which the hydrofoil performance characteristics are calculated, is translated to a range of $-10.6° < \alpha < 11.5°$. By having a more even distribution of the angle of attack on the upstream and downstream halves of the turbine, the optimum lift to drag characteristics can be maintained over a greater proportion of the rotor circumference.

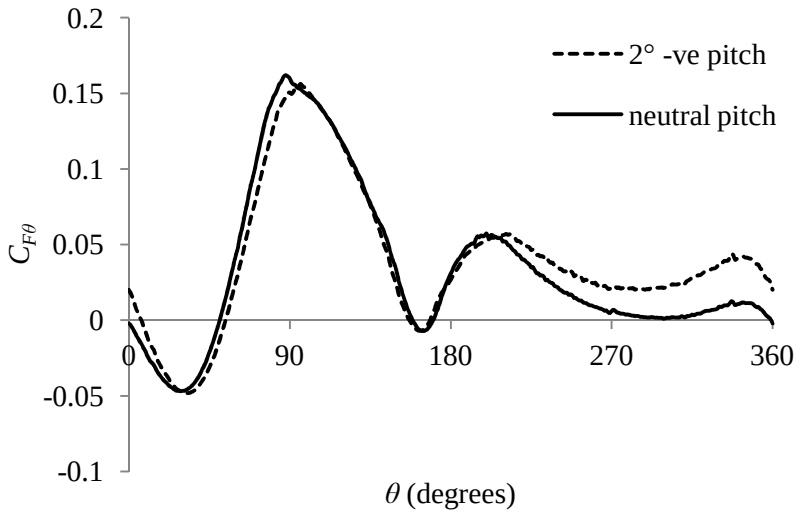

Figure 7.47 - Comparison of tangential force coefficient predictions by the NS-BE models for the six parallel-bladed device with fixed offset pitch at a Froude number of 0.09, blockage B=0.5

As shown in Figure 7.47, the increased magnitude of the apparent angle of attack on the downstream half of the device leads to an increase in the torque produced by the turbine.

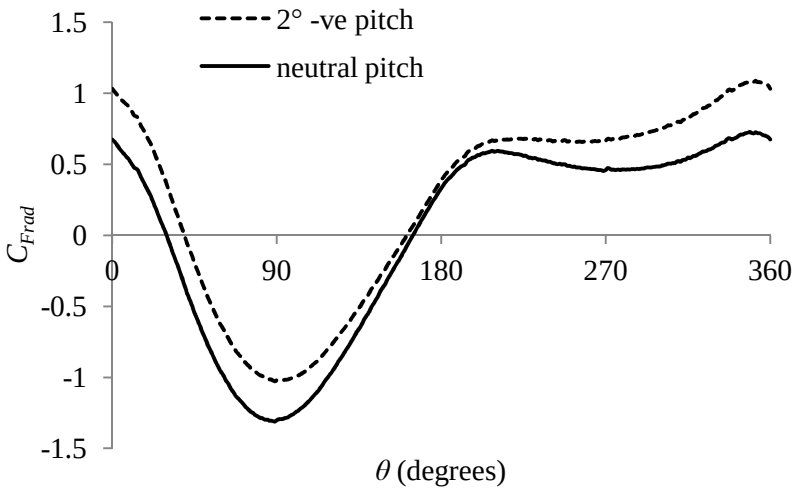

Figure 7.48 - Comparison of radial force coefficient predictions by the NS-BE models for the six parallel-bladed device with fixed offset pitch at a Froude number of 0.09, blockage B=0.5

The greatest stresses in the THAWT device are caused by forces normal to the blade chord, about which the hydrofoil section is weakest, and are approximately equal to the radial force produced by the blade. Figure 7.48 shows that while the range of the radial force remains relatively unchanged by applying a 2° negative fixed offset pitch, the maximum absolute force is reduced.

By applying the negative fixed offset pitch, there are now two occasions in the rotational cycle where the maximum absolute radial force occurs; one at approximately 90° of rotation and one at approximately 350°. The peak in stress at 350° occurs as a result of a greater effective angle of attack occurring on the blade approaching the oncoming flow, which has been accelerated around the device.

7.3.7. Effect of blockage on blade forces

Increasing the blockage ratio of the device by 25% from B = 0.5 to B = 0.625 causes a beneficial increase in the predicted kinetic power coefficient and a detrimental increase in thrust. As shown by Figure 7.49, for a Froude number of 0.13, the increase in blockage ratio also results in an increase in the range of radial force by 32%. The increase in radial force is likely to be detrimental to the structural performance of the device and confirms that there will be a trade-off between hydrodynamic and structural performance when considering the choice of blockage ratio for the device.

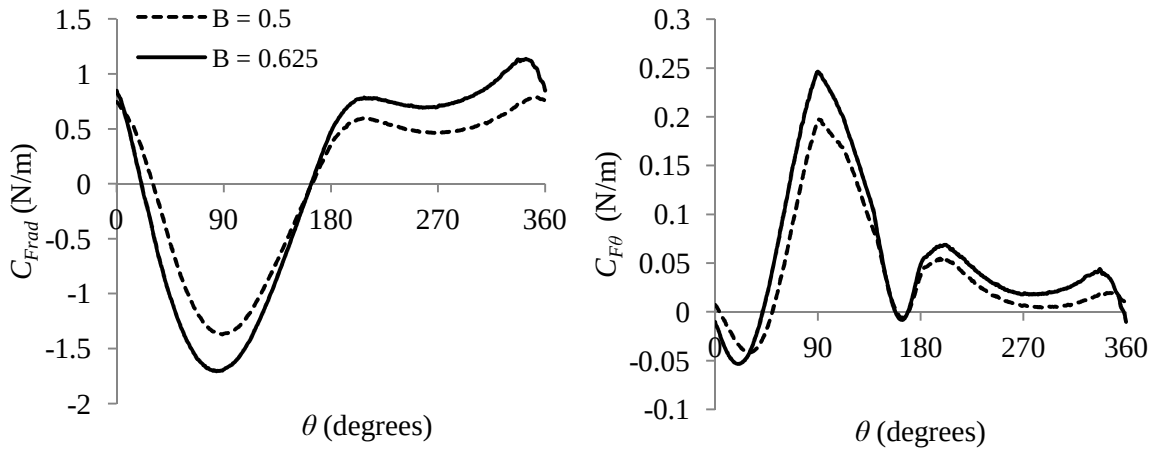

(a) Radial force coefficient *(b) Tangential force coefficient*

Figure 7.49 - Comparison of radial and tangential force coefficients predicted by the NS-BE model for the six parallel bladed device at a Froude number of 0.13 and blockage ratios of 0.5 and 0.625

7.3.8. Force comparisons with the analytical preliminary analysis

The preliminary analysis, described in Chapter 3, predicts the magnitude of the force that would be expected at the most upstream point of the rotor, as shown in equation 7.23, which suggests that the expression shown in equation 7.24 is constant.

$$\frac{F_L}{pgh^2} \propto \frac{{\lambda_p}^2 \mathrm{Fr}^2 sB}{n} \qquad 7.23$$

$$\frac{F_L}{pgh^2} \times \frac{n}{{\lambda_p}^2 \mathrm{Fr}^2 sB} = C \qquad 7.24$$

By individually varying the Froude number Fr, solidity *s*, blockage ratio *B* and number of blades *n* away from a base configuration in simulations of the NS-BE model, the accuracy with which the preliminary analysis predicts the variation in blade force is explored. For each change of a given parameter, the tip speed ratio of peak power has been extracted from the NS-BE prediction, from which the maximum blade force has been taken.

The base configuration, the range of each variable explored and the values of *C* predicted by the NS-BE model over the range of explored variables are given in Table 7.6. For reference, the NS-BE model predicts that the base configuration listed in Table 7.6 results in a C_{base} value of 1.70.

	Base value	**Range of explored values**	**Range of NS-BE predicted *C***
Froude number	0.14	0.08 – 0.21	1.59 – 1.70
Solidity	0.2	0.12 - 0.28	1.63 – 1.70
Blockage ratio	0.5	0.45 – 0.56	1.61 – 1.78
Number of blades	6	4 - 8	1.70 – 1.70

Table 7.6 – Parameters for a base configuration and the range of values which were explored

As shown in Table 7.6, over the range of explored variables the blade force scaling is consistent to within 7%, when compared to numerical predictions by the NS-BE model. This suggests that the preliminary analysis provides good approximations of the blade force scaling for realistic configurations of device design.

It should be noted however that the prediction of force scaling with solidity is unlikely to be accurate as solidity reaches significantly high values. As the solidity tends towards a value of $s = 1$ (i.e. a solid cylinder) no flow will pass through the rotor, at which point no power will be produced and the only force on the upstream blade would be the increase in pressure due to the stagnation point of the flow upstream of the cylinder. This would not be accurately modelled by the NS-BE model and would invalidate the majority of the assumptions of the preliminary analysis. However, both methods should be accurate for moderate values of solidity.

Prediction of force scaling with a variation in the number of blades is perfectly matched between the preliminary analysis and the NS-BE analysis. This is due to the fact that by maintaining a constant solidity between NS-BE simulations, the forces applied to the fluid remain consistent and 'smeared' around the actuator cylinder with the same distribution. The interpretation of how much force is applied by a single blade is calculated during the post-processing phase, and is simply a division by the number of blades.

7.3.9. Validity of preliminary analysis assumptions

For all of the cases compared to the preliminary analysis, the maximum radial force has occurred at approximately the most leading point on the rotor, which indicates that this assumption is valid for the preliminary analysis. However, it should be noted that with the use of negative pitch, it may be possible to change the point of maximum absolute radial force to a location on the downstream half of the device, in which case the scaling of force predicted by the preliminary analysis may no longer be accurate.

7.4. Results of the FS-NS-BE model

The tabulated results for the NS-BE-FS model are shown in Table 7.3. In modelling the free surface deformation of the fluid domain the mean ratio of C_{Pkn}/C_{Pke} for all of the analysed tests has increased from 0.98 for the NS-BE model to 1.11 for the NS-BE-FS model, with the most significant increase occurring in the higher Froude number tests. Figure 7.50

demonstrates that the free surface deformation causes a shift of the entire power curve to greater power.

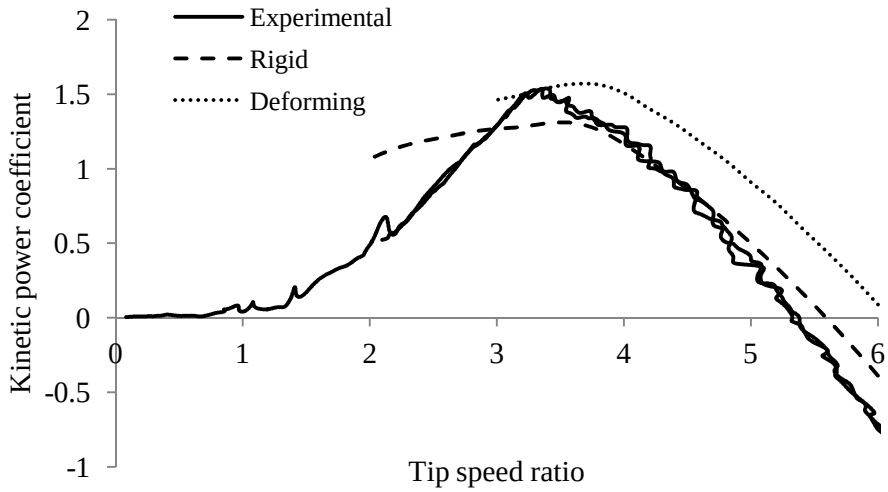

Figure 7.50 - Comparison of kinetic power coefficients measured during experiment and predicted using the NS-BE and NS-BE-FS models for the six parallel-bladed device at Fr *= 0.13 and B = 0.5*

7.4.1. Comparison of basic three and six parallel-blade tests at $B = 0.5$

As shown in Figure 7.51 the mean ratio of C_{Pkn}/C_{Pke} predicted by the NS-BE-FS model for the basic three and six parallel-bladed tests is 1.17 with a standard deviation of 0.095, which is higher than the mean and standard deviation of 1.05 and 0.087 for the NS-BE model.

While the NS-BE model was inconsistent with the accuracy of performance prediction of the device over the range of Froude number, it can be seen that by allowing the free surface to deform, the variation in the kinetic power coefficient follows a more consistent gradient when using the NS-BE-FS model. This suggests that the additional power available to the device as the free surface deforms is being modelled more consistently.

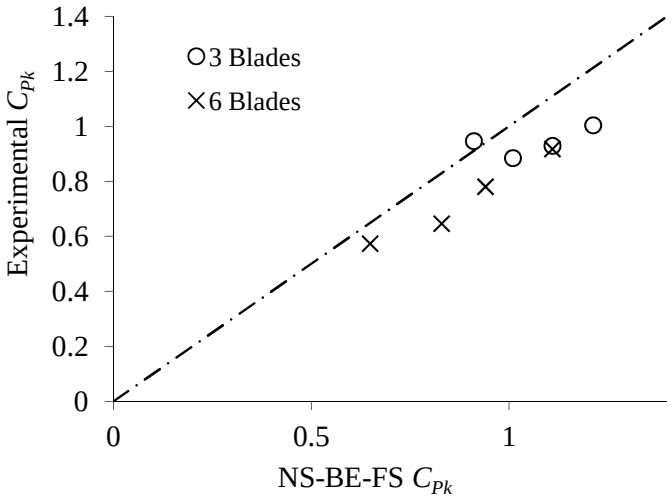

Figure 7.51 - Comparison of kinetic power coefficients predicted using the NS-BE-FS model and recorded by experiment for the parallel-bladed devices at a blockage ratio of 0.5

By modelling the free surface deformation the induction factor at the upstream point of the device is increased, as shown in Figure 7.52. As would be expected, the increase in the induction factor becomes more significant as the Froude number increases, due to the greater induced depth changes.

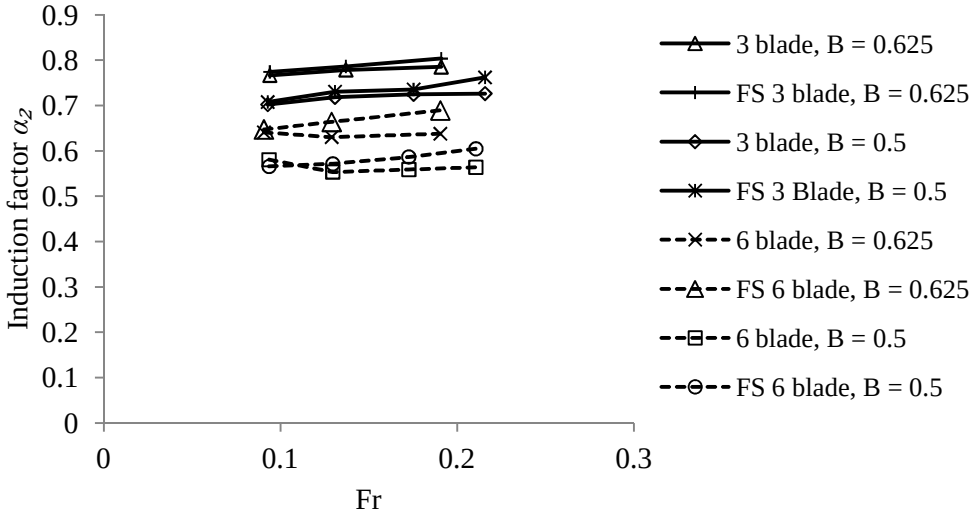

Figure 7.52 - Comparison between of predictions of upstream induction factor by the NS-BE model and the NS-BE-FS model for the parallel-bladed tests

As well as causing an increase in the ratio of C_{Pkn}/C_{Pke}, applying free surface deformation results in an increase of the mean ratio of $\lambda_{pn}/\lambda_{pe}$ from 1.15 for the NS-BE model to 1.18 for the NS-BE-FS model. This increase in λ_p is assumed to occur due to the increase in the induction factor through the device at higher Froude numbers, caused by the narrowing of the flow domain, which results in an increase in the angles of attack experienced by the hydrofoils, and an increased stall tip speed ratio.

The mean ratio of $(dh/h_n)/(dh/h_e)$ is increased from 0.97 with a standard deviation of 0.14 for the NS-BE model to 1.03 and 0.13 respectively for the NS-BE-FS model.

7.4.2. Comparison of fixed offset pitch results

In a similar fashion to the basic parallel-bladed results, the mean ratio of C_{Pkn}/C_{Pke} for the tests with a fixed offset pitch is increased from 0.98 and a standard deviation of 0.090 for the NS-BE model to 1.12 and 0.13 for the NS-BE-FS model, as shown by Figure 7.53.

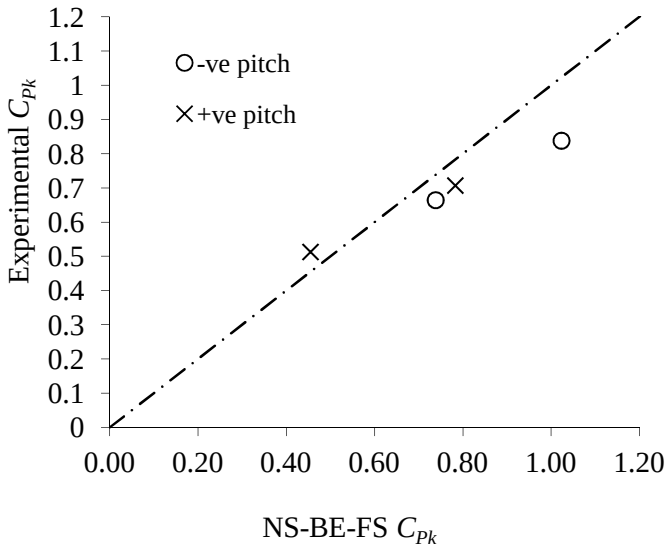

Figure 7.53 - Comparison of kinetic power coefficients predicted using the NS-BE-FS model and recorded by experiment for the fixed offset pitch six parallel-bladed devices at a blockage ratio of 0.5

The mean ratio of $\lambda_{pn}/\lambda_{pe}$ for the fixed offset pitch experiments is increased from 1.14 and a standard deviation of 0.062 for the M-BE model to 1.19 and 0.041 for the NS-BE-FS model. However, the fidelity of the variation in tip speed ratio with a change of pitch shows good correlation with that measured experimentally, as shown in Figure 7.54. This indicates that the relative effect of applying the fixed offset pitch is being accurately modelled.

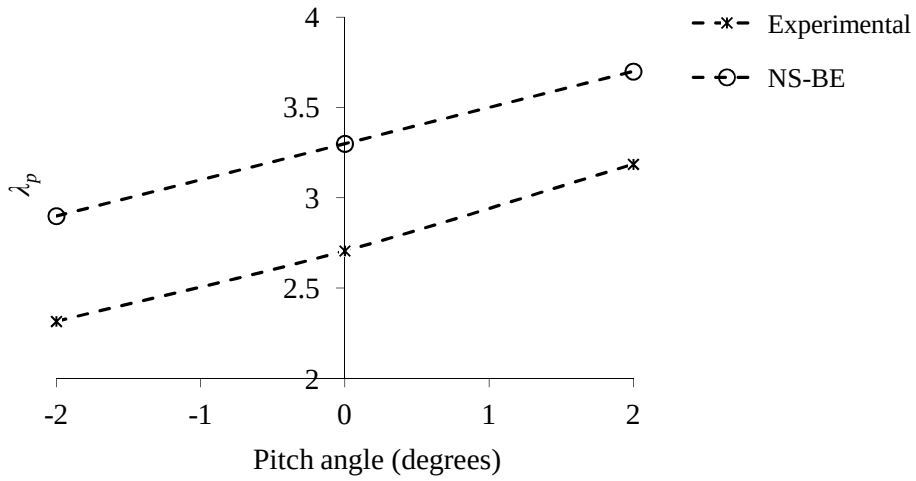

Figure 7.54 - Comparison of tip speed ratio of peak power predicted using the NS-BE-FS model and recorded by experiment for the parallel bladed devices with a fixed offset pitch at B = 0.5

The mean ratio of $(dh/h_n)/(dh/h_e)$ predicted by the NS-BE-FS model is increased to 1.06 with a standard deviation of 0.38 from the NS-BE predictions of 0.98 and 0.39 respectively.

7.4.3. Comparison of increased blockage results

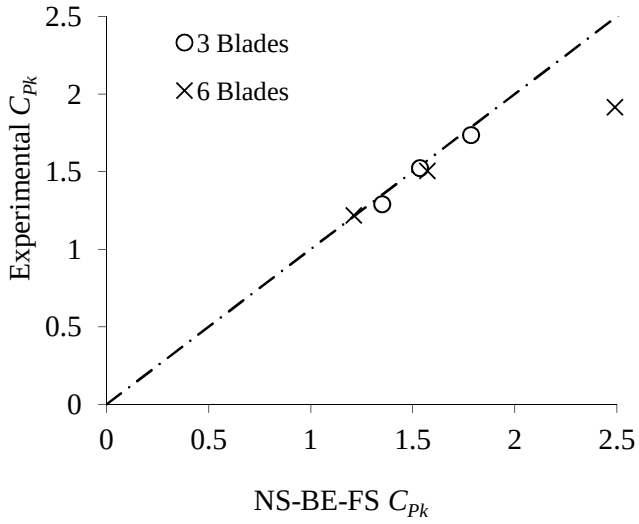

Figure 7.55 - Comparison of kinetic power coefficients predicted using the NS-BE-FS model and recorded by experiment for the parallel bladed devices at a blockage ratio of 0.625

The correlation between the NS-BE-FS model predictions of C_{Pk} and the experimental results is significantly improved when compared to the NS-BE model predictions, as shown in Figure 7.55. The mean ratio of C_{Pkn}/C_{Pke} for the high blockage results is 1.02 with a standard deviation of 0.023. The high blockage six parallel-bladed result at a Froude number of 0.19, is assumed to be erroneous due to the proximity of the free surface to the actuator cylinder, as shown in Figure 7.56.

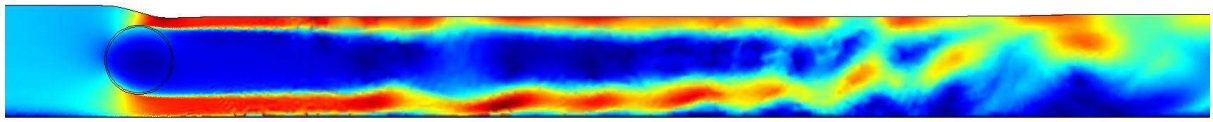

Figure 7.56 - Surface velocity plot produced by the NS-BE-FS model of the six parallel bladed device at a blockage ratio of 0.625, a Froude number of 0.19 and a tip speed ratio of 6

During the experiments, the highly accelerated band of flow above the turbine resulted in a hydraulic jump downstream. Due to the use of the incompressible Navier-Stokes equations and the simple hydrostatic variation of the free surface, the NS-BE-FS model is unable to simulate accurately the nature of a supercritical flow and discontinuities such as a hydraulic jump. However, this is not a significant limitation of the model, as a full scale device in which the bypass flow becomes supercritical is not anticipated to be feasible, and will not be required in subsequent simulations.

When compared to the NS-BE model, the NS-BE-FS model predicts an increase in the mean ratio of $\lambda_{pn}/\lambda_{pe}$ to 1.10 with a standard deviation of 0.034. However, the ratio of

$(dh/h_n)/(dh/h_e)$ predicted by the NS-BE-FS model is increased from 0.80 for the NS-BE model to 0.91.

7.4.4. Summary of NS-BE-FS results and blockage correction

	NS-BE		NS-BE-FS	
	Mean	St. dev	Mean	St. dev
3 blade	1.04	0.074	1.13	0.11
6 blade	1.07	0.11	1.21	0.062
Pitched	0.98	0.090	1.12	0.13
$B = 0.625$	0.88	0.089	1.02	0.023
Over-all	0.98	0.12	1.11	0.12

Table 7.7 – Ratios of kinetic power coefficient predicted by the NS-BE and NS-BE-FS models to experimental results for parallel-bladed experiments

As shown in Table 7.7, by modelling the free surface deformation of the flow domain the predicted power output of the device has been increased. This is due to an increase in the flow velocity through the device, caused by the constriction of the flow boundaries and is more substantial as the flow Froude number is increased.

The increase in power due to the modelling of the free surface deformation has resulted in an over-prediction of the power produced by most of the configurations of the experimental turbine. This is believed to be predominantly due to the fact that the two-dimensional NS-BE and NS-BE-FS models simulate a greater blockage ratio than the three-dimensional blockage ratio of the experimental turbine.

The blockage ratio of a device is defined as the proportion of the channel area occupied by the turbine apparatus. Due to the two-dimensional nature of the NS-BE models, the blockage ratio B becomes the ratio of flow depth occupied by the turbine, which is 0.5. However, during the experiments the turbine operated with a gap either side of the rotor, which allowed the mounting of the device and prevented high drag due to shearing of the thin layer of water near the walls, as shown in Figure 7.57.

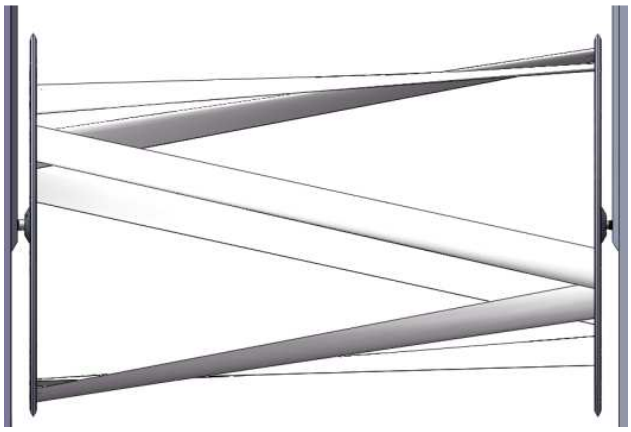

Figure 7.57 - CAD rendered image of the experimental apparatus, demonstrating the gap between the turbine end-plates and the flume wall

Accounting for the space at the side of the rotor reduces the proportion of the area occupied by the device and periphery to $B = 0.47$. While a reduction in blockage ratio from 0.5 to 0.47 initially appears relatively insignificant, Figure 7.58 demonstrates that at a Froude number of Fr = 0.14, the average during the experimental tests, reducing the blockage ratio from 0.5 to 0.47 results in a decrease in the available power by a factor of 0.86, as predicted by LMADT-OCF.

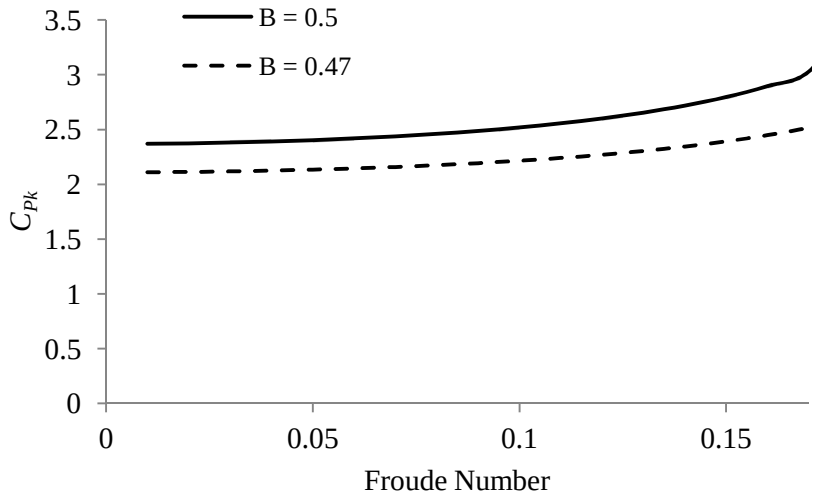

Figure 7.58 - Predictions using LMADT for Open Channel Flow (Houlsby et al., 2008a) of the peak attainable kinetic power coefficient for devices of blockage ratios of 0.5 and 0.47

A blockage correction can be applied by using LMADT-OCF to calculate the ratio of available power for each experimental test, at blockage ratios of 0.5 and 0.47, using the value of thrust predicted in the NS-BE-FS model. Applying this blockage correction to the power coefficients predicted by the NS-BE-FS model, reduces the mean ratio of C_{Pkn}/C_{Pke}, over the range of $B = 0.5$ results, to 0.98 with a standard deviation of 0.098, as shown in Table 7.8. A

blockage correction cannot be applied to the higher blockage data, due to a theoretical supercritical bypass at the relevant Froude number flows.

	NS-BE-FS		**NS-BE-FS blockage corrected**	
	Average	St. dev	Average	St. dev
3 blade	1.13	0.11	0.97	0.10
6 blade	1.21	0.062	1.04	0.05
Pitched	1.12	0.13	0.97	0.11
Over-all	1.11	0.12	0.98	0.10

Table 7.8 – Ratios of kinetic power coefficient predicted by the NS-BE-FS model, with and without blockage correction, to experimental results for parallel-bladed experiments

Due to the two-dimensional nature of the NS-BE models it is not possible to incorporate the effect of flow past the sides of the device, although it should be noted that a full scale device is expected to be made of many multi-bay devices in a fence array. It is there anticipated that the depth ratio will be more accurate when simulating a full scale device.

7.4.5. Comparison of NS-BE and NS-BE-FS blade forces

The increased velocity through the turbine due to the constraint of the free surface has caused the forces produced by the rotor blades to increase, relative to the rigid lid model, resulting in an over-estimate of the power produced by the device. It is thought that the most significant influence on this over-estimate is the simulation of a higher two-dimensional blockage ratio than the three-dimensional blockage ratio of the experimental turbine. However, it is hypothesised that the blockage ratio simulated by the NS-BE and NS-BE-FS models will be representative of the blockage ratio of a full scale, multi-bay device, where gaps between devices will be a smaller proportion of the channel area.

If there are no appreciable differences in the forces predicted by the NS-BE and NS-BE-FS models, the economies in simulating a rigid lid model, as opposed to simulating the free surface deformation, would suggest that the NS-BE model should be used for future simulations. However, if the differences are significant, the additional computational time will result in a more accurate model of the blade forces, which will in turn allow for a greater confidence in predictions of the operating lifetime of a device design.

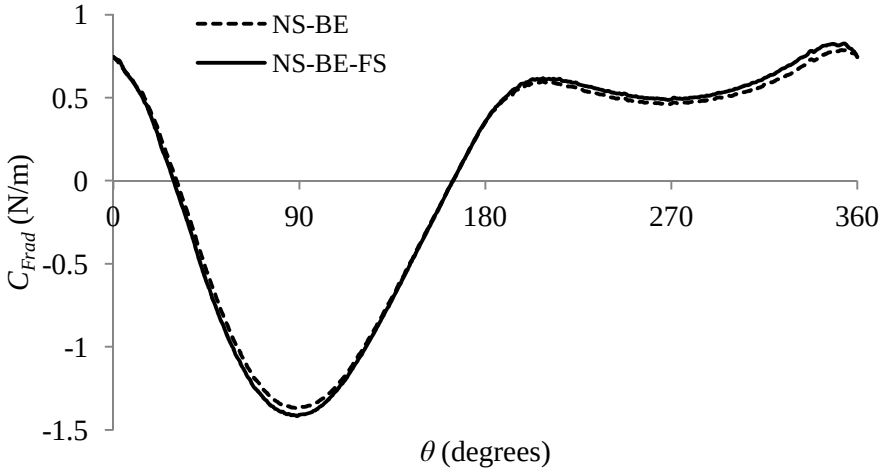

Figure 7.59 - Radial force coefficient predicted using the NS-BE and NS-BE-FS models for the six parallel bladed device at a Froude number of 0.13, a blockage ratio of 0.5 and at λ_p=3.1

As shown in Figure 7.59 for a Froude number of 0.13 the effect of modelling the free surface is relatively insignificant on the radial force, which is the dominant force in the structural analysis. The peak-to-peak amplitude of the radial force is increased by a factor of only 1.04. As illustrated in Figure 7.60, this effect becomes more significant as the Froude number is increased, where modelling the free surface deformation at a Froude number of 0.21 causes an increase in the peak-to-peak amplitude of the predicted radial force by a factor of 1.11. In order to accurately predict the blade forces that are produced in higher Froude number flows, the NS-BE-FS is used for the structural analysis of Chapter 8 and the case study of Chapter 9.

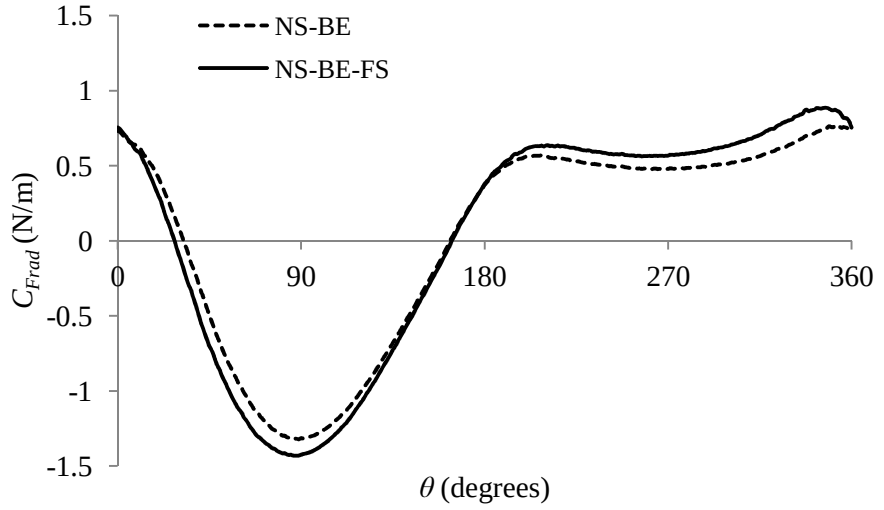

Figure 7.60 - Radial force coefficient predicted using the NS-BE and NS-BE-FS models for the six parallel-bladed device at a Froude number of 0.21, a blockage ratio of 0.5 and at λ_p=3.1

Analysis of the forces predicted by the NS-BE and NS-BE-FS models are conducted using the blade forces at the tip speed ratio of peak power. However, the mean ratios of $\lambda_{pn}/\lambda_{pe}$ for

the NS-BE and NS-BE-FS models, over the range of the compared tests, are 1.12 and 1.16 respectively. Assuming that the blade forces scale as predicted by the preliminary analysis of Chapter 3, it would be anticipated that the blade forces are over-estimated by factors of 1.26 and 1.35 for the NS-BE and NS-BE-FS models respectively.

It can therefore be assumed that the forces predicted by the NS-BE-FS at the predicted values of λ_p will be an overestimate of the true forces experienced by the blades. A structural analysis using these forces can therefore be assumed to be conservative.

7.5. Application to truss turbine

The NS-BE and NS-BE-FS models are limited to two-dimensional analyses of the THAWT device. While this is unsuitable for a detailed analysis of the truss configuration of the device, the effect on the hydrodynamic performance of the truss geometry can be loosely explored, and the change in the blade forces for use in future structural analyses can be predicted.

As shown in Figure 7.61, the radius of the straight truss blades varies at each end and along the entire blade length. However, the radii of the blade ends in the experimental rotor of Chapter 4 have been chosen so that the mean blade radius matches the parallel device at 0.25m. It is therefore anticipated that a two-dimensional analysis of the truss device with a radius of 0.25m should be a good approximation for the mean active radius of the rotor.

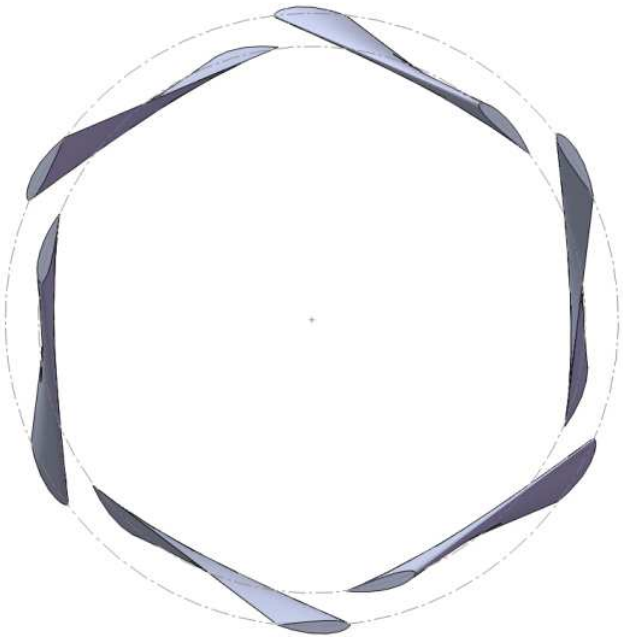

Figure 7.61 - An axial view in a rendered image of the blades of the truss turbine

When predicting the performance of a swept wing, it is common to calculate the lift produced by the hydrofoil due to the component of flow normal to the blade axis, which is

simply a cosine reduction of the free-stream velocity (Abbott and Von Doenhoff, 1959). The blades of the truss configured THAWT device sweep in both the radial and tangential direction. The average radial sweep angle of the experimental prototype is 1.96°, which is likely to have a negligible effect on the direction and magnitude of blade forces, when compared to the parallel configuration. However, the average tangential sweep of the blades is 12.0°, and would be anticipated to reduce the radial blade force acting on the blade by approximately 4%, predicted using the cosine reduction of free-stream velocity. Considering that future variations of the turbine may exhibit higher sweep angles, it is felt that the effect of the tangential sweep on the blade hydrodynamics should be accounted for.

The effect of applying the cosine rule to the swept blades of the truss configured THAWT device is to marginally increase the angle of attack perpendicular to the blade axis and to reduce the magnitude of the force produced by the blades. There is no predicted reduction in the lift to drag ratio of the hydrofoils, which would suggest that the efficiency of the device should remain relatively unchanged. However, the power produced and true efficiency of the truss device during experiments were reduced when compared to the parallel-bladed device. While the application of the cosine normalisation method is accurate for attached flow, research shows that swept wings, during transition or stall, experience detrimental changes in the lift and drag which are not predicted (Carta, 1985, Uranga, 2011). At the Reynolds number experienced by the experimental turbine of Chapter 5, where transition effects are likely to be significant, the effect of blade sweep may have had a substantial impact on the device performance. The variation of this effect as the Reynolds number is increased to a full scale device is unclear.

Numerical simulations of swept wings have shown that the pressure-lift and drag coefficients, calculated using the velocity component normal to the blade axis, remain approximately unchanged over a range of sweep angles (Uranga, 2011). However, the path of the flow across the chord tends to follow a path close to the free-stream direction, which would suggest that the magnitude and component of viscous drag is unlikely to vary from that calculated in the free-stream direction.

In order to simulate this in the NS-BE-FS simulations, a method similar to that used by McIntosh (2009) has been implemented, where the coefficient drag at zero angle of attack is taken as an approximate viscous component. Additional drag due to blade incidence is taken

as an approximate inviscid drag coefficient, which is applied in the direction perpendicular to the blade axis, as shown in Figure 7.62.

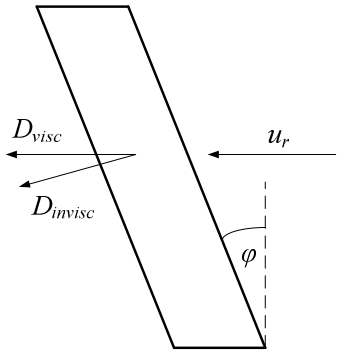

Figure 7.62 - Direction of drag components on a swept blade

In this process the viscous drag is calculated using the viscous drag coefficient and the true resultant velocity. The pressure-form lift and drag produced by the hydrofoils are calculated using the vector of resultant velocity, which has been projected onto a plane perpendicular to the blade axis, U_{r*}, as shown in Figure 7.63.

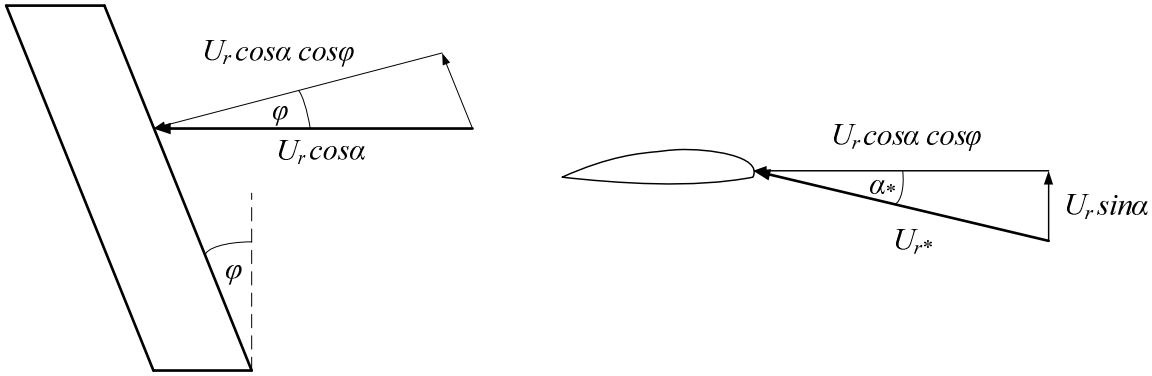

(a) in plane parallel to blade chord and blade axis *(b) perpendicular to blade axis*

Figure 7.63 - Components of velocity acting on a swept blade

By applying a sweep to the rotor blades, the angle of attack perpendicular to the blade axis is marginally increased. This results in an increase in the tip speed ratio of peak power, in order to maintain the optimum distribution of angle of attack.

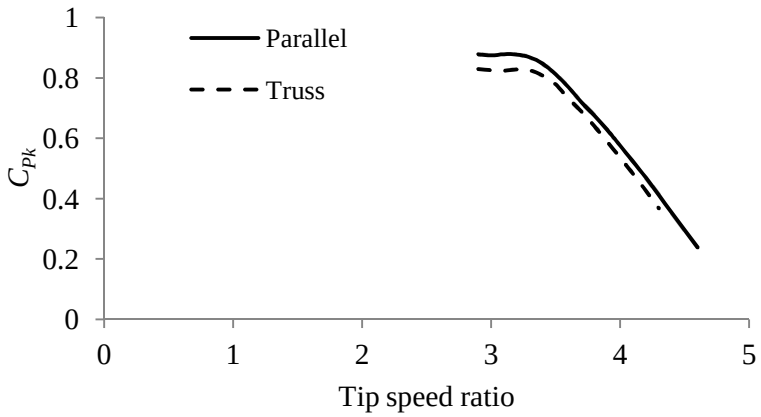

Figure 7.64 - Comparison of power curves for the truss and parallel case using the NS-BE-FS model

As shown in Figure 7.64, the predicted power of coefficient for the truss rotor is reduced by a factor of 0.94, when compared to the parallel device, which is less severe than the reduction measured during experiments of 0.92. The disparity between the experimental results and the numerical simulations are assumed to be a result of the additional effects of sweep on a hydrofoil during transition or stall.

7.6. Limitations of the NS-BE models

Whilst the NS-BE and NS-BE-FS models are able to simulate the performance of the parallel-bladed device with sufficient accuracy, it should be noted that several aspects of the flow physics and the flow phenomena of a full scale device have been modelled.

Due to the two-dimensional nature of the NS-BE models three dimensional flow phenomena have not been accounted for. A more comprehensive model of the device should simulate the blade end effects

7.7. Conclusions

The NS-BE model demonstrates a significant improvement in the accuracy of prediction of the performance of the parallel-bladed THAWT device over previous models. The flexibility of the model allows many variants of the turbine configuration and upstream flow parameters to be accurately simulated. The fidelity of these simulations, when compared with the experimental results, suggests that a time averaged, actuator cylinder, representation of the turbine rotor is suitable for obtaining approximations of the turbine performance and blade forces.

As well as allowing the performance and forces of the device to be predicted, the ease of measuring parameters such as the flow induction factors and hydrofoil angles of attack allows

the hydrodynamics behind the turbine to be better understood. The NS-BE model has highlighted the fact that negative pitch not only contributes to the reduction in blade forces and stresses by reducing the operating tip speed ratio, but the amount of power produced is maintained by increasing the amount of power from the downstream half of the device.

By applying a free surface approximation to the basic NS-BE model, resulting in the NS-BE-FS model, the predicted kinetic power coefficient is increased. However, applying a blockage correction using LMADT-OCF, and comparing with the previous experimental results, indicates that the NS-BE-FS model under-estimates the performance of the $B = 0.5$ devices by a factor of 0.98 and with a standard deviation of 0.098. It is felt that the NS-BE-FS model is sufficiently accurate for application to the subsequent structural analyses.

It is noted that the model would be improved by a more accurate model of the blade performance characteristics. This would ideally be capable of simulating the effects of a curved blade in Darrieus motion, undergoing dynamic stall.

Chapter 8

Finite Element Structural Analysis

The main anticipated benefit of the truss configured THAWT device, over existing designs of tidal stream turbine is that it can be relatively easily scaled, allowing energy to be extracted from a large area of flow, while minimising the complexity of the device and the number of foundations. The ability of the device to produce power has been demonstrated experimentally in Chapter 5, but the structural performance of such a design must be explored to assess its feasibility and how it might be optimised. The blade forces that act on the THAWT device have been predicted using the NS-BE-FS code in Chapter 7, but a method is required to predict how these forces will be transferred to the foundations and the stresses that will be induced in the rotor blades.

This chapter outlines the development of a numerical finite element model of the THAWT device, which can be used to predict the stresses induced in the members of a rotor. The objective is to allow the analysis of a full scale design to be assessed, and to explore the effects that variations in the design configuration and the upstream flow conditions have on blade induced stresses. An accurate structural model is necessary to understand the trade-off between the hydrodynamic and the structural performance of the THAWT device, which has been previously highlighted by the preliminary analysis outlined in Chapter 3.

8.1. Numerical structural analysis

In order to apply the predicted blade forces predicted in Chapter 7 to the structure of the THAWT device, it was decided that the Finite Element analysis package ABAQUS would be used, due to the flexibility in the range of elements available for analysis, the deep ABAQUS knowledge base within the Department of Engineering Science at Oxford University and the convenience of a commercial FE code, as opposed to writing a custom piece of FE software.

The analysis performed in this chapter is a static analysis of the rotor, which assumes that the only loading is due to the hydrodynamic blade forces and the turbine centripetal acceleration. The validity of these assumptions is explored in section 8.9.

As well as allowing the exploration of the structural properties of the single bay experimental prototypes, described in Chapter 4, a finite element structural model of the THAWT device is extended to model the multi-bay application of the rotor.

8.2. Basic configuration

The basic configuration of device that has been chosen as a metric for comparison against variations in design configuration, is the six parallel-bladed device, as shown in Figure 8.1

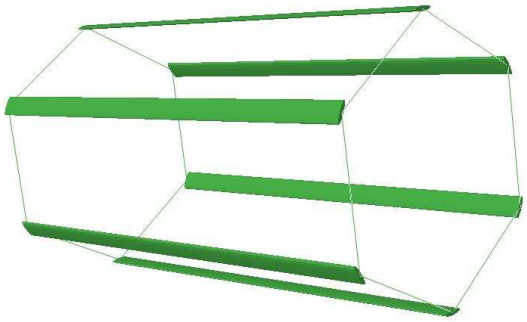

Figure 8.1 – Six parallel bladed device rendered in ABAQUS

The structural performance of this device is explored at full scale with corresponding flow conditions, given in Table 8.1.

	Parallel device
Mean turbine diameter (m)	10.0
Bay length (m)	10.0
Flow depth (m)	20.0
Flow velocity (m/s)	2.0
Froude number	0.143
Fixed offset pitch (°)	0.0
Blade thickness (%)	21.0
Solidity	0.25
Blade chord (m)	1.31

Table 8.1 – Basic case specification of device used for the structural analysis

Simulations of a device of this configuration and scale using the NS-BE-FS model, described in Chapter 7, predict that a peak of approximately 510 kW will be produced at a tip speed ratio of approximately 2.5.

The dimensional scaling of stresses, derived in Chapter 3, indicates that the stresses vary with the inverse square of the blade thickness to chord ratio. While the structural benefits of a thicker hydrofoil are significant, the reduction in hydrodynamic performance due to early boundary layer separation means that high thickness foils are rarely used, so there are very few published data for sections of a greater thickness than 24%. Some work has been

performed in reducing the drag produced by particularly thick sections, for the root sections of conventional axial-flow wind turbines, by using a blunt trailing edge (Dam *et al.*, 2010), but the hydrodynamic performance of these sections is still significantly poorer than a thinner section. Therefore, in order to meet the demands of using a relatively thick hydrofoil section while maintaining sufficient hydrodynamic performance, it was decided that the initial structural analysis of the THAWT device would be performed with a NACA 0021 section, due to the availability of lift-drag characteristics over a range of Reynolds number (Sheldahl and Klimas, 1981).

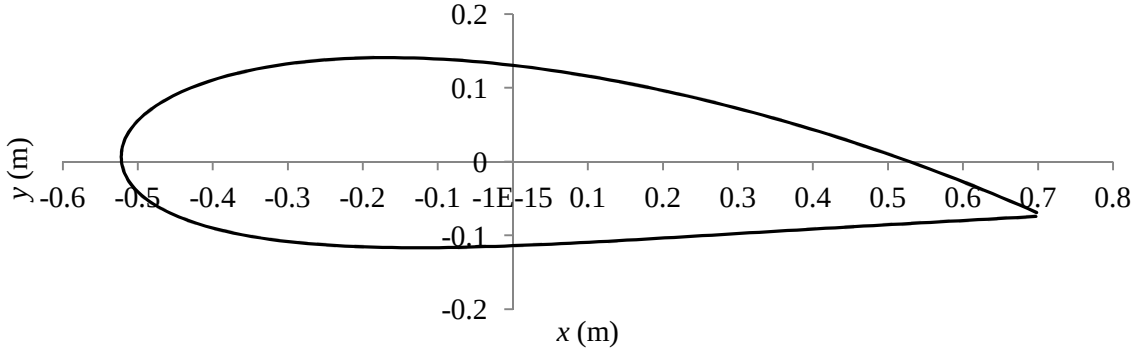

Figure 8.2 – Profile of NACA 0021 section, wrapped onto turbine circumference, used for parallel turbine analysis

With a chosen wall thickness of 40mm, an analysis of the NACA 0021 section using two-dimensional warping elements in ABAQUS predicts that the structural properties of the hydrofoil are as shown in Table 8.2.

I_{xx} (m^4)	8.13×10^{-4}
I_{yy} (m^4)	1.32×10^{-2}
I_{xy} (m^4)	7.55×10^{-4}
J_{eff} (m^4)	2.54×10^{-3}
A_s (m^2)	0.10

Table 8.2 – Section properties of NACA 0021 used in structural analysis

8.3. Adopted material properties

Glass and carbon fibre reinforced composites are commonly used for the construction of wind turbine blades and are a suitable material for the manufacture of the relatively complex THAWT truss blades. While exhibiting the greater strength and modulus, the high cost of carbon fibre reinforced plastics (CFRP) generally limits its use to a reinforcement material (Gurit, 2011). It has therefore been decided to perform initial structural analyses using the properties of glass fibre reinforced plastic (GFRP). A feasible design using GFRP should be

economical and relatively easy to manufacture using existing techniques from the wind industry. Increases in scale or performance could possibly be achieved at a later date using CFRP as a reinforcement material in areas of high stress or where a higher modulus is required.

Designing a structural member using GFRP is far from trivial. The heavily anisotropic nature of the composite material structure has resulted in highly complex techniques for accurately analysing the performance of composite layups (Barbero, 2008). However, the main objective of this structural analysis is to indicate the effect on the structural performance of varying the device configuration, and to provide a rough estimate of the stresses which a material in a given design must be capable of withstanding. It was therefore decided that the detailed design of a blade section is outside the scope of this project due to time constraints, and so an estimate of a suitable blade material layup must be made. This allows the feasibility of such a design to be ascertained by comparing the maximum expected stresses to the capabilities of a composite layup, taking buckling and fatigue into consideration. It was therefore decided to approximate the material as homogenous, with properties that are estimates of a real composite layup.

In a composite layup, uniform direction fibres (UD) are laid in the direction in which the maximum stress is expected to occur and therefore resist the greatest forces in the section. However, layers of UD fibre are weak in directions perpendicular to the reinforcement fibres, because the only resistance to force in these directions comes from the binding resin, which will yield at a stress of an order of magnitude lower than the fibres. Very few composite structures are loaded only in one direction, and so layers of fibre often aligned ±45°, called biaxial layers, are used in a layup to offer resistance to shear and torsion within a section.

Using materials suggested by a senior engineer at Gurit (McEwen, 2009), suppliers of composite materials to the wind and marine technology industries, with a recommended ratio of UD and biaxial fibres, the volume averaged properties of a composite layup of two UD layers for each layer of biaxial material are shown in Table 8.3.

	Sparpreg 1600g (Gurit, 2009a)	**WE91-2 600g (Gurit, 2009b)**	**Combined 2:1 layup**
Ply type	UD	Fleeced biax	
Young's Modulus *E* (GPa)	42	15	35.5
Ply thickness (mm)	1.1	0.7	2.9
Volumetric density (kg/m³)	2000	1600	1900
Shear modulus *G* (GPa)	3.8	3.0	3.6
Tensile strength (MPa)	945	135	750
Compressive strength (MPa)	840	435	740

Table 8.3 – Material properties used for the ABAQUS analysis

8.4. Choice of element type

8.4.1. Blade elements

In a finite element analysis the choice of structural element is driven by maximising the economies of computational effort whilst producing results of sufficient accuracy. A lack of symmetry in the loading of the THAWT device about any axes means that a full three-dimensional analysis is necessary to model the structural response of the device, for which there are three basic element types available (Astley, 1992).

Solid elements use shape functions to describe the displacement of nodes in order to solve for the stress and strain within the element. This approach is very accurate when a high element density is used and is able to model almost any shape of object. However, the large number of nodes that are required to resolve high order solutions within three-dimensional elements result in a large number of degrees of freedom, which are computationally expensive to solve.

Shell elements reduce the number of degrees of freedom that are required, when compared to solid elements, by commonly assuming that lines normal to the material plane remain normal, and therefore reduce each element to a two-dimensional problem. Shell elements are limited to accurately modelling plane stress problems in which the thickness of the object is much smaller than the other two dimensions.

Beam elements further reduce the number of degrees of freedom, by assuming that planes normal to the axis of the element remain plane, which reduces the problem to a one-dimensional solution for each element. Beam elements offer an accurate solution for problems in which one geometric dimension of the object is much larger than the other two, although with the extra facility of shear deformation offered by elements, such as the Timoshenko beam elements, the accuracy of the solution can be enhanced.

Due to the large aspect ratio of the members of the THAWT device, the logical choice is to use beam elements, which offer the greatest economy of computational effort, as they significantly reduce the number of degrees of freedom that must be solved, when compared to solid or shell elements. Beam elements also allow the degrees of freedom at the blade joints to be modified simply, without having to create a full joint design, as would be necessary with solid or shell elements.

Of the Timoshenko beam elements offered by ABAQUS the highest order elements model cubic variations in displacement and linear variations in curvature and stress.

8.4.2. Support structure

The elements of the support structure, which join the blades at the end of the rotor, are initially modelled as rigid members, with all relative displacement between elements constrained. Reference points at the centre of these support structure, shown in Figure 8.3, represent the shafts of the rotor and are constrained with the appropriate boundary conditions.

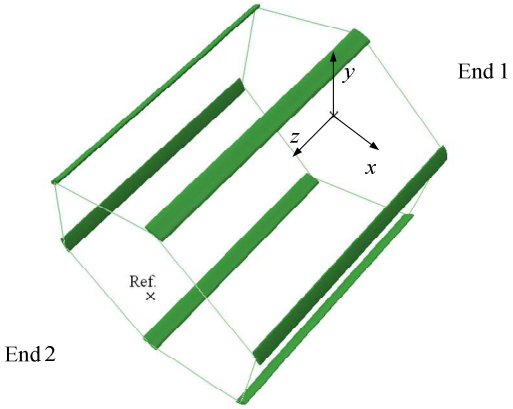

Figure 8.3 – Position of reference points for rigid support degrees of freedom

It is assumed that at full scale the displacements normal to the turbine axes would be fully restrained, however the only constrained moment is about the axis of the rotor, in the direction of torque, as shown in Table 8.4.

	End 1	**End 2**
δ_x	Constrained	Constrained
δ_y	Constrained	Constrained
δ_z	Constrained	Free
θ_x	Free	Free
θ_y	Free	Free
θ_z	Constrained	Free

Table 8.4 – Displacement and moment constraints at the centre of the support structures

8.4.3. Joint degrees of freedom

At the nodes which join the deformable blade elements to the rigid support elements all degrees of freedom are initially constrained, so that the blades are effectively cantilevered at each end, to achieve the theoretical moment distribution shown in Figure 8.4.

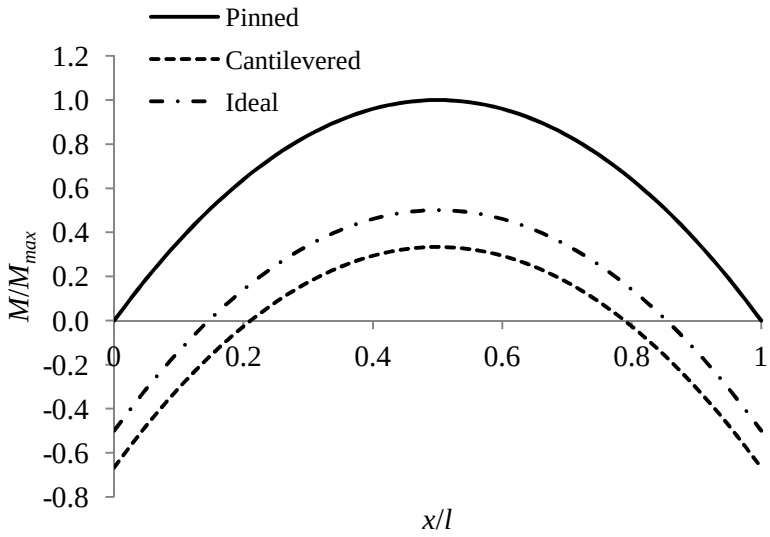

Figure 8.4 – Bending moment distributions in members under uniform load with variation in end degrees of freedom

By constraining all degrees of freedom, the maximum theoretical bending moment occurs at the supports and is two thirds of the maximum theoretical bending moment at the centre of a pinned blade. However, the ideal case is one in which the moment achieved at the supports is half of the maximum theoretical bending moment at the centre of a pinned blade, resulting in the lowest stresses due to bending. These cases will be explored briefly in sections 8.8.6 and 8.8.9 by varying the constrained degrees of freedom at the blade ends and by varying the stiffness of the support elements.

8.5. Order of convergence

The Timoshenko beam elements must be able to accurately represent the turbine blades, which experience a uniformly distributed load about multiple axes, as well as torsion. The highest order terms in the element shape function are cubic, which when differentiated produce a linear expression for curvature and therefore moment. The moment distribution in a beam supporting a uniformly distributed load varies quadratically, so several beam elements are required to model accurately the moment and stress distribution in the beam. A convergence test has been carried out to understand how many elements are required to obtain a solution of a given accuracy, relative to the analytical solution.

Figure 8.5 shows a model of a 10 m long single spanning rectangular member, which has been created with section and material properties to match those described in Table 8.1 and Table 8.3. All of the degrees of freedom of the end nodes have been restrained so that the beam has fixed end supports. If the response of the member to a uniformly distributed loading case is accurately predicted, when compared to the analytical solution, then it can be assumed that the member is capable of accurately representing the turbine blades in the more complex global model.

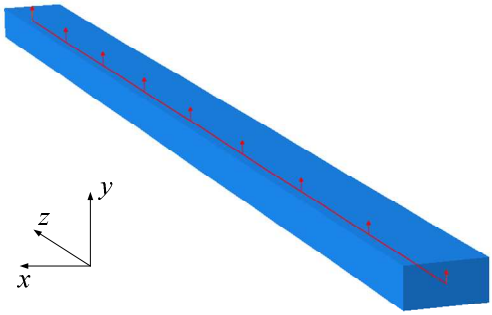

Figure 8.5 – Rendered image of a beam in ABAQUS

A uniformly distributed load of 10 kN/m was applied to the length of the beam in the *y*-direction. The analytical solutions for the displacements, moments and stresses are listed in Table 8.5 and can be calculated using equations 8.1 to 8.3 (Benham and Warnock, 1976).

Deflection due to bending δ_b (m)	8.363×10^{-3}
Deflection due to shear δ_s (m)	3.378×10^{-4}
Total deflection δ (m)	8.701×10^{-3}
Support bending moment (kNm)	83.33
Mid-span bending moment (kNm)	-41.67

Table 8.5 – Analytical solutions to beam bending

$$\delta_b = \frac{wL^4}{8EI} \qquad 8.1$$

$$\delta_s = \frac{wL^2}{8GA_s} \qquad 8.2$$

$$\sigma = \frac{My}{I} \qquad 8.3$$

The results from the FE model are shown in Table 8.6, which demonstrates that the number of nodes required to obtain an accurate solution to the bending problem is relatively small, with more than 14 elements producing an error in the calculation of mid-span moment of less than 1%.

No. elements	Element size (m)	End deflection (mm)	% error	Support moment (kNm)	% error	Mid-span moment (kNm)	% error
2	2.500	8.70	0.01%	62.50	25.00%	-62.5	50.00%
4	1.250	8.70	0.00%	78.13	6.25%	-46.875	12.50%
8	0.625	8.70	0.00%	82.03	1.56%	-42.9688	3.13%
16	0.313	8.70	0.00%	83.01	0.39%	-41.9922	0.78%
32	0.156	8.70	0.00%	83.25	0.10%	-41.748	0.20%
64	0.078	8.70	0.00%	83.31	0.02%	-41.687	0.05%

Table 8.6 – ABAQUS solutions to convergence tests

All subsequent members in this chapter are composed of 20 elements to produce accurate representations of the moment distributions in the blades and supports, while allowing solutions to be obtained in a suitable amount of time.

8.6. Multi-cell analysis technique

The members of the THAWT truss are composed of hydrofoil sections, which are a relatively uncommon section shape for a structural design. Based on the section properties of a given element, ABAQUS calculates the resultant section forces and moments, as shown in Figure 8.6.

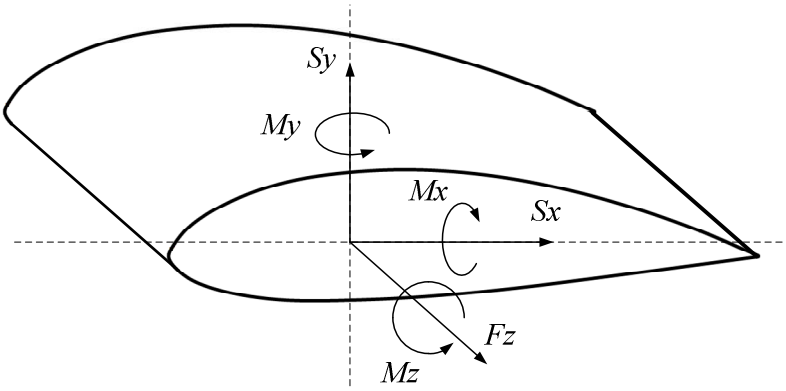

Figure 8.6 – Forces and moments acting on a blade element

Due to the relatively complex combination of forces and moments, the point of maximum stress within the aerofoil section cannot be easily predicted and must be calculated. In order to achieve this, a multi-cell analysis technique has been developed. The analysis of multi-cell sections has previously been solved by Alfano et. al. (1996) using graph theory. However, it was felt that graph theory was not necessary for this task as open sections would not be dealt with.

8.6.1. Basic principles

Bending moments about the *x* and *y* axes and the force in the *z* direction cause longitudinal stresses in the *z* direction. Shear forces in the *x* and *y* direction and the moment about the *z*

axis cause shear stresses to act in the plane of the section and contribute to the total stress acting on an element of the section. Therefore, in order to maintain a simple analysis it has been decided to analyse the stresses in the current axes, rather than converting all forces, moments and section properties to the principal axes of the section. The longitudinal stress generated by the *x* and *y* bending moments and the force in the *z* direction are therefore calculated using equation 8.4.

$$\sigma_z = \frac{y\left(M_x I_{yy} + M_y I_{xy}\right) - x\left(M_y I_{xx} + M_x I_{xy}\right)}{\left(I_{xx} I_{yy} - {I_{xy}}^2\right)} + \frac{F_z}{A_s} \qquad 8.4$$

Equation 8.4 requires the origin for the coordinate system to be located at the centroid of the section, where equations 8.5 and 8.6 are satisfied.

$$\oint x t_w ds = \oint x dA = 0 \qquad 8.5$$

$$\oint y t_w ds = \oint y dA = 0 \qquad 8.6$$

8.6.2. Derivation of shear stress due to shear forces

To calculate the stresses generated by the two shear forces and the axial moment, a set of simultaneous equations are set up to solve for the shear flows within the thin walled section.

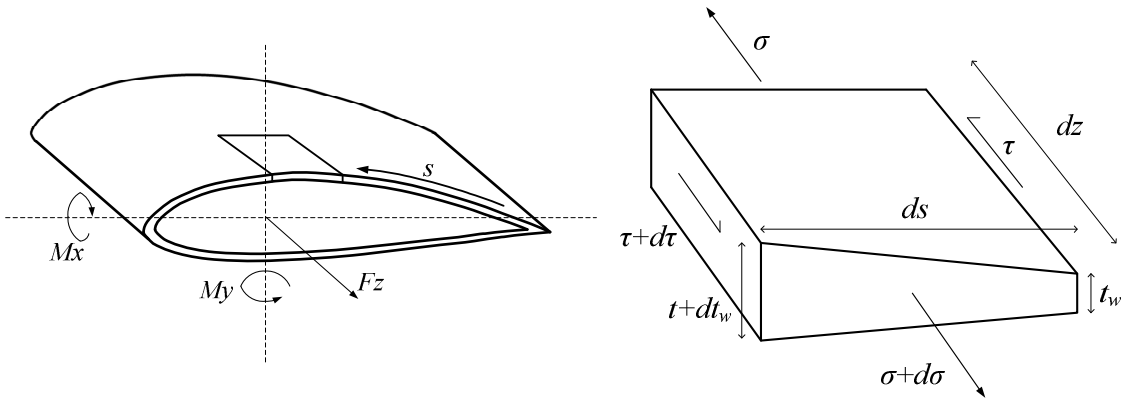

(a) Hydrofoil section *(b) Infinitesimal element of section*

Figure 8.7 – Resultant forces and stresses in a hydrofoil section

A thin walled section under bending and axial force experiences direct stresses and shear stresses, as shown in Figure 8.7. The resultant force acting on the small section in Figure 8.7(b) is equal to the part of the total axial force acting through the section. By balancing the forces acting in the *z*-direction, an equilibrium relationship can be established between the shear force, direct stress and axial force, as shown in equation 8.7.

$$t_w\left(\frac{\mathrm{d}\tau}{\mathrm{d}s}+\frac{\mathrm{d}\sigma}{\mathrm{d}z}\right)+\tau\frac{\mathrm{d}t_w}{\mathrm{d}s}=\frac{t_w}{A_s}\frac{\mathrm{d}F_z}{\mathrm{d}z} \qquad 8.7$$

By noting that the shear flow q is equal to the shear stress τ multiplied by the thickness t_w of a given element, a partial differential equation for the change in shear flow and shear stress with respect to the distance around the section is derived, as shown in equation 8.8.

$$\frac{\mathrm{d}q}{\mathrm{d}s}=t_w\frac{\mathrm{d}\tau}{\mathrm{d}s}+\tau\frac{\mathrm{d}t_w}{\mathrm{d}s} \qquad 8.8$$

Substituting equations 8.4 and 8.8 into equation 8.7 produces an expression for the increase in shear flow due to moments about the section, as shown in equation 8.9.

$$\frac{\mathrm{d}q}{\mathrm{d}s}=t_w\left(\frac{y\left(\mathrm{d}M_xI_{yy}+\mathrm{d}M_yI_{xy}\right)-x\left(\mathrm{d}M_yI_{xx}+\mathrm{d}M_xI_{xy}\right)}{\mathrm{d}z\left(I_{xx}I_{yy}-{I_{xy}}^2\right)}\right) \qquad 8.9$$

Equations 8.10 and 8.11 define the gradient in moment due to the shear force in the given coordinate system.

$$\frac{\mathrm{d}M_y}{\mathrm{d}z}=S_x \qquad 8.10$$

$$\frac{\mathrm{d}M_x}{\mathrm{d}z}=-S_y \qquad 8.11$$

Substituting equations 8.10 and 8.11 into equation 8.9 and integrating around the perimeter of the section allows the shear flow at any point to be calculated, as shown in equation 8.12. This expression contains a constant of integration q_0, which can be resolved using a boundary or closure condition.

$$q=\int_0^s\frac{x\left(-S_xI_{xx}+S_yI_{xy}\right)+y\left(-S_yI_{yy}+S_xI_{xy}\right)}{\left(I_{xx}I_{yy}-{I_{xy}}^2\right)}t_w\mathrm{d}s+q_0 \qquad 8.12$$

8.6.3. Solution technique

The problem is discretised by separating the hydrofoil shape into a series of nodes which are connected by surfaces, over which the shear flow varies, as shown in Figure 8.8.

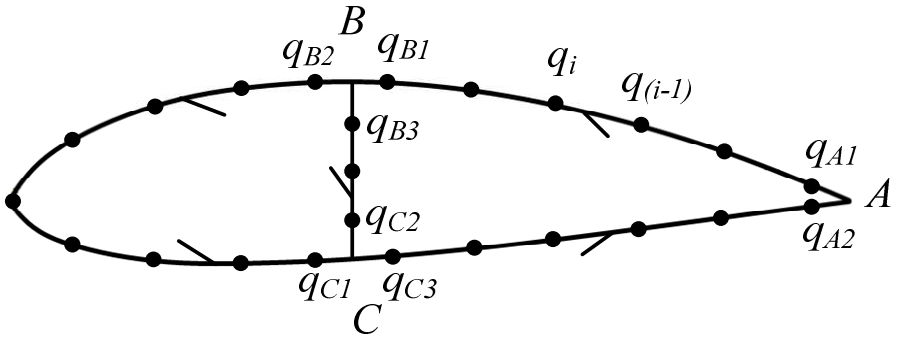

Figure 8.8 – Discretised blade section showing shear flow direction

The increase in shear flow across a surface can be written as shown in equation 8.13.

$$q_i - q_{(i-1)} = \frac{x_i\left(-S_x I_{xx} + S_y I_{xy}\right) + y_i\left(-S_y I_{yy} + S_x I_{xy}\right)}{\left(I_{xx} I_{yy} - {I_{xy}}^2\right)} t_{wi} s_i \qquad 8.13$$

Shear flow continuity equations are included for the nodes which do not have contributing shear surfaces. For the example in Figure 8.8 these would be:

$$q_{B2} = q_{B1} - q_{B3} \qquad 8.14$$

$$q_{C3} = q_{C1} + q_{C2} \qquad 8.15$$

$$q_{A1} = q_{A2} \qquad 8.16$$

Equation 8.16 provides the closure condition, which also implies that the integral of the shear flow around the section is zero, as shown in equation 8.17.

$$\oint \frac{x\left(-S_x I_{xx} + S_y I_{xy}\right) + y\left(-S_y I_{yy} + S_x I_{xy}\right)}{\left(I_{xx} I_{yy} - {I_{xy}}^2\right)} t_w ds = 0 \qquad 8.17$$

With n nodes and m cells, this provides $n - m$ independent equations. To solve for the n values of shear flow and the additional twist per unit length of the section (θ/l), $m + 1$ additional equations are required. For each of the m cells of the section an equation for the twist of the cell is written, as shown in equation 8.18, which is derived from basic torsion theory (Timoshenko and Goodier, 1970).

$$\oint \tau ds = 2A_e G \frac{\theta}{l} \qquad 8.18$$

where A_e is the area enclosed by the mid-line of the profile thickness. By using a single variable for the twist angle, the section is constrained to twist by the same amount in each cell.

The final equation that is required is the specification that the sum of the contributing moments from the shear surfaces should equal the applied torsion, as shown in equation 8.19 (Benham and Warnock, 1976).

$$\oint q r_s ds = M_z \qquad 8.19$$

A solution may now be found which will yield the shear flows around the section and the twist of the section. The actual value of the twist relies on the input of an accurate shear modulus, enclosed area and member length.

8.6.4. Shear centre (X_c, Y_c)

If the section in question is non-symmetric, an applied shear will induce torsion about the axis of the beam. It is possible to calculate the location of the shear centre for the section, the point through which a load should be applied so that no torsion is induced in the section. This can be done by solving a set of slightly modified simultaneous equations to those described in section 8.6.3. Equation 8.19, the sum of the moments due to shear equals the torsion about the blade axis, is replaced with equation 8.20; no twist about the blade axis and a single shear force is applied in the *x* direction.

$$\theta = 0 \qquad 8.20$$

The solutions to the simultaneous equations are the shear flows that occur in a non-twisting section due to a single shear force.

However, there will be a torsion about the centre of the current coordinate system if it is not coincident with the shear centre. Using equation 8.19 the generated torsion can be calculated, which would be opposed if the shear force were placed at a distance Y_c from the centroid as specified by equation 8.21.

$$Y_c = \frac{M_z}{S_x} \qquad 8.21$$

The *x*-coordinate for the shear centre can be calculated using the same technique.

8.6.5. Equivalent torsion constant J_{eff}

The equivalent torsion constant may be calculated using the same technique as outlined in section 8.6.3. Instead of applying shear forces and a torsion to the section, only a torsion, M_z, is applied. J_{eff} is then calculated using equation 8.22.

$$\frac{M_z}{J_{eff}} = G\frac{\theta}{l} \qquad 8.22$$

8.6.6. Method of application

The above technique can be applied to any closed shape of thin walled section. The initial step is to specify an outer profile for the shape, using nodes that are numbered in the same fashion as those in Figure 8.8, i.e. starting at the right hand side and moving anti-clockwise. The thickness of the section can be specified either as uniform or varying at each node point, as shown in Figure 8.9.

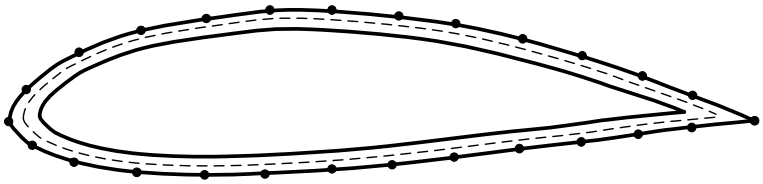

Figure 8.9 – Image showing inner, outer and mid profiles of a noded hydrofoil section

Similar to most thin walled problems, the calculations of shear flow are performed at the mid-section of the wall thickness and so it is necessary to identify node and surface offsets from the outer profile. Figure 8.10 shows that the mid-way nodes (*N*) are located a distance of half the section thickness on a line that runs perpendicular to the vector between the profile nodes (*P*) either side. The distances for each connecting surface (*s*) are easily calculated.

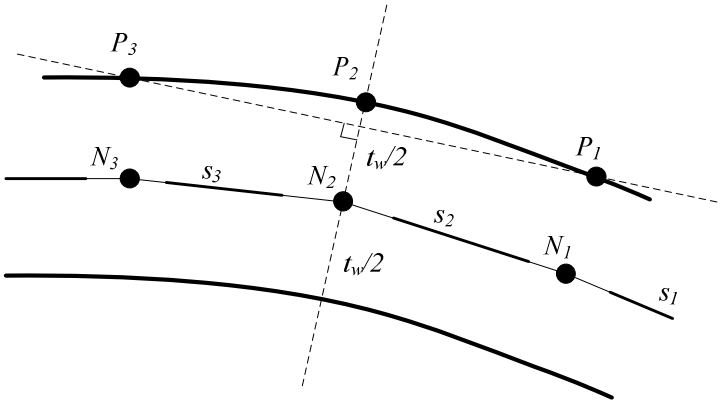

Figure 8.10 – Technique for placing nodes at mid points of section wall thickness

The process of locating the mid-section line can cause intersections at sharp corners, such as the trailing edge of the hydrofoil section, as shown in Figure 8.11. The nodes outside of these intersections are ignored during the calculations of shear flow.

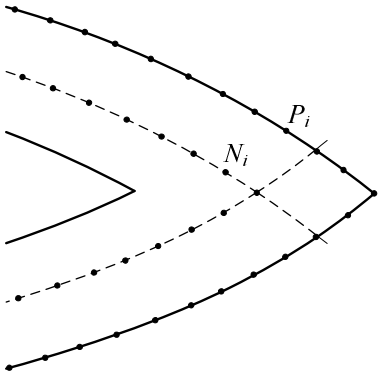

Figure 8.11 – Diagram showing hydrofoil profile nodes and crossing of calculated mid-section

Nodes and surfaces are added for any vertical shear webs which are desired within the section, which can be specified by their percentage distance along the chord. For each cell, a closed “loop” is specified. Each loop contains a list of the included nodes, where the sign of

the node identifier represents a positive or negative contribution to the torsion within the loop, which is used for constructing equation 8.18.

The area of each cell, the entire enclosed area and the total material area are calculated for use in equations 8.4 and 8.18. All node positions are re-centred on the centroid of the section, about which the perpendicular radii are calculated, for use in equation 8.19.

The second moments of area of the section are calculated by simply summing the contribution of each surface using equation 8.23, and the corresponding equations for I_{yy} and I_{xy}.

$$I_{xx} = \int ydA \qquad 8.23$$

The shear centres are calculated using the routine described in section 8.6.4.

All of the accumulated data is stored so that it can be quickly used for the analysis of a beam element without having to be recalculated each time. For each element of hydrofoil section the shear stress can be calculated using the approach outlined in section 8.6.3. The stress due to the bending moment about the *x* and *y*-axes are calculated using equation 8.4, before the maximum total stress, including contributions by the shear stress, is calculated using equation 8.24.

$$\begin{matrix}\sigma_{max} \\ \sigma_{min}\end{matrix} = \frac{\sigma_z}{2} \pm \left\{\left(\frac{\sigma_z}{2}\right)^2 + \left(\frac{\tau}{2}\right)^2\right\}^{1/2} \qquad 8.24$$

The maximum stress within the entire structure can then be easily found by searching.

8.6.7. Multi-cell validation - tube section

In order to assess whether the multi-cell analysis is capable of accurately predicting the resulting stresses in a given section a series of benchmark validation tests have been performed.

The first simple benchmark tests are the torsion and shearing of a circular tube, as shown in Figure 8.12. The bending of the tube is not performed as this is relatively trivial.

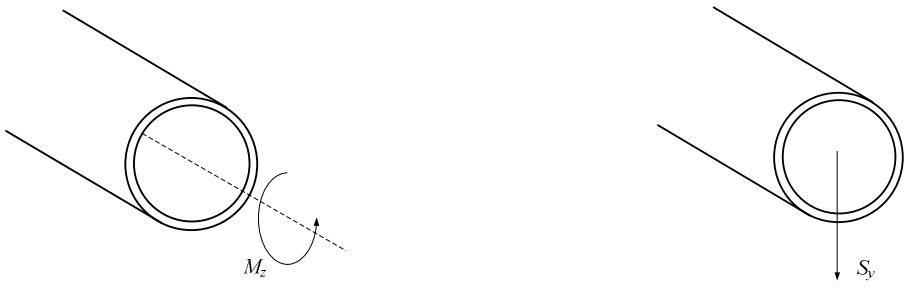

(a) Torsion *(b) Shear*

Figure 8.12 – Validation tests performed on a circular tube section

Table 8.7 shows the dimensions of the tube and the material properties (of mild steel) used for the analysis.

Outer radius (m)	0.03
Wall thickness (m)	0.002
Tube length (m)	0.2
G (GPa)	80.8

Table 8.7 - Tube dimensions and material properties

When a torsion of 0.1 Nm is applied about the axis of the tube section the theoretical shear stress and twist of the section can be calculated using equations 8.25 and 8.26 (Timoshenko and Goodier, 1970).

$$\tau = \frac{M_z r}{J} \qquad 8.25$$

$$\theta = \frac{M_z L}{GJ} \qquad 8.26$$

The section properties, shear stress and section twist predicted using a 72 node multi-cell analysis are compared to the theoretical values in Table 8.8.

	Theory	**Multi-cell analysis**	**Error (%)**
Second moment of area I_{yy}=I_{xx} (m^4)	1.534×10^{-7}	1.532×10^{-7}	0.13
Torsion constant J (m^4)	3.068×10^{-7}	3.058×10^{-7}	0.33
Section area A (m^2)	3.644×10^{-4}	3.652×10^{-4}	0.22
Shear stress τ (Pa)	9.452×10^{3}	9.465×10^{3}	0.14
Section twist θ (°)	8.086×10^{-7}	8.094×10^{-7}	0.10

Table 8.8 - Section properties, shear stress and section twist predicted using torsion theory and multi-cell analysis

The multi-cell analysis technique is satisfactorily able to predict the section properties as well as the shear stress and section twist to within 0.5% of the theoretical calculations.

When a vertical shear force of 1 kN is applied to the tube section the maximum theoretical shear stress can be calculated using 8.27.

$$\tau_{max} = \frac{S_x}{\pi r t_w} \qquad 8.27$$

The shear stress predicted using the multi-cell analysis is compared to the theoretical values in Table 8.9. The multi-cell analysis predicts the maximum shear stress within a satisfactory accuracy.

	Theory	**Multi-cell analysis**	**Error (%)**
Shear stress τ (MPa)	5.488	5.486	0.04

Table 8.9 - Shear stress predicted using torsion theory and multi-cell analysis

8.6.8. Multi-cell validation - box section

A small increase in the complexity of the problem is introduced by simulating torsion and shear for a rectangular section, as shown in Figure 8.13.

(a) Torsion *(b) Shear*

Figure 8.13 – Validation tests performed on a rectangular box section with points of significance highlighted for shear tests

Table 8.10 shows the dimensions of the box section and the material properties (of mild steel) used for the benchmark tests.

Box outer width (m)	0.05
Box outer depth (m)	0.03
Box thickness (m)	0.002
Box length (m)	0.2
G (GPa)	80.8

Table 8.10 - Tube dimensions and material properties

When a torsion of 10 Nm is applied about the axis of the turbine section the theoretical shear stress and twist of the section can be calculated using equations 8.28 and 8.26 (Timoshenko and Goodier, 1970).

$$\tau = 2qA_e \qquad 8.28$$

The section properties, shear stress and section twist for a 40 node box section, predicted using the multi-cell analysis, are compared to the theoretical values in Table 8.11.

	Theory	**Multi-cell analysis**	**Error (%)**
Second moment of area I_{xx} (m^4)	4.513×10^{-8}	4.629×10^{-8}	2.51
Second moment of area I_{yy} (m^4)	1.016×10^{-7}	1.056×10^{-7}	3.94
Torsion constant J_{eff} (m^4)	9.507×10^{-8}	9.385×10^{-8}	1.3
Section area A (m^2)	3.04×10^{-4}	3.11×10^{-4}	2.3
Shear stress τ (Pa)	1.860×10^{6}	1.844×10^{6}	0.86
Section twist θ (°)	2.604×10^{-4}	2.637×10^{-4}	1.27

Table 8.11 - Section properties, shear stress and section twist predicted using torsion theory and multi-cell analysis

The increased error in the multi-cell prediction of the section properties of the rectangular section, relative to tube section, are due to the inaccuracy at the corners of the thin walled

assumption. This has resulted in greater second moments of area and section area than the true values. As the wall thickness is reduced, the error in prediction of the section properties are also reduced. This problem is not anticipated to be as significant when performed on an aerofoil section where there are fewer corners and these are dealt with, as described in section 8.6.6. Despite the relatively poor predictions of the section parameters the shear stress and section twist are predicted to within approximately 1% of the theoretical values, which is deemed acceptable.

When a vertical shear force of 1 kN is applied to the box section the theoretical shear stress can be calculated using equation 8.29 (Timoshenko and Goodier, 1970).

$$\tau = \frac{S_x A' \bar{y}}{t_w I_{xx}} \qquad 8.29$$

The shear stress predicted at the salient points highlighted in Figure 8.13(b) using the multi-cell analysis is compared to the theoretical values in Table 8.12. The multi-cell analysis predicts the maximum shear stress within a satisfactory accuracy.

	Theory	**Multi-cell analysis**	**Error (%)**
Shear stress at a τ (Pa)	0	0	0.00
Shear stress at b τ (Pa)	7.455×10^6	7.239×10^6	2.90
Shear stress at c τ (Pa)	9.617×10^6	9.635×10^6	0.19

Table 8.12 - Shear stress predicted using torsion theory and multi-cell analysis

The error in shear stress at the corner of the rectangle section is relatively high due to the thin walled assumptions of the multi-cell analysis technique. However, the maximum shear stress is calculated with a relatively high accuracy.

The accuracy of the section property calculation and the stress prediction both increase as the wall thickness is decreased.

8.6.9. Multi-cell validation - hydrofoil section

In order to assess the accuracy of the multi-cell analysis technique on a hydrofoil section, which will be the main structural member for the THAWT device, the properties of the section described in section 8.2 have been predicted using the multi-cell analysis and compared to a two-dimensional ‘warping element’ meshed model in the commercial FE program, ABAQUS. In this model the nodal degrees of freedom of the finite element, cross-section model represent warping displacements, in a similar fashion to Saint-Venant’s “semi-

inverse method" (Timoshenko and Goodier, 1970), which allow the shear centre and beam torsional rigidity to be accurately determined.

The predictions of the section properties are given in Table 8.13.

	ABAQUS	Multi-cell analysis	Error (%)
Second moment of area I_{xx} (m^4)	8.13×10^{-4}	7.95×10^{-4}	2.2
Second moment of area I_{yy} (m^4)	1.32×10^{-2}	1.29×10^{-2}	2.2
Product moment of area I_{xy} (m^4)	7.55×10^{-4}	7.27×10^{-5}	3.8
Torsional constant J_{eff} (m^4)	2.54×10^{-3}	2.34×10^{-3}	6.1
Material area A_m (m^2)	0.101	0.100	0.7
Shear centre X_c (m)	-0.20	-0.21	4.4
Shear centre Y_c (m)	6.42×10^{-3}	5.13×10^{-3}	20.1

Table 8.13 – Predictions of the hydrofoil section properties by ABAQUS and multi-cell analysis

The second moments and product of inertia, and material area are calculated within a satisfactory error. The larger errors in the calculation of the torsional constant and positions of the shear centre are due to the inaccuracies of the thin walled assumptions. However, neither value is considered to be critical in the calculation of the structural performance of the THAWT device. The significant decrease in time required to calculate the stresses within the section, when compared to the two-dimensional meshed model, result in a satisfactory level of performance from the multi-cell analysis technique.

While the multi-cell technique allows for the calculation of shear stresses within a multi-cell structure, only single celled sections have been analysed in this thesis, due to the lack of significant additional strength from shear webs, described in Chapter 9. However, the multi-cell technique allows for the more detailed design of hydrofoil sections in future work.

8.7. Uniform load

In order to build confidence in the structural FE model, the complexity of the problem is progressively incremented. While the blade loading of the physical THAWT device varies similar to that predicted in Chapter 7, a preliminary analysis is carried out in which a uniform load is applied to the model. During this preliminary analysis the expected theoretical section forces and moments can be calculated and used as a validation.

8.7.1. Single bay parallel model

The NS-BE-FS model predicts that a parallel-bladed device of design configuration and flow parameters, described in Table 8.1, will induce an average stream-wise thrust of 525 kN.

In this preliminary analysis the blade forces are applied as a distributed load in the stream-wise direction of 8.75 kN/m on each blade, as shown in Figure 8.14.

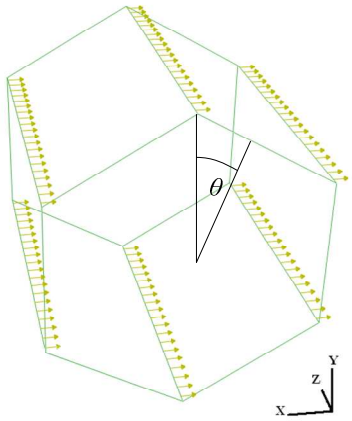

Figure 8.14 – Rendered image of the uniformly distributed load in ABAQUS

The structural performance of the turbine is simulated for incremental rotations of 5° about the rotor axis. The moments and magnitudes of mid-span displacement predicted by the FE structural model accurately match those predicted by simple beam theory, as shown in Figure 8.15. For each rotation of the rotor, the stress at each node of the hydrofoil section is calculated using the multi-cell analysis technique described in section 8.6.

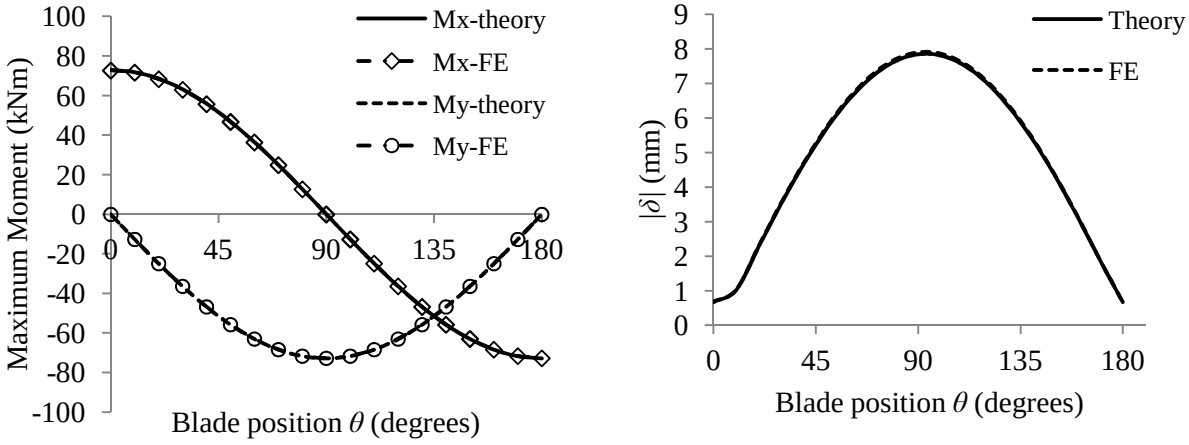

(a) Maximum moment *(b) Root sum of squares of displacement*

Figure 8.15 – Comparison of theoretical predictions and finite element simulations

Table 8.14 shows that the maximum stress induced in the parallel-bladed device is due almost exclusively to the component of bending stress.

Maximum stress (MPa)	16.46
Component due to bending (MPa)	16.69
Component due to axial force (MPa)	-0.28
Component due to shear (MPa)	0.94

Table 8.14 – Maximum stress and components of that stress during a rotation of the single bay uniformly loaded parallel-bladed device

The maximum stress occurs due to the bending component about the weaker *x*-axis of the hydrofoil section, which results in the point of maximum stress on the top surface of the hydrofoil, at the point of greatest distance from the neutral axis, as shown in Figure 8.16.

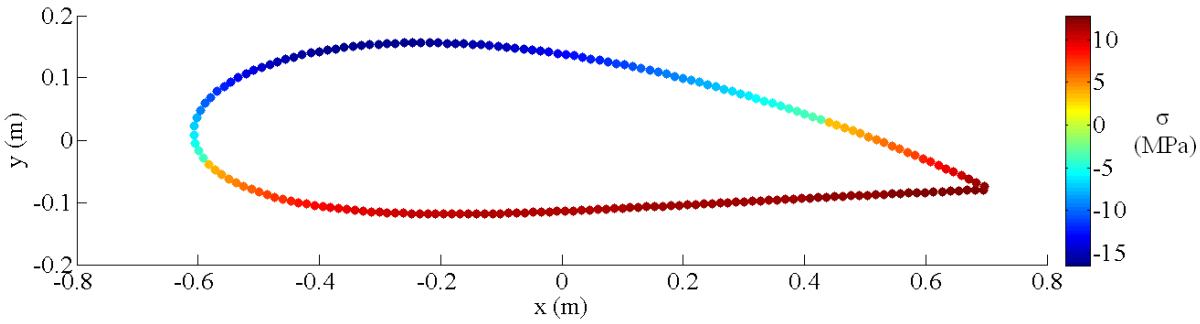

Figure 8.16 – Distribution of stress around the hydrofoil section for the element of maximum stress in the parallel bladed device with a uniform load

8.8. NS-BE-FS loading

While confidence has been established in the FE structural model with simple uniform loading, the accurate prediction of the structural response of a deployed turbine will depend heavily on the accuracy of the loading applied to the model. The NS-BE-FS model offers the most accurate prediction of blade forces after validation against experimental results in Chapter 7.

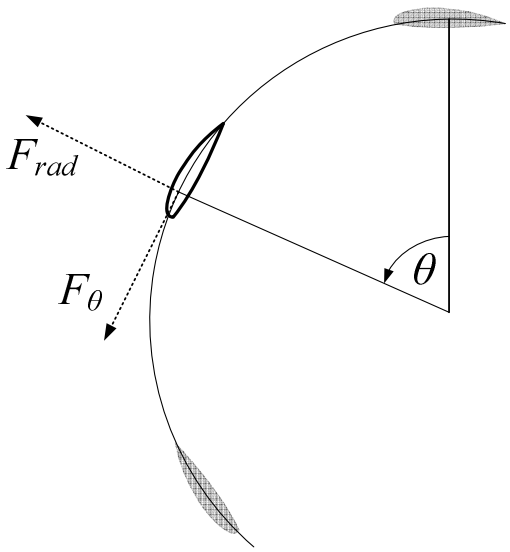

Figure 8.17 – Sign convention of blade forces in a plane perpendicular to the blade axis

Components of radial and tangential force are predicted by the NS-BE-FS model for use in the structural analysis, defined as positive in the directions shown in Figure 8.17.

8.8.1. Comparisons of loading

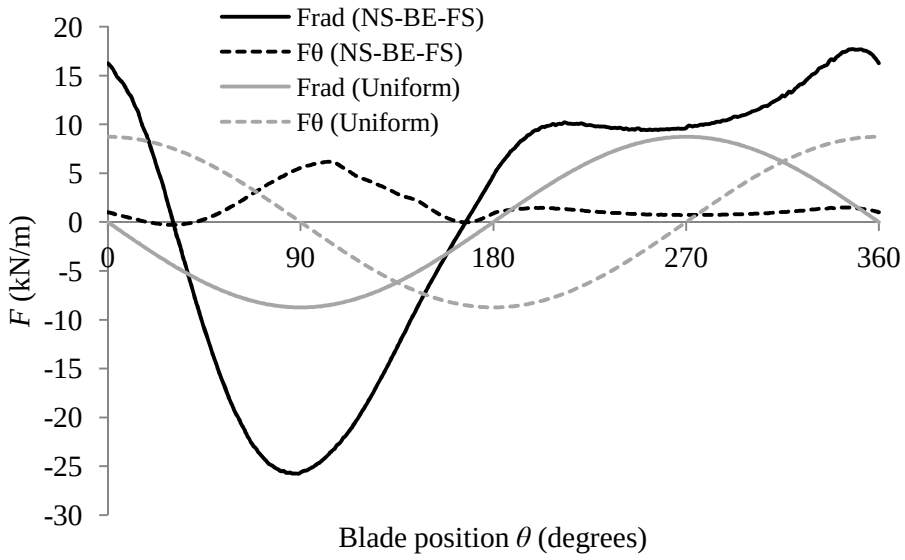

Figure 8.18 – Radial and tangential components of distributed force predicted by the NS-BE-FS model, for the parallel device of configuration and flow parameters given in Table 8.1

As shown in Figure 8.18 the predicted loading by the NS-BE-FS model for the parallel-bladed device differs significantly from the uniform loading case, with the vast majority of the blade force concentrated in the radial direction. The peak in radial force, which is anticipated to produce the peak stresses via bending about the weaker blade axis, is approximately three times greater than the peak radial force applied in the uniform loading case, and occurs at approximately 89° of rotation.

8.8.2. Multi-bay parallel

Figure 8.19 shows a multi-bay variant of the parallel bladed device, where the degrees of freedom of the blade ends are restrained, which is necessary so that the structure does not become a mechanism.

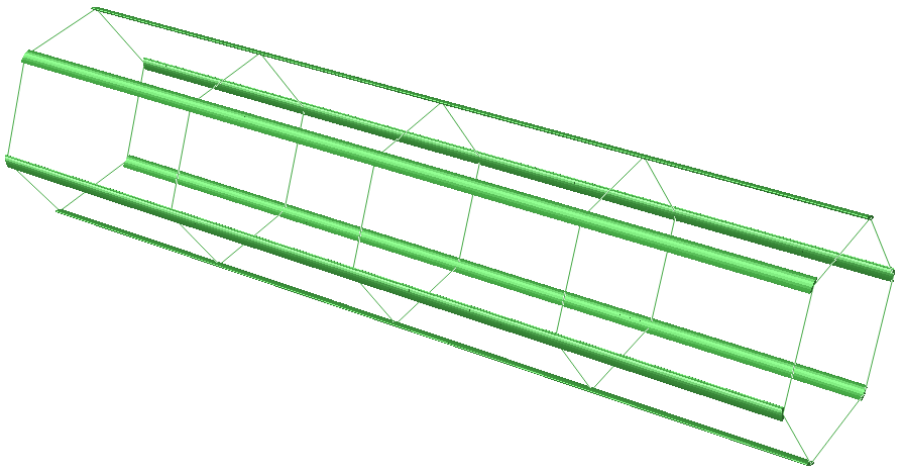

Figure 8.19 – Rendered image of a four bay parallel-bladed rotor in ABAQUS

As shown in Figure 8.20, the concentration of radial load in the NS-BE-FS simulations at the upstream point causes an increase in the maximum stress in the single bay configuration from 16.5 MPa to 52.1 MPa.

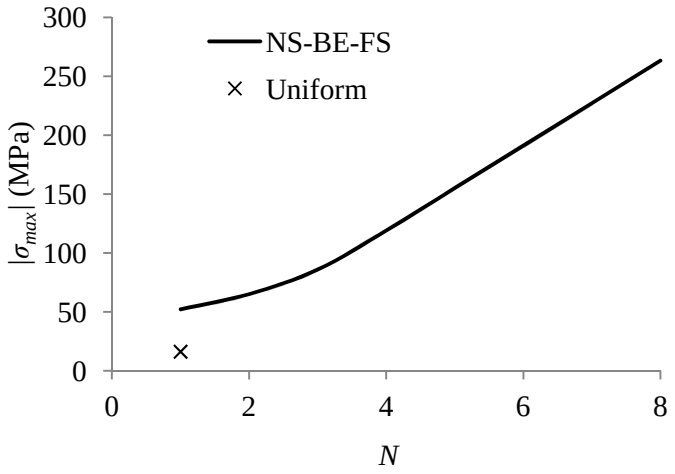

Figure 8.20 – Variation in maximum absolute stress for the parallel-bladed, uniformly loaded single bay and NS-BE-FS loaded multi-bay devices

Whilst it might be expected that the bending stress should increase quadratically with the number of bays, or length of rotor, Figure 8.20 actually shows an approximately quadratic increase until three bays of device, after which the stress scales linearly with the number of bays. For up to three bays of device the high peak in radial force at the upstream point of the rotor dominates the magnitude of the peak stress, through bending about the hydrofoil minor axis, due to the local loading. However, Figure 8.21 shows that a parallel-bladed rotor with several bays does not deform like a beam and normal planes do not remain plane to the 'neutral axis'. Instead each bay shears individually and so the hydrodynamic loads are transferred from bay to bay via a shearing action rather than a bending action. The increase in stress at the end supports is therefore due to the increase in stream-wise force on the rotor, with an increasing number of bays, rather than an increase in transferred moment, which would be expected in a conventional beam.

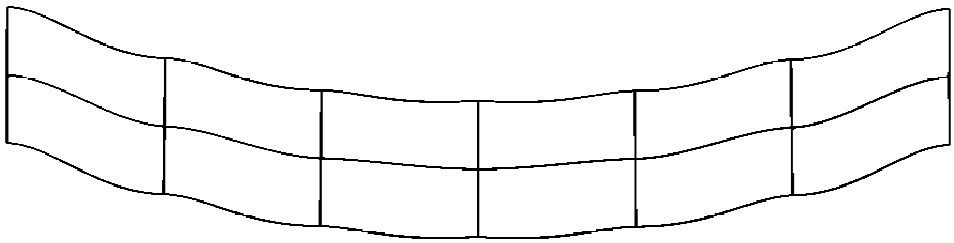

Figure 8.21 – Exaggerated image of deflection of a six bay parallel-bladed device under uniform load

The deflection of a uniformly loaded beam with built-in supports would be expected to increase quartically with length. However, due to the shearing of the bays the deflection of the device with three or more bays actually increases approximately cubically with the number of bays, as shown in Figure 8.22.

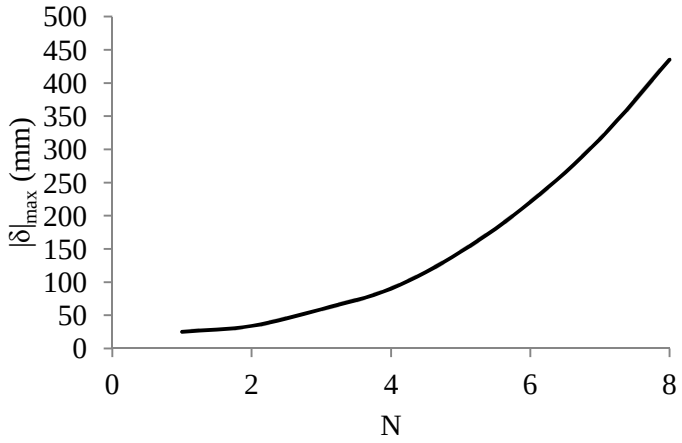

Figure 8.22 – Deflection of a six bay parallel-bladed device under NS-BE-FS load

The maximum stress in the single bay device occurs at the upper surface of the hydrofoil section, because of the relatively large bending moment due to hydrodynamic lift occurring about the weaker axis of the section, and little moment is generated about the stronger axis of the foil. However, when the device is used in a multi-bay configuration the maximum stress occurs at the trailing edge of the foil, the point furthest from the neutral axis of the section, as shown in Figure 8.23.

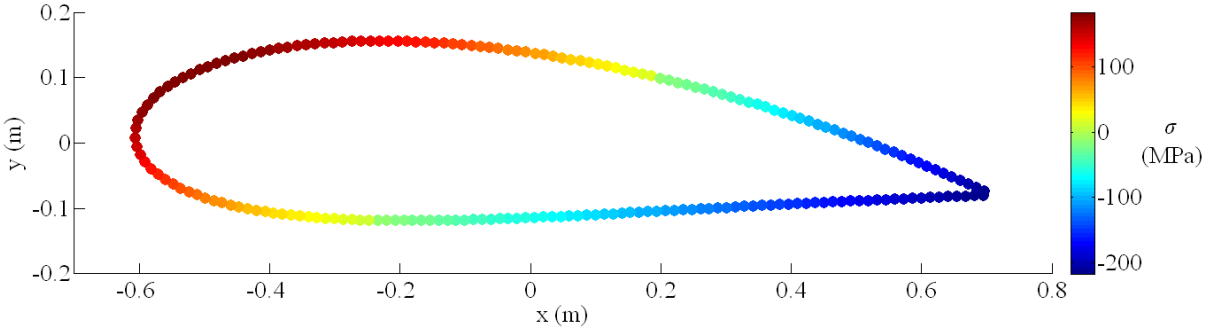

Figure 8.23 – Distribution of stress around the hydrofoil section for the element of maximum stress in the multi-bay parallel bladed device

This occurs in the blade members whose chords are parallel with the main direction of thrust and deflection, which act as shear webs and resist a greater proportion of the shear force and moment at the rotor ends than blades whose chords are perpendicular to the main direction of thrust and deflection. Figure 8.24 shows that as the number of bays increase, the

bending moment and shear acting in the plane of the blade chord increase significantly when compared to those acting in the plane normal to the blade chord.

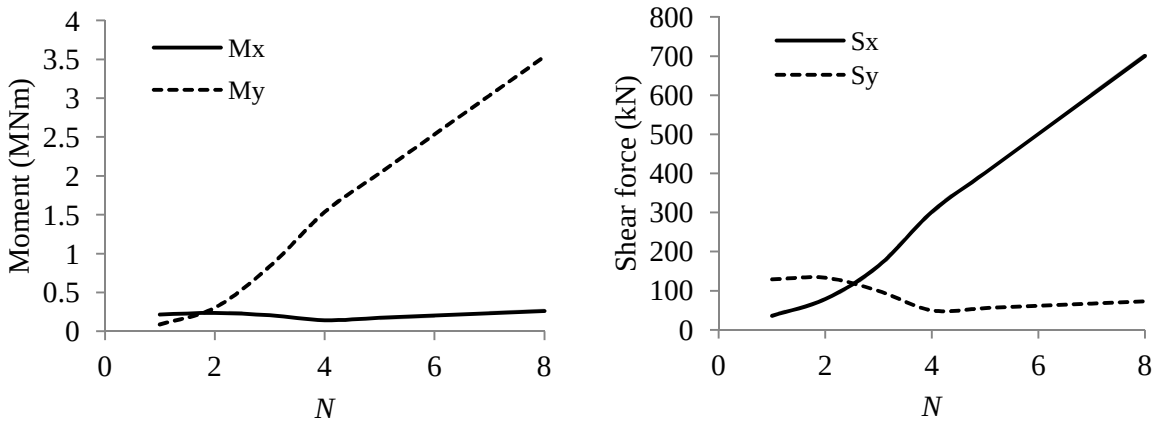

(a) Moment *(b) Shear force*

Figure 8.24 – Components of moment and shear at the point of maximum stress in the NS-BE-FS loaded parallel-bladed device

As shown in Figure 8.25, the maximum stress in the parallel-bladed device occurs almost exclusively due to the increasing bending stress. While the shear force in the chord-wise direction increases rapidly with the number of bays, the upper and lower hydrofoil surfaces act like shear webs, so that the component of shear stress does not increase significantly. The component of axial stress is negligible.

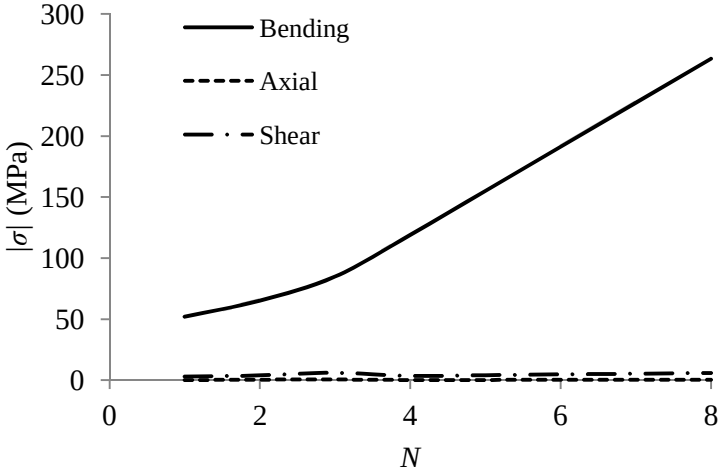

Figure 8.25 – Variation in components of the maximum stress with an increase in the number of bays for the NS-BE-FS loaded parallel-bladed device

The maximum stress always occurs in the elements which join the blades to the end supports, for all number of bays.

8.8.3. Single bay truss model

The design parameters for the truss configuration, which has been modelled for comparison with the parallel bladed variant, are given in Table 8.15. The section properties are given with reference to a plane perpendicular to the blade.

Mean turbine diameter (m)	10.0
Solidity	0.25
Blade outer radius (m)	5.54
Blade inner radius (m)	4.94
Bay length (m)	10.0
Angle subtended by blade ξ (°)	46.1
Average tangential swept angle φ (°)	20.4
Blade length (m)	10.8
Fixed offset pitch (°)	0.0
Blade thickness (%)	21.0
Blade chord (m)	1.22

Table 8.15 – Truss configuration specification of device used for the structural analysis

In a similar fashion to the experimental device, described in Chapter 4, at the joints with the support members the blades are offset circumferentially and each element of the blade member is oriented so that the blade chord is tangential to the pitch circle, as shown in Figure 8.26. This results in a blade which twists along its length.

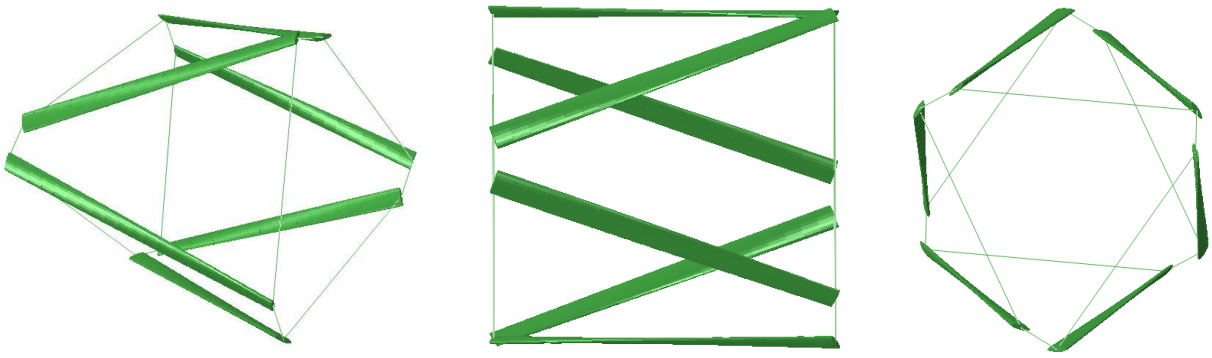

(a) Oblique view *(b) Stream-wise view* *(c) Axial view*

Figure 8.26 – Rendered images of a single bay truss device in ABAQUS

The results in Chapter 5 and Chapter 7 show that for a given set of flow parameters and averaged design parameters, the peak power output for a parallel and truss configured device occur at a different tip speed ratios and values of thrust. The NS-BE-FS model predicts that the operating conditions for a parallel and a truss configured device, defined in Table 8.1 and Table 8.15, experiencing a set of flow conditions, matching those given in Table 8.1, produce peak performances as described in Table 8.16.

Configuration	Parallel	Truss
Peak power (kW)	510	485
Tip speed ratio of peak power	2.5	2.7
Thrust (kN)	525	511

Table 8.16 – Performance of the full scale parallel and truss device, as predicted using the NS-BE-FS model

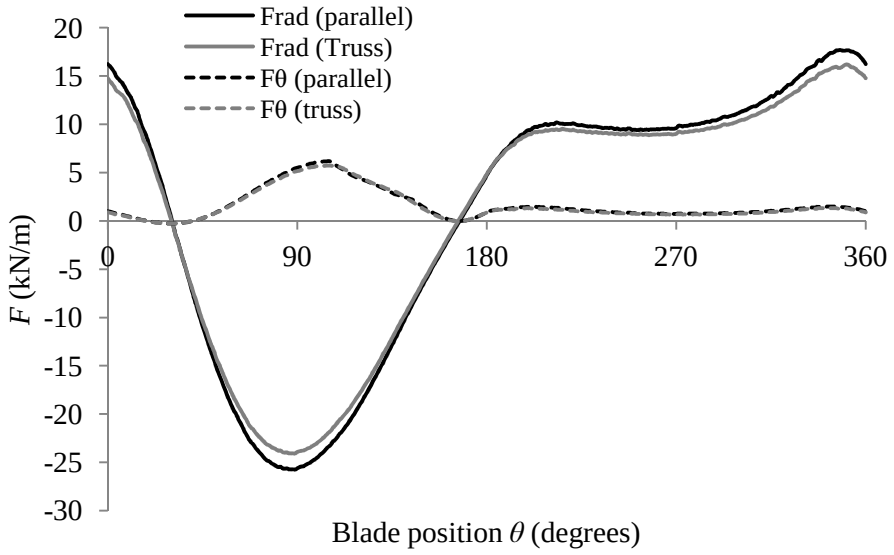

Figure 8.27 – Comparison between NS-BE-FS predictions of radial and tangential components of distributed force for the parallel and truss configurations

Figure 8.27 shows that the members of the truss device experience lower radial and tangential force components than the parallel configured device. However, as shown in Table 8.17 the stress induced in the blades of the single bay truss device are higher than those experienced by the parallel bladed device, due to a combination of an increase in blade length and a decrease in blade profile thickness, which is necessary to maintain a consistent solidity.

Maximum stress (MPa)	60.91
Component due to bending (MPa)	60.31
Component due to axial force (MPa)	0.34
Component due to shear (MPa)	3.93

Table 8.17 - Stress induced in the single bay NS-BE-FS loaded truss-bladed device

In a similar fashion to the parallel-bladed device, the maximum stress occurs on to the top surface of the hydrofoil section at the profile point furthest from the neutral axis.

When combined with the fact that a truss configured device produces less power than a parallel-bladed device, the increase in blade stress in the truss rotor shows that for a single bay device a parallel-bladed turbine is a more desirable configuration.

8.8.4. Multi-bay truss

A model of the multi-bay truss has been created in a similar fashion to the parallel bladed device. However, the geometry of each consecutive bay is rotated by 60° so that the blade geometry remains continuous, as shown in Figure 8.28.

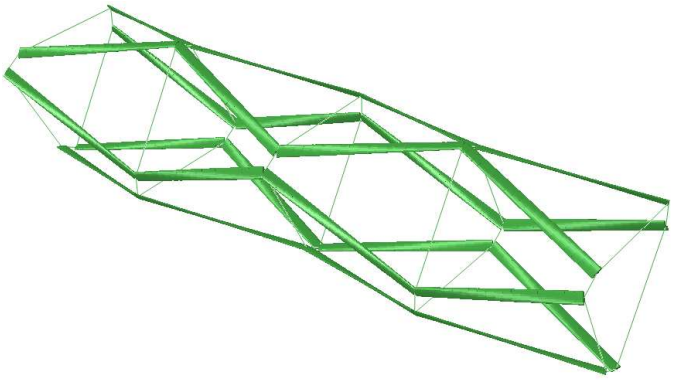

Figure 8.28 – Rendered image of a four bay truss bladed rotor

Figure 8.29 shows that as the number of bays increases, the increase in stress in the truss rotor is significantly lower than that in the parallel-bladed device. Despite experiencing a greater stress on a single bay, a truss configuration results in a reduction in maximum stress for a multi-bay configuration, when compared to a parallel-bladed device. For example, a six bay truss-bladed device is estimated to experience approximately 40% of the stress that would be induced in a parallel-bladed device of the same dimensions.

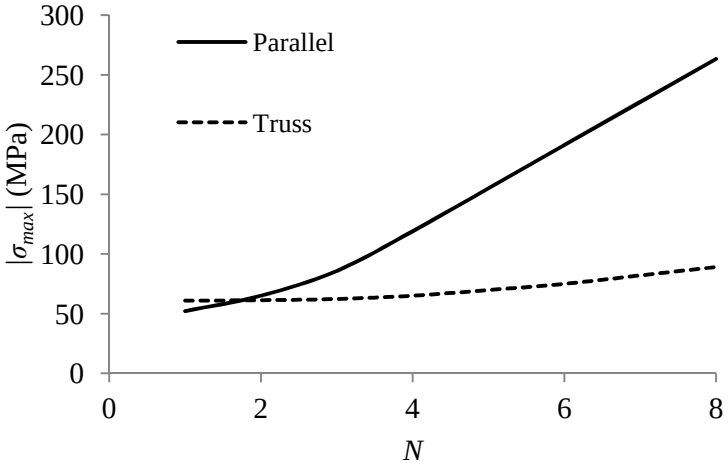

Figure 8.29 – Comparison of maximum induced stress

Unlike the parallel-bladed device the truss device acts similar to a beam and planes normal to the 'neutral axis' remain approximately plane, as shown in Figure 8.30. Increasing the length of the rotor therefore causes a quadratic increase in the stress due to a transfer of bending moment, through each section of the structure to the supports.

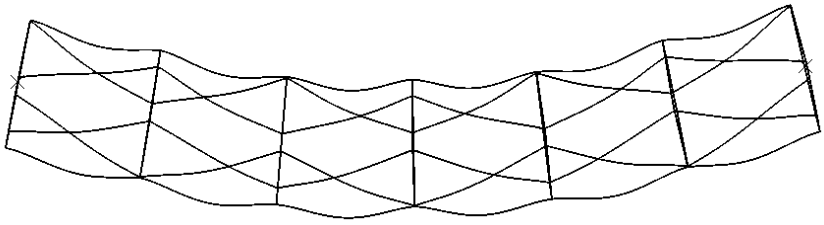

Figure 8.30 – Exaggerated image of deflection of a six bay truss-bladed device under uniform load

Due to the fact that the truss device acts like a beam, the mechanism by which the hydrodynamic forces are transferred to the rotor supports is predominantly through axial forces in the blades, similar to a conventional truss. Figure 8.31(a) demonstrates that the amount of bending that contributes to the maximum stress in the truss rotor remains relatively constant as the number of bays is increased. This is predominantly the bending stress induced by the loading of the individual blade. The increase in stress is caused by an increase in the axial component of stress as the number of bays is increased. Figure 8.31(b) shows that as the number of bays is initially increased, the built-in supports of the truss and parallel-bladed configurations cause the maximum stress to occur at the cantilevered supports at the ends of the rotor, which do not experience significant axial forces. However, as the number of bays is increased, the rising axial force in the truss configuration moves the location of the maximum stress to the middle bays of the rotor.

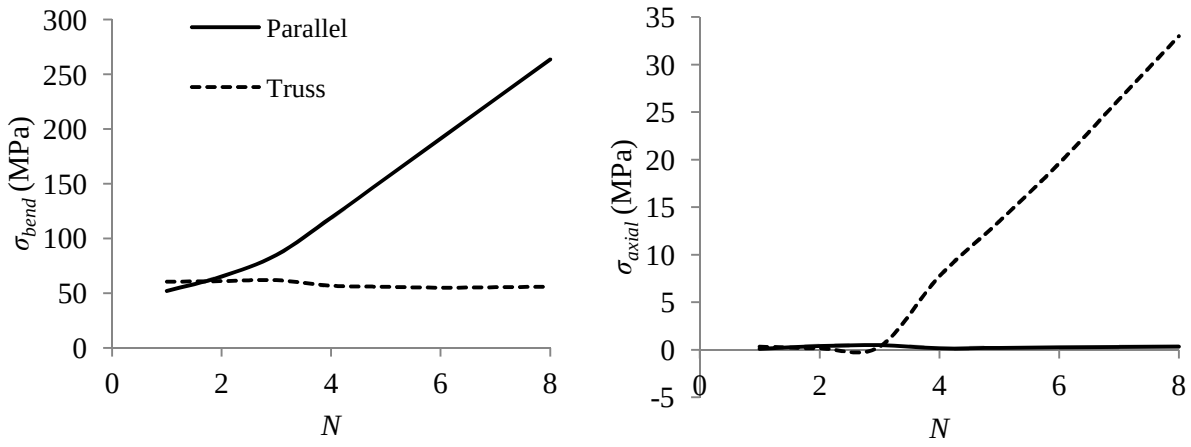

(a) Stress due to bending component *(b) Stress due to axial component*

Figure 8.31 – Comparison of the maximum blade stress due to bending and axial components of section force and moment

Figure 8.32 shows that the greatest axial force occurs in the middle bays of the multi-bay truss rotor, as would be expected in a deflecting beam.

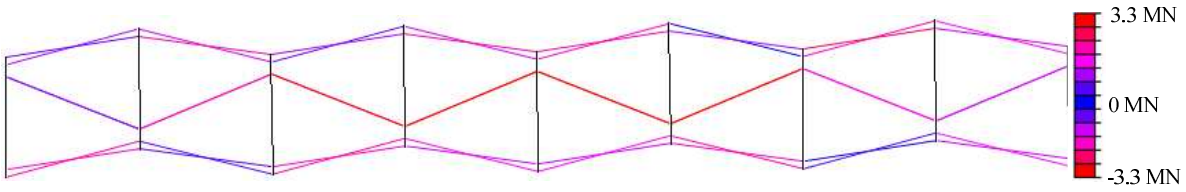

Figure 8.32 – Axial force distribution in an 8-bay truss configuration device with NS-BE-FS loading

Components of shear remain relatively constant and insignificant for both the truss and the parallel device over the range of number of bays.

In a similar fashion to the parallel-bladed device, the point of maximum stress occurs on the top surface of the hydrofoil section for a single bay. However, as the number of bays increases the built-in condition for the blade ends allow small additional components of force and moment to be transferred to the blades, so that the point of maximum stress moves to the trailing edge of the hydrofoil, as shown in Figure 8.33.

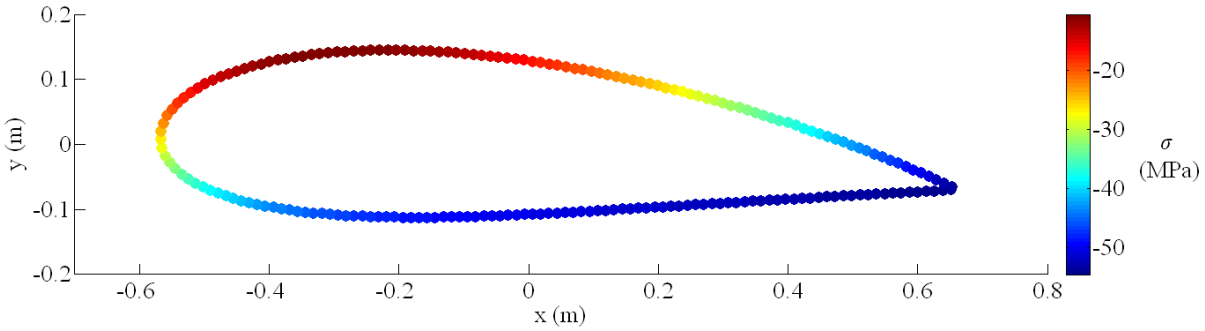

Figure 8.33 – Distribution of stress around the hydrofoil section for the element of maximum stress in the multi-bay truss bladed device

By using a truss configuration rather than a parallel configuration, not only is the maximum stress reduced, but there is also a significant decrease in the maximum deflection of the rotor, as shown in Figure 8.34.

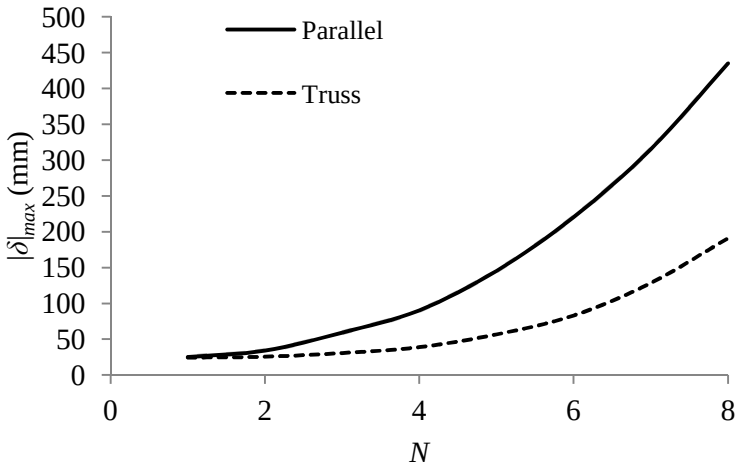

Figure 8.34 – Comparison of maximum deflection for the truss and parallel configurations

8.8.5. P-Δ considerations in buckling

The increase in axial forces within the structure of the truss rotor, as the number of bays is increased, suggests that buckling of the blade members may become significant.

A beam loaded in compression, such as that shown in Figure 8.35, can fail due to buckling instability at a load significantly lower than that required to yield the structural material, as derived by Euler (Williams and Todd, 2000). The theory assumes that the compressive load will cause a moment in the deflected beam that will cause buckling failure. The critical load for buckling failure depends on the end constraints and flexural strength of the beam.

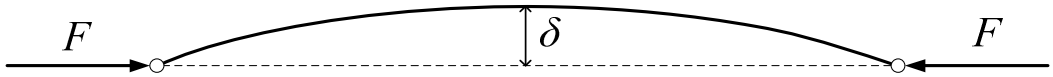

Figure 8.35 – Simply supported beam deflecting under a compressive load

Oran (1976) outlined an improved method for predicting the critical buckling load of a beam, which proved to be highly accurate even when the deformations of the structure are quite large. This work was later unified with a shear deflection theory to provide a complete solution to the buckling problem (Martin, 1994, Bienen, 2007). However, the low failure strain of composite materials, which are most likely to be utilised in the THAWT device, mean that large deformations are unlikely to occur before bending failure of the members, and the more complex techniques of buckling prediction are assumed unnecessary.

For the built-in blade members of the multi-bay devices analysed in sections 8.8.2 and 8.8.4 the minimum axial load which can theoretically cause failure by buckling is given in equation 8.30.

$$F_e = \frac{4\pi^2 EI}{L^2} \qquad 8.30$$

By searching within each analysis for the element with the greatest compressive axial force, the risk of buckling can be explored. As shown in Figure 8.36, despite neither configuration of turbine experiencing axial compressive forces of a great enough magnitude to cause member buckling, the truss rotor experiences a significantly greater risk of buckling when compared to the parallel-bladed device.

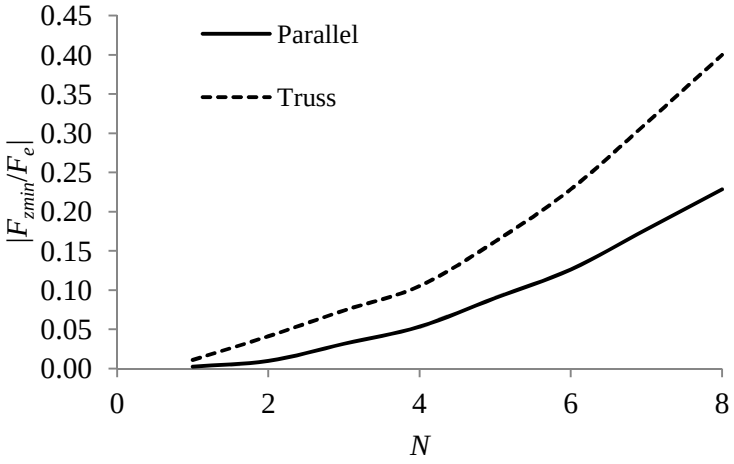

Figure 8.36 – Proportion of Euler buckling load experienced

The lateral loading of the blade causes additional deflection, however the critical axial load required to cause buckling of the member remains unchanged.

8.8.6. Pinned truss frame

The most conservative estimate of structural performance on the truss configuration is provided by releasing the angular constraints at the blade ends to produce a pin jointed frame. In order to explore this, the simulations of the truss turbine described in section 8.8.4 have been repeated, with the blade end constraints on rotation about the *x* and *y*-axes removed. Rotations about the blade axis remain constrained, as the blades are not allowed to freely pitch in practice.

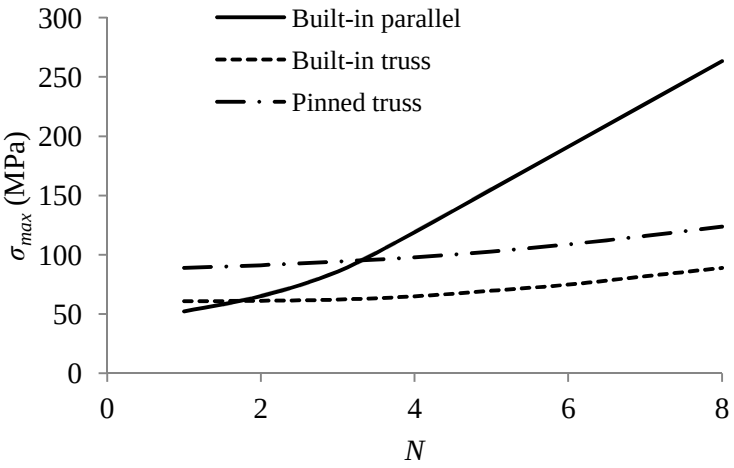

Figure 8.37 – Comparison of maximum induced stress for a NS-BE-FS loaded device over a range of number of bays

The induced stress in a single bay of the truss configuration is increased by a factor of 1.46 as a result of replacing the built-in condition at the blade ends with a set of pinned constraints. This agrees with the expected increase in bending stress due to an increase in maximum

bending moment by a factor of 3/2. As shown in Figure 8.37, the offset of increased stress remains as the number of bays is increased. This effect is due to the bending stress component in both the built-in and pinned configuration remaining relatively constant, while the axial stress components increases for four or more bays in a similar fashion, as shown in Figure 8.38.

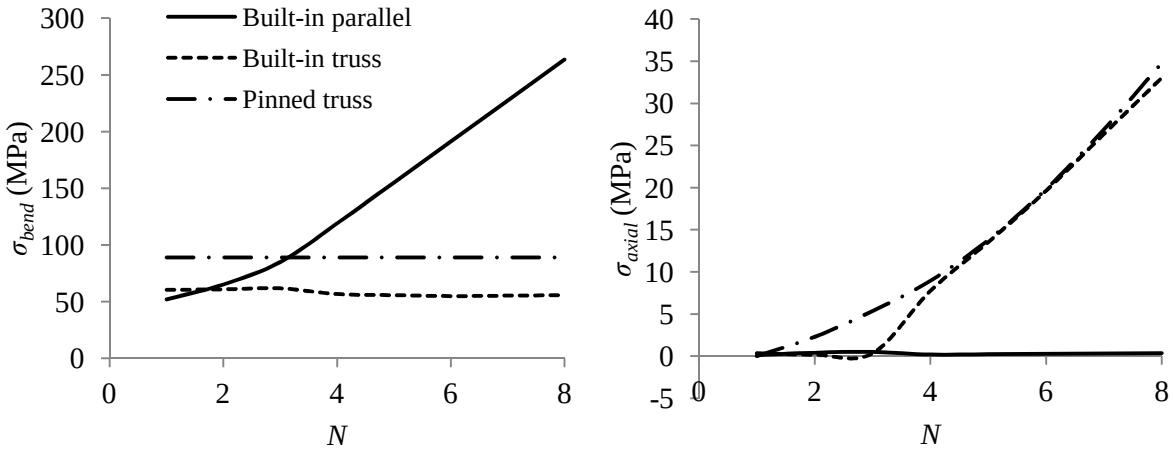

(a) Stress due to bending component *(b) Stress due to axial component*

Figure 8.38 – Comparison of absolute components of the maximum stress due to bending and axial components of section force and moment in the NS-BE-FS loading case

Figure 8.38(b) demonstrates that the occurrence of the maximum stress in the truss configuration of device differs between the built-in and the pinned blades, for rotors of up to four bays. The maximum stress in the single bay pinned truss is not restrained to the cantilevered end supports, so the contribution of axial stress to the maximum stress increases with the number of bays for rotors of two or more bays.

Due to the release of moment at the end of the pinned blades ends there is little transfer of section forces and moments between blades, other than axial force. This means that the section forces other than the axial force remain relatively constant, regardless of the number of bays. A blade is only required to resist the transmitted axial force and the bending moment that is applied locally from the hydrodynamic force. The bending moment about the weaker axis of the hydrofoil therefore dominates the position of the maximum stress in the section, which occurs on the top surface of the hydrofoil for any number of bays.

However, due to the release of the angular degrees of freedom at the blade ends, the axial compressive force required to cause buckling is reduced by a factor of 4, when compared to a built-in member. Due to a similar magnitude of maximum axial compressive force in the

built-in and the pinned structures, the likelihood of failure by buckling is therefore significantly increased, as shown in Figure 8.39.

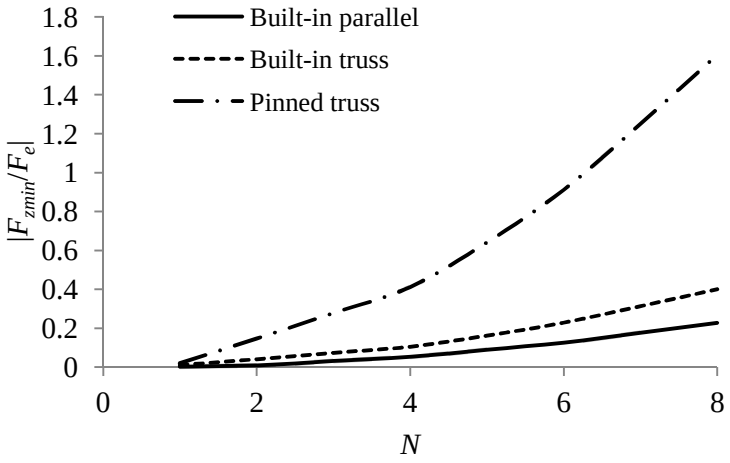

Figure 8.39 – Comparison of the proportion of Euler buckling load experienced for NS-BE-FS loaded devices

With a release of the rotational constraints on the blade ends the stiffness of the pinned truss device is significantly reduced, when compared to the built-in variant, as shown in Figure 8.40.

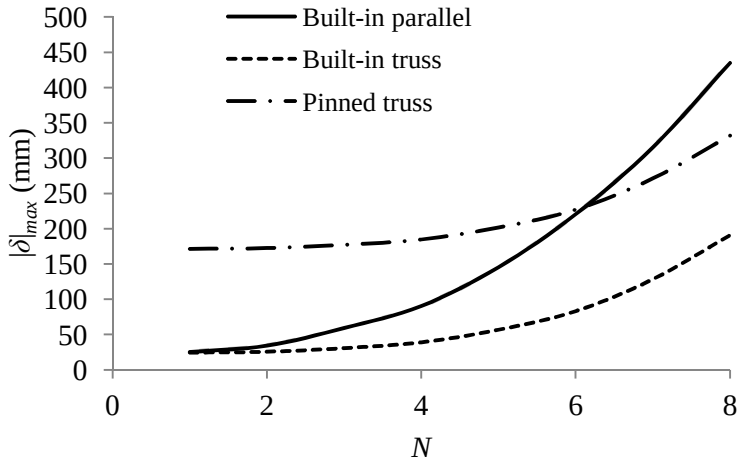

Figure 8.40 – Comparison of maximum deflection for the pinned truss and built-in truss and parallel configurations

8.8.7. Fatigue considerations

As shown in Figure 8.41, the stress ratio can have a significant effect on the alternating stress (or half-amplitude of stress) that can be maintained over a given number of cycles, on a standard piece of GFRP laminate. As the number of cycles approaches 10^8 the highest levels of stress can be maintained in a compression-compression loading scheme, but as the mean

stress approaches zero, the available material strength reduces significantly and continues to reduce for higher mean stress.

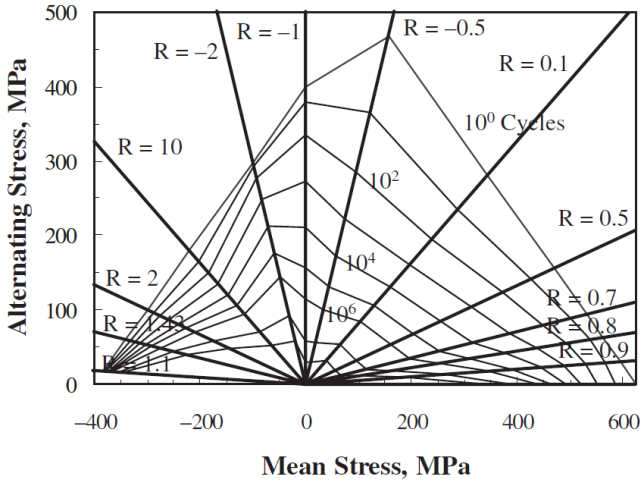

Figure 8.41 - Goodman diagram illustrating the variations in fatigue life with stress ratio for an example multi-directional ply laminate of glass reinforced composite (Sutherland and Mandell, 2005) permission to use figure granted by John Wiley and Sons

Uniform loading produces the same magnitude of stress on the upstream and downstream halves of the device in each node of each hydrofoil section, but opposite in sign, resulting in a zero mean stress and a stress ratio of -1. However, the uneven distribution of loading predicted by the NS-BE-FS model produces differing amplitudes of stress on the upstream and downstream halves of the device and non-zero mean stress.

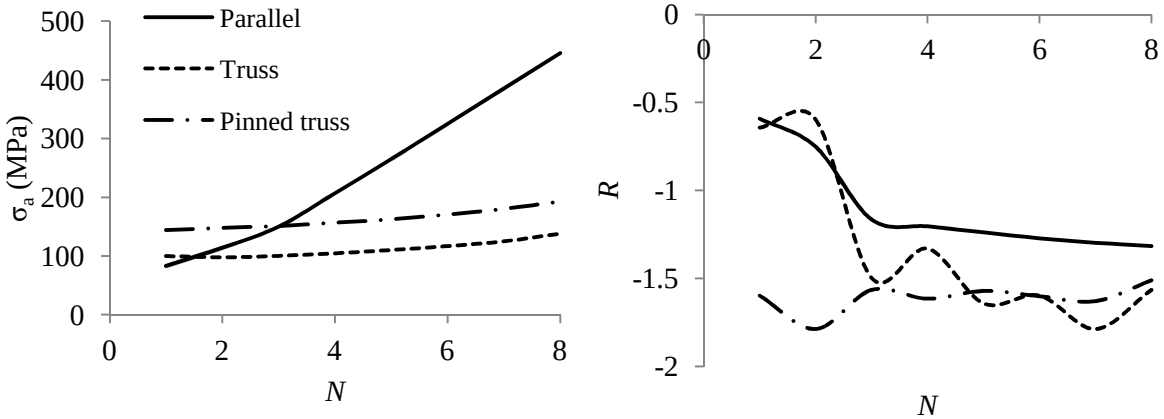

(a) Maximum stress amplitude *(b) stress ratio*

Figure 8.42 – Comparison of maximum stress amplitude and the corresponding stress ratio

Figure 8.42(a) demonstrates that even the single bay built-in supported truss device experiences a half-amplitude of stress of approximately 50 MPa, which is likely to cause material failure over 10^8 cycles. However, it should be noted that this is the peak value of

stress and does not represent the average over the tidal cycle. A full fatigue analysis over the lifetime of the device is required to predict if material failure would occur.

For all of the single bay devices, the greatest stress is due to the peak lift force at approximately 90° of rotation. However, whilst the greatest moment in the built-in blades is a hogging moment at the blade ends, the greatest moment in the pinned blades is a sagging moment at the centre of the blade. As the node on the hydrofoil profile with the greatest distance from the neutral axis is the same in both configurations, the built-in blades experience a peak stress which is tensile and the pinned blades experience a peak stress which is compressive. For the single bay rotors, the mean stress at the point of maximum stress amplitude is therefore tensile for the built-in blades and compressive for the pinned blades, as shown in Figure 8.42(b). This effect continues in the pinned rotor, as the peak stress is consistently generated at 90° of rotation due to a sagging moment. However, as the number of bays is increased the parallel-bladed device experiences a peak stress due to the inter-bay shearing at approximately 180° degrees of rotation, which results in a mean stress at the point of peak amplitude much closer to zero, and a stress ratio close to -1. The complex superposition of forces in the built-in truss configuration result in a significant reduction in the mean stress at the point of peak magnitude, so that a four or more bay truss device, with either built-in or pinned blade supports, would maintain a higher material strength for a given number of fatigue cycles.

The desire to produce a fatigue cycle with a more compressive mean stress has also been experienced in other designs of cross-flow device using more conventional materials (Zanette *et al.*, 2010).

8.8.8. Additional centripetal loading

As well as experiencing a hydrodynamic load due to the blade and flow velocity, the members of the THAWT device experience an additional force due to the centripetal acceleration of the rotating blades. The magnitude of the radial force per unit length is simply calculated using equation 8.31, which assumes that the blade centre is full of water.

$$F_c = mr\omega^2 \qquad 8.31$$

Because the centripetal force acts equally on all blades in any position there is no effect on the total thrust or power produced by the device. However, as shown in Figure 8.43 the effect

of the centripetal force is to increase the radial force experienced by a single blade by 1.7 kN/m, causing a decrease in the peak absolute force of 6.5%.

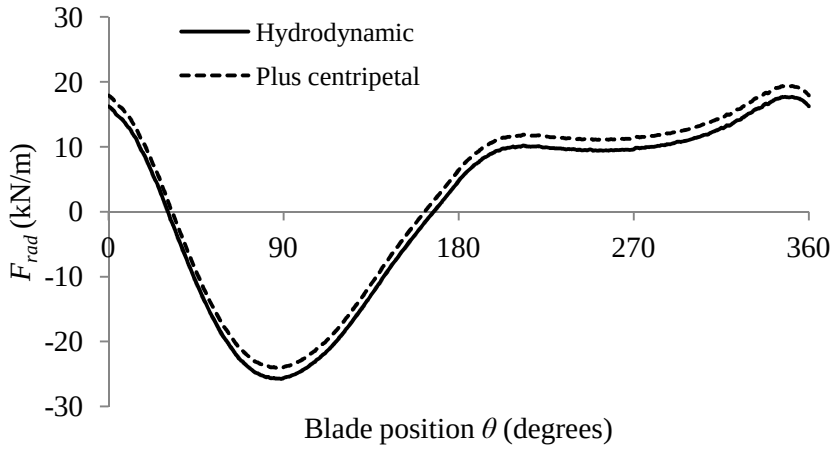

Figure 8.43 – Comparison of loading with and without centripetal forces of the parallel-bladed device

The increase in radial force due to the centripetal loading causes a decrease in the maximum tensile stress experienced by the hydrofoil nodes of the rotor, however the maximum compressive load is also increased and so the amplitude remains relatively unchanged, as shown in Figure 8.44.

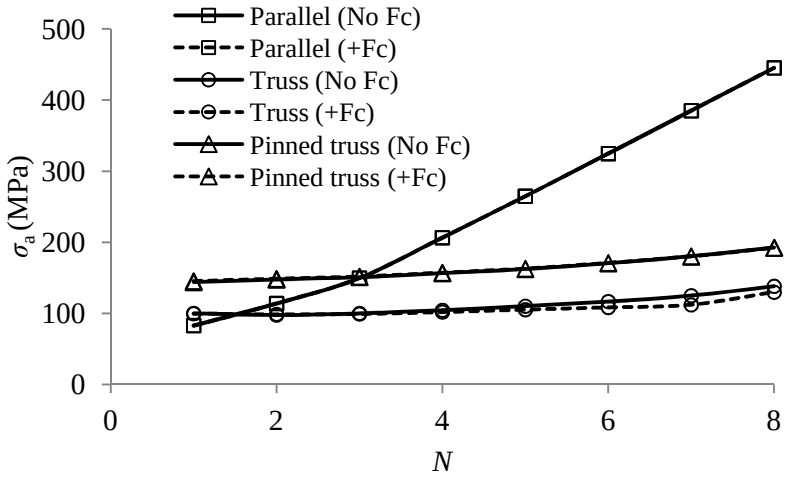

Figure 8.44 – Comparison of peak stress amplitude with and without centripetal loading

Despite the lack of change in the stress amplitude, the additional centripetal force has caused a reduction in the peak stress for each configuration, and a stress ratio closer to -1, as shown in Figure 8.45.

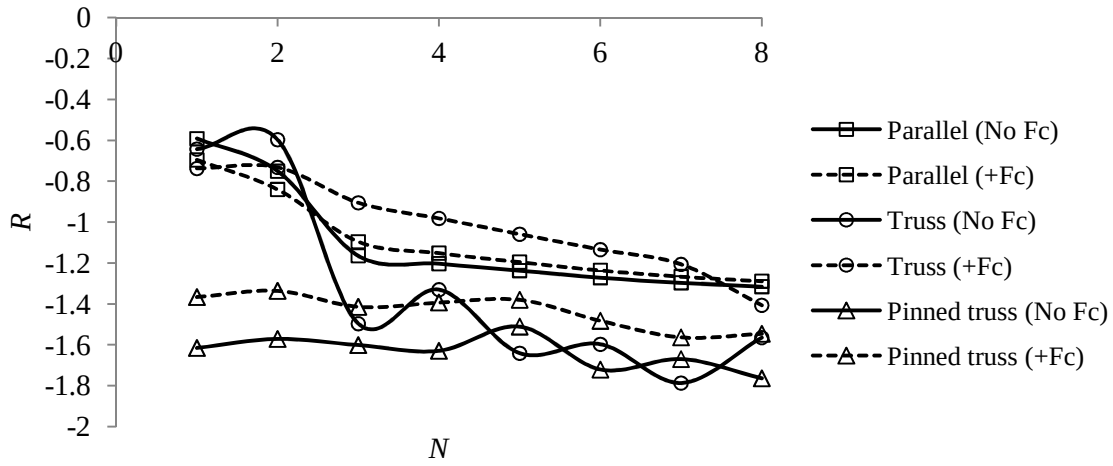

Figure 8.45 – Comparison of stress ratio at peak amplitude with and without centripetal loading

8.8.9. Non-rigid supports

While idealised rigid inter-bay supports offer a simple basis on which the blade structural mechanics of the THAWT rotor can be analysed, a rigid inter-bay support is not possible in practice. The choice of either the material or shape of the inter-bay supports are not clearly defined, but the most suitable design is one which minimises parasitic drag and weight, whilst maintaining a sufficient degree of strength. Composites are therefore a likely material choice, due to their good strength to weight ratio.

The end plate system used in the Newcastle experiments, described in Chapter 4, are aluminium plates. Whilst being simple to manufacture and allowing for many configurations of device to be tested, the aluminium plates are heavy and would not be feasible on a full scale.

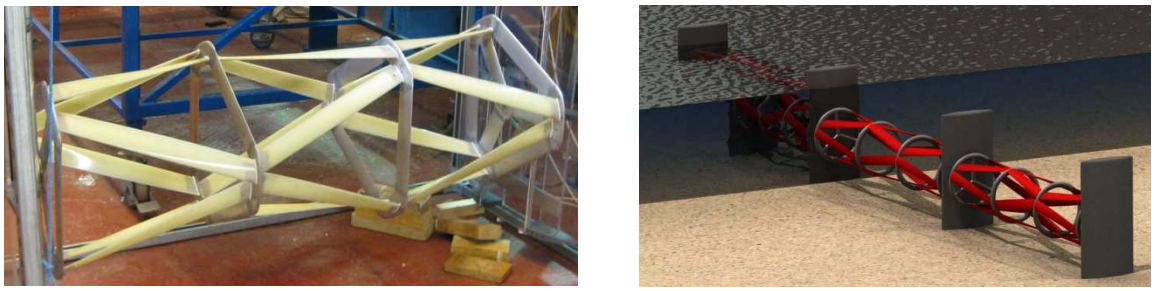

(a) Straight member supports *(b) Ring member supports*

Figure 8.46 – Truss turbine rotors using different support member configurations

Figure 8.46 shows two alternative designs of support member, which would substantially reduce the weight of the end plate design. The straight member support configuration offers an axially stiff support structure, but the sweep of the streamlined members relative to the rotation of the rotor is likely to result in a contribution of profile drag, which will reduce the

torque produced by the device. While the ring support member solution resolves the issue of parasitic profile drag, the axial stiffness and ease of manufacture is likely to be reduced.

A comprehensive study of the shape of the support structure is beyond the scope of this thesis, so in order to briefly explore how the blade structural mechanics are affected by a non-rigid support structure the straight member support configuration is used, as shown in Figure 8.47. In order to maintain a simple analysis of the new structural members in the model, the support member profile is the same NACA0021 section as the blade members, prior to 'wrapping' onto the rotor circumference.

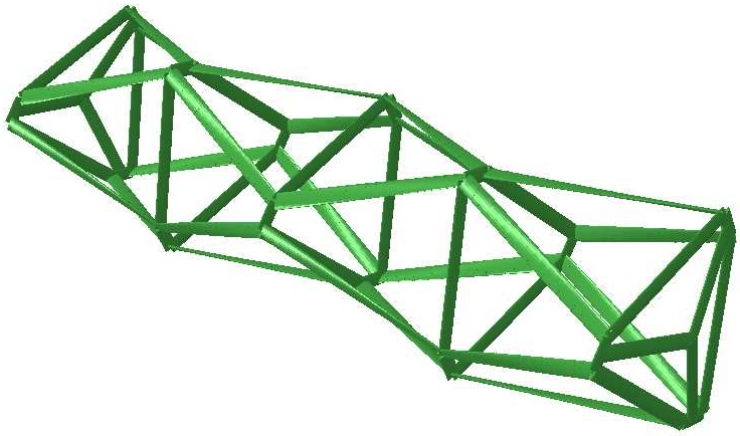

Figure 8.47 – Rendered image in ABAQUS of a non-rigid supported truss frame

The stress induced in the blade members is highly dependent on the section properties of the support structure. As shown in Figure 8.48, applying section properties of the same scale as those used for the blade members results in a significant rise in blade stresses for the built-in truss, and a significant rise in maximum deflection for all configurations.

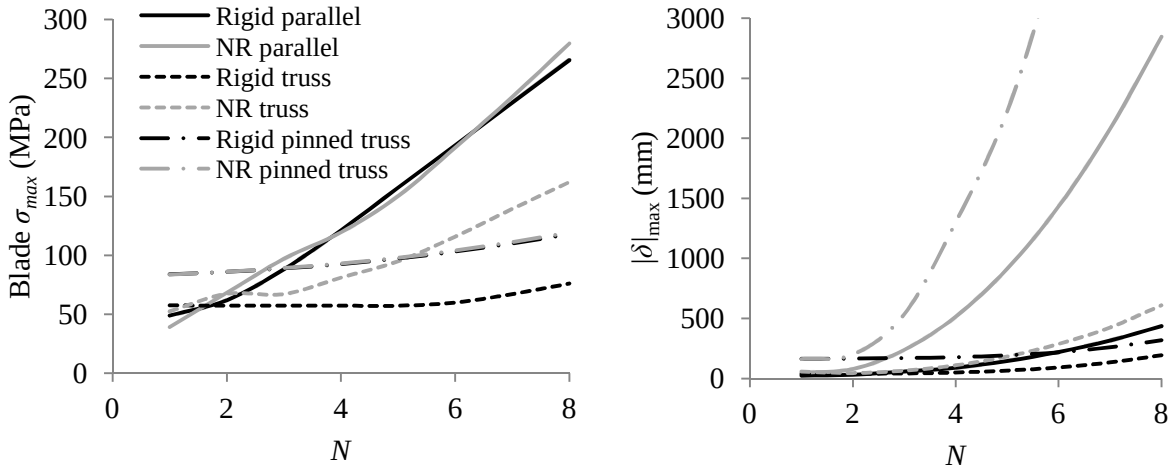

(a) Maximum blade stress *(b) Maximum deflection*

Figure 8.48 – Structural performance of the non-rigid supported THAWT device with support members at a scale factor of 1

A multi-bay design using this configuration is unlikely to be feasible due to the rapidly increasing stresses in the support members, as shown in Figure 8.49.

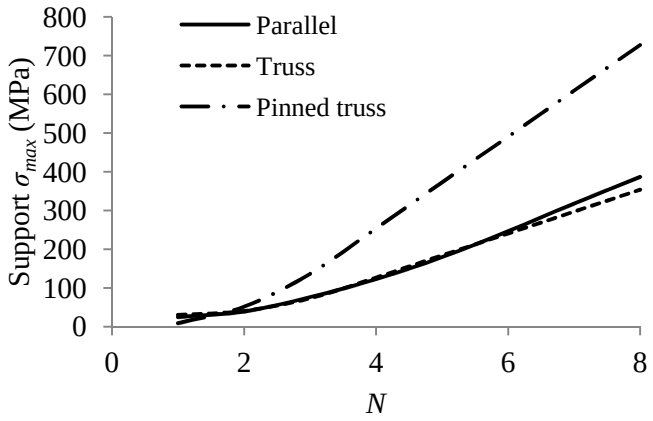

Figure 8.49 – Maximum magnitude of stress induced in the non-rigid support members of the THAWT device with support members at a scale factor of 1

However, by linearly scaling the dimensions of the support members using a geometric scaling factor, the levels of stress induced in the blade members and support members of a multi-bay device return to more realistic values, when considering the likely fatigue strength of the materials, as shown in Figure 8.50.

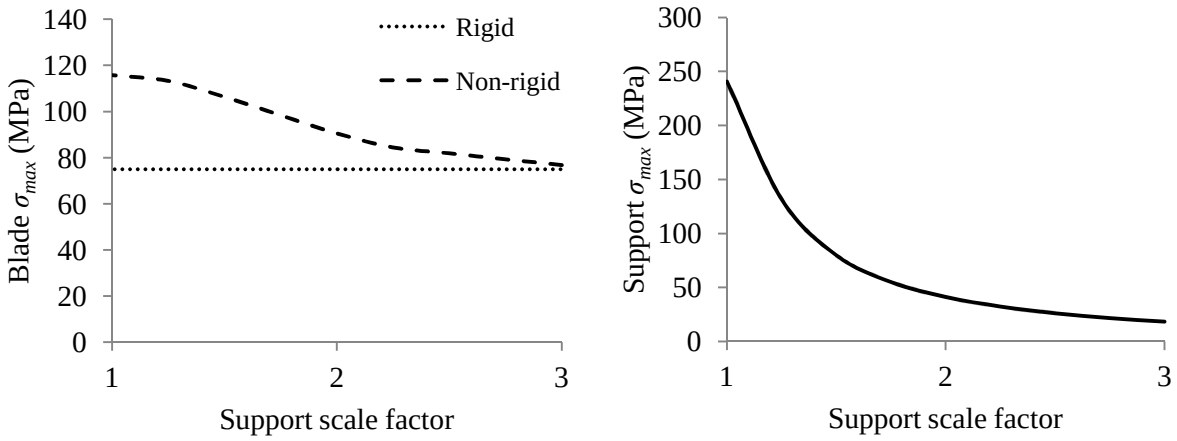

(a) Maximum blade stress *(b) Maximum support member stress*

Figure 8.50 – Maximum magnitude of stress induced in a six bay built-in truss device with a varied support member scale factor

A scale factor of 2 was chosen, at which point the maximum stress amplitude is feasible and further increases in member size have relatively little effect on the stress induced in the blade and support members.

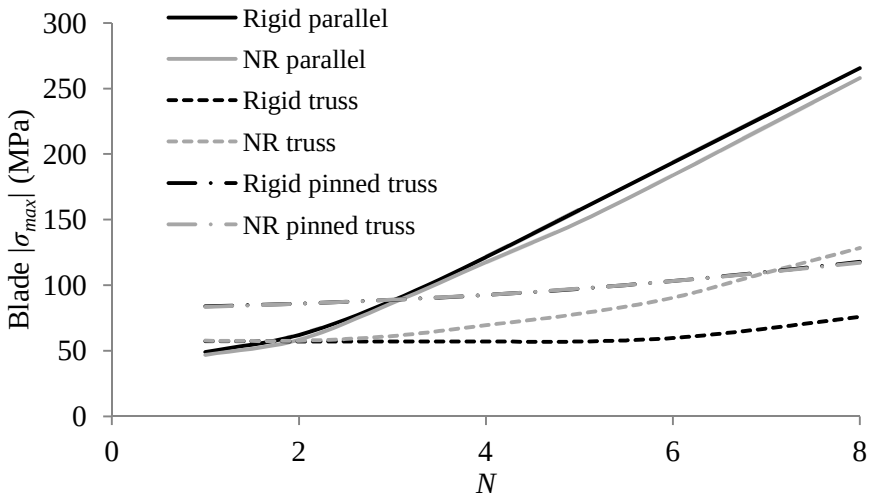

Figure 8.51 – Comparison of maximum absolute blade stress between rigid and non-rigid support structure configurations with a support member scaling factor of 2 (pinned truss curves are overlaid)

As shown in Figure 8.51, use of the non-rigid support structure results in a minor reduction in the blade stress in the built-in parallel configuration and almost no change in the pinned truss configuration. The breakdown of the components of stress in Figure 8.52 demonstrates that the decrease in stress in the parallel configuration occurs due to a reduction in the bending stress, which is probably due to a relaxation of the built-in moments. The pinned truss does not experience any additional bending moments from the support structure and no significant increase in axial stress.

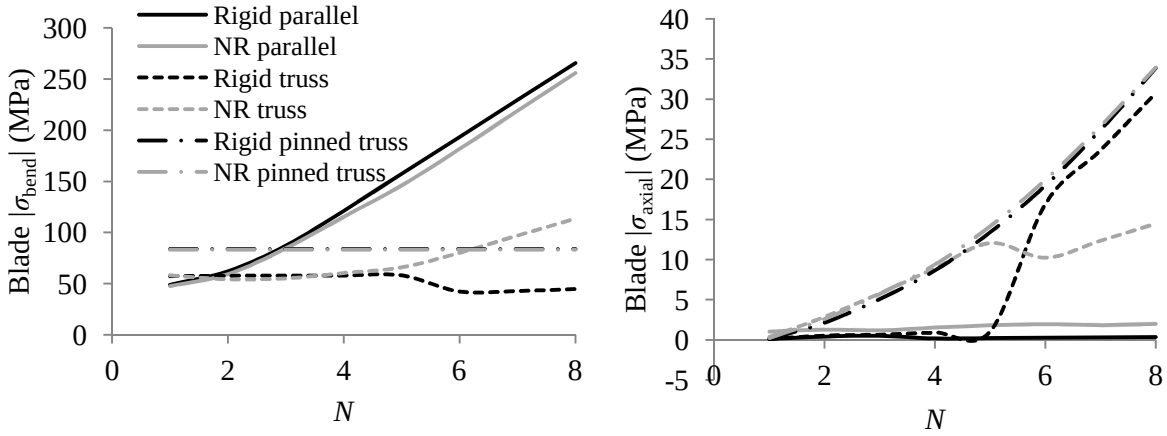

(a) Stress due to bending component *(b) Stress due to axial component*

Figure 8.52 – Comparison of blade stresses due to bending and axial components of section force and moment at the location of peak stress for the rigid and non-rigid support structures with a support scale factor of 2

However, the blade stress in the non-rigid built-in truss increases at a greater rate than the rigid configuration, due to a rise in the bending stress as the number of bays is increased. In contrast to the rigid supported built-in truss, which transitions from a bay shear mechanism to an axial dominated stress as the number of bays is increased, the non-rigid built-in truss

transitions to a bay shear mechanism as the number of bays is increased. Careful design of the support structure should allow the occurrence of the shear mechanism in the built-in truss at the desired number of bays to be avoided.

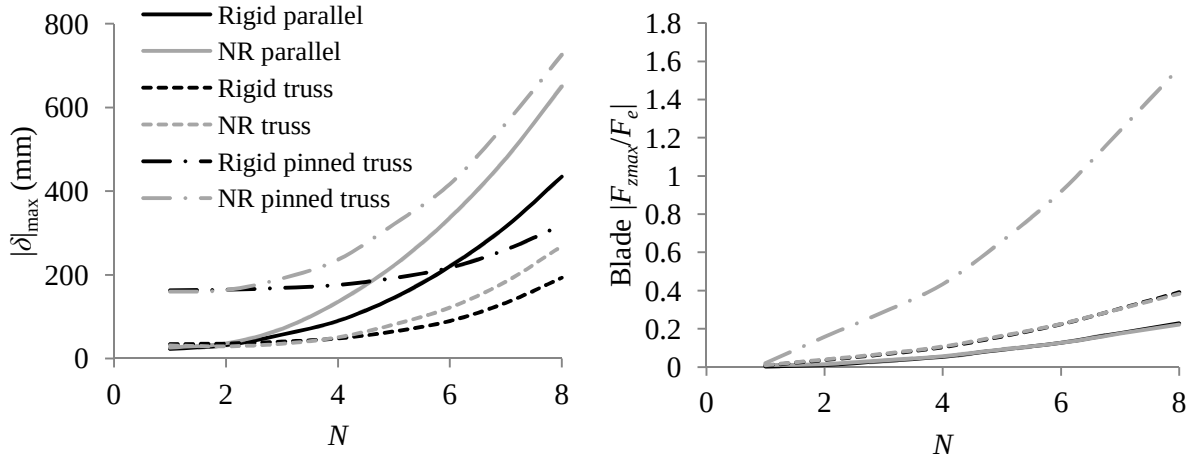

(a) Maximum deflection *(b) Percentage of Euler compressive buckling load*

Figure 8.53 – Comparison of deflection and risk of Euler buckling for the rigid and non-rigid support structures with a support scale factor of 2

The additional compliance and reduction in stiffness of the rotor, due to the non-rigid support members, results in an increased maximum deflection as shown in Figure 8.53(a). The increase in deflection is most severe in the case of the pinned bladed truss. With no significant change in the magnitude of the maximum compressive forces in the structure the risk of buckling remains unchanged from the rigid support case, as shown in Figure 8.53(b).

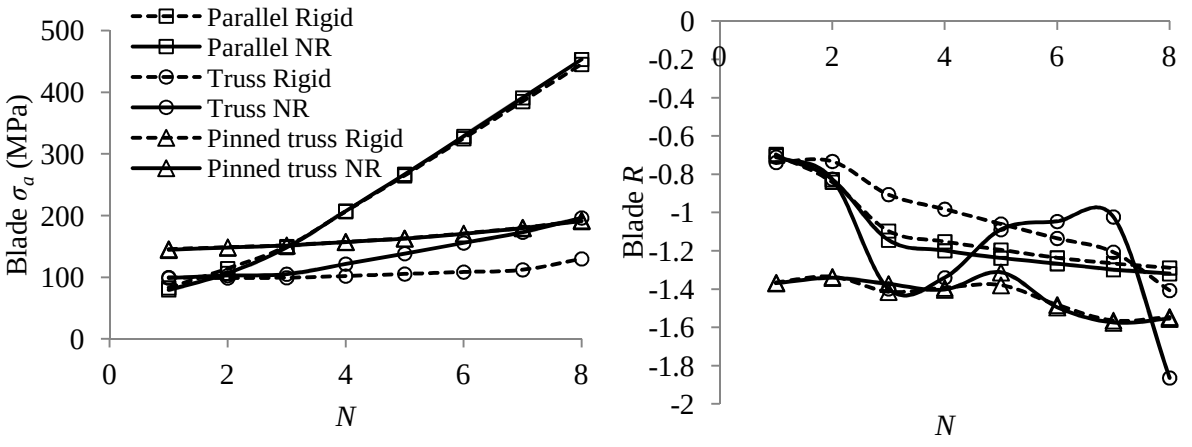

(a) Peak stress amplitude *(b) Stress ratio at peak stress amplitude*

Figure 8.54 – Comparison of fatigue stress indicators for the rigid and non-rigid support structures with a support scale factor of 2

As shown in Figure 8.54(a) the negligible change in the maximum stresses of the parallel and pinned truss configurations is matched in the peak stress amplitudes. The peak stress

amplitude of the built-in truss is increased and approximately matches that of the pinned configuration for 8 bays. The stress ratios at peak stress amplitude also reflect the same trends, however the stress ratio of the built-in truss is substantially variable and does not appear to follow any discernible pattern, perhaps due to the changing mechanism defining the maximum stress.

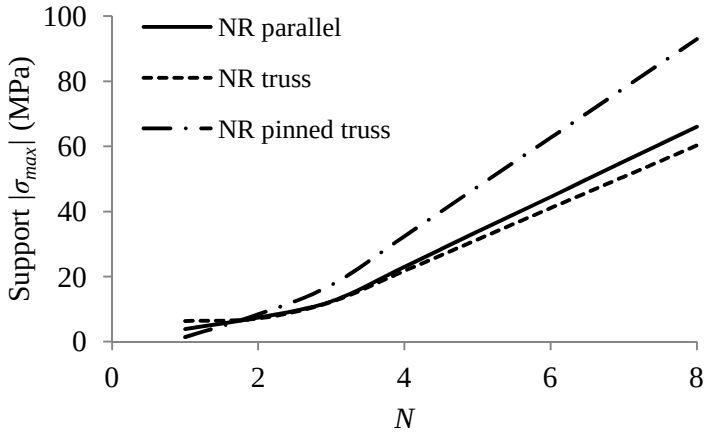

Figure 8.55 – Comparison of maximum absolute support member stress with a support member scaling factor of 2

Despite the distinct differences in the rate of increase of blade stress with the number of bays for the three configurations, the differences in the support member stresses are less significant, as shown in Figure 8.55, with the pin-bladed truss support members experiencing the greatest stress.

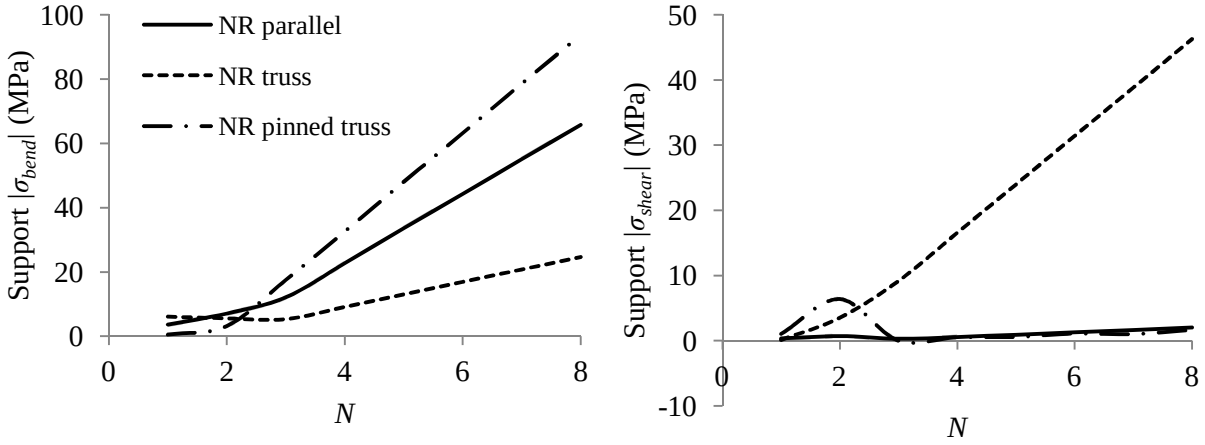

(a) Bending component *(b) Shear component*

Figure 8.56 – Comparison of support member stress due to bending and shear components of section force and moment at the location of peak stress for the non-rigid support structures with a support scale factor of 2

However, the components of support stress for the built-in truss configuration differ significantly from those of the parallel and pin-bladed truss, which are dominated simply by

bending stress, as shown in Figure 8.56. The stress induced in the support members of the built-in truss configuration is dominated by significant shear forces in both the *x* and *y*-axes of the section. The use of shear webs is likely to reduce the stress induced due to shear components in the non-rigid truss configuration.

The axial stress induced in the support members of all three configurations are insignificant and do not exceed 1 MPa. This indicates that the perceived hydrodynamic benefits of using a ring configuration of support members may outweigh the reduction in structural performance. However the ease of manufacturing is still likely to be an issue with the use of the ring configuration.

8.9. Validity of a static analysis

The FE analysis has been performed assuming static loading of the rotor at any given position of rotation. It is assumed that a static analysis is valid if there are no additional forces as a result of resonating vibrations. While a dynamic analysis of the turbine would indicate whether the frequency of rotation and forcing is likely to induce resonance in the rotor, a much more comprehensive structural model would be required and is beyond the scope of this project. A first order estimate of the natural frequency of a beam is given by equation 8.32 (Howatson *et al.*, 1991), where the value of *k* depends on the support conditions of the beam.

$$\omega_0 = k\sqrt{\frac{EI}{mL^4}} \qquad 8.32$$

The mass per unit length which is applied in equation 8.32 is a combination of the blade material mass and an added mass due to the displaced fluid around the body. To a first order approximation, it is assumed that the added mass for a hydrofoil shape is a cylinder whose diameter is equal to the chord length of the blade (Brennen, 1982).

The natural frequency for a pin supported truss rotor blade, with structural and material properties as described in sections 8.3 and 8.8.3, is predicted at 1.94 Hz, which is significantly higher than the anticipated frequency of blade loading of 0.16 Hz, one period of loading per turbine rotation, in a 2 m/s flow. It can therefore be assumed that an individual rotor blade would not be expected to experience a force at a frequency close to its natural frequency.

The same methodology can be applied to a multi-bay bay truss rotor, which acts like a beam. The equivalent flexural stiffness, *EI*, of a four bay rotor is calculated using equation

8.33 (Howatson *et al.*, 1991), based on the thrust load on the entire structure and the maximum deflection at the centre.

$$\delta_c = \frac{wL^4}{384EI} \qquad 8.33$$

Assuming that the added mass is now six times the added mass of a single blade, the natural frequency for a four bay rotor is predicted at approximately 1.62 Hz. However, with six blades the forcing frequency is possibly six times the frequency of rotation, at 0.95 Hz. This simple analysis indicates that there is a safety factor of approximately 1.6 on the resonant forcing, which means that the dynamic response of the THAWT device should be explored in further structural analyses.

8.10. Comparisons with preliminary analysis

The preliminary analysis, described in Chapter 3, predicts the blade stress that would be expected at the most upstream point of the rotor, as shown in equation 8.34, which suggests that the expression shown in equation 8.35 is constant.

$$\frac{h\sigma_{max}}{F_L} \propto \frac{n^3\beta^2}{s^3\left(t/c\right)^2 B} \qquad 8.34$$

$$\frac{h\sigma_{max}}{F_L} \times \frac{s^3\left(t/c\right)^2 B}{n^3\beta^2} = C \qquad 8.35$$

By individually varying the ratio of bay length to diameter β, solidity s, thickness to chord ratio t/c, and geometric scale h away from a base configuration for simulations of the FEA model , the accuracy with which the preliminary analysis predicts the variation in blade stress is explored. This exercise is performed for single and four bay variants of the built-in parallel, built-in truss and pinned truss configurations, with non-rigid supports of a section scaled from the blade members by a factor of two. The loading pattern used to predict the values of C is unchanged between the different variants of turbine, so that the value of F_L is unchanged. The values of C for the base configuration and for each of the different variants of turbine are given in Table 8.18.

	Single bay			Four bay		
	Parallel	**Truss**	**Pinned Truss**	**Parallel**	**Truss**	**Pinned Truss**
C_{base}	0.052	0.065	0.093	0.131	0.078	0.104

Table 8.18 – Values of C_{base} for the single and four bay built-in parallel, built-in truss and pinned truss turbine variants, as predicted by the FEA model

For each variation of design parameter, the value of C is calculated and converted to a ratio of C/C_{base} to show how the configuration variation affects the accuracy of the scaling assumptions. The base configuration, the range of each variable explored and the range of C/C_{base} predicted by the FEA model are given in Table 8.19.

			Single bay			Four bay		
	Base	**Range**	**Parallel**	**Truss**	**Pinned Truss**	**Parallel**	**Truss**	**Pinned Truss**
β	1	0.5 – 1.5	0.99 - 1.01	0.82 - 2.31	0.83 - 2.28	1.00 - 1.00	0.84 - 2.08	0.83 - 2.25
s	0.3	0.125 – 0.5	0.98 - 1.03	0.91 - 1.09	0.95 - 1.09	0.79 - 1.80	0.79 - 1.85	0.95 - 1.09
t/c	0.2	0.15 – 0.27	0.92 - 1.11	0.94 - 1.06	0.94 - 1.09	1.00 - 1.02	0.99 - 1.04	0.97 - 1.05
h	20	10 – 30	0.97 - 1.03	0.97 - 1.03	0.97 - 1.03	0.99 - 1.01	0.97 - 1.03	0.97 - 1.03

Table 8.19 – Range of C/C_{base} for the individually varied values of turbine configuration

As shown in Table 8.19, the preliminary analysis predicts the scaling of blade stress with a variation in blade thickness to chord ratio t/c and geometric scale h for all of the variants of turbine with sufficient accuracy. However, some significant inaccuracies occur in the prediction of scaling with the length to width ratio and turbine solidity.

8.10.1. Length to width ratio scaling

As shown in Table 8.19, with a varied length to width ratio the blade stress scaling is consistent to within 1% for both the single bay and four bay variants of the parallel-bladed device. However, as demonstrated in Figure 8.57, the scaling of stress with a change in β is inaccurate for both the built-in and pinned truss variants.

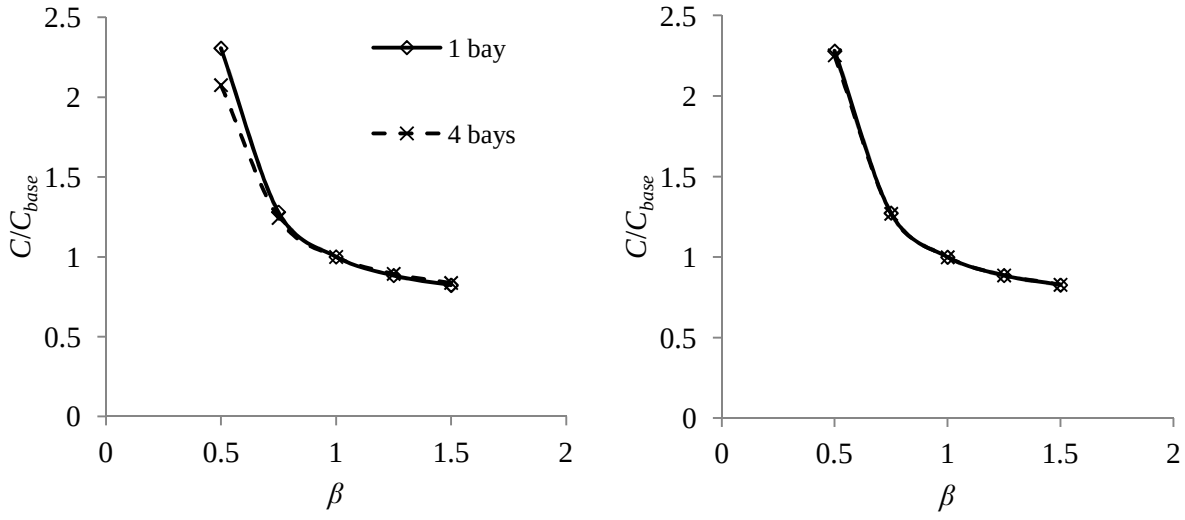

(a) Built-in truss *(b) Pinned truss*

Figure 8.57 – Comparison of C/C_{base} for the built-in and pinned truss devices with 1 and 4 bays over a range of length to width ratios

The difference between the FEA model predictions and the preliminary analysis is due to the changes in the turbine geometry that occur when the length to width ratio is varied. The preliminary analysis assumes that a change in the length to width ratio of the turbine is simply a change to the length of the turbine blade. However, when the length to width ratio of the truss device is varied the blade sweep angle is also varied, which results in further changes to the blade and chord length that are not predicted by the preliminary analysis.

8.10.2. Solidity scaling

As shown in Table 8.19, the preliminary analysis accurately predicts the scaling of stress in the single bay parallel bladed device over a range of design solidities within approximately 3%. The FEA predictions of the blade stresses in the single bay truss variants of the turbine over a range of solidities also show good fidelity with the preliminary analysis, with errors less than approximately 9%.

However, the accuracy of the preliminary analysis decreases as the number of bays of the built-in turbines increase. The error in blade stress scaling is increased to 80% and 85% respectively for the parallel and truss-bladed built-in devices. The error in the blade stress prediction for the pinned truss device remains at approximately 9% for a four bay rotor.

8.11. Concluding remarks

A static beam element FE model has been chosen as a suitable method of modelling the structural performance of configurations of the THAWT device. A multi-cell analysis technique has been employed to calculate the stresses in the hydrofoils, which has been successfully validated against theoretical solutions of standard section shapes.

Three main configurations of the THAWT device have been simulated; parallel, truss-bladed, with all degrees of freedom constrained at the blade ends, and a truss bladed device, with the degrees of freedom in the main bending dimensions released. The models have been extended to multi-bay configurations by stacking individual bays end to end, initially with a rigid support structure in between each bay.

Applying the loads predicted by the NS-BE-FS model, indicates that the increase in stress with an increase in the number of bays varied significantly between the parallel and truss configurations. The disparity appears to be dominated by a difference in the mechanism by which the applied load is transferred to the rotor supports, with the parallel configured device

shearing bay by bay and the truss configured devices deforming similar to a beam with planes normal to the neutral axis remaining relatively plane.

The different mechanisms of load transfer are also accompanied by significantly different components of stress and the significant increase in bending moment with an increase in the number of bays experienced by the parallel bladed device does not occur in the truss configurations. However, the truss devices experience a significant increase in blade axial force, indicating that there is likely to be a number of bays at which the failure mechanism in the truss devices transitions from failure due to bending stress to failure due to buckling.

Comparisons with the fatigue life of likely materials indicate that blade fatigue is likely to be a critical design criterion, however a more complete fatigue analysis is required to assess the feasibility of a device in a specific tidal regime.

Replacing the idealised rigid support members of the rotor with realistic sections and material properties indicates that significant forces are transferred through the support members, and that an increased stiffness is required relative to the blade members. A more comprehensive blade design, incorporating features such as shear webs in the support structure members, may offer improved structural performance.

A comparison with the preliminary analysis of Chapter 3 indicates that the effect of scaling of the rotor geometric scale and blade thickness to chord ratio are relatively accurately predicted by the preliminary analysis. However, the accuracy of the preliminary analysis technique is reduced when predicting the scaling of blade stress for the truss turbine, over a range of length to width ratios, and for the multi-bay built-in configurations, over a range of turbine solidities.

Chapter 9

Case study at Papa Westray

The feasibility of a design of THAWT device is heavily reliant on the trade-off between the structural and hydrodynamic performance of the turbine. Dominating factors of a design are likely to be site-specific, such as the variation in flow velocity over a tidal cycle and the amount of channel friction. In order to explore the main design considerations likely to be encountered, one of the main objectives of this thesis is to integrate the hydrodynamic and structural models of the THAWT device, to predict how the power produced and expected lifetime of a device are affected by various aspects of design configuration, at a chosen tidal location.

9.1. Site specification

The proper selection of a tidal location and device is likely to be a complex problem. Current estimates of the power potential of tidal sites are based on the kinetic energy flux (DTI, 2004). However, this is a relatively poor measure of the available energy, due to the effect that a device has on the channel flow.

Figure 9.1 – Map of possible tidal fence location at Papa Westray

In order to explore the effect that a device has on a realistic channel, a tidal site has been chosen based on the survey performed by Black and Veatch during the first round of tidal stream energy resource assessments in the UK (Black&Veatch, 2005). The 2 km wide channel separating the Scottish islands of Westray and Papa Westray, shown in Figure 9.1,

has been chosen as a representative average tidal location, as shown in Figure 9.2, which shows key parameters for typical candidate sites around the UK.

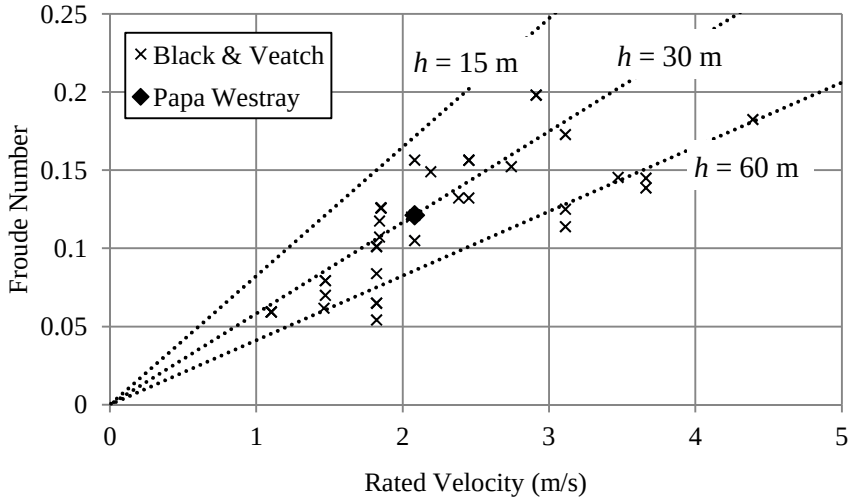

Figure 9.2 - Froude number of potential tidal stream sites around the UK based on data in (Black&Veatch, 2005)

The undisturbed flow conditions at the Papa Westray site are given in Table 9.1.

Average peak spring velocity V_{sp} (m/s)	2.93
Average peak neap velocity V_{np} (m/s)	1.46
Ratio of ebb/flood velocities	0.84
Mean depth (m)	30
Average peak spring elevation (m)	1.63
Average peak neap elevation (m)	0.68
Fr at peak spring	0.17
Fr at peak neap	0.085

Table 9.1 – Undisturbed flow parameters at Papa Westray based on data in (Black&Veatch, 2005)

9.2. Effect of thrust on channel flow

In a tidal channel, such as the Papa Westray channel, the flow is driven by a head difference between the inlet and outlet. The volume flow rate depends on the balance between the driving head difference, flow acceleration and the losses due to channel friction, turbine thrust and exit flow separation (Garrett and Cummins, 2005b). A Linear Channel Momentum model (LCM), which simulates the relationship between these variables in a one dimensional linear channel over a tidal cycle, has been developed by Vennel (2010), where the variation in velocity is calculated by solving equation 9.1.

$$\frac{\partial u}{\partial t} = a\sin(\omega t + \phi_g) - \left(\frac{C_D}{h} + \frac{C_T}{L_c}\right)|u|u \qquad 9.1$$

In order to understand the effect that a device has on the channel dynamics, the driving head and channel friction must be ascertained. However, in the absence of the availability of either piece of information, from which the other may be derived, the most appropriate value to estimate is the coefficient of friction. A coefficient of friction of 0.01 has been chosen as a conservative estimate, based on the assessment of potential tidal channel sites performed by Salter (2009). Furthermore this is also anticipated to offer a conservative estimate of the energy available from the site. In an iterative process, values of driving head are varied until the correct channel velocity parameters are obtained, as shown in Figure 9.3.

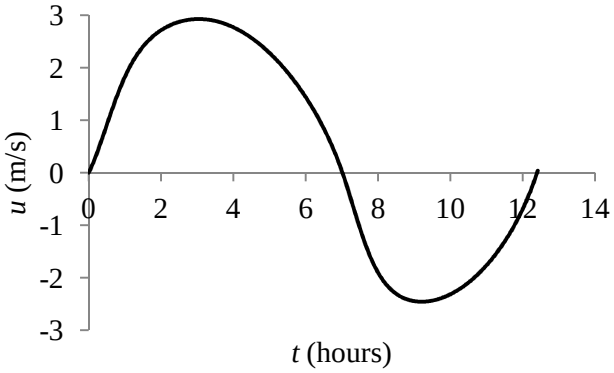

Figure 9.3 – Time series of velocity at spring tide in the Papa Westray channel predicted by the LCM model, with a constant driving head of 0.146 m and a driving head semi-amplitude of 0.885 m

A semi-amplitude of driving head of 0.885 m and constant driving head of 0.146 m result in the appropriate undisturbed spring tide conditions. Having established a model which is matched to the undisturbed channel at spring tide, additional thrust from a tidal device is applied to predict the relationship between device thrust, reduction of flow velocity and the amount of available power. For the specific thrust, Froude number and blockage ratio at each time step, Linear Momentum Actuator Disc Theory for Open Channel Flow (LMADT-OCF) (Houlsby *et al.*, 2008a) has been used to predict the amount of power extracted from the flow and the amount of power that is lost due to downstream mixing. It is assumed that the length scale of wake mixing is significantly less than the length of the channel and that any increase in friction, due to an accelerated bypass flow, is negligible.

In order to extract energy from a flow a device must offer additional retarding thrust, resulting in a reduction in the volume flow rate. Figure 9.4 shows the reduction in volume flow rate when a fence of tidal devices of blockage ratio $B = 0.5$, spanning the entire channel width, is applied with a varying thrust coefficient.

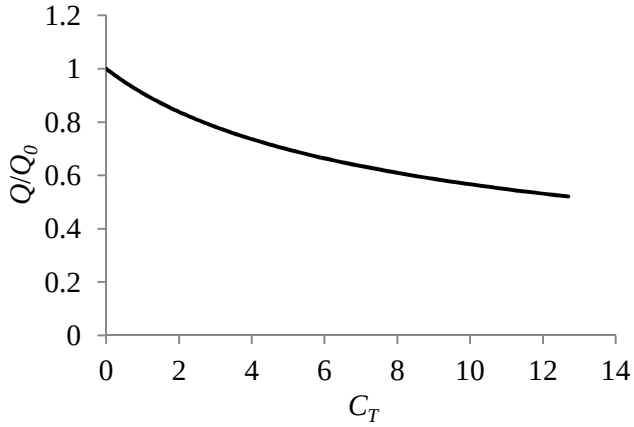

Figure 9.4 – Variation of channel flow velocity with thrust coefficient for a single device in the Papa Westray channel at spring tide, predicted by the LCM model

As the thrust is increased the amount of power extracted from the flow also increases, but an increase in the mixing losses and a reduction in the amount of flow passing through the device mean that a maximum occurs in the amount of power available to the device. Figure 9.5 shows the total power extracted from the flow and the amount of power that would be produced by an inviscid turbine. The difference between these two values represents the power lost due to downstream mixing of the flow. For low values of thrust, very little power is extracted from the flow, insignificant velocity gradients in the wake result in small mixing losses and the turbine has a negligible effect on the volume flow rate of the channel. However, above a given value of thrust the flow through the turbine is choked and instead bypasses the device, causing all of the power extracted from the flow to be lost in downstream mixing. It should be noted that the choking of the flow through the device differs from the definition of flow choking by Garret and Cummins (2005a), where the channel volume flow rate is choked.

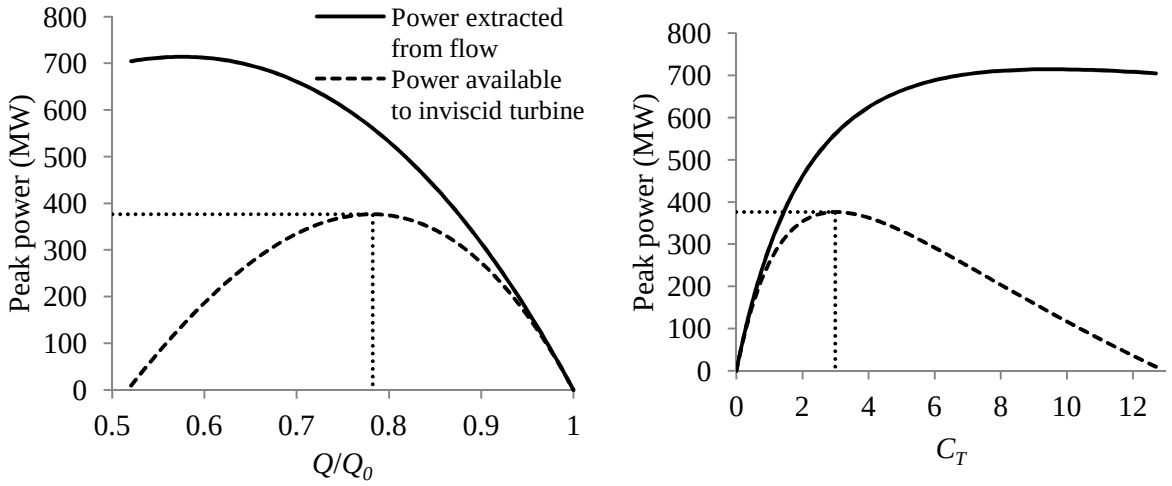

(a) Peak power vs. flow-rate reduction *(b) Peak power vs. thrust coefficient*

Figure 9.5 – Variation of peak power at spring tide, predicted by the LCM model

As shown in Figure 9.5 the maximum peak power available during a spring tide to a single fence of tidal device of blockage ratio 0.5 and thrust coefficient of 3.0 is approximately 376 MW, and induces a reduction in flow velocity to roughly 78% of the undisturbed flow velocity. The amount of power is therefore significantly greater than the 230 MW that is predicted by an energy flux calculation of the undisturbed channel, assuming a peak efficiency of extraction equal to the Lanchester-Betz limit of 59%.

When focussing on the mean power output over a spring tidal period, as shown in Figure 9.6, the maximum available average power of 132 MW occurs at a slightly elevated coefficient of thrust of 3.2 and a reduction in velocity to 77% of the undisturbed value.

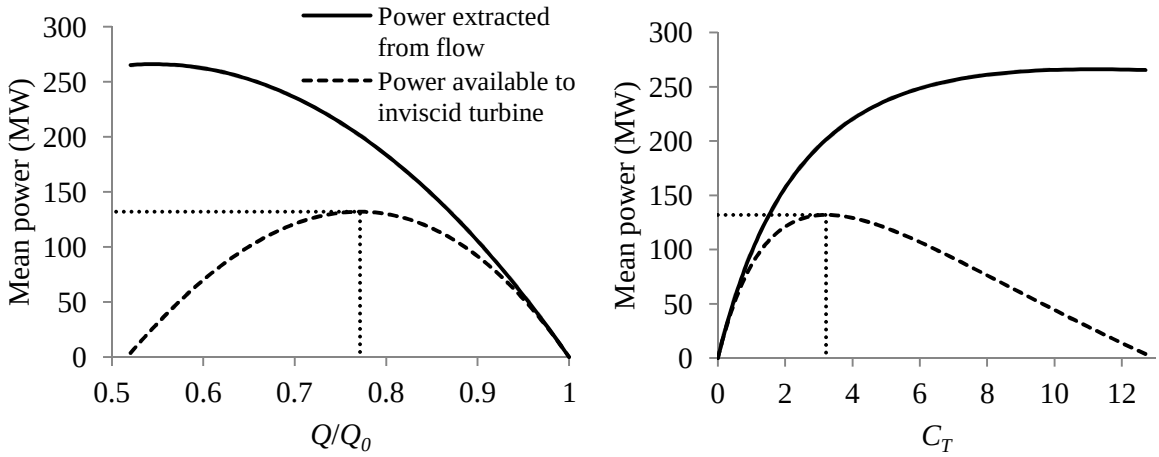

(a) Mean power vs. flow-rate reduction *(b) Mean power vs. thrust coefficient*

Figure 9.6 – Variation of mean power with thrust and reduced flow-rate at spring tide, predicted by the LCM model

While a designer might choose to simply maximise the power produced by the device, with a finite tidal resource it may be more desirable to maximise the efficiency with which a single device extracts energy. The bypass mixing efficiency, the proportion of extracted energy that is made available to a device of a given blockage ratio, is defined as shown in equation 9.2.

$$\eta_{mix} = \frac{P_{inviscid}}{P_{extracted}} \qquad 9.2$$

Figure 9.7, demonstrates that the losses due to downstream mixing are minimised for a device of zero thrust, which will in turn generate zero power.

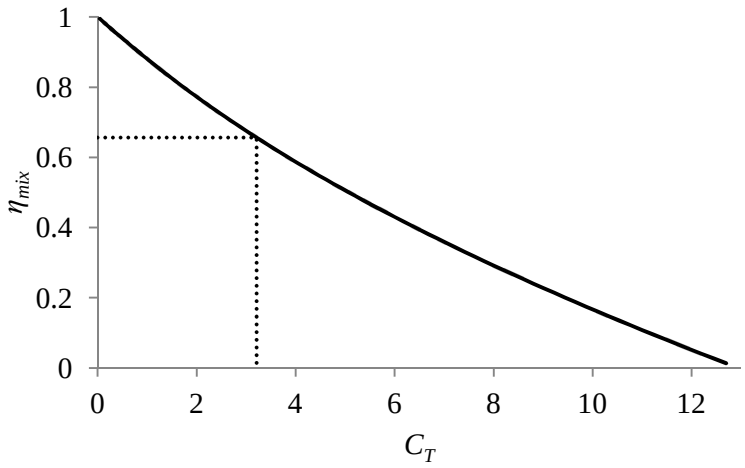

Figure 9.7 – Variation of bypass mixing efficiency against thrust coefficient at spring tide, with efficiency and thrust at peak power highlighted

A more useful indicator of the performance of a device might be some combination of the mean inviscid power and the mixing efficiency. As an example, Figure 9.8 shows the case if these two factors are combined as a product. Obviously this simple product should be weighted depending on the impact of each variable to the desired design criterion, but this initial investigation weights the two parameters evenly.

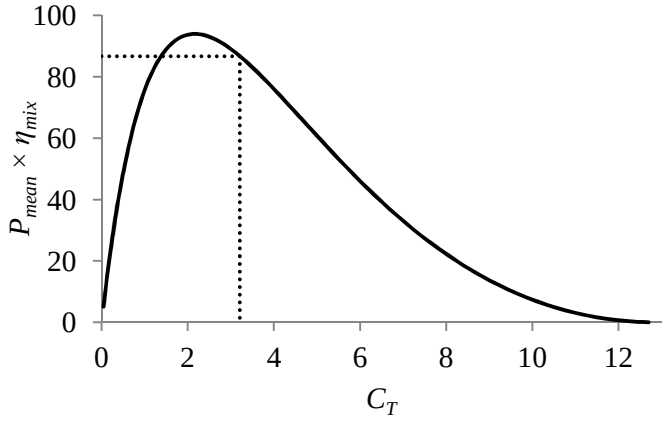

Figure 9.8 – Graph of product of mean power output and bypass mixing efficiency against thrust coefficient at spring tide, with product and thrust at peak power highlighted

As shown in Figure 9.8, the optimal operating point according to the product criterion occurs at a reduced thrust coefficient, when compared to the peak mean power point. By operating at the peak product point, as opposed to the peak power point, the mean power available and the device thrust are reduced by factors of 0.95 and 0.69 respectively. However, the efficiency with which energy is made available to the device is increased from 66% to 75%. It is clear that operating in this regime has significant benefits, in terms of maximising the available resource, whilst maintaining a high level of device performance.

However, if a tidal device of such a high thrust were not feasible, a designer might choose to install two rows of tidal fence in the channel. As shown in Figure 9.9, by using two rows of device the peak mean power available at spring tide is increased by 30% to 171 MW. The maximum occurs at a thrust coefficient, for each row of device, of 2.3 and a reduction in flow velocity to 71% of the undisturbed value. The bypass mixing efficiency with which energy is made available for extraction also increases, from 66% to 74%.

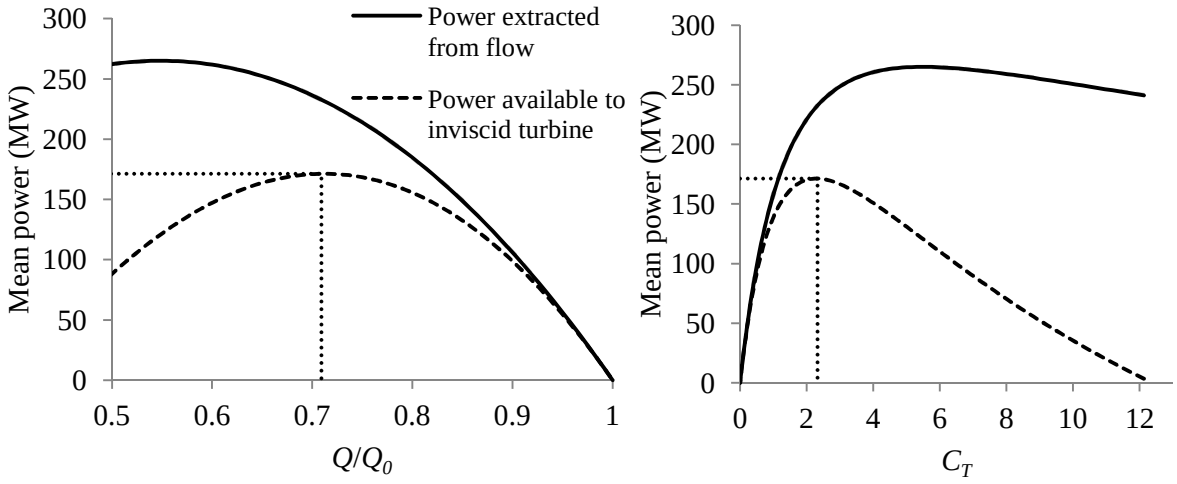

(a) Mean power vs. flow-rate reduction *(b) Mean power vs. thrust coefficient*

Figure 9.9 – Variation of mean power with thrust and reduced flow-rate for two rows of device at spring tide, predicted by the LCM model

While the mixing efficiency of each device, at a given thrust, remains the same for each row of turbine, by using two rows of turbines the amount of thrust applied by each can be reduced, but extracting greater amounts of power overall. It should be noted the configuration of turbine array in which the greatest amount of power is made available for extraction, is an infinite number of rows of device, each extracting an infinitesimal amount of power. However, it is fairly obvious that a solution using many rows of devices is economically infeasible. In the case of the Papa Westray channel, the question must be asked as to whether the 30% increase in available power will economically and environmentally justify doubling the number of rotors and foundations, and further reducing the flow velocity in the channel.

It should be noted that the values of power quoted in this section are those which would be achieved by a device with no viscous drag. The proportion of this power that is converted to useful power will depend on the viscous efficiency of the device, which varies significantly between designs and configurations of device.

9.3. Turbine life model

By combining the predictions of the LCM model with those of the hydrodynamic and structural models of Chapter 7 and Chapter 8, the peak power produced and blade stress induced by a given design of THAWT can be predicted over the tidal cycle. By modelling the accumulation of material damage, due to fatigue, the amount of time which a device is likely to survive before failure is predicted.

It should be noted that the LCM model simulates an idealised installation of the THAWT device in which the rotor achieves a blockage ratio of $B = 0.5$ over the entire channel area and the added channel thrust of the turbine has no effect on the head difference across the channel. Also, by approximating the performance of the device using the idealised numerical models of Chapter 7 and Chapter 8, the effects on the hydrodynamic and structural performance of the device from complex flow phenomena, such as turbulence intensity, shear profiles, wave loading and gusting flow, are not accounted for.

Figure 9.10 shows the variation in flow velocity over a fortnight cycle in the Papa Westray channel, based on the flow parameters in Table 9.1.

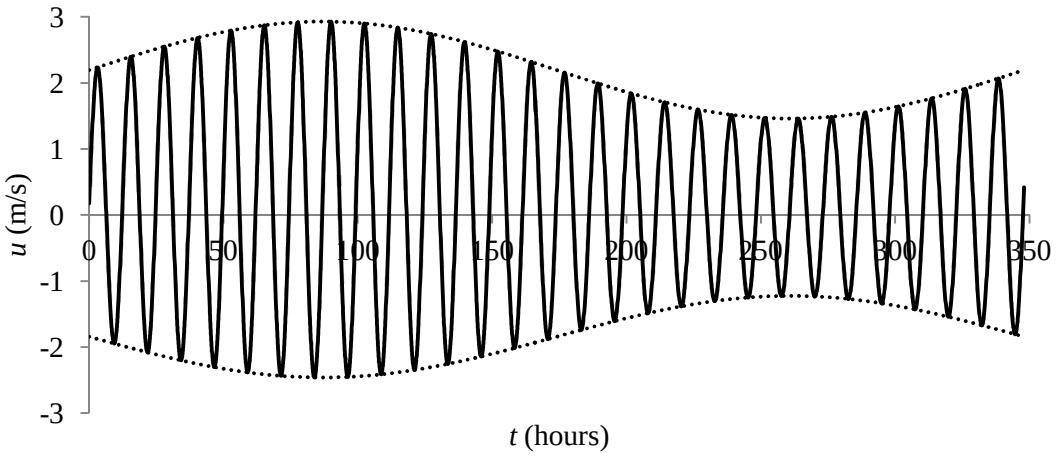

Figure 9.10 – Variation of undisturbed flow velocity over a fortnight tidal cycle

The tidal cycle is discretised into segments of 12.42 hours, corresponding to a single cycle of a semidiurnal tide. The driving head required to achieve the corresponding undisturbed flood and ebb tides during each segment are calculated using the LCM model.

Based on the thrust predicted by the NS-BE-FS model of Chapter 7, a subsequent run of the LCM model produces the time series of flow velocity that is expected with the additional thrust from a fence of tidal devices, as shown in Figure 9.11.

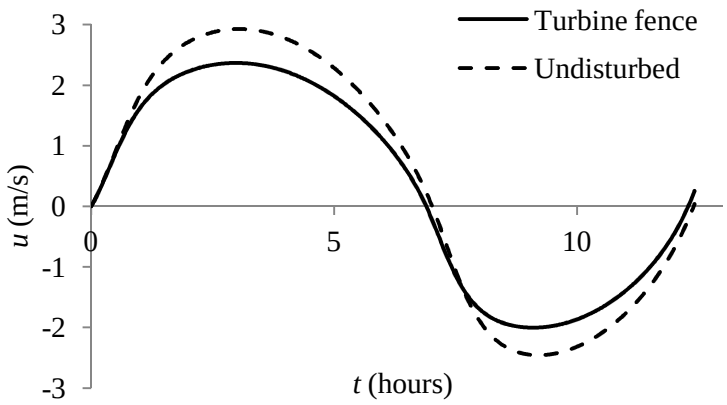

Figure 9.11 – Comparison of flow velocities over a spring tidal period with and without a tidal fence

This time series is subsequently discretised into 79 segments, and the velocity for each is used to calculate the power output and the number of turbine rotations, based on the performance predictions of the NS-BE-FS model for the swept truss blade forces, as described in section 7.5. Despite small variations in the blockage ratio, due to the surface elevation changing during a tidal cycle, the NS-BE-FS simulations of the THAWT device are conducted at a steady blockage ratio of 0.5. The maximum error in the blockage ratio is therefore approximately 5%.

The blade stress amplitude and mean blade stress at a given flow velocity are predicted using the Finite Element structural analysis of Chapter 8. The stress state and number of turbine rotations are used to calculate the accumulated damage during the segment and to assess whether the current stress state induces failure of the blade, as described in section 9.4.

This process is carried out for a given design of turbine over consecutive fortnightly tidal cycles until the fatigue failure criterion is met. The onset of the fatigue failure criterion therefore defines the expected lifetime of the device, and the power predicted by the NS-BE-FS model can be integrated up to that time to predict the total power produced.

The performance of a basic configuration of THAWT device, described in section 9.5, is assessed over the expected lifetime, before the length to width ratio β and rotor solidity s are varied to explore how the feasibility and optimisation of a device might be improved.

9.4. Fatigue life calculation

While the accumulation of damage through fatigue cycles is relatively well understood in common homogenous structural materials, such as metals, the effect of fatigue on fibre reinforced composites is less well known. Due to the variety of fibre reinforcements, bonding epoxies and geometry of the layups of these two constituents, the mechanical properties of

composite materials vary significantly. With the additional considerations of complex fatigue mechanisms such as fibre de-bonding and delamination (Gamstedt and Sjogren, 1999) the prediction of fatigue life of composite materials is a complex issue.

A comprehensive analysis of the fatigue life of glass fibre reinforced plastics (GFRP) has been performed by Mandell et al. (2003), using a large series of fatigue tests, performed on a relatively 'industry standard' layup. By combining tests at several values of stress ratio, a comprehensive model has been created of how different stress cycles accumulate as fatigue damage, as shown in Figure 9.12.

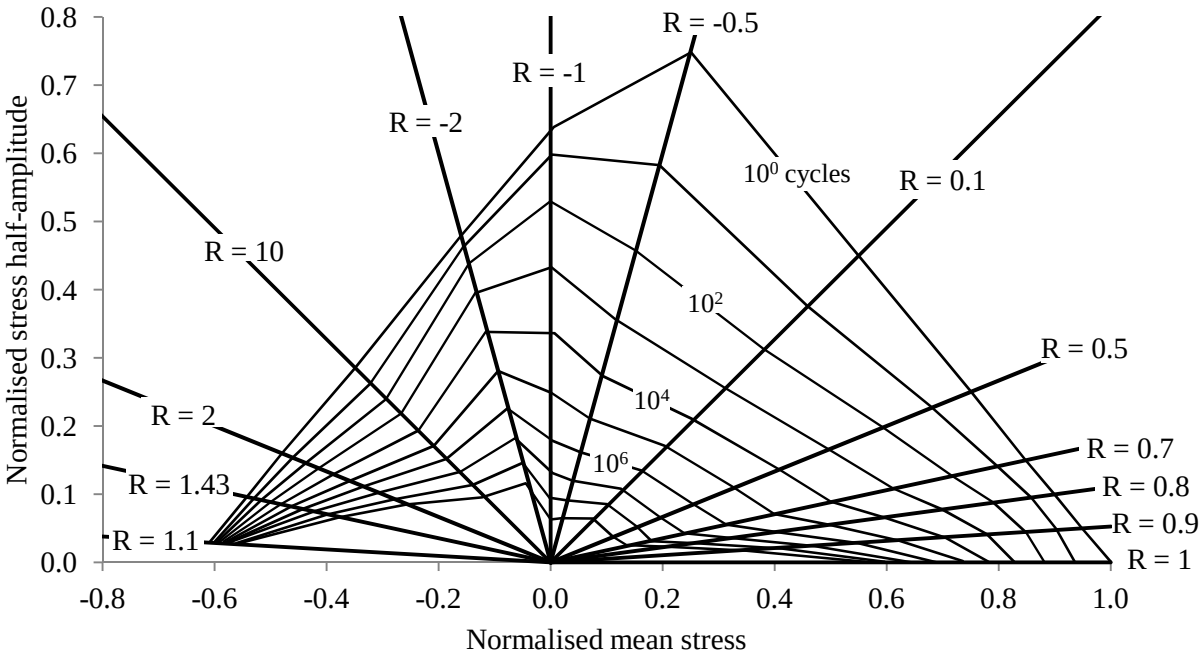

Figure 9.12 – Goodman diagram for a standard GFRP layup based on data in (Mandell et al., 2003)

Further research by Sutherland and Mandell (2005) produced a '95/95' fit of this data, which predicts the number of fatigue cycles for each stress state that 95% of samples would be expected to survive. The '95/95' fit was taken as a lower bound of the expected material lifespan. This model was validated by applying various material strength degradation models to experimental samples, loaded with a stress pattern that had been recorded during tests of an axial-flow wind turbine. This work indicated that the best method of predicting fatigue failure under variable loading, which offered the greatest accuracy and most realistic simulation of the path to failure, was a generalised non-linear residual strength model of the form

$$\left[\frac{\sigma_R}{\sigma_0}\right]_i = 1 + \left(\frac{\sigma_i - \sigma_0}{\sigma_0}\right)\left(\frac{N_i + (N_{i-1})^*}{N_{fi}(\sigma_m, \sigma_a)}\right)^{\nu} \qquad 9.3$$

where N_i is the current number of stress cycles $(N_{i-1})^*$ is the number of previous equivalent cycles determined for the current stress level and v is the degradation parameter. The number of previous equivalent cycles is the number of cycles which would give the current residual stress ratio $[\sigma_R/\sigma_0]_i$ if cycled only at the current stress state $(\sigma_m, \sigma_a)_i$.

The residual compressive or tensile strength after i steps is given by equation 9.4, which implies that the residual tensile and compressive strengths reduce proportionately as a monotonically decreasing function.

$$(\sigma_R)_j = \left(\frac{\sigma_R}{\sigma_0}\right)_i (\sigma_0)_j \qquad 9.4$$

Failure occurs when a tensile stress exceeds the current tensile residual strength, or when a compressive stress exceeds the current compressive residual strength.

As shown by Sutherland and Mandell (2005) the generalised residual strength method offers a more accurate prediction of fatigue life than the simple Miner's rule approximation, which is often recommended in wind turbine design guidelines (DNV, 2010). The chosen degradation parameter v = 0.265, for the fatigue calculations of the THAWT device, was found to result in the best fit to experimental data (Wahl, 2001).

9.5. Basic turbine design

A basic configuration of THAWT device has been chosen, and variations in design parameters indicate the impact such changes have on the feasibility of the device.

In order to maintain consistency between chapters, the basic geometry closely matches that of the structural analysis of Chapter 8, with the main configuration parameters listed in Table 9.2.

Mean turbine diameter D (m)	15.0
Solidity s	0.25
Bay length of diameter ratio β	1.0
Average blade tangential swept angle φ (°)	20.4
Fixed offset pitch (°)	-2.0
Blade thickness to chord ratio (%)	24.0
Composite Young's modulus (GPa)	35.5
Composite tensile strength (MPa)	750
Composite compressive strength (MPa)	480

Table 9.2 – Basic truss configuration specification of device used for the case study analysis

The turbine diameter of 15 m has been chosen in order to maintain a blockage ratio of 0.5. The change to a fixed offset pitch of -2° was chosen as both experimental and numerical

simulations of the device suggest that this will optimise the performance of the turbine. One area which has been identified with significant potential to reduce blade stress is the thickness to chord ratio. Thick hydrofoil sections are prone to flow separation due to premature boundary-layer transition, and so performance characteristics for foils are rarely published for thickness to chord ratios greater than 24% (Dam *et al.*, 2010). For this reason a blade thickness of 24% was chosen, and the drag coefficients used in the NS-BE-FS model are increased, relative to the NACA0021 data of Sheldahl and Klimas (1981), by a factor of 1.075, predicted using the Xfoil panel method (Drela, 2004).

The blade section shown in Figure 7.46 has been chosen after a simple optimisation study, in which the blade stress was minimised, while attempting to restrict the amount of blade material. The thickness of the majority of the section is given in metres by $0.04\times\cos(\varphi)$ for a six-bladed device of solidity of 0.25 and scales linearly with variations in the blade chord length. The sections of reinforcement are twice the thickness of the basic shell.

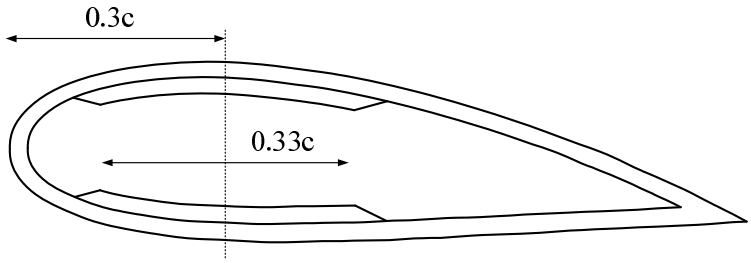

Figure 9.13 - Image of blade section used for case study analysis

It should be noted that the foil section illustrated in Figure 9.13 represents the necessary section at the point of highest stress in the structure. It is likely that the wall thickness of the sections elsewhere would be reduced in order to minimise the amount of material used. The use of support sections of twice the chord length of the blade members has been implemented, due to the analysis of Chapter 8, and all blade dimensions and layups have been scaled appropriately. It is acknowledged that there is substantial scope for further optimisation of this section and the impact that it has on the blade member stresses and deflections.

The power coefficient predicted by the NS-BE-FS model has been reduced by an arbitrary factor of 0.85 in order to represent the losses due to the support members of the truss rotor.

9.6. Results

9.6.1. Basic configuration

The NS-BE-FS model predicts that the truss configured device of s = 0.25, β = 1 and D = 15 m achieves a kinetic power coefficient over the anticipated range of flow velocities, as shown in Figure 9.14. This compares favourably with the performance of the more conventional low blockage MCT Seagen device, which achieves a kinetic power coefficient of approximately 0.38 (MCT, 2009).

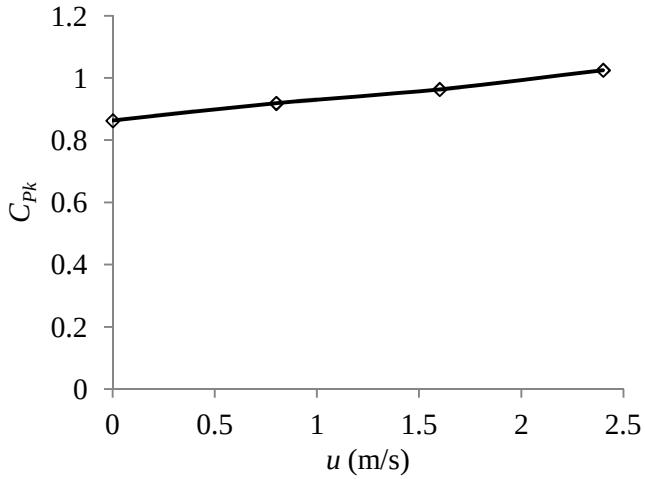

Figure 9.14 – Variation of predicted kinetic power coefficient over a range of flow velocity, for the truss device with β = 1 and s = 0.25

Over the entire tidal cycle in the Papa Westray channel, the NS-BE-FS model predicts that a single 15 m long bay of the truss device produces a peak power of 1.57 MW and an average power of 0.31 MW, with an average thrust coefficient of approximately 2.4. When the device spans the entire width of the 2 km channel LMADT-OCF predicts that on average a total of 104.5 MW is removed from the flow. 29 MW of the extracted energy is lost as mixing losses, leaving 75.5 MW of power available to the device. Of this available power, the NS-BE-FS model predicts that on average 41.9 MW is extracted as useful power, which is approximately 40% of the total power and 55% of the available power.

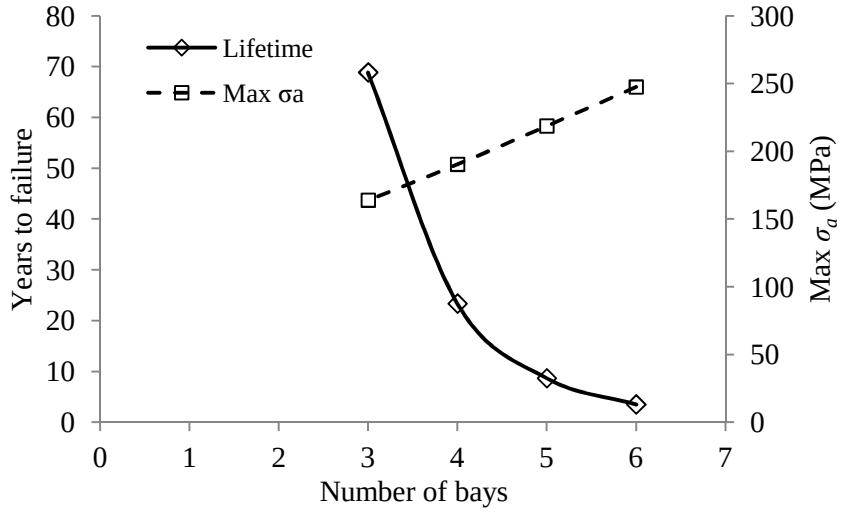

Figure 9.15 – Variation of predicted device life and induced blade stress amplitude over a varied number of bays, for the truss device with $\beta = 1$ and $s = 0.25$

The expected lifetime of a device, before fatigue failure of the blade material, is heavily dependent on the induced blade stress amplitude. As shown in Figure 9.15, despite a linear variation in the maximum induced blade stress amplitude with the number of bays, the expected lifetime of the device increases exponentially as the number of bays is reduced.

Due to the fact that the efficiency of the device does not change as the number of bays is increased, the main benefit of increasing the number of rotor bays is to reduce the number of required foundations and generators, as shown in Figure 9.16. The cost of foundations is anticipated to be the most significant capital cost in the installation of a turbine array.

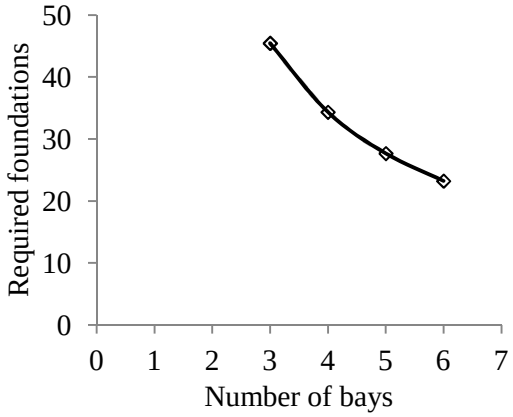

Figure 9.16 – Variation in the number of required foundations over a varied number of bays, for the truss device with $\beta = 1$ and $s = 0.25$

It is evident that a five or six bay device, of the current configuration, is not feasible due to expected lifetimes of approximately 8.7 and 3.5 years respectively. The 23.3 years expected lifetime of the four bay device is shorter than the anticipated required lifetime of a renewable device of 25 – 30 years. Whilst adopting a three bay design significantly increases the

anticipated life of the device to 68.9 years, the cost of foundations increases by approximately 1.33, when compared to the four bay design.

9.6.2. Variation of bay length to width ratio β

One method which can be used to maintain a longer device is to reduce the bay length to width ratio of the turbine, β. As shown in Figure 9.17, by decreasing the bay length to width ratio, the lifetime of a device of a given length is significantly increased. This is due to a reduction in the bending load experienced by an individual turbine blade. By moving from the four bay truss with a length to width ratio of β = 1, to a 10 bay truss with a length to width ratio of β = 0.5, the average power produced by the device is reduced by a factor of 0.83. However, the lifetime of the device is increased from approximately 23.3 years to 176.2 years and the number of required foundations is reduced by a factor of 0.8.

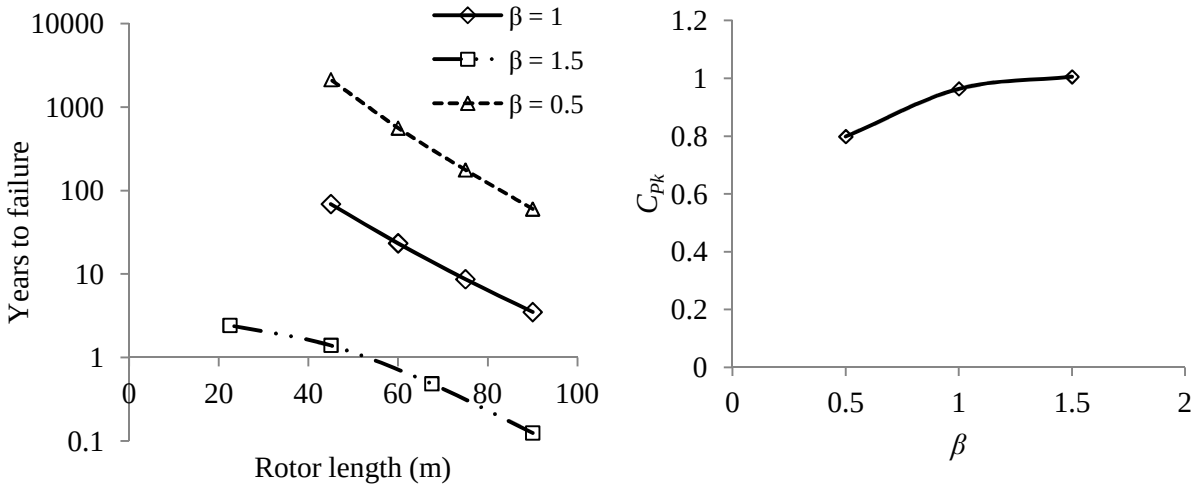

(a) Years to failure *(b) Kinetic power coefficient at 1.6 m/s*

Figure 9.17 – Variation in device lifetime and kinetic power coefficient for a range of length to width ratios at s = 0.25

An expected life of 176.2 years may be significantly higher than the desired design lifetime, but this approach demonstrates that reducing the length of an individual bay can be used to reduce the stress induced in the device and the number of required foundations, without significant drops in the power output. However, as the number of bays is increased, the axial loads that the blade members are subjected to will also increase, so that the device is more susceptible to failure by member buckling, as mentioned in Chapter 8.

9.6.3. Variation of solidity

As indicated in Chapter 5 there is a trade-off in the choice of device solidity, between the hydrodynamic and structural performance of the rotor. Figure 9.18(a) demonstrates that reducing the solidity of the device is likely to increase the power produced.

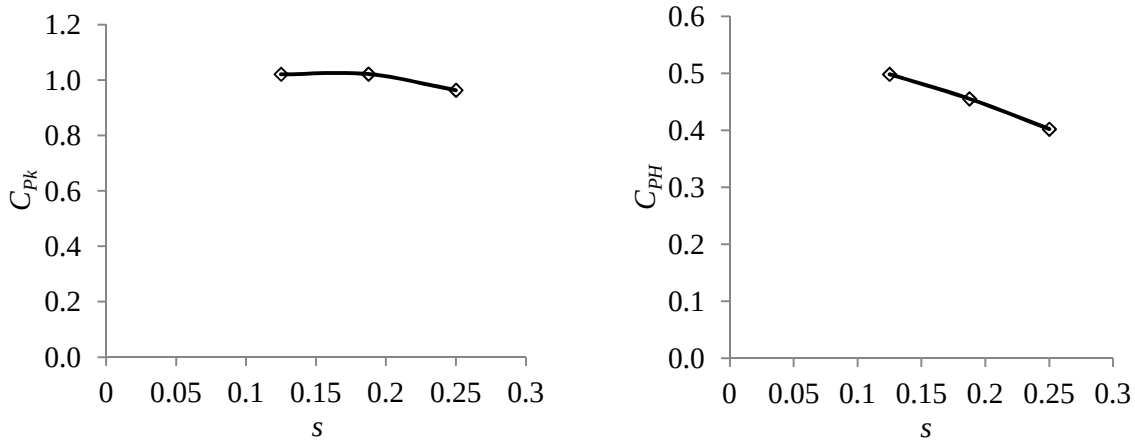

(a) *Kinetic power coefficient* *(b) Head power coefficient*

Figure 9.18 –Kinetic and head power coefficients predicted by the NS-BE-FS model for a range of solidity at β = 1

Furthermore, by reducing the solidity of a device, the thrust produced by the tidal fence is significantly reduced and the corresponding head efficiency, with which the turbine converts extracted power into useful power, is significantly higher, as shown in Figure 9.18(b).

However, as shown in Figure 9.19, the increase in stress amplitude and the accompanying dramatic decrease in design lifetime, which result from reducing the solidity of the device, mean that the structural considerations dominate and indicate that higher solidity devices would be more economical.

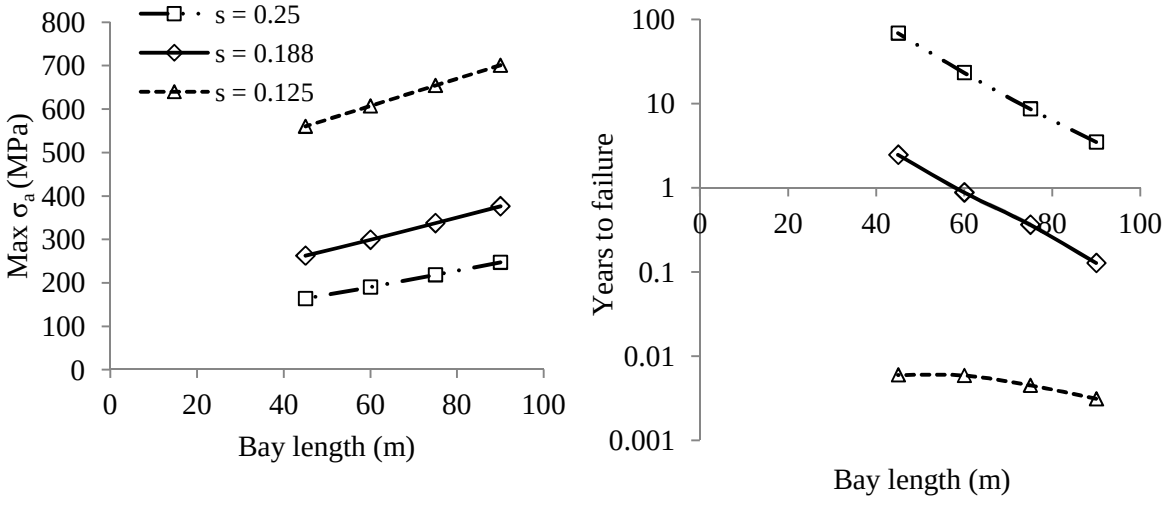

(a) Maximum stress amplitude (b) *Years to failure*

Figure 9.19 – Variation in blade stress amplitude and device lifetime for a range of solidity at β = 1

9.6.4. Alternative variations to the design configuration

The preliminary analysis of Chapter 3 suggests that the blade thickness of the rotor blades has a significant impact on the induced blade stresses. It is assumed that the blade thickness of 24%, used in this analysis, is the maximum that would be feasible due to the lack of adoption of higher thickness blades for all but the most extreme applications. However, without comprehensive numerical modelling it is difficult to predict the lift and drag characteristics of a hydrofoil of higher thickness, which may prove to be suitable for the THAWT device application.

While the preliminary analysis of Chapter 3 does not indicate a reduction in blade stress with a reduction in blockage ratio, the results from Chapter 5 indicate that a reduction in blockage is likely to cause a reduction in the operational tip speed ratio. It might therefore be possible to reduce blade stresses with a reduction of blockage ratio. This has not been studied for the Papa Westray channel due to the anticipated reduced influence that blockage has on the blade stressing, when compared to other variations in design parameter. However, while reducing the blockage ratio of the device is likely to reduce the induced stress, maintaining a bay length to width ratio means that for a given number of bays, the rotor length will decrease. This will result in an increased number of foundations and is assumed to adversely affect the economic feasibility of the device.

9.6.5. Power capping or cutting

The results that have so far been analysed in this section assume that the turbine operates at the peak power point over the entire tidal cycle. However, there are several benefits to capping the maximum power generated by the device. As demonstrated by the preliminary analysis of Chapter 3 and Figure 9.20, the induced blade stress amplitude increases quadratically with an increase in flow velocity. Due to the increments in stress amplitude having a substantial effect on the number of fatigue cycles before material failure, avoiding the areas of maximum stress is favourable.

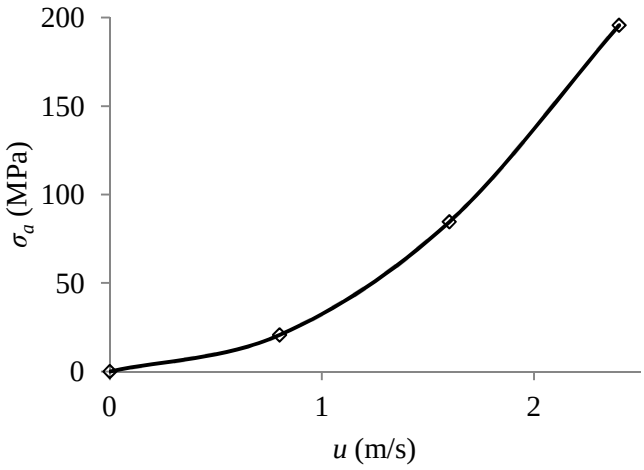

Figure 9.20 – Variation of induced blade stress amplitude with velocity for a four bay truss device with β = 1 and s = 0.25, predicted using the FE analysis of Chapter 8

By capping the amount of power produced by the device, it is also possible to produce a more consistent amount of power over a sustained period of time, as shown in Figure 9.21, which is likely to be favourable when integrating tidal devices with the national electricity grid. The losses in a standard generator at very low speed result in a significant drop-off in the amount of power generated (McIntosh, 2009), as shown in Figure 9.21 where it is assumed that no power is generate below approximately 10% of the rated power.

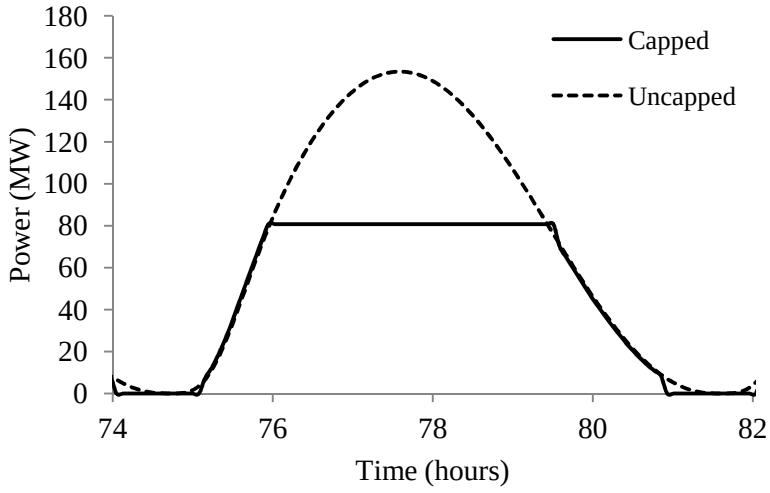

Figure 9.21 – LCM simulation of the Papa Westray channel for a β = 1 and s = 0.25 truss device, with power capped at 50% of the maximum power available

By capping the amount of power that is extracted by a device, the size of generator that is required can be significantly reduced, while the total amount of energy extracted is only marginally reduced.

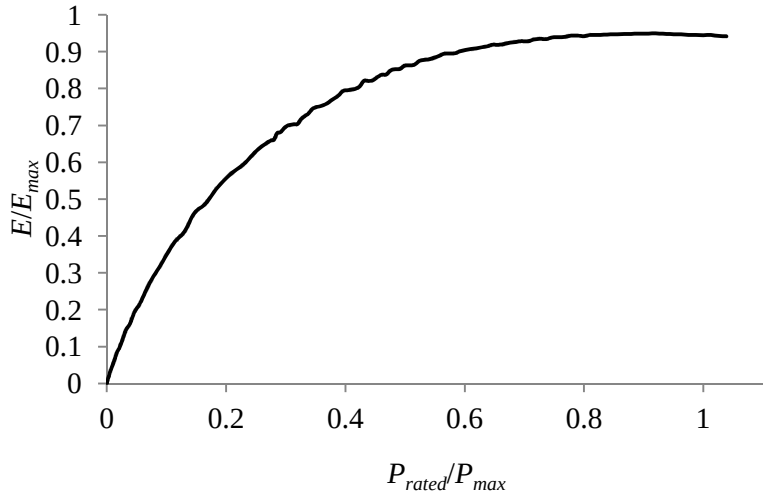

Figure 9.22 – Variation in extracted mechanical energy over a range of rated power caps, for a β = 1 and s = 0.25 truss device

Figure 9.22 demonstrates that as the rated power of a generator is reduced, from that required to operate at peak output over the entire tidal cycle, there is an initial increase in the energy extracted, due to the fact that more power is extracted during the lower velocity flows. However, further reductions in the rated capacity of the generator reduce the amount of mechanical power extracted. It should be noted that by reducing the size of generator to half of the rated capacity, required to operate over the entire tidal cycle, the amount of mechanical extracted energy is reduced by approximately 14%. By reducing the rated power in this way, the capacity factor of the generator is increased from approximately 19% to 34%.

The choice of reduction in rated power is likely to depend heavily on economic factors. However, it appears obvious that capping the power of a given device is likely to be significantly beneficial, and has been adopted by the current market leaders, Marine Current Turbines (MCT, 2009).

Axial-flow turbines, such as the MCT Seagen device, are able to regulate the maximum power that is produced using pitch controlled blade stall or feathering. However, the mechanism by which the power of the truss THAWT device might be capped is unclear. Without the ability to feather the blades of the fixed truss rotor, the likely mechanism of reducing the power generated at any given flow velocity is to operate at a tip speed ratio lower than the tip speed ratio of peak power, as shown in Figure 9.23. Operating in this region will require robust speed control of the device, which is likely to be undergoing severe blade stall and unsteady torque. The effect that blade stall has on the fatigue of the device is unclear and

cannot be simulated by the NS-BE-FS model, and should therefore be analysed in order to assess the feasibility of power regulation by blade stall control.

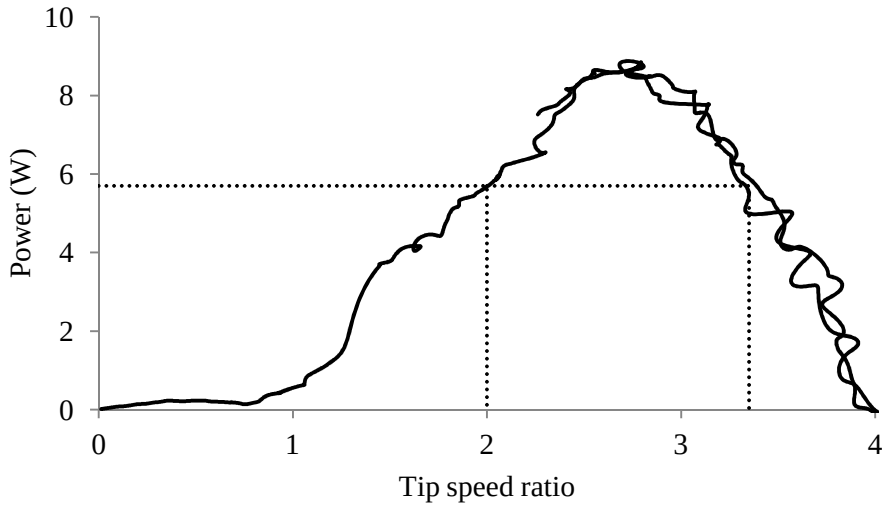

Figure 9.23 – Experimental power curve for the truss device at a Froude number of 0.13, demonstrating the reduction in power when reducing or increasing the operating tip speed ratio

The power produced by the device can also be reduced by operating at an increased tip speed ratio, as shown in Figure 9.23. However, the blade stresses in this region are likely to be greater than those at the operating point and so increasing the operating tip speed ratio is not anticipated to be an economic method of power capping.

9.7. Device environmental impact

After growing confidence in the safety of tidal turbines with respect to marine life (Riddoch, 2008), the environmental impact of a tidal device has been limited to factors, such as the wake-induced velocity and acoustic intensity of a device (Li and Calisal, 2010). Despite the acceptance that arrays of devices will impart a significant momentum loss to a channel flow (Antheaume *et al.*, 2008), macro scale research on the effect of this thrust on the channel flow characteristics are relatively new (Draper *et al.*, 2010) and are often site-specific (Atwater and Lawrence, 2010). It is therefore necessary to also assess whether the installation of a tidal device, and the resulting reduction in volume flow rate through the domain, are likely to adversely affect the local ecosystem.

9.8. Conclusions

A synoptic analysis of truss THAWT device in the Papa Westray channel has been used to demonstrate that a design of device is technically feasible, which is able to operate for a realistic lifetime of 25 or more years. By operating at a kinetic power coefficient significantly

greater than the Lanchester-Betz limit, the device is likely to be economically competitive when compared with alternative designs.

It has been shown that the structural considerations of design configuration dominate over the hydrodynamic considerations. This results from the significant effect of fatigue cycling on the expected operating lifetime.

Methods for reducing blade stress and increasing the operating lifetime of a device have been proposed, including a reduction in the bay length to width ratio and the capping of the rated power of the device. As well as reducing blade stressing, capping the rated power of the device allows for the use of a smaller generator, which achieves a higher capacity factor and a more consistent power output, without significantly reducing the total energy extracted.

Chapter 10

Conclusions and Future Work

In order to investigate the technical feasibility of the truss configured THAWT device, and to understand how the trade-off between the hydrodynamic and structural performance of the turbine affects the economic viability, a series of objectives were identified:

- Demonstrate that a truss THAWT device is capable of achieving an efficiency and power output similar to that of the parallel-bladed device, which has been shown to exceed the Lanchester-Betz limit in small scale tests.
- Develop a model of the device hydrodynamics which is capable of predicting the power output and blade forces with a sufficient degree of fidelity and accuracy.
- Develop a structural model of the THAWT rotor, which is capable of predicting the induced blade stresses, based on the blade loads predicted by the hydrodynamic model.
- Integrate the hydrodynamic and structural models of the THAWT device to predict how the power produced and expected lifetime of a device are affected by various aspects of design configuration, in a given tidal location.

10.1. Fluid dynamics

1. Experimental tests of a $1/20^{th}$ scale prototype of the THAWT turbine have shown that the truss configured device is capable of producing power with an efficiency greater than the Lanchester-Betz limit, with a maximum measured C_{pk} of 0.85 at a Froude number of 0.21.

2. The results from the experimental tests have been used to validate a Navier-Stokes actuator cylinder numerical model of the device, which is capable of simulating the deformation of the open channel free surface (NS-BE-FS). The NS-BE-FS model has shown that a relatively simple numerical model of the device is capable of matching experimental results with good accuracy and fidelity, and allows the mechanics affecting the hydrodynamic performance of the device to be better understood.

3. The significance of modelling the free surface deformation has been shown to vary with the Froude number of the flow, in agreement with the analytical linear momentum actuator disc for open channel flow derived by Houlsby *et al.* (2008a), and is likely to cause

an increase in the blade loading by a factor of 1.11 for a Froude number of 0.21, when compared to a non-deforming free surface analysis.

4. The NS-BE-FS model has demonstrated that the high thrust THAWT device causes significant deflection of the incident flow, resulting in significantly different blade loading and device performance when compared to a more conventional low solidity cross-flow device.

5. Experimental test configurations with increased blockage and reduced solidity have been shown to result in an increase in hydrodynamic performance. However, preliminary dimensional analyses indicate that these configuration variations will also induce a significant increase in blade stresses.

6. Experimental and numerical modelling has indicated that negative fixed offset pitch significantly improves the performance of the device and is anticipated to reduce blade stresses due to a lower operating tip speed ratio.

10.2. Structural analysis

A static beam finite element analysis of the various configurations of the THAWT device has been implemented, with fluid loading predicted using the NS-BE-FS model. A multi-cell blade section analysis technique is derived and used to predict the location and magnitude of the stresses in the structure.

1. The structural analysis has shown that the maximum stress induced in the truss configured device increases with an increase in the number of bays at a significantly lower rate than a device with a parallel configuration of blades. The difference in the rate of increase of blade stress is due to differing mechanisms in the transfer of the blade forces to the rotor supports, with the parallel-bladed device shearing bay by bay and the truss configured device bending like a beam, with shear planes remaining approximately plane to the neutral axis.

2. A comparison of the induced stresses in blade members made of a realistic glass fibre reinforced polymer, against the fatigue strength of the material over approximately 1×10^8 loading cycles, indicates that cyclic fatigue is likely to limit the length and operating lifetime of a THAWT rotor.

3. Decreasing the bay length to width ratio of a truss configured rotor reduces the bending stress in the blade members, but increases blade axial loads and may cause buckling of the blade members to become the dominant failure mechanism.

10.3. Full scale performance

The NS-BE-FS and finite element structural models have been combined with a Linear Channel Momentum model to simulate the Papa Westray channel, chosen as a representative tidal site, with idealised flow conditions to explore the effect of installing a tidal array on channel flow and the implications to the technical feasibility of the THAWT device.

4. It has been shown that in the idealised flow conditions of the Papa Westray channel that an array of THAWT device, which produces a greater amount of power than the equivalent swept area of conventional axial flow devices, is technically feasible and is capable of resisting the applied hydrodynamic loads over 25 or more years.

5. When considering the accumulation of fatigue damage the structural considerations in the design of a device substantially outweigh the influence of variations in hydrodynamic performance. For example, despite improving the hydrodynamic performance of the device, reducing the solidity of the THAWT rotor is shown to render the turbine infeasible due to a significantly reduced operating lifetime.

6. The peak stresses may be reduced by decreasing the bay length to width ratio. This allows the spacing between device supports to be increased, which reduces the number of required foundations and is anticipated to significantly improve the economic feasibility of an array.

10.4. Completed further work

The accuracy of the prediction of the structural and hydrodynamic performance of the THAWT device have a strong influence on the degree of over engineering that is necessary in order to design a full scale device that is guaranteed to survive for a given operational lifetime. Whilst the hydrodynamic and structural performance of the THAWT device can be approximated using numerical models, the validation of these models using scale experiments is necessary to gain confidence in their accuracy. Comparison against as many measurements as possible will therefore allow for the most comprehensive validation.

A further series of experimental tests at Newcastle University were carried out in January 2011 on a 1.5 m long three bay truss rotor and a 1.5 m long single bay parallel-bladed device.

Measurements of blade strain, device thrust and upstream and downstream flow profiles and depth were taken, which will allow for the validation of the entire flow domain and local blade hydrodynamics. The data from these tests have not been comprehensively analysed and are therefore not presented in this thesis.

Further tests on devices of increased scale, and especially offshore prototypes, will reduce the inaccuracies due to Reynolds number scaling and flow turbulence and stratification.

10.5. Future Work

10.5.1. Hydrodynamic modelling

The aspect of the NS-BE-FS model which has been identified as the most significant in improving the accuracy of the model is the simulation of the blade lift and drag characteristics. This requires a technique for predicting the lift and drag of the wrapped and swept blades, in curvilinear motion and with unsteady flow phenomena such as dynamic stall. With the current methods available for simulating blade mechanics, it is debatable whether this technique should be applied by simulating the individual blades or by corrections to the lift and drag curves applied in an embedded blade element method. The level of turbulence modelling that is required depends on the smallest significant scale of turbulence, which is likely to be a benefit of the actuator cylinder method.

Modelling the device in three dimensions is likely to allow a more accurate simulation of the blockage effects, the affect of the varied truss radius and the simulation of the turbine support structure.

Simulations of the full scale device should obviously include as much detail of the site-dependent flow properties, including the velocity profile, turbulence and flow stratification.

10.5.2. Structural analysis

A dynamic analysis of the THAWT structure should be conducted in order to increase the confidence that no loading will occur at a frequency close to the fundamental frequency of the rotor. Whilst a beam element analysis may allow for the accurate prediction of the section forces and moments, a more comprehensive analysis of the hydrofoil sections should be carried out in order to optimise the required composite design of the blades. This is often carried out in the wind industry using a shell finite element analysis. Shell or solid finite element analyses of the structure will also allow for a more comprehensive design of the

support structure and joints, so that the moments experienced by the rotor blades are minimised.

The analysis of the fatigue properties of the likely blade material should be significantly improved, possibly with experimental validation, as the fatigue damage accumulation is possibly the most important aspect of accurately predicting the operating lifetime of the device.

10.5.3. Basin scale analysis

A more comprehensive model of a chosen tidal location will improve the accuracy of modelling the effect that the device has on the channel flow and offer a more accurate prediction of the energy that is available to the device. There is some debate as to the scale that such a model should extend. However, when considering the scale of the THAWT devices that are proposed, it is likely that simulating the boundary conditions substantially further than the channel boundaries will be necessary.

10.5.4. Motor and foundation design

While the power takeoff and foundation design have been largely ignored during the course of this investigation, minimising the costs of these two design considerations is likely to have the most significant impact on the economic feasibility of a full scale installation.

Intelligent choice of the generator design, gearing and control is likely to have a significant impact on the amount of required maintenance, which is also a significant economic factor in the design of a marine turbine. The successful development of a control methodology for power capping of the THAWT device is also likely to have a significant effect on the blade stressing and operating lifetime of the device.

While further work will improve the accuracy in the prediction of the THAWT performance, the work in this thesis has established and combined a set of numerical models, which predict the hydrodynamic and structural performance of the turbine with sufficient confidence to assess the feasibility of such a device at a full scale installation and to optimise its performance.

Bibliography

Abbott, I. H. & Von Doenhoff, A. E. (1959). *Theory of wing sections : including a summary of airfoil data*, New York, Dover.

Alfano, G., de Sciarra, F. M. & Rosati, L.: (1996). Automatic analysis of multicell thin-walled sections, *Computers & Structures*, **59**, (4), pp. 641-655.

Antheaume, S., Maître, T. & Achard, J.-L.: (2008). Hydraulic Darrieus turbines efficiency for free fluid flow conditions versus power farms conditions, *Renewable Energy*, **33**, (10), pp. 2186-2198.

Arbic, B. K. & Garrett, C.: (2010). A coupled oscillator model of shelf and ocean tides, *Continental Shelf Research*, **30**, pp. 564-574.

Armaly, B. F., Durst, F., Pereira, J. C. F. & Schonung, B.: (1983). Experimental and theoretical investication of backward-facing step flow, *Journal of Fluid Mechanics*, **127**, pp. 473-496.

Ashwill, T. D. & Leonard, T. M. (1986). Developments in Blade Shape Design for a Vertical Axis Wind Turbine, *Sandia National Laboratories*, Report No. SAND86-1085.

Astley, R. J. (1992). *Finite elements in solids and structures : an introduction*, London, Chapman & Hall.

Atwater, J. F. & Lawrence, G. A.: (2010). Power potential of a split tidal channel, *Renewable Energy*, **35**, (2), pp. 329-332.

Bahaj, A. S., Molland, A. F., Chaplin, J. R. & Batten, W. M. J.: (2007). Power and thrust measurements of marine current turbines under various hydrodynamic flow conditions in a cavitation tunnel and a towing tank, *Renewable Energy*, **32**, (3), pp. 407-426.

Ball, D. J., Stansby, P. K. & Alliston, N.: (1997). Modelling shallow water flow around pile groups, *Proceedings of the Institution of Civil Engineers Water, Maritime and Energy*, **118**, pp. 226-236.

Banfield, S.: (2006). *Investigation into a transverse horizontal axis tidal turbine for electricity generation*. Masters Project, Oxford University, Department of Engineering Science

Barbero, E. J. (2008). *Finite element analysis of composite materials*, Boca Raton ; London, CRC Press.

Batten, W. M. J., Bahaj, A. S., Molland, A. F. & Chaplin, J. R.: (2006). Hydrodynamics of marine current turbines, *Renewable Energy*, **31**, (2), pp. 249-256.

Bechly, M. E.: (1997). Structural design of a composite wind turbine blade using finite element analysis, *Computers & structures*, **63**, (3), pp. 639.

Bell, J. H. & Mehta, R. D. (1988). Contraction design for small low-speed wind tunnels, *National Aeronautics and Space Administration*, Report No. NASA-CR-177488.

Benham, P. P. & Warnock, F. V. (1976). *Mechanics of solids and structures*, London, Pitman.

Bienen, B.: (2007). *Three-Dimensional Physical and Numerical Modelling of Jack-Up Structures on Sand*. PhD Thesis. Perth, University of Western Australia, School of Civil and Resource Engineering

Black&Veatch. (2005). Phase II UK Tidal Stream Energy Resource Assessment, *Carbon Trust*.

Bossanyi, E. A.: (2003). GH Bladed - Theory Manual, [Accessed April 2011], http://ocw.tudelft.nl/fileadmin/ocw/courses/OffshoreWindFarmEnergy/res00099/Theory_Manual.pdf.

Brahim, M. T., Allet, A. & Parschivoiu, I.: (1995). Aerodynamic Analysis Models for Vertical-Axis Wind Turbines, *International Journal of Rotating Machinery*, **2**, (1), pp. 15-21.

Brennen, C. E. (1982). A review of added mass and fluid inertial forces, California, *Naval Civil Engineering Laboratory*, Report No. CR82.010.

Brochier, G., Fraunié, P., Béguier, C. & Paraschivoiu, I.: (1986). Water Channel Experiments of Dynamic Stall on Darrieus Wind Turbine Blades, *Journal of Propulsion and Power*, **2**, (5), pp. 445-449.

Bryden, I. G., Couch, S. I., Owen, A. & Melville, G.: (2007). Tidal current resource assessment, *Proceedings of the Institution of Mechanical Engineers Part a-Journal of Power and Energy*, **221**, (A2), pp. 125-135.

Bryden, I. G., Naik, S., Fraenkel, P. & Bullen, C. R.: (1998). Matching tidal current plants to local flow conditions, *Energy*, **23**, (9), pp. 699-709.

Burgess, D. W.: (2006). *Transverse Horizontal Axis Water Turbine for extracting power from rivers in remote locations*. Masters Project, Oxford University, Department of Engineering Science

Burrows, R., Walkington, I. A., Yates, N. C., Hedges, T. S., Li, M., Zhou, J. G., Chen, D. Y., Wolf, J., Holt, J. & Proctor, R.: (2009). Tidal energy potential in UK waters, *Proceedings of the Institution of Civil Engineers, Maritime Engineering*, **162**, (MA4), pp. 155-164.

Burton, T., Sharpe, D., Jenkins, N. & Bossanyi, E. (2001). *Wind Energy handbook*, John Wiley & Sons Ltd.

Callaghan, J. (2006). Future Marine Energy, *The Carbon Trust*, Report No. CTC601.

Camporeale, S. M. & Magi, V.: (2000). Streamtube model for analysis of vertical axis variable pitch turbine for marine currents energy conversion, *Energy Conversion and Management*, **41**, (16), pp. 1811-1827.

Carrica, P. M., Wilson, R. V. & Stern, F. (2005). An Unsteady Single-Phase Level Set Method for Viscous Free Surface Flows, *University of Iowa, Iowa Institute of Hydroscience and Engineering*, Report No. 444.

Carta, F. O. (1985). Dynamic Stall of Swept and Unswept Oscillating Wings, East Hartford, *United Technologies Research Center*.

Cartwright, D. (1993). Theory of ocean tides with application to altimetry. In: RUMMEL, R. & SANSÒ, F., editors. Satellite Altimetry in Geodesy and Oceanography: Springer Berlin / Heidelberg. p. 100-141.

COMSOL. (2008). COMSOL Multiphysics Modelling Guide. v.3.5a,

Consul, C.: (2008). *Design and Analysis of the aerofoil sections for THAWT*. Transfer report, University of Oxford, Department of Engineering Science

Consul, C. A., Willden, R. H. J., Ferrer, E. & McCulloch, M. D., (2009). Influence of Solidity on the Performance of a Cross-Flow Turbine. *EWTEC*; Upsala, Sweden.

Dam, C. P. v., Copperman, A., McLennan, A., Chow, R. & Baker, J.: (2010). Thick Airfoils with Blunt Trailing Edge for Wind Turbine Blades, *ASME Turbo Expo 2010: Power for Land, Sea and Air*, June 14-18, Glasgow, UK.

Darrieus, G. J. M.: (1931). inventor^inventors; "Turbine having its rotating shaft transverse to the flow of the current". United States Patent 1,835,018.

Davis, T. A.: (2004). Algorithm 832: UMFPACK, an unsymmetric-pattern multifrontal method, *ACM Transactions on Mathematical Software*, **30**, (2), pp. 196-199.

DECC. (2010). Severn Tidal Power: Feasibility Study Conclusions and Summary Report, *HM Government*.

Delft, D. R. V. v., Winkel, G. G. d. & Joose, P. A.: (1997). Fatigue behaviour of fibreglass wind turbine blade material under variable amplitude loading, *AIAA Aerospace Sciences Meeting and Exhibit*, January 6-9th, Reno.

Denny, E.: (2009). The economics of tidal energy, *Energy Policy*, **37**, (5), pp. 1914-1924.

DNV. (2010). Design and Manufacture of Wind Turbine Blades, Offshore and Onshore Wind Turbines, Report No. DNV-DS-J102.

Draper, S., Houlsby, G. T., Oldfield, M. L. G. & Borthwick, A. G. L.: (2010). Modelling tidal energy extraction in a depth-averaged coastal domain, *IET Renewable Power Generation*, **4**, (6), pp. 545-554.

Drela, M.: (2004). X-Foil Subsonic Airfoil Development System, [Accessed November 2007], http://web.mit.edu/drela/Public/web/xfoil/.

DTI. (2004). Atlas of UK Marine Renewable Energy Resources, *Department of Trade and Industry*.

DTI. (2006). Energy Review - The energy challenge, *Department of Trade and Industry*.

DTI. (2007). Meeting The Energy Challenge: A White Paper on Energy, *Department of Trade and Industry*.

Egbert, G. D. & Ray, R. D.: (2001). Estimates of m2 tidal energy dissipation from topex/poseidon altimeter data, *Journal of Geophysical Research*, **106**, (C10), pp. 22475-22502.

Egbert, G. D., Ray, R. D. & Bills, B. G.: (2004). Numerical modelling of the global semidiurnal tide in the present day and in the last glacial maximum, *Journal of Geophysical Research*, **109**, pp.

Ekaterinaris, J. A. & Platzer, M. F.: (1998). Computational prediction of airfoil dynamic stall, *Progress in Aerospace Sciences*, **33**, (11-12), pp. 759-846.

Etheridge, D. W. & Kemp, P. H.: (1978). Measurements of turbulent flow downstream of a backward-facing step, *Journal of Fluid Mechanics*, **86**, pp. 545.

Fanucci, J. B. & Walters, R. E. (1976). Innovative Wind Machines: The Theoretical Performances of a Vertical Axis Wind Turbine, *Proceedings of the Vertical Axis Wind Turbine Technology Workshop*, Report No. SAND 76-5586.

Ferziger, J. H. & Peri'c, M. (2002). *Computational methods for fluid dynamics*, Berlin; London, Springer.

Fountain, H. (2010). Technology That Generates Tidal Megawatts Like Clockwork. New York Times. 6th May 2010;Sect. 6.

Fraenkel, P.: (2002). Power from marine currents, *Proceedings of the Institution of Mechanical Engineers, Part A: Journal of Power and Energy*, **216**, (1), pp. 1-14.

Fraenkel, P. (2011). Underwater Windmills - Harnessing the World's Marine Currents. *Ingenia*.

Francis, M. S. & Keesee, J. E.: (1985). Airfoil dynamic stall performance with large-amplitude motions, *AIAA*, **23**, (11), pp. 1653-1659.

Freris, L. L. (1990). *Wind Energy Conversion Systems*, Prentice Hall International.

Fujisawa, N. & Shibuya, S.: (2001). Observations of dynamic stall on Darrieus wind turbine blades, *Journal of Wind Engineering and Industrial Aerodynamics*, **89**, (2), pp. 201-214.

Gamstedt, E. K. & Sjogren, B. A.: (1999). Micromechanisms in tension-compression fatigue of composite laminates containing transverse plies, *Composites Science and Technology*, **59**, (2), pp. 167-178.

Garrett, C.: (1972). Tidal Resonance in the Bay of Fundy and Gulf of Maine, *Nature*, **238**, (5365), pp. 441-443.

Garrett, C. & Cummins, P.: (2005a). The power potential of tidal currents in channels, *Proceedings of the Royal Society A*, **461**, (2060), pp. 2563-2572.

Garrett, C. & Cummins, P.: (2005b). The power potential of tidal currents in channels, *Proceedings of the Royal Society a-Mathematical Physical and Engineering Sciences*, **461**, (2060), pp. 2563-2572.

Gorlov, A.: (1997). inventor^inventors; " Helical turbine assembly operable under multidirectional fluid flow for power and propulsion systems". United States Patent 5642984.

Gretton, G. & Bruce, T.: (2005). Preliminary Results from Analytical and Numerical Models of a Variable-Pitch Vertical-Axis Tidal Current Turbine, *6th European Wave and Tidal Energy Conference*, Glasgow.

Gross, R., Heptonstall, P., Anderson, D. & Green, T. (2006). The Costs and Impacts of Intermittency, *UKERC*.

Guasch, O. & Codina, R.: (2007). A heuristic argument for the sole use of numerical stabilisation with no physical LES modelling in the simulation of incompressible turbulent flows, *Journal of Computational Physics*, pp. Submitted for publication.

Gurit. (2009a). SparPreg - UD Prepreg for SPRINT-quality Blade Spars and Roots, *Gurit Internal report*, Report No. PDSWE-SparPreg-4-0309.

Gurit. (2009b). WE91-2 - Prepreg, *Gurit Internal report*, Report No. PDSWE-WE91-2-2-0907.

Gurit. (2011). Guide to Composites, [Accessed June 2011], http://gurit.com/guide-to-composites.aspx.

Hartman, D. & Corning, O., (2006). Analysis of Wind Turbine Blade Failure Modes. *Composites and Polycon*; St. Louis.

Hindmarsh, A. C., Brown, P. N., Grant, K. E., Lee, S. L., Serban, R., Shumaker, D. E. & Woodward, C. S.: (2005). SUNDIALS: Suite of Nonlinear and Differential/Algebraic Equation Solvers, *ACM Transactions on Mathematical Software*, **31**, (3), pp. 363-396.

Houlsby, G. T., Draper, S. & Oldfield, M. L. G. (2008a). Application of Linear Momentum Actuator Disc Theory to Open Channel Flow, *University of Oxford*, Report No. OUEL 2296/08.

Houlsby, G. T., Oldfield, M. L. G. & McCulloch, M. D.: (2008b). inventor^inventors; "Water Turbine". British patent WO/2008/145991.

Howatson, A. M., Lund, P. G. & Todd, J. D. (1991). *Engineering Tables and Data*, Chapman and Hall.

Howell, R., Qin, N., Edwards, J. & Durrani, N.: (2010). Wind tunnel and numerical study of a small vertical axis wind turbine, *Renewable Energy*, **35**, (2), pp. 412-422.

Jeffreys, H.: (1921). Tidal Friction in Shallow Seas, *Philosophical Transactions of the Royal Society of London. Series A, Containing Papers of a Mathematical or Physical Character*, **221**, pp. 239-264.

Jha, A. (2010). Sun, Wind and Wave-Powered: Europe unites to build renewables 'supergrid'. Guardian Newspaper. 4th January.

Johansen, J., Sørensen, N. N., Michelsen, J. A. & Schreck, S.: (2002). Detached-eddy simulation of flow around the NREL Phase VI blade, *Wind Energy*, **5**, (2-3), pp. 185-197.

John, V. & Knobloch, P.: (2007). On spurious oscillations at layers diminishing (SOLD) methods for convection-diffusion equations: Part I - A review, *Computer Methods in Applied Mechanics and Engineering*, **196**, (17-20), pp. 2197-2215.

Khan, M. J., Bhuyan, G., Iqbal, M. T. & Quaicoe, J. E.: (2009). Hydrokinetic energy conversion systems and assessment of horizontal and vertical axis turbines for river and tidal applications: A technology status review, *Applied Energy*, **86**, (10), pp. 1823-1835.

Khan, M. J., Iqbal, M. T. & Quaicoe, J. E.: (2006). Design considerations of a straight bladed Darrieus rotor for river current turbines, *2006 IEEE International Symposium on Industrial Electronics, Vols 1-7*, pp. 1750-1755.

Kong, C., Bang, J. & Sugiyama, Y.: (2005). Structural investigation of composite wind turbine blade considering various load cases and fatigue life, *Energy*, **30**, (11-12), pp. 2101-2114.

Leclerc, C., (1997). Why use natural laminar low airfoils in vertical axis wind turbine applications? *Aerospace Sciences 35th meeting and exhibit*; Reno.

Leishman, J. G.: (2002). Challenges in modelling the unsteady aerodynamics of wind turbines, *Wind Energy*, **5**, (2-3), pp. 85-132.

Li, Y. & Calisal, S. M.: (2010). Numerical analysis of the characteristics of vertical axis tidal current turbines, *Renewable Energy*, **35**, (2), pp. 435-442.

MacLeod, A. J., Barnes, S., Rados, K. G. & Bryden, I. G., (2002). Wake effects in tidal current turbine farms. *MAREC Conference*; Newcastle.

Madsen, H. A.: (1982). *The Actuator Cylinder, A Flow Model for Vertical Axis Wind Turbines*. PhD dissertation, Aalborg University,

Mahrenholtz, O. & Markiewicz, M. (1999). *Nonlinear Water Wave Interaction*, Computational Mechanics.

Mandell, J. F., Samborsky, D. D., Wahl, N. K. & Sutherland, H. J.: (2003). Testing and analysis of Low Cost Composite Materials Under Spectrum Loading and High Cycle Fatigue Conditions, *ICCM14*, San Diego.

Manwell, J. F., McGowan, J.G. and Rogers, A.L. (2002). *Wind energy explained*, John Wiley and Sons Ltd.

Martin, C. M.: (1994). *Physical and numerical modelling of offshore foundations under combined loads*. DPhil Thesis, University of Oxford, Department of Engineering Science

Massey, B. S. & Ward-Smith, A. J. (1998). *Mechanics of fluids*, Cheltenham, Stanley Thornes.

McAdam, R.: (2007). *Design, build and test of a horizontal axis marine turbine*. Masters project, Oxford University, Department of Engineering Science

McAdam, R. A., Houlsby, G. T., Oldfield, M. L. G. & McCulloch, M. D.: (2010). Experimental testing of the transverse horizontal axis water turbine, *IET Renewable Power Generation*, **4**, (6), pp. 510-518.

McCroskey, W. J. (1981). The Phenomenon of Dynamic Stall, *National Aeronatics and Space Administration*, Report No. B1264.

McCroskey, W. J., McAlister, K. W. & Carr, L. W. (1982). An Experimental Study of Dynamic Stall on Advanced Airfoil Sections, *NASA Technical Memorandum*, Report No. 84245.

McEwen, L.: (2009). Re: Follow up from EWTEC, Personal communication.

McIntosh, S.: (2009). *Wind Energy for the Built Environment*. PhD Thesis, Cambridge University, Department of Engineering

MCT. (2009). Marine Current Turbines reveals details of SeaGen's Operating Performance. [Accessed June 2011]; Available from:

http://www.marineturbines.com/3/news/article/26/marine_current_turbines_reveals_details_of_seagen_s_operating_performance/.

Migliore, P. G. & Wolfe, W. P.: (1979). Some effects of Flow Curvature on the Performance of Darrieus Wind Turbines, *17th Aerospace Sciences Meeting*, 15-17th January, New Orleans.

Migliore, P. G., Wolfe, W. P. & Fanucci, J. B.: (1980). Flow Curvature Effects on Darrieus Turbine Blade Aerodynamics, *Journal of Energy*, **4**, (2), pp. 49-55.

Miner, M. A.: (1945). Cumulative Damage in Fatigue, *Journal of Applied Mechanics-Transactions of the Asme*, **12**, (3), pp. A159-A164.

Myers, L. & Bahaj, A. S.: (2007). Wake studies of a 1/30th scale horizontal axis marine current turbine, *Ocean Engineering*, **34**, (5-6), pp. 758-762.

National Statistics. (2005). Environmental accounts: Emissions; atmospheric, [Accessed May 2008], http://www.statistics.gov.uk/StatBase/Expodata/Spreadsheets/D5540.xls.

Newman, B. G.: (1983). Actuator-Disc Theory for Vertical-Axis Wind turbines, *Journal of Wind Engineering and Industrial Aerodynamics*, **15**, pp. 347.

Newman, J. N. (1977). *Marine hydrodynamics*, Cambridge, Mass., MIT Press.

O'Rourke, F., Boyle, F. & Reynolds, A.: (2009). Tidal energy update 2009, *Applied Energy*, **87**, (2), pp. 398-409.

Oldfield, M. L. G., (2004). Applied fluid mechanics. *Lecture 5: Open channel flow*; University of Oxford: Second year fluids lecture course.

Oran, C. & Kassimali, A.: (1976). Large deformations of framed structures under static and dynamic loads, *Computers & structures*, **6**, pp. 539.

Paraschivoiu, I.: (1982). Aerodynamic Loads and Performance of the Darrieus Rotor, *Journal of Energy*, **6**, (6), pp. 406-412.

Paraschivoiu, I. (2002). *Wind turbine design with emphasis on Darrieus concept*, Polytechnic International Press.

Paraschivoiu, I. & Allet, A.: (1988). Aerodynamic Analysis of the Darrieus Wind Turbines Including Dynamic-Stall Effects, *Journal of Propulsion and Power*, **4**, (5), pp. 472-477.

Peace, S.: (2003). Why not vertical axis?, *Refocus*, **4**, (3), pp. 30-3.

Philippidis, T. P. & Vassilopoulos, A. P.: (2002). Complex stress state effect on fatigue life of GRP laminates. Part I, experimental, *International Journal of Fatigue*, **24**, (8), pp. 813-823.

Ponta, F. L. & Jacovkis, P. M.: (2001). A vortex model for Darrieus turbine using finite element techniques, *Renewable Energy*, **24**, (1), pp. 1-18.

Ponta, F. L. & Jacovkis, P. M.: (2003). Constant-curl Laplacian equation: a new approach for the analysis of flows around bodies, *Computers & Fluids*, **32**, (7), pp. 975-994.

Rainey, R. C. T.: (2009). The optimum position for a tidal power barrage in the Severn estuary, *Journal of Fluid Mechanics*, **636**, pp. 497-507.

Reddy, T. S. R. & Kaza, K. R. V. (1987). A Comparative Study of Some Dynamic Stall Models, *NASA Technical Memo*.

Riddoch, L. (2008). Could active sonar systems, trained by humans, help unlock tidal energy in the UK? *Engineering and Technology*.

Roache, P. J. (1998). *Verification and validation in computational science and engineering*, Albuquerque, N.M., Hermosa Publishers.

Salter, S. H.: (2009). Correcting the Under-estimate of the Tidal-Stream Resource of the Pentland Firth, *EWTEC 2009*, Uppsala, Sweden.

Salter, S. H. & Taylor, J. R. M.: (2007). Vertical-axis tidal-current generators and the Pentland Firth, *Proceedings of the Institution of Mechanical Engineers, Part A: Journal of Power and Energy*, **221**, (2), pp. 181-199.

Schaff, J. R. & Davidson, B. D.: (1997). Life Prediction Methodology for Composite Structures. Part II—Spectrum Fatigue, *Journal of Composite Materials*, **31**, (2), pp. 158-181.

Sheldahl, R. E. & Klimas, P. C. (1981). Aerodynamic Characteristics of Seven Symmetrical Airfoil Sections Through 180-Degree Angle of Attack for Use in Aerodynamic Analysis of Vertical Axis Wind Turbines, *Sandia National Laboratories*, Report No. SAND80-2114.

Shi, Y.: (2008). *PIV analysis of the Transverse Horizontal Axis Water Turbine*. DPhil Transfer Report, Oxford University, Department of Engineering Science

Shiono, M., Suzuki, K. & Kiho, S.: (2000). An Experimental Study of the Characteristics of a Darrieus Turbine for Tidal Power Generation, *Electrical Engineering in Japan*, **132**, (3), pp. 38.

Solomon, S., Qin, D., Manning, M., Chen, Z., Marquis, M., Averyt, K. B., Tignor, M. & Miller, H. L. (2007). *Climate Change 2007: The Physical Science Basis. Contribution of Working Group I to the Fourth Assessment Report of the Intergovernmental Panel on Climate Change*, Cambridge University Press.

Strickland, J. H. (1975). Darrieus turbine: a performance prediction model using multiple streamtubes, *Sandia Labs*, Report No. SAND-75-0431.

Strickland, J. H., Webster, B. T. & Nguyen, T.: (1979). Vortex model of the Darrieus turbine: an analytical and experimental study, *American Society of Mechanical Engineers, Winter Annual Meeting*, 2-7 December, New York.

Sutherland, H. J.: (2004). Effect of Mean Stress on the Damage of Wind Turbine Blades, *Journal of solar energy engineering*, **126**, pp. 1041.

Sutherland, H. J. & Mandell, J. F.: (2005). The effect of mean stress on damage predictions for spectral loading of fibreglass composite coupons, *Wind Energy*, **8**, (1), pp. 93-108.

Swidenbank, R.: (2009). *Computational Analysis of a Transverse Horizontal Axis Water Turbine*. Masters Thesis, University of Oxford, Department of Engineering Science

Tang, D. M. & Dowell, E. H.: (1995). Experimental investigation of three-dimensional dynamic stall model oscillating in pitch, *Journal of Aircraft*, **32**, (51), pp. 1062-1071.

Tchon, K.-F. & Paraschivoiu, I.: (1994). Navier-Stokes simulation of the flow around an airfoil in darrieus motion, *Journal of fluids engineering*, **116**, (4), pp. 870-876.

Templin, R. J. (1974). Aerodynamic performance theory for the nrc vertical axis wind turbine, *NRC of Canada*, Report No. LTR-LA-160.

Timoshenko, S. P. & Goodier, J. N. (1970). *Theory of Elasticity*, McGraw Hill.

Uranga, A.: (2011). *Investigation of transition to turbulence at low Reynolds numbers using Implicit Large Eddy Simulations with a Discontinuous Galerkin method*. Cambridge, MIT, Deparment of Aeronoautics and Astronautics

Vennell, R.: (2010). Tuning turbines in a tidal channel, *Journal of Fluid Mechanics*, **663**, pp. 253-267.

Wahl, N. K.: (2001). *Spectrum Fatigue Lifetime and Residual Strength for Fiberglass Laminates*. PhD Thesis. Montana, Montana State University, Mechanical Engineering

Wang, L. B., Zhang, L. & Zeng, N. D.: (2007). A potential flow 2-D vortex panel model: Applications to vertical axis straight blade tidal turbine, *Energy Conversion and Management*, **48**, (2), pp. 454-461.

Whelan, J., Thompson, J., Graham, J. M. R. & Piero, J., (2007). Modelling of free surface proximity and wave induced velocities around a horizontal axis tidal stream turbine. *Proc. 7th European wave and tidal energy conference*; Porto, Portugal.

Williams, M. S. & Todd, J. D. (2000). *Structures : theory and analysis*, Basingstoke, Macmillan.

Wilson, R. E.: (1978). Vortex Sheet Analysis of the Gyromill, *ASME Journal of Fluids Engineering*, **100**, (3), pp. 340-342.

Young, Y. L., Motley, M. R. & Yeung, R. W.: (2010). Three-Dimensional Numerical Modeling of the Transient Fluid-Structural Interaction Response of Tidal Turbines, *Journal of Offshore Mechanics and Arctic Engineering*, **132**, (1), pp. 011101-12.

Zanette, J., Imbault, D. & Tourabi, A.: (2010). A design methodology for cross flow water turbines, *Renewable Energy*, **35**, (5), pp. 997-1009.

Zienkiewicz, O. C., Taylor, R. L. & Nithiarasu, P. (2005). *The finite element method for fluid dynamics*, Amsterdam ; London, Elsevier Butterworth-Heinemann.